The Pennsylvania State University

The Graduate School

College of Engineering

CHARACTERISTICS OF A ROTOR OPTIMIZED FOR HOVER AND

FORWARD FLIGHT

A Thesis in

Aerospace Engineering

by

Christopher M. Kroninger

Submitted in Partial Fulfillment

of the Requirements

for the Degree of

Master of Science

May 2008

The thesis of Christopher M. Kroninger was received and approved[*] by the following.

Farhan Gandhi
Professor of Aerospace Engineering
Thesis Advisor

Mark D. Maughmer
Professor of Aerospace Engineering

George A. Lesieutre
Professor of Aerospace Engineering
Head of the Department of Aerospace Engineering

[*] Signatures are on file in the Graduate School.

Abstract

A methodology has been implemented to minimize the total power consumption of a rigid hingeless rotor. The baseline rotor has a 20ft radius with both 10% root cutout and blade solidity and operates at a C_T of 0.007 in hover. The rotor is optimized at five advance ratios, 0.0, 0.1, 0.2, 0.3, and 0.4. A free wake model is developed with a lifting line to model the wing. The input of the code can be either the desired circulation or pitch distribution. A gradient based optimizer built around the free wake analysis allows the distribution to be modified at 15 radial by 36 azimuthal elements. A perturbation contour is added to the original distribution to obtain an improved distribution and then a new perturbation contour is found in an iterative process. This process repeats until the change in power is less than one percent for a given perturbation contour. The resulting optimized contours yield savings in hover of 30.0% with more modest gains of a few percentage points in forward flight. The main source of power savings is a reduction in induced power at all speeds. The lift distributions tended to move lift production inboard although this would be accomplished in different regions of the disk depending on the flight speed. The optimized solutions also responded to sharp and discrete features in the wake. Effects of trailing vortices near the disk can be seen in the downwash and the optimized twist distribution seeks to follow these features. The lift and twist distributions vary with significant non-linearity both radially and azimuthally. There is also little coherence radially between the magnitude and phase of respective harmonics composing these distributions.

Table of Contents

List of Figures

List of Tables

Nomenclature

Variables:

a_1	core growth coefficient
c	blade chord (m,ft)
C_D	vehicle drag coefficient
c_d	sectional drag coefficient
c_ℓ	sectional lift coefficient
$D_{parasite}$	vehicle parasite drag (N,lbs)
d	sectional drag (N/m,lbs/ft)
F_r	blade force component in the radial direction (N,lbs)
F_z	blade force component in the z-direction (N,lbs)
F_θ	blade force component in the azimuthial direction (N,lbs)
H	vehicle lateral force (N,lbs)
$\vec{l}$	sectional lift vector (N/m,lbs/ft)
l	sectional lift (N/m,lbs/ft)
M_x	vehicle pitching moment (N·m,lbs·ft)
M_y	vehicle rolling moment (N·m,lbs·ft)
N	number of blades
n	iteration variable
P	vehicle rotor power (N·m/s,lbs·ft/s)
Q	vehicle rotor torque (N·m,lbs·ft)
R	length from rotor hub to blade tip (m,ft)
$\vec{r}$	position vector (from vortex filament location s) (m,ft)
r	distance along blade (m,ft)
r_o	blade cut-out (m,ft)
S	vehicle flat plat area (m^2,ft^2)
s	position vector on vortex filament (m,ft)
T	vehicle thrust force (N,lbs)
t	time (s)
$u_{induced}$	x-component of the induced velocity (m/s,ft/s)
u_{local}	x-component of the velocity relative to the blade section (m/s,ft/s)
u'	x-component in the rotor disk plane (m/s,ft/s)
V	vehicle longitudinal force (N,lbs)
$\vec{V}_{induced}$	velocity induced by vorticity (m/s,ft/s)
$\vec{V}_{local}$	velocity relative to the blade element (m/s,ft/s)
$\vec{V}_\infty$	free stream velocity or flight speed (knots,m/s,ft/s)
$v_{induced}$	y-component of the induced velocity (m/s,ft/s)
v_{local}	y-component of the velocity relative to the blade section (m/s,ft/s)

v'	*y*-component in the rotor disk plane (m/s,ft/s)
W	vehicle weight (N,lbs)
$w_{induced}$	*z*-component of the induced velocity (m/s,ft/s)
w_{local}	*z*-component of the velocity relative to the blade section (m/s,ft/s)
w'	*z*-component in the rotor disk plane (m/s,ft/s)

α_{aero}	aerodynamic angle of attack (radians,degrees)
α_{geo}	geometric angle of attack (radians,degrees)
α_{shaft}	vehicle shaft angle of attack (radians,degrees)
Γ	sectional circulation vector (m^2/s,ft^2/s)
δ	vortex core growth rate
θ	blade twist (radians,degrees)
θ_{col}	collective pitch (radians,degrees)
θ_{c1}	longitudinal cyclic pitch (radians,degrees)
θ_{s1}	lateral cyclic pitch (radians,degrees)
θ_{tip}	blade twist at the tip (radians,degrees)
λ	inflow ratio
μ	advance ratio
π	3.14159
ρ	density of air (kg/m^3,slug/ft^3)
σ	rotor solidity
υ	kinematic viscosity
Ψ	rotor angle (radian,degrees)
Ω	angular velocity (radians/s,degrees/sec)

Abbreviations:

ANM	Analytical/Numerical Matching
ATB	Active Twist Blade
BVI	Blade Vortex Interaction
CAMRAD	Comprehensive Analytical Model of Rotorcraft Aerodynamics and Dynamics
CAMRAD II	Comprehensive Analytical Model of Rotorcraft Aerodynamics and Dynamics II
CDI	Continuum Dynamics Inc.
CFD	Computational Fluid Dynamics
HHC	Higher Harmonic Control
IBC	Individual Blade Control
MiTE	Miniature Trailing-Edge Effectors
NACA	National Advisory Committee of Aeronautics
NASA	National Aeronautics and Space Administration
PSU	The Pennsylvania State University
UMARC	University of Maryland Advanced Rotorcraft Code
VTM	Vortex Transport Method

Acknowledgments

I would like to thank Farhan Gandhi, my advisor, for his input on the research and comments on my thesis as well has the resources he has provided me along the way. These enabled me to pursue this research while at Penn State and to continue it from afar while starting my engineering career, the opportunity of which I am further indebted to him. The input of Mark Maughmer in editing this work has provided an appreciated perspective and has certainly improved the work. Thanks to Matt Floros for running the CAMRAD II comparisons for my validation and to T. Alan Egolf for a discussion of my free wake analysis and data. I am also grateful to Penn State and the Aerospace Department which includes many people who have put me on a path toward accomplishing this work. The thesis process has not only taught me much about this topic, but it has afforded me the even greater opportunity to learn about myself as a researcher. As with any novice, I have found a great many weaknesses in my effort, the knowledge of which will improve my future endeavors.

Finally I would like to thank my parents for their support throughout my life and school. Most especially, I must acknowledge the many sacrifices made by my wife in both lost time together on countless evenings and weekends and to her deferred career during this period. April has brought balance to my life by both pushing me ahead at times and reminding me to take a break at others. I am grateful to have her support.

Chapter1:   Introduction

Selecting a blade twist for a helicopter requires settling on some compromise effective from hover up to the desired forward flight speed. Deciding how to make this decision is challenging as the ideal blade geometry in hover varies a great deal from that which is best in forward flight. For example, CDI[1] has developed an ideal twist distribution in hover based on minimizing the induced power which has resulted in 25 degrees of non-linear twist characterized by a "twist bucket" at the tip to accommodate passage of the previous trailing vortex filament moving in close proximity to the blade. For forward flight Cattopadhyay et al.[2] has suggested that much less twisted blade is appropriate. For an advance ratio of 0.3, they found a non-linear pitch with a maximum of 6° of twist to be optimum. Keys et al.[3] have demonstrated the difficulty negotiating this compromise by testing two blades differing only in the magnitude of their linear twist: -11.5˚ verses -17.3˚. In hover, they found a 2.4% reduction in power using the higher twist but in forward flight, there tended to be about a 5% increase in required power. Currently, according to Leishman[4], most helicopter blades have been designed to incorporate a negative linear twist between eight and 15°.

Contrasting sources of power consumption over the flight regime drives this difference in ideal rotor twist distributions. The major contribution to power consumption at low advance ratios is induced drag while at higher speeds the induced power drops off and the parasite power of the vehicle becomes the larger contributor[4]. Throughout the traditional flight regime, the profile power of the rotor disk tends to increase only modestly with increasing advance ratio relative to the changes in parasite or induced power. Since parasite drag is largely a function of the vehicle and the induced drag tends to be a larger portion of the power consumption than that of the profile drag, many recent studies have looked to minimize rotor induced power while ignoring profile drag[1, 5, 6, 7, 8].

Improvements in both material technology and computational performance are allowing for better prediction and manufacturing of tailored rotor blades for higher performance rotors. While many aspects of a rotor blade will affect its power consumption, taper, sweep, anhedral, rotor speed, airfoil, etc., only the circulation

distribution will be varied in this study. Among the techniques posed for obtaining more ideal lift distributions is a passive one, tailoring the blade such that its twisting deformations improve the performance of the blade over that of an untailored blade. By varying the blades mass and stiffness distribution Blackwell and Merkley[9] showed analytically it was possible to tailor the dynamic response to gain power reductions. Active methods have also been employed to obtain an improved twist distribution. In one of the seminal works on higher harmonic control, Stewart[10] showed that second harmonic control can be used to reduce flapping and to avoid stall by redistributing the disk loading toward the retreating side of the disk. Recent work by Cheng and Celi[11] using more contemporary analysis have confirmed that second harmonic control can be used to reduce power consumption by very modest amounts, on the order of 1-2%, as well as increase thrust or reduce required rotor angular velocity depending on the parameter of interest.

Besides the traditional actuation at the root, one method to achieve twist control is through actuators embedded in the skins of a rotor blade to allow for twist control down the span of the blade. One example of this is the NASA/ARMY/MIT active twist rotor blade[12] which is a 1.4 meter blade with a -10° pretwist made of fiberglass and actuated by layers of PFC (Piezoelectric Fiber Composite) embedded in the airfoil skins. This blade in a bench test at one and 10 Hz was able to produce a twist rate of about 1°/m, Bernhard et al. [13] Wind tunnel tests of this rotor at the NASA Langley Transonic Dynamics Tunnel demonstrated power decreases of between 1.1 and 1.9% using only second harmonic control, Sekula,[14] and Wilber.[15] With the advent of smart material actuation, flaps are also becoming a viable concept, which was not the case several years ago as the control systems would have been prohibitively heavy and intrusive[16]. Flaps allow for Individual Blade Control (IBC) rather than a harmonic control over the entire blade system. The University of Maryland[17] has built a Froud Scaled Model blade which exhibited ± 6° of flap deflection at 4/rev. Although their focus was on vibration reduction, trailing edge flaps could, in principle, be used to obtain a more efficient lift distribution. Fulton and Ormiston[18] have demonstrated similar deflections for a model helicopter in hover.

Miniature Trailing-edge Effectors (MiTE) are an example of active control where a tiny flap (only a few percent of the chord) can be deployed near the trailing edge of the

rotor blade. They are deployed perpendicular to the body usually near the trailing edge to increase c_ℓ for a minimal actuation force penalty. They can vary the amount of deployment allowing for smooth actuation variation. They could be distributed and actuated in spanwise segments thus allowing for changing the spanwise lift distribution. Kinzel et al.[19] have produced CFD results and validated them with experimental data obtained at the NASA Ames Compressible Dynamic Stall Tunnel of a VR-12 airfoil with MiTE's. Maughmer et al.[20] extended this work for application to helicopter flight using the data collected in the CFD models to create an unsteady airfoil model for a blade element analysis with deployable Gurney flaps. Results demonstrate that at high speeds where the retreating blade begins to stall, the deployment of the flaps decreases required power by eliminating stall. At low speeds, there are no differences as the blades are not near stall and therefore the MiTE's are not deployed.

Blade morphing is a method of changing the airfoil characteristics through altering the airfoil shape. It has the potential to reduce drag because the conformable surface does not require seams or hinges which can cause higher drag and within limits can conform to a set of more ideal shapes as it moves around the rotor disk. Anusonti-Inthra[21] looked at conformable rotor airfoils for reducing vibration using distributed piezoelectric actuators. He was able to create a structure which produced 4.24° of trailing edge deflection while the structures shape remaining insensitive to the aerodynamic loads it experienced, less than 0.24° aerodynamically induced deflection. This resulted in about a 25% increase in lift and 11% increase in drag in full deflection over that of an undeflected airfoil. These technological advancements will allow for much greater flexibility in obtaining a desired lift distribution and should allow for reductions in power consumption.

Given all these developing capabilities, it is important to understand what the ideal lift distribution should be. The goal of this study is to determine the ideal lift distribution to minimize power consumption through a range of advance ratios and to understand the component powers and sources of power reduction. This is valuable for both understanding the upper limit of a helicopter's performance and how the above mechanisms should be applied.

1.1 Optimization

Historically there have been many attempts to find the minimum power required for a given flight scenario. Among the earliest was finding the optimum lift distribution to minimize the induced drag of a fixed wing aircraft accomplished by Munk[22]. He demonstrated that for a fixed wake of trailing vorticity shed parallel to the free stream velocity behind a wing with no roll-up at the tips that the lift distribution which yields a constant downwash over the entire span of the wing produces the least induced drag. It is found that this constant downwash distribution is the result of an elliptical spanwise loading. For an untwisted planform with an ideal constant airfoil cross-section, an elliptical chord distribution yields an elliptical lift distribution and constant downwash[23]. This solution, despite these assumptions remains a very good approximation of ideal distribution for high aspect ratio wings. Betz[24] describes a similar condition for a "lightly loaded" screw propeller. This is a prescribed helical wake where the free stream flow is axial relative to the rotor disk. The phrase "lightly loaded" implies that there is no contraction of the wake – therefore the near-wake geometry is the same as the far-wake, which is only a valid assumption for low thrust coefficients. In this case, he found that the lift distribution which consumed the least power due to induced drag was that which produced a helical far-wake and therefore constant induced axial flow. Thus, the same condition as Munk described for a fixed wing aircraft, a constant induced downwash or inflow. Although Betz described the condition for minimum induced power, he did not provide the actual circulation distribution which would produce this condition. Prandtl described a method for approximating the flow-field around this "screw propeller". This method is a two-dimensional approximation looking at the *r-Z* plane (his solution assumes the flow is unchanging in the azimuth) and treats the helical sheets cutting through this plane as discrete lines of vorticity emanating from the axis of the screw to a point equivalent to the radius of the blades of the propeller. The flow field describes the "leakage" of fluid or induced flow around the edge of the helical wake and provides the circulation distribution over the propeller blades. Goldstein[25] found an exact analytic solution for the condition Betz described. Using Bessel functions, he was able to describe the flow field in the far-wake analytically and therefore the circulation distribution necessary to create it. This analytic solution, while impressive, does not

provide much information for analyzing a helicopter. The wake in forward flight is obviously skewed making the propeller wake incompatible. However, even for hover, there is both the question of wake contraction and the formation of the tip vortices. The strong tip vortices of a helicopter typically descend much slower than the rest of the wake. They basically serve as the interface between the internal downwash and external induced upwash[26]. In Goldstein's solution all the trailing vorticity retreats at the same rate, which would tend to occur with higher free stream axial velocity. The circulation gradient also does not change as rapidly at the tips for a propeller and are therefore not as strong. Therefore Goldstein's solution becomes increasingly in error as the free stream axial flow decreases, and it is not valid for hover where all the axial flow is induced[27]. In climb this solution is increasingly valid with increased speed of assent.

Another approach apart from the wake models just considered are the solutions provided by Blade Element-Momentum Theory (BEMT). Using this method, Gessow[28] showed that a constant downwash in hover will occur with a twist distribution of,

$$\theta(r) = \theta_{tip} \cdot \frac{R}{r} = \alpha_{eff} + \frac{w_{ind}}{\Omega r}.$$ (1.1.1)

This distribution yields a constant effective angle of attack α_{eff} and constant downwash. He also demonstrated that minimum blade profile power can be obtained using the following chord distribution,

$$c(r) = c_{tip} \cdot \frac{R}{r},$$ (1.1.2)

where by the airfoil is operating at c_{d_o} at every point on the blade. This method also leads to the ideal torque coefficient,

$$C_Q = \frac{C_T^{3/2}}{\sqrt{2}} + \frac{\sigma}{9} \cdot c_{d_o},$$ (1.1.3)

This solution provides a good reference value but under predicts any likely obtainable value. Harris and McVeigh[29] suggest a reasonable upper limit for figure of merit of 0.85. The problem with the BEMT conclusion is that it is based on an actuator disk which spreads the effect of the blades evenly all the way around the azimuth. It also does not satisfy the boundary condition that the circulation go to zero at the blade tips, thus yielding an infinite span-wise circulation slope at the tips of the rotor blades.

Prouty[30] also used an actuator disk to model a helicopter in forward flight. He resolved the wake of an infinite blade model into a single sheet of trailing vorticity which looks much like the wake a fixed wing aircraft would create. In fact, like a fixed wing wake, the wake would be unchanging in the longitudinal direction since it is shed from an infinite number of blades. The induced velocity could then be found by integrating the effects of the vorticity laterally through the wake. The induced velocity vary laterally, but, ignoring fore/aft variation across the disk, this method naturally leads to the same result as the fixed wing solution for minimum power consumption, an elliptical lift distribution with a constant downwash. He used this formulation as the basis for an induced power efficiency factor that would serve the same purpose as Oswald's Efficiency Factor in the fixed wing arena.

Harris and McVeigh[29] explored the application of lifting line theory to rotorcraft and the production of uniform inflow. They noted a discrepancy between BEMT's prediction that a uniform bound circulation strength down the span of the blade will yield a constant downwash and the non uniform inflow produced by a helical tip vortex which would represent the result of constant circulation strength. They also compare the ideal solution for fixed wing aircraft with a potential for rotorcraft. They suggested that a rotor blade in hover with ideal twist should compare closely with that of a fixed wing aircraft with ideal lift distribution. This is because the local velocity the blade experiences increases proportionally to radius while ideal twist is inversely proportional thus having a canceling effect resulting in the same near-wake on the blade as an untwisted fixed wing in forward flight. There are secondary effects such as the curvature of the shed wake and the interaction with other blades' wakes which do alter the solution. Therefore, to first order effects, the ideal solution should be similar to that of a fixed wing.

Theodorsen[31] used Betz's principle for minimum induced power for propellers to model the "static propeller" or hovering helicopter. His principle basically states that in the far-wake, the induced axial velocity of the wake must be constant everywhere. In hover, the symmetry of the scenario allows the optimization problem to be posed as one equation and one constraint. Written as a ratio, the solution where by the ratio of the first derivative of the power by circulation and thrust by circulation, $\frac{\partial P}{\partial \Gamma} \bigg/ \frac{\partial T}{\partial \Gamma}$, is constant at all

points along the blade is therefore the ideal. This equation implies that there is no region of the blade where extra benefit could be gained by changing the circulation. Using this method with a blade element formulation of power and thrust, he found that not only is the downwash constant in the far-wake but also at the disk. Having come to this conclusion and knowing the far-wake solution from Goldstein, he was able to calculate the radial contraction of the wake with axial distance and thus fully describing the wake. His ideal solution has a contracting wake with a uniform downwash at any given horizontal cross-section, but later results have shown that this does not reflect an ideal geometry of a typical helicopter wake.

Moffitt and Bissell[27] demonstrated a corrected solution with the inclusion of a term in the power equation missing from Theodorsen's formulation which accounted for changes in power due to changes in induced velocity. They describe the optimum lift distribution around the rotor disk in hover based on minimizing total power. They numerically performed a formal optimization to minimize total power while maintaining a given thrust. Their approach used a wake geometry model based on empirical data governed by a few major parameters. Profile drag was modeled using higher order algebraic expressions. This wake geometry (which reflects measurements taken by Langrebe[26]) creates a quickly contracting wake most of which occurs within one revolution. Sheets of vorticity in the wake descend at a rate which varies linearly with radial distance from the hub. The tip vortices descend slower and their descent rate is a function of the peak circulation. This solution is compared with experimentally obtained data from the blades of the UH-60. They found that the anticipated constant downwash only occurs on the inner 75% of the blade. The outer 25% reflects the region of the blade which is strongly influenced by the tip vortices descending slowly and remaining close to the disk. They also found that the ideal circulation distribution was not flat but had a large spike at the tip. The twist is not far from the ideal BEMT twist in hover but with a twist bucket at the tip. They also looked at the optimal twist distribution in forward flight imagining that the blade could twist azimuthially in an unconstrained fashion. This model uses a rigid helical wake. They found continued improvement with forward flight speed over the baseline rotor on the order of 10%. In comparing the major differences between the baseline and optimized solutions, they note that the optimized solution tends

toward a more symmetric loading fore and aft as well as eliminating the negative lift on the advancing tip.

Prior to Moffitt[27], Blackwell and Merkley[32] explored ideal loading in forward flight to design an aeroelastically conformable rotor. In order to accomplish this, they first had to determine the ideal twist distribution which they would attempt to match. Consideration was given to several possible ideal rotors include maximum L/D, maximum c_ℓ, or minimum c_d, but minimizing the ratio of rotor torque to lift was settled upon. This solution was determined using calculus of variations. Because of the difficulty in minimizing the induced drag, it was excluded from the calculations. Two advance ratios were considered, 0.3 and 0.4. The results of this analysis were twist distributions for each speed that varied azimuthally and radially. Compared to the baseline rotor modeled after the UH-60A, the major change is a lessening of twist on the advancing side where the blade would be producing negative drag and more twist on the retreating side were the blade is in need of high angle of attack. In stalled regions, the twist is lowered so as not to stall. Contour plots of the relative angle of attack between the optimum and baseline solution display a smoother contour for the optimum which lacks large spikes, presumable beyond the stall angle, which are present in the baseline. Results of the conformable rotor are discussed in section 1.3.

Bennett[33] demonstrated the applicability of formal optimization theory to aid in the design of helicopter components. He briefly described optimization theory and presented four example cases. Included in the optimization examples are the designs of a blade flexure, mast, and blade mass distribution and the twist distribution for hover. The baseline rotor used the NACA 0012 airfoil. The hover optimization minimized power while varying the pitch at 10 radial stations. The constraints were that the thrust must equal a specified value and that the twist not exceed 30° anywhere on the blade. The analysis was performed using BEMT and used airfoil data to capture viscous effects. The solution obtained closely resembled that of the ideal twist distribution describe by BEMT.

Walsh et al. [34] looked at formal optimization using HOVT (a strip momentum theory analysis) and the Rotorcraft Flight Simulation Computer Code C-81 which is a forward flight analysis to design an optimal blade. A single point optimizer, the

Constrained Function Minimization (COMMIN) code, was used to minimize power while maintaining certain constraints. As well as maintaining a specified thrust coefficient, the rotor was required to maintain certain performance standards outside of hover. First, in forward flight, the required power was not to exceed the engine power. Second, airfoil stall was not permitted except in the reverse flow region. Finally, the capability of performing a certain pull-up maneuver with the engine power was maintained. The blade geometry variables included blade radius, taper radius, root chord, tip chord, and maximum twist (which are assumed linear from tip to root). They compared using this formal optimization with the conventional design process which they describe as iterating between chord and twist distributions. The formal optimization results they obtained were described as being similar to those obtained by the conventional design approach, but much more efficiently in both time and man-power.

Hall and Yang[35] developed an approach for forward flight similar to that of Goldstein in that it relies on a non-contracting wake or the "lightly-loaded" assumption. It couples a near-wake solution where the forces, moments, and power are calculated with a far-wake solution where the circulation can be determined numerically from the geometry just as Goldstein did analytically in axial flight. With the sheets serving as the boundary conditions for predicting the flow between the shed helical vortex sheets, a far-wake velocity distribution was found numerically. Again this relies on a prescribed wake with a certain prescribed inflow and models the rotor as flying at zero shaft-angle. Based on this model and subject to the constraints of balancing the vertical forces and the rolling and pitching moments, the optimal lift distributions for minimum induced power were found. The lift distributions tended to be smoother than a baseline rotor and demonstrated a sharp but smooth drop to zero at the tip. The peak thrust values were on the retreating sides at 200° and 340°. These contours also demonstrate symmetry fore and aft. When a limit in airfoil c_ℓ is imposed, the peak values move further toward the blade tips on the retreating side.

Bliss[36] et al. created a free wake code they called Evaluation of Helicopter Performance using Influence Coefficients (EHPIC) which is designed to find optimal solutions in hover and axial flight. There are several different possible objective functions, which include gross thrust, hover figure of merit, axial propulsive efficiency,

or profile, induced or total power. The code uses a lifting surface method to find and model the bound circulation. This lifting surface method uses influence coefficients through which the effects of perturbations of circulation and wake collocation point positions are converged through several iterations. Airfoil data are used to model the profile drag. The wake is a Eularian-style relaxed wake which employs curved vortex filaments to model the trailing vorticity. The code allows for the vortices to merge into a larger one at the tip just as the sheet rolls up in nature which generally results in the merging of vortices between the first and second blade passage. Inboard vortices are larger than the tip vortex to reflect the fact that the inboard vortices really represent sheets. Convergence is defined as when the root sum square of every position perturbation over a given loop is below an arbitrarily specified value.

The EHPIC[37] code was coupled with an optimizer and is presented by Quackenbush et al. Initial studies with the EHPIC code once attached to an optimizer have been presented. The initial work was to demonstrate that one could use a free wake for optimization. Optimization was performed with the variables of twist, taper, anhedral, and sweep at 15 radial segments. Initial results performed with just two trailing filaments suggested this was possible and the two filament models showed large reductions in power as compared to baseline models. One demonstrated effect on the circulation and twist distributions in hover was a bump near the tip due to close blade/vortex interaction. The circulation distribution also tends to be flatter inboard. They moved on to a more realistic models with a tip vortex and 3 inboard large core vortices with 2-3 turns of free wake. Initial results still tended to flatten the circulation distribution over the span of the blade with almost all of the performance improvements due to reduced induced drag. Finally, an initial constraint on airfoil stall limiting $c_{\ell\,max}$ to 0.8 is included in one trial which demonstrates a reduced circulation inboard near the root where the blade reduced its angle to prevent stall. They generally found that compared to twist distributions of current helicopters, the optimized twist distribution tends to flatten the circulation distribution except for a twist bucket at the tip like that exhibited on the UH-60, which they describe as moving the blade out of the way of the forming tip vortices.

Davis et al. [38] have performed an optimization for the blades of a Variable Diameter Tilt Rotor (VDTR) using a modified version of EHPIC for a dual point objective function. For this case, an objective function is formed by a weighted average of the power in cruise and hover. This weighting factor is varied from zero to one to analyze the full range from forward flight to hover and anywhere in between. Optimization used 16 variables for chord, twist, and sweep for a total of 48 variables. Optimizing for twist and chord, they show the ability to improve performance over the entire flight regime while sweep has little effect because of the low tip mach numbers in hover and axial flight.

Several works in recent years have focused on a multi-disciplinary approach to optimization where a blade might be optimized for minimum power but subject to constraints and variables over a wide range of disciplines. This work recognizes that the aerodynamics of a blade can not be decoupled from its structural response and vehicle effects and should be designed with these effects in mind. Mantay and Adelman[39] discussed a NASA/Army joint effort to create a comprehensive optimization code to increase performance while decreasing vibration and noise. The objective function to be minimized is a weighted summation of horsepower and oscillatory loads transmitted to the hub. Design variables included gross blade dimensions, including blade radius, taper radius, root chord, tip chord and twist, as well as the mass distribution while constraints included operational requirements such as not exceeding possible engine power, as well as limiting airfoil stall and trimming the vehicle. Aerodynamic analysis was accomplished using inflow models in hover and climb and CAMRAD's wake model in forward flight. The result of this work is a blade design with significant power improvements though no specific description of the lift or circulation distributions is provided.

Chattopadhyay et al.[2] performed a multilevel optimization where by several cost functions are decoupled and optimized independently in succession. The first level optimizes for minimum power constrained to a constant thrust and minimum solidity. Level two sought to reduce static and vibratory loads while step three took the blade stiffness coefficients calculated on level two and sought to minimize the blade weight.

The aerodynamic model has seven variables which are coefficients of two cubic shape functions for chord and twist,

$$\bar{c}(x) = c_0 + c_1 \cdot (x - 0.75) + c_2 \cdot (x - 0.75)^2 + c_3 \cdot (x - 0.75)^3, \qquad (1.1.4)$$

$$\bar{\theta}(x) = \theta_1 \cdot (x - 0.75) + \theta_2 \cdot (x - 0.75)^2 + \theta_3 \cdot (x - 0.75)^3, \qquad (1.1.5)$$

which generally limited the results to a rather smooth profile. In an earlier work, Chattopadhyay[40] performed a similar analysis using a the shape functions,

$$\bar{c}(x) = \left[1 - x(\lambda - 1) \right] \cdot \left[1 - x^{1/\alpha} \right]^p, \qquad (1.1.6)$$

$$\bar{\theta}(x) = 1 + x^\delta \cdot (\tau - 1). \qquad (1.1.7)$$

The chord is a rectangle distribution with a curved-off tip while the variable α defines whether the chord distribution has a contour with a positive or negative curvature. For blade stiffness the blade geometry was varied at 10 radial stations where the thickness is varied on all side elements of the cross-section. The analysis was performed using tools contained in CAMRAD. The aerodynamic model includes a uniform inflow model and trimmed the helicopter using a wind-tunnel trim data. Optimization is conduced using the CONMIN optimization code. The blade is optimized for one design point at an advance ratio of 0.3. Results showed that compared to a straight rectangular blade with linear twist, a 19.8% improvement in power coefficient is obtained. The optimized blade has a nearly linear chord distribution but a very non-linear distribution in twist with a six degree range from root to tip.

Zibi[41] also performed a similar study for optimal blade design for high speed forward flight (μ=0.463). His analysis also used CONMIN with an aeroelastic performance code R85 developed by Eurocopter. The objective was to minimize power by varying airfoil, twist and rotor planform. Constraints included limiting loading on the pitch links. Results showed a trend toward maximizing chord when an airfoil is operating at a high *L/D* and including tip sweep to reduce drag divergence due to high Mach numbers at the tip.

Two authors have recently published studies minimizing rotor induced power using a free-wake. Rand[7,8] describes a methodology for finding the optimal circulation distribution using a prescribed wake code as well as the free vortex wake code in CAMRAD II. The blade is modeled as a lifting-line. He sites the weak coupling

between the wake geometry and the circulation strength as justification for initially using a prescribed wake code. His methodology used a gradient based optimization to minimize induced power while maintaining a thrust coefficient of 0.0088 and zero hub moments while the shaft angle of attack is always set to zero. The wake is modeled with a single peak for the tip vortex and therefore, the work is limited to advance ratios of less than 0.25 because above that the blade circulation on the tip on the advancing side begins to go negative causing counter-rotating vorticity in that tip region. The circulation is modeled using Fourier coefficients around the azimuth for which Rand asserts that few harmonics are required to model this effectively. For the hover case, once the lift distribution is found, one can find the minimum profile drag chord distribution but this can not be easily accomplished in forward flight. Data are presented for two cases (hover and an advance ratio of 0.25) but no generalizations were drawn from the results. In hover, they found that the circulation was basically flat up from the root up to the tip where the circulation drops off to zero. The forward flight data no longer demonstrated the forward/aft symmetry seen in Hall[35], despite similar flight conditions although it is pointed out that these contours are smoother than a baseline rotor's respective circulation distributions. Performance data from hover to an advance ratio of 0.25 showed that the optimized induced power was, as expected, always less than the reference rotor but above the ideal.

Wachspress, Quackenbush, and Solomon[1] also used a free wake to study induced drag solutions in forward flight and hover. Using their method of influence coefficients in the EHPIC code, they found the twist to minimize the total power on a helicopter in hover for helicopters of varying numbers of blades. The contours included the "twist bucket" but not the peak reflected in the circulation as predicted by Moffit[27]. They suggest that since the induced power is the much larger component in hover, including the profile power does not significantly change the twist distribution. Circulation contours tended to be largely flat with a slight slope which changes as a function of the number of blades.

They also used a relaxed wake model, the CHARM code, to compare several cases in forward flight. The forward flight cases were performed with a shaft angle of zero and trimmed to zero flapping in most cases. To explore only the induced power,

they subtracted off the ram power and what they termed the rotor parasite power which for a shaft angle of zero is the product of flight speed and longitudinal rotor force. There were three parts the forward flight section. The first was a parametric study of linear washout. Since the contour drag was excluded, optimum washout tended to be very high, between 20° and 30°. Effects like stall and compressibility were added but had little effect because they only affected the theoretical lift-curve slope. The second part assigned the circulation directly in mode shapes that varied linearly with radial position and either did not vary azimuthally or did so on the first and second harmonic. These demonstrated lower power consumption for slopes which decreased with radial position (tending toward an elliptical distribution) and optimal one and two per revolution circulations had minimums at 90 and 75 as well as 225 respectively. The third part applied higher harmonic pitch controls over a first harmonically trimmed rotor. Only two advance ratios were presented and second and third harmonic inputs were found to be beneficial with the three per revolution being more effective at 0.2 and two per revolution at 0.4. At 0.4, forth and fifth harmonics were basically found to be ineffective to detrimental depending on the phase angle.

Sun et al. [42] have introduced a method which coupled a 2-D CFD approach with a free-wake code with curved elements. The CFD is used to capture the unsteady effects of the airfoils as well as optimize them for a particular blade. The airfoils are optimized by using a perturbation contour super-imposed on current airfoil contours and seek to maximize the period averaged *L/D*. Then the free wake method is used to optimize the twist and chord distributions. This procedure is performed at an advance ratio of 0.25 and produces a 2.64% decrease in thrust to torque ratio.

Within this list of optimization techniques, all can be broadly characterized as either a parametric study where component variables are systematically varied verses methods which used some optimality condition to solve for a distribution. Optimizing a distribution will be used because it is not limited to specific mode shapes or gross variables but only by the size of the discritization of the model.

1.2 Airloads Prediction

There are generally three categories of models used for helicopter performance prediction.   In order of historical development, they are inflow models, wake models, and other CFD approaches. The relative merits and drawbacks of each are briefly described below as well as an elaborate survey of wake models, the method chosen for this study.

1.2.1 Inflow Models

This method was introduced by Froude and Rankine in the form of momentum theory. Initially these made use of basic control volume conservation laws to determine inflow, thrust, and rotor power. These models traditionally treated the blades as an actuator disk which has no thickness but sustained a finite pressure difference across the disk, thus producing thrust. Momentum theory is applicable to forward flight as well as hover. Glauert provided a formula for the inflow at a given advance ratio based on the inflow through the disk due to flying forward at an angle of attack as well as the induced inflow. Unfortunately momentum theory can only capture gross effects in the wake. Blade element (or strip) theory can be applied to extend the accuracy of momentum theory to account for radial variation.

While in hover, Blade Element-Momentum Theory (BEMT) allows for prediction of inflow, thrust, and power distributions, in forward flight, one must prescribe an inflow distribution in order to obtain the forces and moments. The simplest model assumes a constant inflow though many have proposed different potential models ranging from linear to trigonometric forms. These models have become quite sophisticated today. Mangler[43] used a Fourier series to more accurately model the inflow distribution. Peters et al. [44] have extended this work on a similar track, modeling the rotor inflow using Legendre's equations in elliptical coordinates. This satisfies the continuity equation as Legendre's equations are solution to Laplace's equation in elliptical coordinates. Using this method, one can capture the unsteady pressure on the rotor blades rather than over the entire disk.

1.2.2 Computational Fluid Dynamic Models

A second possibility and an increasingly viable method for modeling helicopter performance is through CFD approaches. With current computational resources, fully three-dimensional Euler or Navier-Stokes (N-S) models are not yet feasible for design optimization. Leishman[4] suggests these models are still very grid dependent and too slow for full design work, although they have been valuable for studying some features such as tip vortex formation. Some hybrid methods may soon be feasible for optimization. Anusonti-Inthra[45] produced a fully coupled hybrid particle VTM-CFD model where a three dimensional Navier-Stokes (N-S) CFD mesh is built around a blade to only a few chord lengths away from the blade in any direction. The N-S CFD region is effective in capturing vorticity production and blade loading as well as the effects of unsteadiness, compressibility, and stall which inviscid methods can not capture. The particle Vortex Transport Method (VTM) is a larger over-laid grid, extending three to five rotor radii from the axis of rotation, which takes the vorticity produced in the N-S region and determines how the wake will evolve. This induced velocity is also fed back into the N-S model as a boundary condition for the next time step. The particle VTM method has the benefit of requiring fewer grid points than the N-S and does not diffuse the vorticity away as N-S approaches tend to do. Bhagwat et al.[46] have also created a hybrid approach between HELIX-I$_A$, a Vorticity Embedding (VE) method; and TURNS, a RANS CFD approach. The CFD mesh is again encapsulated with the VE grid as in the above method. They noted the importance of capturing the descent rate of the tip vortex between its formation to the first blade passage for which there is a difference between that predicted by HELIX-I$_A$ alone and the hybrid method. Beyond the first blade passage, trailing vortex descent rates are consistent. For now, these methods remain too computationally intensive for this work.

Vortex Wake Models:

A final methodology and the one chosen for this research is wake modeling. Wake models attempt to capture the effects of interactions between the rotor blades and their wakes. These models can be broadly generalized as either prescribed wake models where the wake follows a course tracked out by the rotor blades through space or whose

position is empirically described by models such as that created by Landgrebe[26] and Egolf,[47, 48] or a free (or force-free) wake, where the wake is allowed to distort in the presence of the velocity field it creates. These models are founded on Helmholtz's Theorem which states that a vortex filament in an inviscid flow can not end in a flow and therefore a vortex in a flow field must form a closed path or end at a physical barrier. In the case of a wing or rotor blade, any change in circulation on the wing must be shed into the wake which trails behind it. This wake of vorticity induces a flow field which is super-imposed over the free stream velocity and affects the aerodynamic forces produced by the blade.

Prescribed wakes are less numerically intensive but require the user to make assumptions about how the wake will deform. The wake geometry and the velocity field it induces influence the bound circulation and therefore, the more accurate the wake is, the more accurately the forces will be predicted. Prescribing a wake geometry is not a simple task, as the geometry is complicated and is a function of many variables. For example, in hover, there is a significant amount of wake contraction and the trailed sheets quickly roll-up into the tip vortices. Approaches to prescribing wakes have varied from ignoring these affects, as Hall[35] and Goldstein[25] have done using the lightly-loaded rotor assumption, to incorporating some empirical observations into the wake model as Landgrebe[26] and Moffitt[27] have done. No matter the model, prescribed wake models can not be used for performance optimization unless the model makes some provision for changes in wake geometry as the circulation distribution changes. Otherwise any optimization will exploit the fixed geometry and load the blade in a non-physical manner. Landgrebe's model,[26] for example, takes into account the changing descent rate of the tip vortices depending not only on the thrust coefficient but also the blade twist. Ultimately though, any inaccuracies in the model will be reflected in the optimized solution, so there is an incentive to use as accurate of a model as possible.

Increases in computational speeds have recently made free wake optimization more feasible. Free wake methods are attractive because they incorporated a flexible wake geometry in the solution and therefore remove the limitations imposed by the prescribed-wake models. Of the free wake models, there are two approaches, time marching and relaxation. Time marching methods usually begin with a prescribed wake

or no wake at all. Over successive time steps, new vortex filaments are shed into the wake at the trailing-edge of the rotor blade while the entire wake convects through the velocity field. In a steady problem, eventually this method will converge to a periodic solution. Time marching (or Lagrangian) methods have the advantaged of being capable of modeling unsteady problems including maneuvering flight, although they have the disadvantage of traditionally being unstable in and near hover. Relaxation (or Eularian) techniques begin with a prescribed wake as an initial guess and this is allowed to "relax" until the individual vortex filaments are tangent to the flow at control points throughout the flow field. This wake tends to be more stable in hover depending on the chosen algorithm. Below is a brief description of various free wake codes which have been described in the literature.

Scully, [49,50,51] Clark and Leiper,[52] and Landgrebe[53] all laid some early ground work for free wake codes. Scully's work is of particularly note as it formed the foundation of early versions of existing comprehensive codes such as the CAMRAD series and UMARC. Scully wrote an iterative relaxation free wake analysis for hover which tracks the motion of a single trailing vortex at the tip. The inboard sheet is modeled as one prescribed vortex at the mid-span of the blade with the possibility of shed vortices. The shed vorticity is basically ignored for his analysis making the assumption that, at the low advance ratios used in his study, lift does not change drastically around the azimuth and therefore minimal vorticity is shed into the wake. The tip vortex is composed of 15° linear segments with a circular arc filament used to capture the self induced velocity on a point itself. In a later version of the code, provisions for inboard sheets were made instead of using a vortex filament. The possibility to model linear variation across the filaments and sheets were also included. In hover six to 12 turns of free wake are added to a semi-infinite vortex cylinder to fulfill the conservation of mass boundary condition. In forward flight, he used two to four rotations. In order to help stabilize the distortion (relaxation) routine, the previous distortion velocity is averaged with the current value. He also employed an artificially large vortex cores to smooth the blade loading.

Clark and Leiper[52] devised a relaxation full-span free-wake code for hover performance integrated with lifting line theory that employs empirical airfoil data and

blade flapping. The trailing filaments are spaced unevenly along the span to collect more at the tip. The code uses straight vortex filaments to approximate the curved contracted helical filaments in the near-wake. Lacking data on viscous core thickness, the tangential vortex velocity is ignored for any region over 400 feet per second. In the far-wake, 60° segments of a vortex ring form steps for 30 revolutions below two free turns. A predictor-corrector method is used to find the new position of the vortices. It averages the current value with the future to increase stability. Convergence was judged visually by examining figures drawn by computer-aided graphics.

Landgrebe[53] applied a time marching free wake methodology to forward flight. The model only predicted the wake distortion and was not coupled with a performance prediction code. This code is a lifting line method that prescribes the bound circulation and the initial wake geometry. The wake is modeled using the trailing filaments due to spanwise variation, but ignores the shed filaments due to the variation in lift as the blades move around the disk, suggesting this is only a secondary effect. This is justifiable since the shed vorticity will be much smaller than the trailing vorticity at low advance ratios. The vortex core is treated as 1% of the blade radius irrespective of wake age. Within the core, induced velocity is assumed to be zero. The wake was divided into 15° increments with up to 10 radial segments of trailed vorticity and five rotor revolutions. The code uses a first order explicit Lagrangian relationship to determine the change in position over a single time step. These equations are,

$$\Delta x = \left(u_i + V_\infty \cos\alpha\right)\cdot \Delta t / R, \tag{1.2.1a}$$

$$\Delta y = v_i \cdot \Delta t / R, \tag{1.2.1b}$$

$$\Delta z = \left(w_i + V_\infty \sin\alpha\right)\cdot \Delta t / R, \tag{1.2.1c}$$

$$\Delta t = R \cdot \Delta\psi / V_{tip}. \tag{1.2.1d}$$

Convergence is determined when a fixed periodic geometry is reached. In each time step, there was a limit to the induced velocity allowed to help stabilize the code. To increase speed, the far-wake is calculated once initially and this value remains constant for the rest of the calculation. Landgrebe found that the computational cost of several trailing filament was too much for the time and that reasonable results could be obtained without the inboard trailers.

The Comprehensive Analytical Model of Rotorcraft Aerodynamics and Dynamics[54] (CAMRAD) was the first version of a continually evolving rotorcraft performance prediction code written by Johnson. This code couples a blade dynamics and aerodynamics model which can be applied to several helicopter configurations; rigid, gimbaled, or teetering. The bound vorticity is modeled with segments having a linear distribution of circulation. The code has many options for modeling the aerodynamics. For example there are several wake modeling options: one can use a simple assumed prescribed geometry, provide data from experimental measurements, or calculate a free wake. This free wake model includes the explicit iterative relaxation approach taken from Scully. It models only the tip vortex as free. The inboard local wake can be modeled with rectangular sheets of varying numbers or as a prescribed vortex lattice. When using the sheets, directly behind the blade there are many slightly overlapping rectangular sheets over the span of the blade, but the number of sheets decreases while their size increases with distance from the blade finally reducing to just one in the far-wake. The inboard sheets can also be used to model the tip roll-up as the tip sheet is allowed to roll back on the others.

Sadler[55,56] wrote a time marching lifting line approach which uses elements with a linear circulation distribution to represents the bound circulation. The solution begins impulsively from rest and a vortex lattice wake made of linear filaments begins to form behind the wing. To save on computational time, the shed filaments of the vortex lattice are ignored after a specified distance leaving only the trailing filaments. To find the velocity at the junction between two elements, the two elements are modeled as segments of a circular arc so that a self-induced velocity component may be found. The vortex core model is a Rayleigh velocity profile where the peak velocity is specified as a certain percentage of the rotor tip speed. This parameter was varied to match different experimental results. This model also includes vortex stretching, vortex spreading - which is essentially using a extra-large core size for the inboard shed and trailing vorticity since they actually represent more diffuse sheets of vorticity which do not demonstrate extreme peak values, as well as limiting the largest possible velocity in those "sheet" profiles. The core radius of the inboard lines is half the sheet radius. The distortion of the wake is determined using forward explicit Euler integration.

Berry[57] created a time marching free wake method in an attempt to model surface pressures on the fuselage of a helicopter in forward flight with blade flapping and lagging. The model uses a vortex lattice surface to model the blades and wake while the fuselage surface is made of a constant strength source panels. The wake starts impulsively and is allowed to convect with the induced flow field. Since the wake is a vortex lattice, it captures the unsteadiness due to shed vorticity of the flow. No details are provided to describe how the deformation is calculated.

Egolf[47,48] used a time marching approach which modeled the bound circulation as a lifting line and the wake using a vortex lattice method to model the wake, built up from shed quadrilaterals of constant vorticity. These boxes, by forming a closed path, satisfy Helmholtz's Theorem by leaving no vortex filaments ending in the flow field, and therefore model the shed as well as the trailing vorticity. The wake is then essentially a time history of the circulation produced at the rotors as they move away. In order to model the wake motion, an explicit Euler time integration is used. The viscous core vortex size is based on a percentage of the box width which was either 10 or 30% of the width, the difference having little effect on the results. He also used 24 shed lattices with a more densely packed array near the tip to capture the physics of the tip roll-up. Three revolutions of filaments using 7.5° segments were used. A convergence criteria of less than 2% change in the period averaged thrust coefficient per revolution was used.

Bliss et al.[58] introduced the application of a parabolic arc curved filaments rather than a straight-line or circulation arc vortex filaments for modeling the rotor wake. These Basic Curved Vortex Elements (BCVE) allow for modeling the rotor wake with fewer elements than is necessary for the straight line filaments and therefore require less computation time. Along with these elements, it was necessary to devise a method of determining curvature and orientation of the elements. Curved elements necessitate the use of two types. Because the elements are curved it induces a velocity on itself. For a straight line this value is either zero because all the points composing the filament fall on the center of the viscous core or is indeterminate if using the inviscid solution. Therefore they applied Self Induced Vortex Elements (SIVE). The SIVE is accomplished by performing the integral from either end of the filament toward the control point on the curve. Using a specified cut-off distance around the control point allows one to obtain a

finite value as the integrals approach the singularity at the control point. One disadvantage of this method is that it is computationally more time consuming to calculate the induced velocity than it is for a straight line segment. These elements were incorporated as a subroutine to Boeing's B-65 rotor air loads computer program while converting it from a prescribed to free wake code. This method uses a predictor-corrector time-stepping approach to their solution. The far-wake is rigid to allow for proper convergence. Convergence is based on the position of the collocation points remaining constant between iterations.

Quackenbush et al.[59] describe a new methodology which employs a method of influence coefficients in the modeling of a lifting surface with a wake. This code known as EHPIC is a Eularian approach using curved filaments only for hover and axial flight. This method is very similar to that of a lifting-surface method, where one can find influence coefficients which relate the circulation at any point on a lifting surface with an induced velocity at every point on that surface. Looking at planes perpendicular to the tangent of the curve at its collocation point, they sought a solution by which there is no velocity in the normal or binormal directions at the collocation point on any filament. This means the filament is tangent to the flow. In the same manner as the lifting surface method, one can write an influence matrix which relates position perturbations in the normal and binormal directions of a vortex filament to the produced velocity perturbation at every point. This relationship is of course not linear, but for small changes it remains close. Since there is interaction between the lifting surface and the wake, influence coefficients can also be found for their respective perturbation on each other and can be combined in one matrix system,

$$\begin{bmatrix} \Delta q \\ \Delta w \end{bmatrix} = \begin{bmatrix} Q_{qx} & Q_{q\gamma} \\ Q_{wx} & Q_{w\gamma} \end{bmatrix} \begin{bmatrix} \Delta x \\ \Delta \gamma \end{bmatrix} \tag{1.2.1}$$

where Δq and Δw are perturbation velocities, Δx is a perturbation position of the wake, $\Delta \gamma$ is the perturbation circulation on the lifting surface, and the Q's are the influence coefficients. Since the response of the wake is non-linear, it takes several iterations to converge to a correct solution. This model originally used up to seven trailing filaments to model the wake, rather than sheets of vorticity, which were placed at the centroid of vorticity for each blade section. The lifting surface used a row of vortex quadrilaterals

with control points at the center to model the rotor. The far-wake was modeled with helical filaments trailing off the ends of the free wake portion of the wake. EHPIC does not converge to steady solution but averages solution reflecting a real flow.

Bliss and Miller[60,61] introduced a methodology called Periodic Inversion, with the goal of addressing instability of many free-wake methodologies in hover and low advance ratios. This method uses the perturbation version of the governing partial differential equation and transforms the problem to a Eulerian form. This method uses a full span of trailing vortex filaments but no shed filaments. Collocation points remain at a fixed temporal position behind the blade and are forced to converge to positions where vortex filaments are tangent to the pathlines of the flow. This model was formalized by writing the differential equation,

$$\frac{\partial \vec{R}}{\partial \zeta} + \frac{\partial \vec{R}}{\partial \psi} = \frac{\vec{V}(\vec{R})}{\Omega} , \tag{1.2.2}$$

where ζ is the temporal variation or the wake age in the vortex pathline and ψ is the physical angle following the blade path. Rewriting Equation 1.2.1 in perturbation form, one obtains,

$$\frac{\partial \vec{r}_i}{\partial \zeta} + \frac{\partial \vec{r}_i}{\partial \psi} - \frac{1}{\Omega} \cdot \sum_{k=1}^{N} \frac{\partial \vec{V}_i}{\partial R_k} \cdot r_k = \frac{1}{\Omega} \cdot \vec{V}o_i - \left(\frac{\partial \vec{R}_{oi}}{\partial \zeta} + \frac{\partial \vec{R}_{oi}}{\partial \psi} \right) \tag{1.2.3a}$$

where,

$$\vec{R} = \vec{R}o_i + \vec{r}_i , \tag{1.2.3b}$$

and,

$$\vec{V} = \vec{V}o_i + \vec{r}_i \cdot \frac{\partial \vec{V}o_i}{\partial \vec{r}_i} \tag{1.2.3c}$$

where the velocity is linearized by expanded it in a Taylor Series to the first order. This partial differential equation was reformulated using the Lax-Wendroff finite difference scheme to form a second order finite difference equation in both space and time. Immediately behind the blade a boundary condition is applied which is that the trailing vortices are attached to the blade. A second boundary condition enforcing the periodicity of the wake must also be applied. Convergence is defined as when the root-sum-square of the displacement of all the collocation points is below a specified value. This

approach does lead to more stable solutions than pervious methods. They also implement a methodology described as Analytical/Numerical Matching (ANM) which allows for faster computation of induced velocity by using a numerically efficient approximate value of the induced velocity far-a-field of the curved elements. Then it was corrected for filaments that were close in proximity to the point of interest. This is a cost savings as it is numerically more time consuming to calculate the more exact curved vortex solution every time. Employing this method they were able to predict the transition between the largely symmetric, slightly skewed helical wake at low advance ratios to the fully-developed unsteady-asymmetric skewed wake with characteristic tip roll-up which occurs at slightly higher advance ratios.

CAMRAD II[62,63] is the most recent version of Johnson's series of helicopter performance codes. This is a time-accurate relaxation scheme updated from Scully's original method which uses trapezoidal integration to obtain the distortion of the wake. In order to get around the problem of finding the velocity at two time steps as needed for this algorithm, it updates only the bound vortex formed directly behind the rotor without recalculating the rest of the solution. To increase the stability of this scheme he uses a variable relaxation factor that can be applied averaging the pervious values to a current value.

Crourse[64] and Bagai[65,66] took a different direction with their relaxation technique. Instead of in an implicit solution like that used in the Periodic Inversion method, they solved the PDE directly with a pseudo-implicit finite difference predictor-corrector approximation. Bagai uses a third order accurate semi-implicit predictor-corrector method to find the new position after each relaxation step. The goal of Bagai's research was to formally explore the stability of several schemes as well as show the grid sizing necessary to obtain grid independence. This method uses a small number of azimuthal steps of vortex trailers to model the local wake while the far-wake consists of a single trailing vortex placed near the blade tip at the centroid of vorticity. There is also a provision made for the root vortex which they found to be of little importance. The local inboard wake is modeled with the vortex trailers prescribed in the TPP and extend 30° behind the wake. There is no shed vorticity in the wake but the unsteady result is modeled using an indicial response method. As a compromise between using a lifting-

line approach to find the bound circulation, which can not capture some effects like sweep or tip effects, and a lifting surface, which is more computationally intensive, the Weissinger-L method is employed which essentially uses a lifting line at the quarter chord but enforces a flow tangency boundary condition at the three-quarter chord. This allows the bound circulation to reflect effects like sweep while not requiring a significant amount of time beyond a conventional lifting line. The bound circulation is found using the Newton-Raphson method. The wake geometry is solved using the finite difference equation. Convergence is based on the root-sum-square of the displacement of the collocation points between two successive iterations. This code was later employed to model maneuvering flight using velocity source terms to model the maneuvering velocities[67].

Washspress[68] described CDI's CompreHensive Analysis of Rotorcraft aeroMechanics (CHARM) code incorporating about 20 years of experience. The goal was to build a code which removes the need to vary performance coefficients (such as vortex core size or placement) to capture rotorcraft performance. The blade is modeled as a vortex lattice lifting surface which can be set up for any number of elements. The wake is not a vortex lattice but is Constant Vorticity Contours (CVC), which does not require one-to-one correspondence between elements in the wake and surface. These contours allows filaments to be focused where necessary; populating contours more densely in regions of large gradients, while a vortex lattice method requires a fairly uniform distribution of elements and thus more elements to maintain the same resolution. The previously developed curved elements are used to describe these contours and model the shed and trailing vorticity. In the far-wake, the wake can accumulate into two single end vortices (root and tip). Near-wake tip formation is not formed by merging trailing elements but is the result of the elements rotating about themselves. In the far-wake, the vortex profile model is that of Scully's or Vatistas'[69] with n set to one. They found that vortex stretching has a negligible effect and is therefore ignored in their data validation. Airfoil data is used to calculate forces and moments. Convergence is defined as when fluctuations in the loads reach a specified value.

Bhagwat[70] developed a time-marching approach to model the evolution of a rotor wake to explore issues of stability and accuracy. The wake is modeled as a single tip

vortex. This algorithm uses a predictor-corrector second-order backward finite difference (PC2B) to predict the new position of the wake elements and compared it with a Predictor-Corrector Central (PCC) finite difference algorithm. A model differential equation which represented the velocity as an exponential term was represented with the above FDE's. The PC2B algorithm was found to be second-order accurate using linearized stability theory but since the velocity is non-linear, this does not ensure second order accuracy. Bases on comparisons of a vortex ring with linear vortex segments, the suggestion is made that sectors of less than 5° are required to ensure less than 10% error. In comparisons of the two algorithms the PC2B demonstrated that errors in this algorithm will decay toward while the PCC is unstable. He also showed that in order to ensure grid independence, the wake elements in the PC2B must be at least 5°. This code demonstrates accurate and stable wake convergence. Interestingly, although stability in the solution is usually beneficial, the authors cite that in some aspects, the unstable PCC model is actually more reflective of the experimental results. They cite vortex pairing seen in experiments and the PCC solution but not in the PC2B solutions. They also acknowledge the physical instability of a helicopter wake in hover. This code was later applied to modeling maneuvering helicopters[71]. These included successful modeling of a ramp increase in collective pitch as well as pitching and rolling in hover.

Chapter 2:   Analysis Methodology

This methodology is designed for a four blade single main rotor with a rigid in-plane rotor. The code was designed to predict the performance of a rotor given the geometry and trimming with the conventional cyclic and collective pitch inputs or by used prescribing the circulation directly and allows the rotorcraft to trim by uniformly raising and tilting the circulation distribution. By defining circulation, one can ignore the physical airfoil while being able to determine the c_ℓ and corresponding force distributions from this circulation. The rational for doing this is to obtain a general solution similar to that of Munk for a fixed wing aircraft. The blade is modeled as a lifting line which has the disadvantage of not capturing some of the second order effects due to chord-wise variation or tip vortex formation. In pursuit of the general solution, the code allows one to vary the circulation at any point radially and azimuthally. The twist is not constrained to maintain a rigid blade or limit the amount of twisting the blade undergoes.

2.1 Trim:

This model uses longitudinal trim, therefore the forces are balanced in the vertical and longitudinal directions and the pitching and rolling moments are equal to zero.
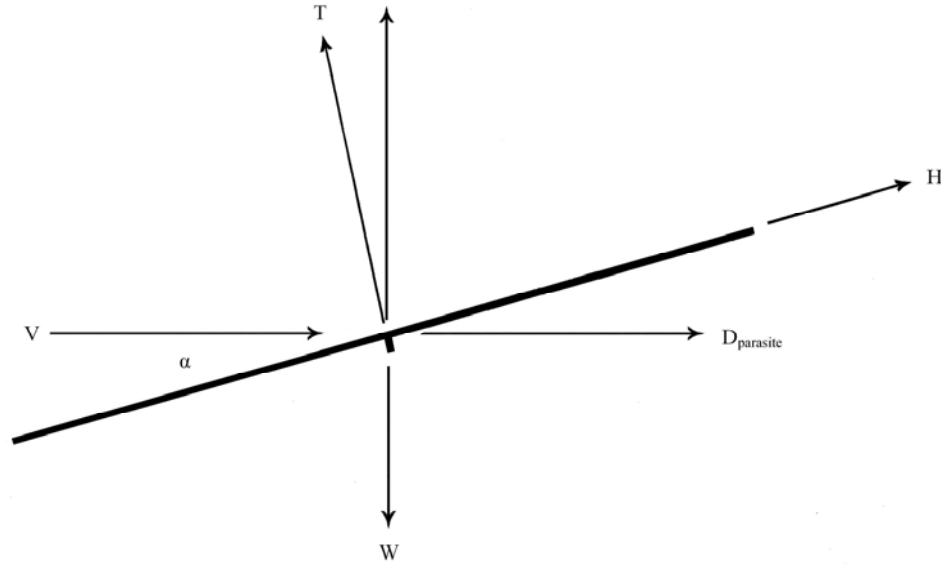
Figure 2.1.1: Trim of the Main Rotor

Expressed in equation form,

$$T \cdot \cos(\alpha_{shaft}) + H \cdot \sin(\alpha_{shaft}) - W = 0 , \qquad (2.1.1a)$$

$$T \cdot \sin(\alpha_{shaft}) - H \cdot \cos(\alpha_{shaft}) - D_{parasite} = 0 , \qquad (2.1.1b)$$

$$M_x = 0 , \qquad (2.1.1c)$$

$$M_y = 0 . \qquad (2.1.1d)$$

where the parasite drag, $D_{parasite}$, is given by the equation,

$$D_{Parasite} = \frac{1}{2} \rho \cdot V_\infty^2 \cdot S \cdot C_D . \qquad (2.1.2a)$$

Here the area, S, is an equivalent flat plate area and C_D is a corresponding drag coefficient to approximate the parasite drag experienced by the helicopter in flight excluding the rotor. The weight is represented by W while the vertical and longitudinal forces and pitching and rolling moments in the rotor disk axis are respectively denoted by the variables T, H, M_x, M_y.   It is important to note that moments due to the offset of

vehicle center of gravity from the rotor hub are ignored are ignored in this analysis. A consequence of using longitudinal trim is that the effects of lateral tilt and the tail rotor force are excluded from the model. Including these would modify the lift distribution but most likely not significantly while their inclusion adds extra time to trim the helicopter.

2.2 Kinematics:

To find the forces at any given blade section, one must know the local relative velocity to the airfoil section. This includes the free stream velocity, the angular rotation of the blade, as well as the induced velocity,

$$\vec{V}_{local} = \vec{V}_{\infty} + \vec{\Omega} \times \vec{r} + \vec{V}_{induced}. \qquad (2.2.1)$$

Note that there are no flapping, lagging, pitching, bending, or twisting motions included here. The blade is assumed to be a hingeless and completely rigid. Since the goal is an ideal lift distribution, it is reasonable to ignore these effects. This equation can be viewed in component form in the local non-inertial blade frame axis as,

$$u_r = u' \cos(\psi) + v' \sin(\psi), \qquad (2.2.2a)$$

$$u_{theta} = \Omega r + u' \sin(\psi) - v' \cos(\psi), \qquad (2.2.2b)$$

$$u_z = w'. \qquad (2.2.2c)$$

where,

$$u' = u_{induced}, \qquad (2.2.2d)$$

$$v' = (v_{induced} - V_{\infty}) \cos(\alpha_{shaft}) + w_{induced} \sin(\alpha_{shaft}), \qquad (2.2.2e)$$

$$w' = -(v_{induced} - V_{\infty}) \sin(\alpha_{shaft}) + w_{induced} \cos(\alpha_{shaft}). \qquad (2.2.2f)$$

For a given blade section, the induced velocity is found as a weighted average of the velocity at the two ends and the middle of that segment using the equation,

$$\vec{V}_{induced} = \frac{\vec{V}_{endpoint} + 2 \cdot \vec{V}_{midpoint} + \vec{V}_{endpoint}}{4}. \qquad (2.2.3)$$

To find the forces, the local angle of attack of the airfoil section must be known as well as the c_{ℓ} which is a function of angle of attack and Mach number. The absolute or aerodynamic angle of attack, these are the same in this diagram since the airfoil is symmetric, is measured from the rotor Tip Path Plane (TPP) to the Zero Lift Line (ZLL)

of the airfoil section while the aerodynamic angle of attack must be given relative to the local velocity,
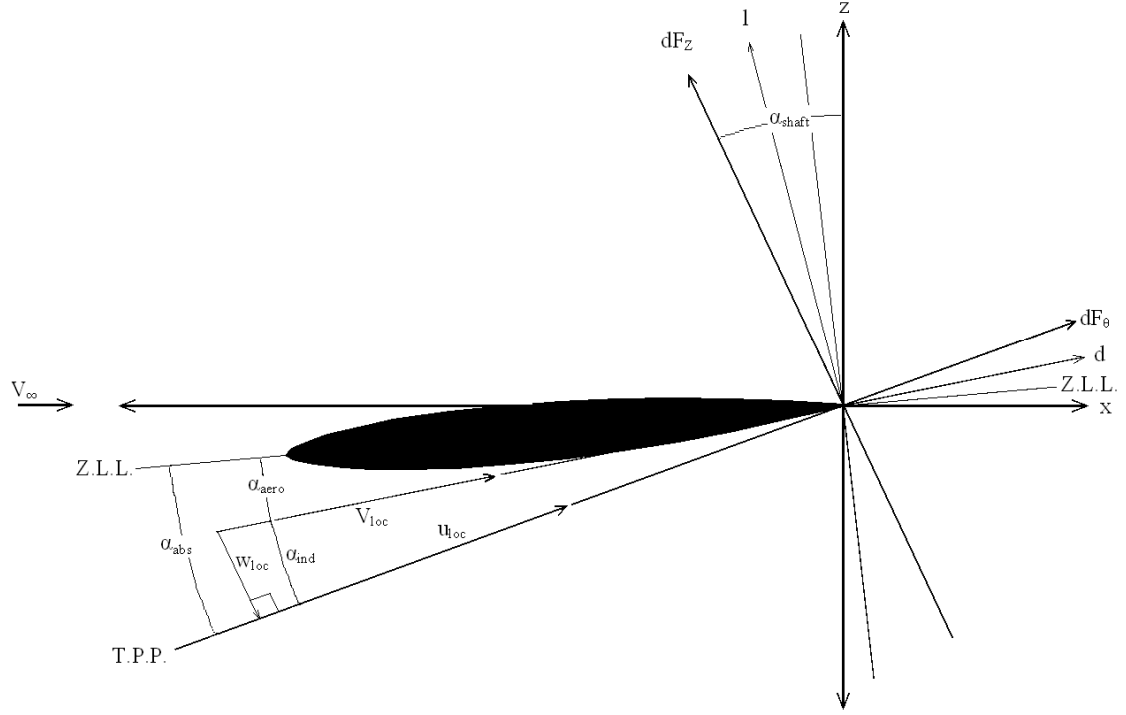
Figure 2.2.1: Respective Airfoil Coordinate Systems

and therefore the aerodynamic angle of attack is given by,

$$\alpha_{aero} = \alpha_{abs} - \tan(\frac{w_{local}}{u_{local}})^{.} \qquad\qquad (2.2.4a)$$

where,

$$\alpha_{abs} = \theta_{twist} + \theta_{col} + \theta_{1c} \cdot \cos(\Psi) + \theta_{1s} \cdot \sin(\Psi). \qquad\qquad (2.2.4b)$$

The absolute angle of attack is the pitch distribution down the span of the blade at any given time. The θ_{col}, θ_{1c}, and θ_{1s} are the collective, lateral cyclic, and longitudinal cyclic pitch controls respectively. The final term in figure 2.2.4a is the induced angle of attack which generally reduces the aerodynamic angle of attack relative to the absolute. The local downwash, W_{local}, in composed of two parts,

$$W_{local} = -V_{\infty} \cdot \sin(\alpha_{shaft}) - W_{ind}^{.} \qquad\qquad (2.2.5)$$

Therefore it is not technically correct to call this last term purely induced. The ram drag, the contribution of the free stream component, is a penalty for tilting the disk to propel forward.

The lift on each section is directed perpendicular to the local velocity and is given by the equation,

$$l = \frac{1}{2} \rho \cdot (\vec{V}_{loc} \cdot \vec{V}_{loc}) \cdot c \cdot c_l .$$

(2.2.5)

Using this angle of attack and the local Mach number the profile drag coefficient, c_d, can be found for any specific airfoil. The corresponding profile drag is found using the equation,

$$d = \frac{1}{2} \rho \cdot (\vec{V}_{loc} \cdot \vec{V}_{loc}) \cdot c \cdot c_d .$$

(2.2.6)

Because the direction of the section lift and drag are functions of the local velocity. They must be rotated to the rotor disk coordinate system in order to find the forces and moments on the disk. Therefore the force distributions along the span of the blade are,

$$\frac{dF_z}{dr} = l \cdot \cos(\alpha_{ind}) - d \cdot \sin(\alpha_{ind}) ,$$

(2.2.7a)

$$\frac{dF_\theta}{dr} = d \cdot \cos(\alpha_{ind}) + l \cdot \sin(\alpha_{ind}) .$$

(2.2.8b)

Note that any forces that may act radially due to a component of profile drag are being ignored. The second equation in this pair includes the induced drag, which is the portion of the lift projected on the tip plane path. In the case of an induced up wash, the sign of α_{ind} is reverse, this induced drag would be locally propulsive. There is also a force induced downward due to the drag force being tilted with the induced angle of attack. In analytic methods, this term is often ignored since it is the product of a relatively small force and small angle but computationally there is no need to ignore this. The aerodynamic forces produced by the rotor blades at any instant in time are given by the equations,

$$H = \sum_{n=1}^{N} \int_{r_o}^{R} \frac{dF_\theta^n}{dr} \cdot \cos(\Psi^n) \cdot dr ,$$

(2.2.9a)

31

$$V = \sum_{n=1}^{N} \int_{r_o}^{R} \frac{dF_\theta{}^n}{dr} \cdot \sin(\Psi^n) \cdot dr , \qquad (2.2.9\text{b})$$

$$T = \sum_{n=1}^{N} \int_{r_o}^{R} \frac{dF_z{}^n}{dr} \cdot dr , \qquad (2.2.9\text{c})$$

$$M_x = \sum_{n=1}^{N} \int_{r_o}^{R} \frac{dF_z{}^n}{dr} \cdot r \cdot \cos(\Psi^n) \cdot dr , \qquad (2.2.9\text{d})$$

$$M_y = \sum_{n=1}^{N} \int_{r_o}^{R} \frac{dF_z{}^n}{dr} \cdot r \cdot \sin(\Psi^n) \cdot dr , \qquad (2.2.9\text{e})$$

$$Q = \sum_{n=1}^{N} \int_{r_o}^{R} \frac{dF_\theta{}^n}{dr} \cdot r \cdot dr , \qquad (2.2.9\text{f})$$

where N is the total number of blades. Finally the total power for the rotor disk is found by multiplying the torque by the angular velocity of the blades,

$$P = Q \cdot \Omega = \sum_{n=1}^{N} \int_{r_o}^{R} \frac{dF_\theta{}^n}{dr} \cdot (\Omega r) \cdot dr . \qquad (2.2.10)$$

To examine just the induced power, one can simply ignore the drag coefficient, c_d, by setting it equal to zero. Spanwise integration along the blade is performed with trapezoidal integration across each discrete element. The final forces, moments, and power for trim and reporting performance are averaged over one period. Finally the forces, moments, and power are all non-dimensionalized by the following quantities,

$$C_{Force} = \frac{Force}{\rho(\Omega R)^2 R^2} , \qquad (2.2.11\text{a})$$

$$C_{Moment} = \frac{Moment}{\rho(\Omega R)^2 R^3} , \qquad (2.2.11\text{b})$$

$$C_{Power} = \frac{Power}{\rho(\Omega R)^3 R^2} . \qquad (2.2.11\text{c})$$

When operating from a prescribed circulation distribution instead of the blade pitch, a different methodology described in section 2.4 is used.

2.3 Lifting-Line Model

This model is a variable prescribed/free wake analysis. The model allows for a relaxed wake to a certain distance to capture the local wake effects and can then transition to a prescribed wake translating at average values at an arbitrary distance down the length of the wake.

In order to translate 2-D airfoil data into 3-D finite wing or blade aerodynamic quantities, the Lancaster-Prandlt[72] lifting line model was used. This method makes note of the fact that there is a pressure differential between the upper and lower surfaces of the rotor blade. At the ends of the blades there is nothing to maintain a pressure difference and therefore air moves from under the blade to the top of it. This process shifts the pathlines of the fluid particles across the top and bottom of the blade in opposite directions (toward the hub on the top; toward the tip on the bottom) so that in the shear layer behind the blade there is vorticity due to these merging layers of opposite lateral flow. This is referred to as the trailing vorticity. Toward the tips of the blade, the trailing vorticity tends to roll-up into strong tip vortices. A lifting line models is predicated on the idea that the change in lift down the span of a blade or around the azimuth of a disk results in vorticity being shed into the wake. This vorticity can be modeled as discritized finite vortex filaments. The vortex filaments in turn induce velocity back onto the blades affecting the aerodynamic forces.

According to Hemholtz Theory[23], a line of vorticity can not end at an arbitrary point in a flow field but must end at a solid surface or form a closed path. This condition can be usefully satisfied with a semi-infinite horseshoe vortex.
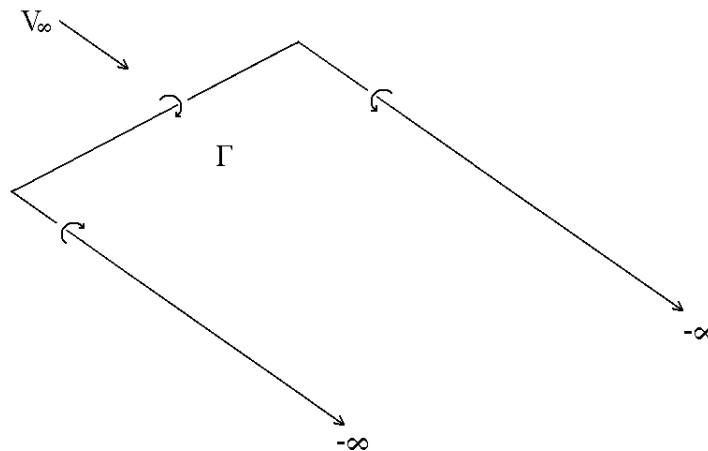
Figure 2.3.1: Trailing Semi-infinite Horseshoe Vortex

These horseshoes create a semi-infinite closed rectangular path which model the airfoil sectional bound vorticity as well as trailing vortices to infinity. The horseshoe can be imagined to close again at infinity with the starting vortex, thus forming a closed path.

For modeling a flow with temporal variation one can employ a finite quadrilateral closed vortex path instead of using Prandlt's Horseshoe vortices. The reasoning for this is the same as above but changes in the lift distribution azimuthally suit this method which accounts for these changes. In figure 2.3.2, one can see that the top portion of the quadrilateral represents the bound vortex (or the blade) while the two sides represent the trailing vortices running along the local pathlines of the flow. Finally, the bottom of the quadrilateral is a shed vortex equal to the strength of the attached vortex but acting in the opposite direction, therefore creating a "ring" of constant circulation.
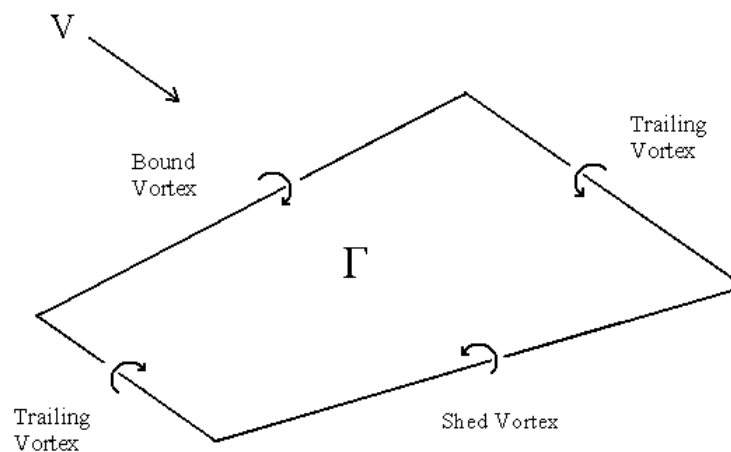
Figure 2.3.2: Configuration of a Finite Vortex Quadrilateral: By virtue of forming a closed path, this vortex element satisfies Helmholtz's equation.

Generally, the strength of the circulation on the blade changes azimuthally and therefore the strength of the shed vortex quadrilaterals will vary down the wake. This means that not only is there an induced velocity due to the change in spanwise circulation but also due to the change with time or azimuth.

As noted above, each vortex filament in the flow-field induces its own flow field and since these vortex filaments are a solution to the linear Laplace's equation, one can use the principle of superposition to find the total induced velocity at a given point due to every filament in the flow-field. Thus many of these vortex rings can be used to build up the entire wake simply by adding all their solutions together. The vortex filaments from adjacent vortex quadrilaterals overlap; the strength of a given filament is the difference between coinciding quadrilaterals as seen in the figure 2.3.3.
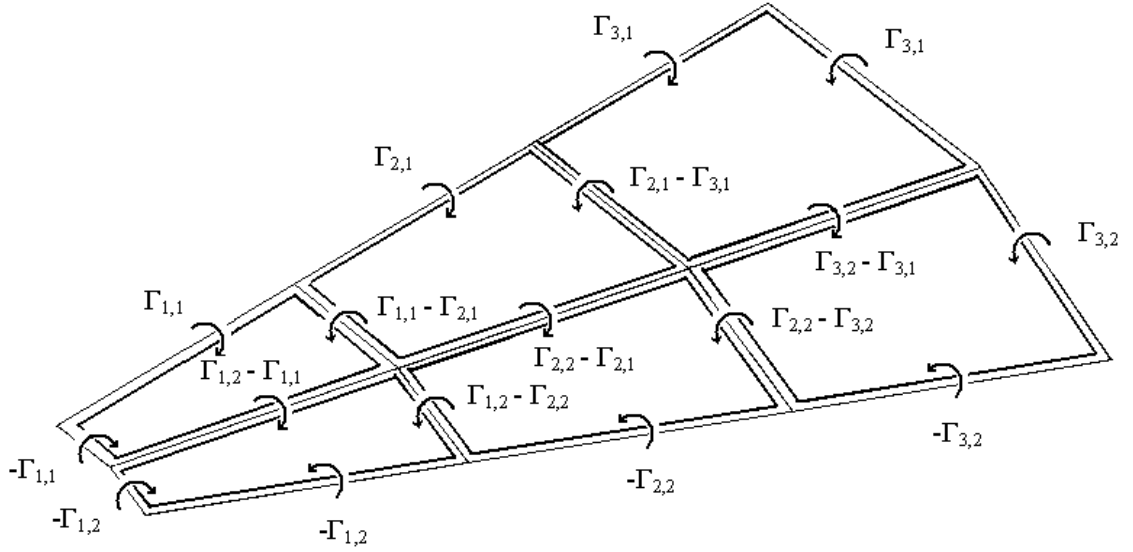
Figure 2.3.3: Wake Built-up of Several Vortex Quadrilaterals

This is true of the shed filaments as well as the trailing filaments except at the edges of the wake where there are no overlapping trailers. The bound filaments are full strength because they represent the blade where the vorticity is produced. The circulation strength of a vortex filament within the wake is therefore,

$$\Gamma_{eff,m} = \Gamma_{n+1,m} - \Gamma_{n,m}.$$ (2.3.1)

The finite straight-line vortex segments that form the more complex structure of the wake, produce an induce a flow-field which can be described using the Biot-Savart Law,[23]

$$\vec{V}_{induced}(\vec{r}) = \int_a^b \frac{d\vec{l} \times (\vec{r} - \vec{s})}{\left|\vec{r} - \vec{s}\right|^3}.$$ (2.3.2)

For an arbitrary filament with end points $\vec{a}_1$ and $\vec{a}_2$, (equation 2.3.2) can be written as,

$$\vec{V}_{induced}(\vec{r}) = \frac{\Gamma_{eff}}{4\pi} \cdot \langle P_x, P_y, P_z \rangle \cdot I .$$ (2.3.3a)

where,

$$I = \frac{4c + 2a}{(4ac - b^2)\sqrt{a+b+c}} - \frac{2b}{(4ac - b^2)\sqrt{a}} ,$$ (2.3.3b)

and,

$$P_x = (r_z - z_a)(y_b - y_a) - (r_y - y_a)(z_b - z_a) ,$$ (2.3.3c)

$$P_y = (r_x - x_a)(z_b - z_a) - (r_z - z_a)(x_b - x_a) ,$$ (2.3.3d)

$$P_z = (r_y - y_a)(x_b - x_a) - (r_x - x_a)(y_b - y_a) ,$$ (2.3.3e)

where,

$$a = (r_x - x_a)^2 + (r_y - y_a)^2 + (r_z - z_a)^2 ,$$ (2.3.3f)

$$b = -2 \cdot \left[(r_x - x_a)(x_b - x_a) + (r_y - y_a)(y_b - y_a) + (r_z - z_a)(z_b - z_a) \right],$$

(2.3.3g)

$$c = (x_b - x_a)^2 + (y_b - y_a)^2 + (z_b - z_a)^2 ,$$ (2.3.3h)

and,

$$\vec{r} = \langle r_x, r_y, r_z \rangle ,$$ (2.3.3i)

$$\vec{a} = \langle x_a, y_a, z_a \rangle ,$$ (2.3.3j)

$$\vec{b} = \langle x_b, y_b, z_b \rangle ,$$ (2.3.3k)

where $\vec{r}$ is an arbitrary point in space. One can see from figure 2.3.4 below that the velocity is inversely proportional to the perpendicular distance from the filament and goes to infinity as the distance tends toward zero. Obviously this singularity is not physical but is a product of a potential flow solution where the circulation is constant about any closed path that includes the vortex. The model of a complex wake such as that produced by a helicopter with this solution will predict unbounded impulsive loading during close vortex interaction which will drive a non-physical solution. To prevent this behavior, the vortex is modeled with a viscous rotational core. The drawback of this approach is that the viscous core parameters have a very strong influence on the outcome and in determining these parameters one usually relies on some empirical assessment that

the wake is behaving as expected. One model commonly used is represented by the
equation,

$$u_\theta = \frac{\Gamma}{2\pi} \cdot \frac{r}{\sqrt[n]{r^{2n} + r_{core}^{2n}}},$$ (2.3.4a)

as described by Vatistas[69]. His experiments suggest that a value of n equals two matches
the physical phenomenon,

$$u_\theta = \frac{\Gamma}{2\pi} \cdot \frac{r}{\sqrt[2]{r^4 + r_{core}^4}}.$$ (2.3.4b)

If n equals one, one obtains the solution used by Scully and still applied in the CHARM
program. As n approaches infinity, one obtains the Rayleigh solution which transitions
from a purely rotational core to a potential region with a discontinuity in the slope
between them at the vortex core radius. All of the possible values for n yield a model
having a core linear distribution which transitions through some core radius to behave as
the potential flow solution. Thus the circulation grows with distance from the center until
it reaches the potential solution and remains constant throughout the inviscid portion of
the solution. This distribution is shown in figure 2.3.4,
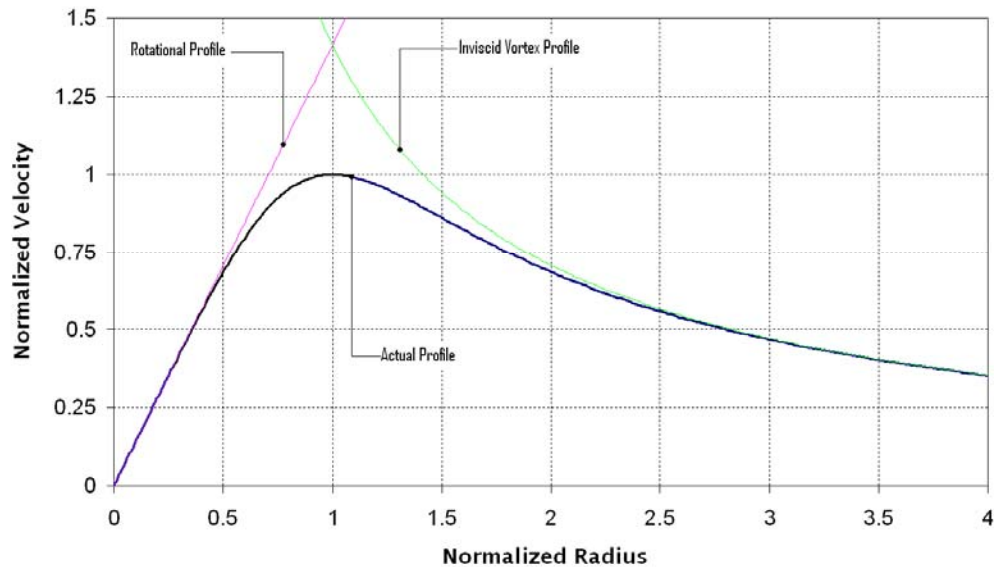
**Figure 2.3.4: Vortex Velocity Profile: Normalized radial velocity profile use to approximate the
viscous core. Velocity and radius normalized by the actual profile's peak velocity and
corresponding radius.**

Using a core model is not only physically more realistic but resolves the numerical complication of having infinite velocity in the flow field. One can see from the above diagram that the velocity is very non-linear which often leads to erratic behavior of the flow field. To save computation time, the code uses the formulation reflected in equation 2.3.3 (the inviscid solution) unless the point of interests falls within a perpendicular distance less than twice the core radius.

This viscous core will spread and the peak velocity will dissipate with time. To model the vortex core growth, a growth rate model modified from Bagai[65] was used,

$$r_c = 0.112\sqrt{4\nu\delta t} + r_{c_o}, \tag{2.3.5a}$$

where,

$$\delta = 1 + a_1\frac{\Gamma}{\nu}, \tag{2.3.5b}$$

and δ is the turbulent viscosity. For the tip vortex, the coefficient a_1 was set to 0.1 and the initial radius, r_o is set to 10% of chord. This core growth can be seen in figure 2.3.5. This model was originally modified from a Navier-Stokes solution for vortex dissipation described by Lamb and Oseen. The root vortex is a source of some consternation because of the direction of the circulation. They will tend to propel themselves up into the rotor disk. If the cores are too small they will inflict severe impulsive forces on the blades in numerous BVI's. There is little experimental data demonstrating root core growth but experiments also don't demonstrate large impulsive forces due to a root vortex either. One can imagine that in the presence of the turbulent interaction with the hub the vortices' cores might grow quite quickly. Therefore core sizing and growth was chosen such that these impulsive forces do not exist on the disk as they are not seen in experimental data. Ultimately it was decided to treat the inboard vortex the same way the inboard trailers are treated.
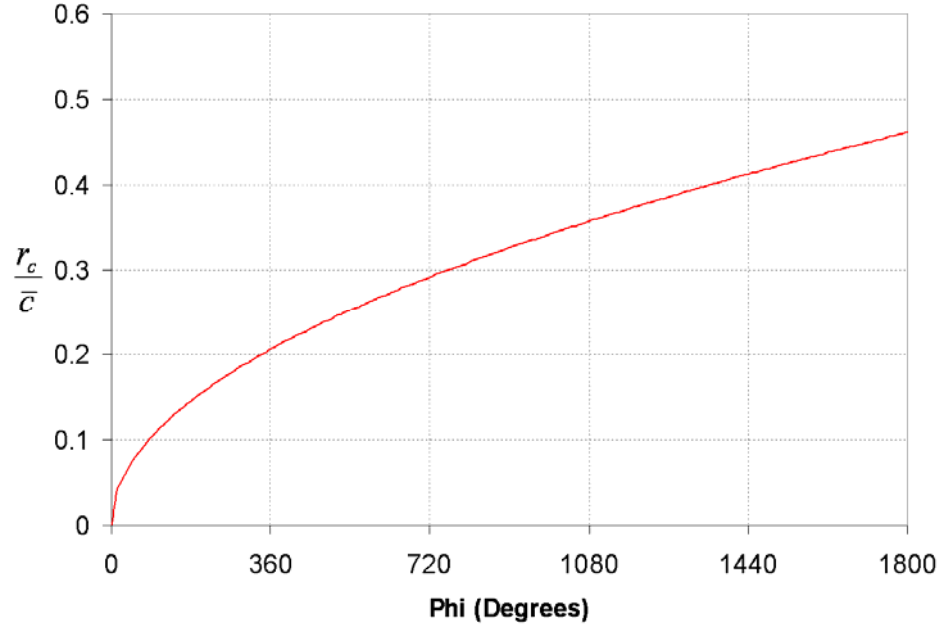
Figure 2.3.5: Viscous Core Growth: Viscous core size normalized by chord length.

For the inboard trailing and shed filaments, the core model is different. Most of what is shed on the inboard part of the blade remains diffuse sheets rather than a strong vortex as at the tip. Therefore, a core size comparable to the one used for the tip vortex is not appropriate. Using such small core sizes would contribute to wake instability and could create artificial BVI effects all around the disk and therefore unreasonable induced velocity profiles. The equation for an infinite vortex sheet of span $2b$ and centered at y = 0 is,

$$ u = \frac{\Gamma}{8b\pi} \cdot \ln\left(\frac{(b-x)^2 + \sqrt{(b-x)^4 + r_o^4}}{(b+x)^2 + \sqrt{(b+x)^4 + r_o^4}} \right), \tag{2.3.6} $$

where $2 \cdot r_o$ is the sheet width. This is obtained by integrating the equation 2.3.4 over the span of a sheet. One could use this equation to model the wake as rectangular wake panels or many other more complicated quadrilateral or triangular panels but, given the number of times this equation must be computed, it would be more time intensive than equation 2.3.4b. One can see for an appropriate core sizing that a standard filament is an appropriate approximation for a sheet. For this analysis inboard core radii are half the distance between the span of each segment and remain constant with wake age.

39
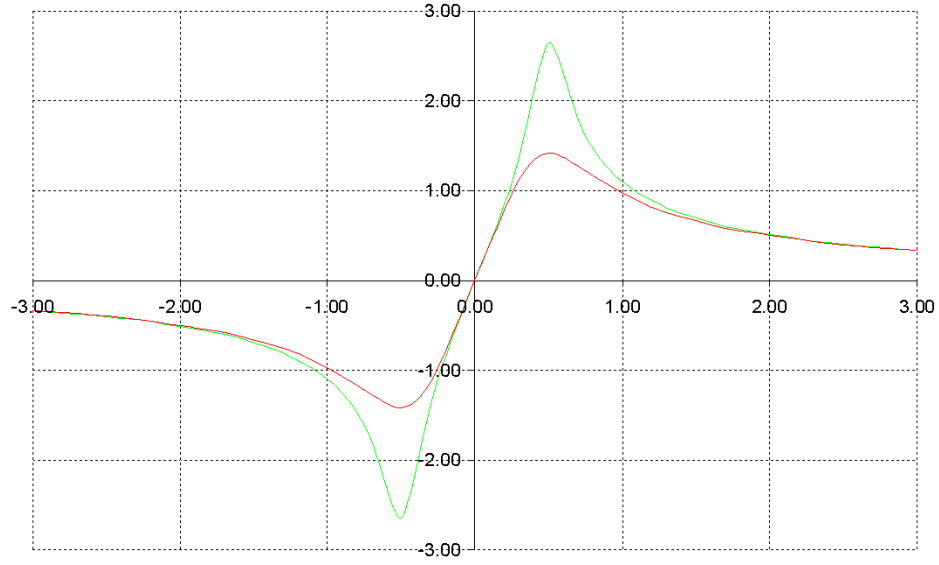
Figure 2.3.6: Viscous Vortex Sheet Comparison (ft/s): Comparison of a viscous vortex sheet (green) and a large core vortex (red).

In order to find the circulation strength of the bound vorticity at each new time (or azimuthal) step, the induced velocity and circulation are found simultaneously. In order to do this, the velocity is broken into two components, one local velocity due to the newly formed vortex ring in one azimuthal step and that from the existing rings. Since the structure of the local newly formed vortex rings are known (the ends lie on the blades or the edge of the wake element which just got swept behind), the only unknown in the way of obtaining the induced velocity is the circulation strength. Therefore, the induced velocity is a linear function of the unknown circulation strength. The set of equations to be solved is,

$$\vec{V}_{induced}(\vec{r}) = \frac{\Gamma}{4\pi} \cdot \left\langle P_x, P_y, P_z \right\rangle \cdot I \,, \tag{2.3.7a}$$

where,

$$\Gamma = \frac{1}{2} V_\infty \cdot c \cdot c_l(\alpha, M), \tag{2.3.7b}$$

and,

$$\alpha = \theta_{twist} - \tan^{-1}\left(\frac{w_{loc}}{u_{loc}}\right). \tag{2.3.7c}$$

One will note that w_{loc} and u_{loc} are functions of $V_{induced}$, and therefore this is a transcendental system of equation. If one is willing to make a small angle approximation as well as use an ideal airfoil, the above system of equations is linearized and can be solved outright as,

$$\Gamma = \frac{V_\infty \theta_{twist}}{\left(\dfrac{2}{ca} + \dfrac{P_z I}{4\pi}\right)}, \tag{2.3.8}$$

But keeping the non-linear system, as is done here, the circulation at each time step must be found iteratively.

2.4 The Wake:

For both the relaxed and prescribed wakes, the initial shed wake is given, as a skewed helix attached to the rotor blade and trailing off to a number of specified revolutions. The shape is given by the equation,

$$\vec{r} = \left\langle U_\infty + U_{induced} \cdot t + r \cdot \cos(\Psi), V_{induced} \cdot t + r \cdot \sin(\Psi), W_{induced} \cdot t \right\rangle \tag{2.4.1a}$$

where,

$$t = \frac{\Psi}{\Omega} \quad . \tag{2.4.1b}$$

Initially the wake is prescribed with arbitrary value of $V_{induced}$ applied uniformly.

Relaxing the wake has the added complexity of requiring the calculation of the velocity at every point in the wake to find the new position of the Lagrangian end points of each filament after each time-iteration. Note that this will allow for vortex stretching. Despite this stretching, the circulation is assumed to be constant as others have found it to be insignificant and ignoring it reduces computation time[1]. Along with finding the position of each filament at each time step, an entire new row of filaments is created at the trailing edge of the blades. While a new row is created, the last row in the wake is dropped to maintain a constant number of shed vortex rings in the wake. Between iterations, the new position of each end point is found with either the first order explicit Euler integration,

$$\vec{r}_2 = \vec{V}(\vec{r}_1) \cdot \Delta t + \vec{r}_1, \tag{2.4.2}$$

which is satisfactory at higher advance ratios where V_∞ is the major component. Or a second order corrector-predictor trapezoidal integration,

$$\vec{r}_2' = \vec{V}(\vec{r}_1) \cdot \Delta t + \vec{r}_1, \tag{2.4.3a}$$

$$\vec{r}_2 = 0.5 \cdot \left(\vec{V}(\vec{r}_2') + \vec{V}(\vec{r}_1) \right) \cdot \Delta t + \vec{r}_1, \tag{2.4.3b}$$

A more accurate position is predicted using a second order accurate predictor-corrector method. This added accuracy comes with a second calculation of the induced velocity with each loop. This approximately doubles the performance time and given the extensive time required for optimization this was only used for hover cases. For hover, one must also apply several lengths of prescribed helical filaments or some other treatment to maintain the mass flow below the disk and stabilize the near wake flow-field. In this code, 20 revolutions of a trailing single tip filament placed below the disk.

2.5 Aerodynamic Coefficients:

This code uses steady airfoil wind tunnel data. When operating with the blade pitch as an input, this model reads the aerodynamic coefficients from tables as a function of angle of attack and Mach number. The program applies a linear interpolation between points in both the angle of attack and Mach number directions. When utilizing the code with circulation as the input, the look-up tables limit the c_ℓ to an attainable value and proceeds from the circulation, to the lift coefficient, angle of attack, and finally the airfoil drag coefficient. In this way, the desired c_ℓ and the induced angle of attack combine to determine the blade pitch. There are potentially several possible angles which will yield a desired c_ℓ, figure 2.4.1. To address this problem, the angle of attack is limited to being within the small range between the positive and negative stall angle. This yields a single-valued function with the minimum drag, but also allows for some extreme behavior in the reverse flow region which the blade may be operating at pitch angles of over 180°.

Working in either mode, the compressibility is accounted for in the wind-tunnel data, which is measured for Mach numbers between zero and one. The unsteadiness in the wake and its effects are captured by the shed vorticity in the wake but dynamic stall, non-circulatory forces, and rotational lift due to the blade pitching are ignored.
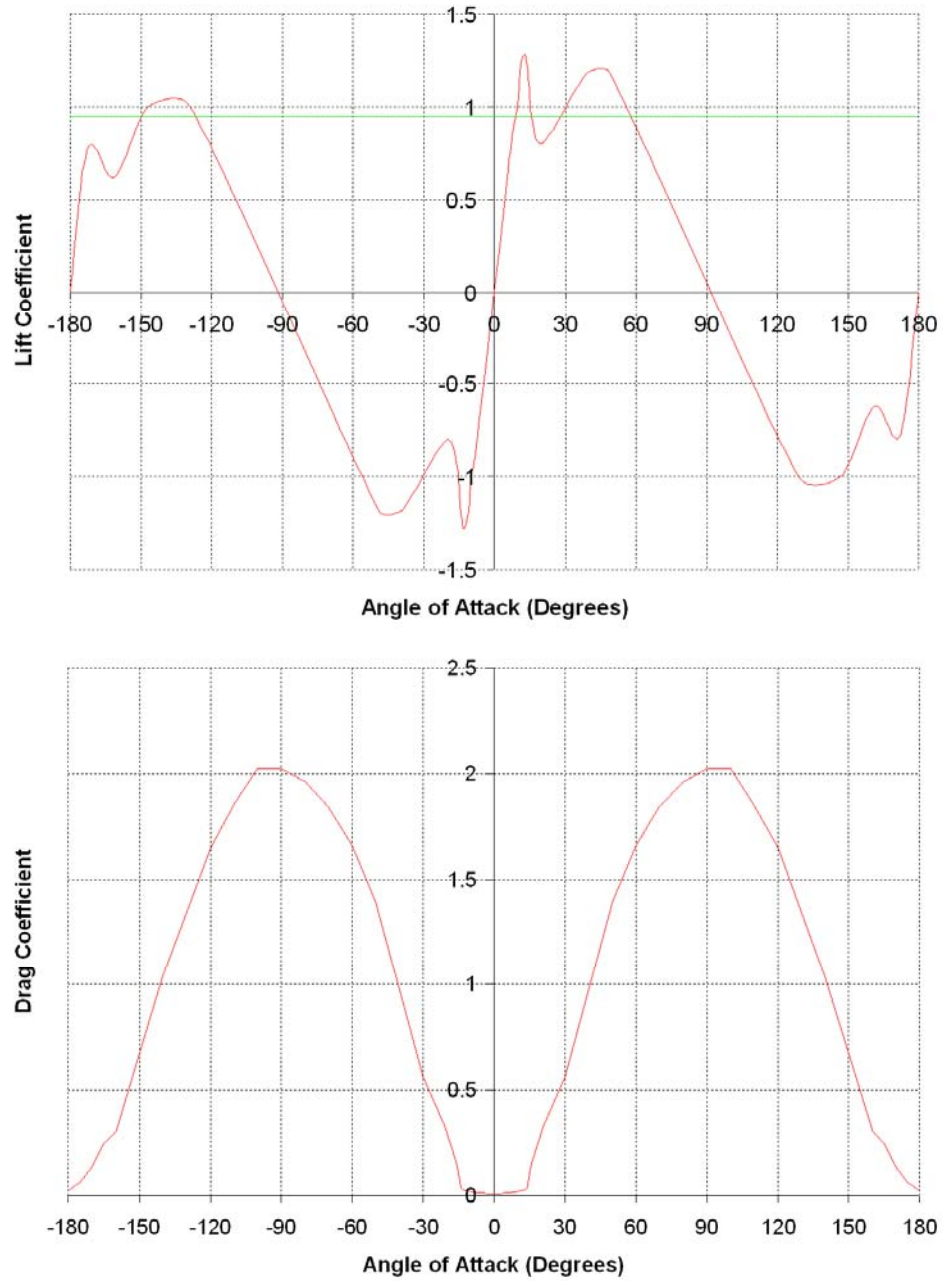
Figure 2.4.1: Lift and Drag Coefficients for the NACA 0012: Lift coefficient verses angle of attack for the NACA 0012. The red line represents the multiple possible solutions for a given angle of attack. At a c_ℓ of 0.95, there are 6 possible angles of attack with difference associated drag coefficients. Data taken for a Mach number of 0.3.

2.6 Convergence Criteria:

The period averaged value of induced velocity is found across the disk and is used to monitor convergence of the solution. Because of instability in this scheme in hover, a second averaging is used to calculate forces, moments, power, and average downwash in these cases. After an initial period of time long enough to obtain a quasi-converged solution, the average of the periodic average after each time step is taken.

2.7 Optimization Technique:

The optimization technique used for this analysis is a gradient based method to minimize the objective function, flight power, while satisfying the constraint equations, namely the longitudinal trim equations. The constraint variables are the circulation distribution and the shaft-angle. In order to optimize the circulation, it is perturbed at each point on the rotor disk. Based on the change in power and trim variables, derivatives are calculated for each. Applying the method of Lagrange Multipliers,[73] new values are extrapolated from the previous circulation distribution to a new distribution.

$$0 = \frac{\partial P_1}{\partial \Gamma_{r_1,\theta_1}} + \lambda_a \cdot \frac{\partial T_1}{\partial \Gamma_{r_1,\theta_1}} + \lambda_b \cdot \frac{\partial M_{x_1}}{\partial \Gamma_{r_1,\theta_1}} + \lambda_c \cdot \frac{\partial M_{y_1}}{\partial \Gamma_{r_1,\theta_1}}, \qquad (2.6.1a)$$

$$0 = \frac{\partial P_2}{\partial \Gamma_{r_2,\theta_2}} + \lambda_a \cdot \frac{\partial T_2}{\partial \Gamma_{r_2,\theta_2}} + \lambda_b \cdot \frac{\partial M_{x_2}}{\partial \Gamma_{r_2,\theta_2}} + \lambda_c \cdot \frac{\partial M_{y_2}}{\partial \Gamma_{r_2,\theta_2}}, \qquad (2.6.1b)$$

$$0 = \frac{\partial P_3}{\partial \Gamma_{r_3,\theta_3}} + \lambda_a \cdot \frac{\partial T_3}{\partial \Gamma_{r_3,\theta_3}} + \lambda_b \cdot \frac{\partial M_{x_3}}{\partial \Gamma_{r_3,\theta_3}} + \lambda_c \cdot \frac{\partial M_{y_3}}{\partial \Gamma_{r_3,\theta_3}}, \qquad (2.6.1c)$$

The values of λ are found at the arbitrary points (r_1,θ_1), (r_2,θ_2), and (r_3,θ_3) where λ_a, λ_b, and λ_c are equal to values such that the above equations are satisfied. Then the perturbation value is found using the expression,

$$\delta\Gamma = P_n + \lambda_a \cdot T_n + \lambda_b \cdot M_{x_n} + \lambda_c \cdot M_{y_n}, \qquad (2.6.2)$$

at every point on the disk. This new distribution is retrimmed and can be further optimized which is necessary since the problem is non-linear. The solution was determined to be converged when a new perturbation contour provided less than 1% power decrease.

Chapter 3:   Validation

Validation of a code of this nature is a time-intensive procedure. Due to a limited amount of time for this project, validation with experimental results was not performed. It can be noted that the creation of this code is not a new concept and various forms of such codes have been validated and are used widely, CAMRAD, UMARC, CHARM, etc. Since this method is similar, it is reasonable to assume the results will be similar. Although no experimental comparisons are performed, it is valid to justify that the code is implemented correctly. With this in mind, there are analytical and computational solutions to which the code can be compared.

3.1 Accuracy:

The analytic solution for the velocity field induced by a vortex ring is known[74]. Looking at the induced velocity in the plane of a vortex ring centered at the origin with a radius of R, the solution can be expressed as,

$$w = \frac{\Gamma}{2\pi xR} \cdot \left[A \cdot K(\tau) + B \cdot E(\tau) \right] \tag{3.1.1a}$$

$$u_r = 0 \tag{3.1.1b}$$

where,

$$A = \frac{x-1}{d_1} + \frac{x+1}{d_2} \tag{3.1.1c}$$

$$B = D \cdot F - A \tag{3.1.1d}$$

$$D = \frac{\tau \cdot (d_1 + d_2)}{1 - \tau^2} \tag{3.1.1e}$$

$$F = 1 - \frac{1 + x^2 - d_1 d_2}{2x^2} - \frac{(1+x) \cdot d_1^2 - (1-x) \cdot d_2^2}{2x d_1 d_2} \tag{3.1.1f}$$

and,

$$d_1 = |x - 1| \tag{3.1.1g}$$

$$d_2 = |x + 1| \tag{3.1.1h}$$

$$\tau = \frac{d_2 - d_1}{d_2 + d_1} \tag{3.1.1i}$$

where $K(\tau)$ and $E(\tau)$ are complete elliptic integrals of the first and second kind respectively.

As seen in the figure 3.1 below, using 10° linear segments to approximate the ring, the velocity predictions match the exact solution closely. Sandeep[75] has demonstrated that compared to helical filaments (including skewed ones), vortex rings represent a limiting case demonstrating the largest error. In general Sandeep demonstrated second order accuracy with decreased filament length. This comparison is a prescribed wake and basically demonstrates that the code is predicting the induced velocity correctly given the vortex filaments' positions and strengths.
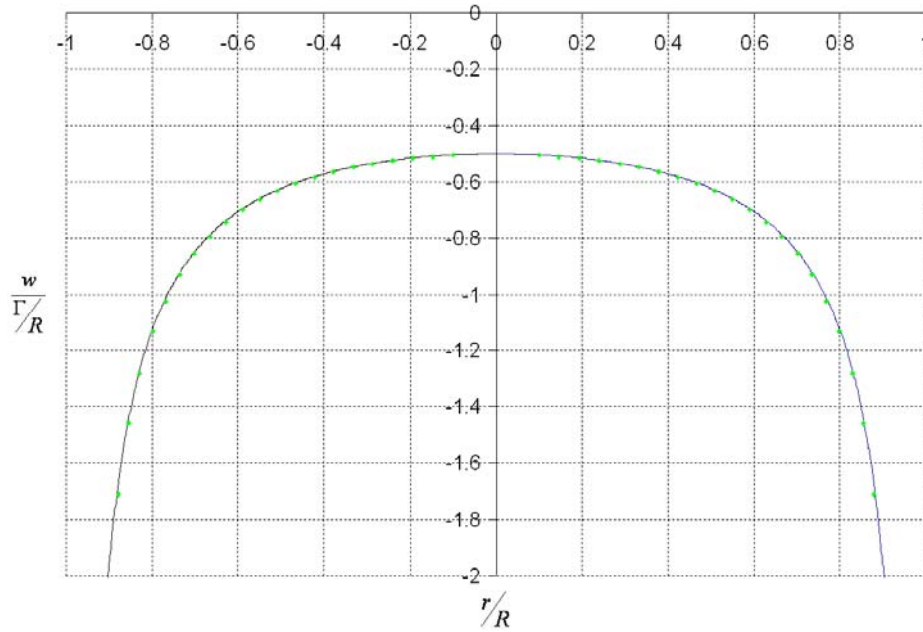
Figure 3.1: Induced Velocity of a Vortex Ring: Comparison of the exact solution of a vortex ring (solid line) and an approximate ring formed by 10 degree linear sectors (dots).

To explore how accurate the predicted position of the relaxed wake will be, one can look at the stability of the system as done by Bhagwat[70]. The differential equation governing the motion of the shed and trailing filaments is,

$$\frac{d\vec{r}}{dt} = \vec{V}(t).$$

3.1.1

which is non-linear by virtue of the velocity term which is given by the Law of Biot-Savart although altered to include a viscous core. A first attempt to assess the accuracy of a FDE is to examine the order of the FDE relative to the PDE. This code uses two

possible methods for calculating the new position of filaments. The first is Euler
integration which can be shown to be only first order accurate. This is demonstrated by
expanding the position vector, r_{n+1}, in a Taylor Series about the point r_n,

$$r_{n+1} = r_n + \Delta t \cdot \frac{d\vec{r}_n}{dt} + \frac{1}{2!} \cdot \Delta t^2 \cdot \frac{d^2 r_n}{dt^2} + \frac{1}{3!} \cdot \Delta t^3 \cdot \frac{d^3 r_n}{dt^3} + \dots , \qquad 3.1.2$$

$$r_{n+1} = r_n + \Delta t \cdot \vec{V}_n(t) + O(2) . \qquad 3.1.3$$

This method is used in forward flight where the errors will be "washed"
downstream with the free stream velocity, thus limiting the effects of the errors in
calculating the solution. Equation 3.1.3 is also used as the predictor step in the
alternative two-step procedure. The second step of this alternative method is essentially
trapezoidal integration or a second order central difference. Expansions about the point
$r_{n+1/2}$, r_n and r_{n+1} are found to be,

$$r_{n+1} = r_{n+\frac{1}{2}} + \Delta t \cdot \frac{d\vec{r}_{n+\frac{1}{2}}}{dt} + \frac{1}{2!} \cdot \Delta t^2 \cdot \frac{d^2 r_{n+\frac{1}{2}}}{dt^2} + \frac{1}{3!} \cdot \Delta t^3 \cdot \frac{d^3 r_{n+\frac{1}{2}}}{dt^3} + \dots , \quad 3.1.4$$

$$r_n = r_{n+\frac{1}{2}} - \Delta t \cdot \frac{d\vec{r}_{n+\frac{1}{2}}}{dt} + \frac{1}{2!} \cdot \Delta t^2 \cdot \frac{d^2 r_{n+\frac{1}{2}}}{dt^2} - \frac{1}{3!} \cdot \Delta t^3 \cdot \frac{d^3 r_{n+\frac{1}{2}}}{dt^3} + \dots , \quad 3.1.5$$

taking the difference of these two expressions yields,

$$r_{n+1} - r_n = 2 \cdot \Delta t \cdot \frac{d\vec{r}_{n+\frac{1}{2}}}{dt} + O(3) , \qquad 3.1.6$$

or,

$$r_{n+1} - r_n = 2 \cdot \Delta t \cdot \vec{V}_{n+\frac{1}{2}}(t) + O(3) , \qquad 3.1.7$$

where,

$$\vec{V}_{n+\frac{1}{2}}(t) = \frac{1}{2} \cdot \left(\vec{V}_n(t) + \vec{V}_{n+1}(\tilde{t}) \right) , \qquad 3.1.8$$

The velocity, $\vec{V}_{n+1}(\tilde{t})$, is the velocity at the time and corresponding position calculated by
the Euler Predictor step. From equation 3.1.6, it is seen that this is second order accurate
and it is used only in hover. The velocity term being non-linear, this analysis is not
guaranteed to be of the order predicted but it is unlikely to perform better.

Now knowing the theoretical linear accuracy of the method, it is also valuable to
ensure that the wake evolution is comparable with other existing applications to

demonstrate that this code has been implemented correctly. Below in figure 3.2 are comparisons of the inflow distribution between the same cases performed in CAMRAD II and the current code. The helicopter configuration is the same as the baseline defined later in chapter 4.1. The inflow distributions show very similar gross patterns and generally equivalent magnitudes. Differences appear due to the proximity of trailing vortices to the rotor disk. CAMRAD II solutions tended to have slightly higher shaft tilt angles which washes the vortices away from the disk plane more quickly. This results in less prominent velocity variations at the disk providing a generally smoother appearance.

a.) Baseline: Inflow (AR=0.4)   b.) CAMRAD II: Inflow (AR=0.4)
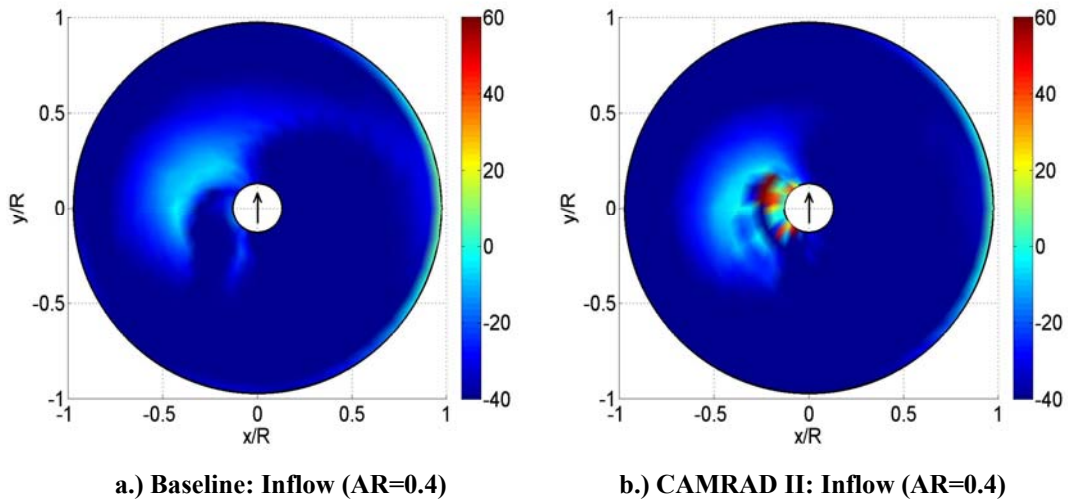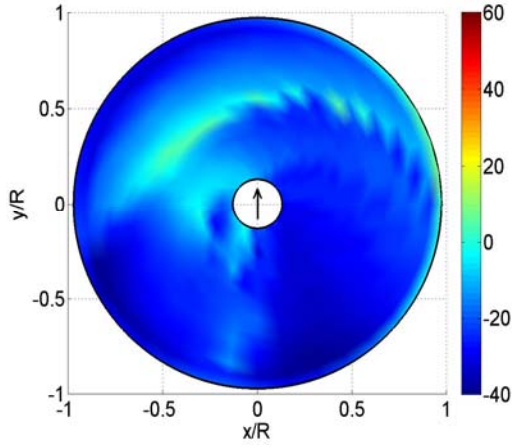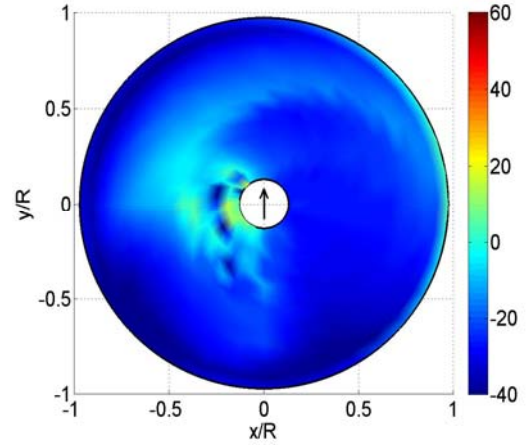
c.) Baseline: Inflow (AR=0.3)   **d.) CAMRAD II: Inflow (AR=0.3)**
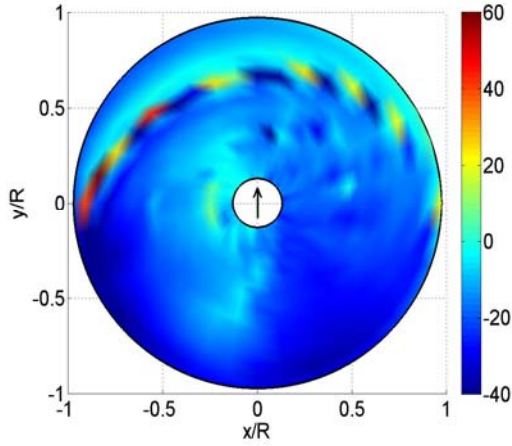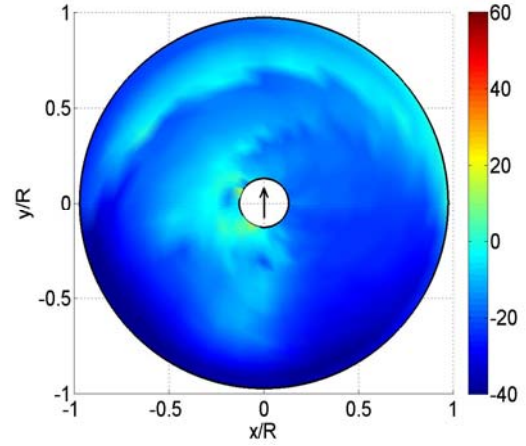
e.) Baseline: Inflow (AR=0.2)   **f.) CAMRAD II: Inflow (AR=0.2)**
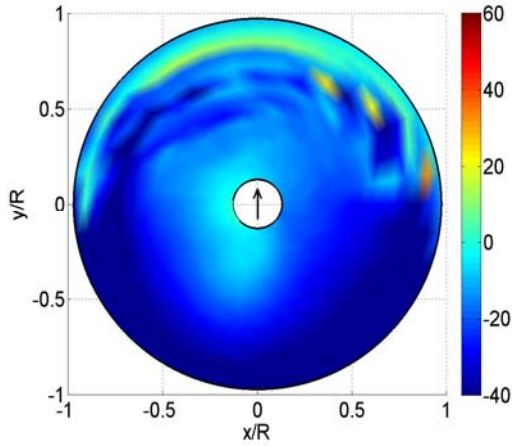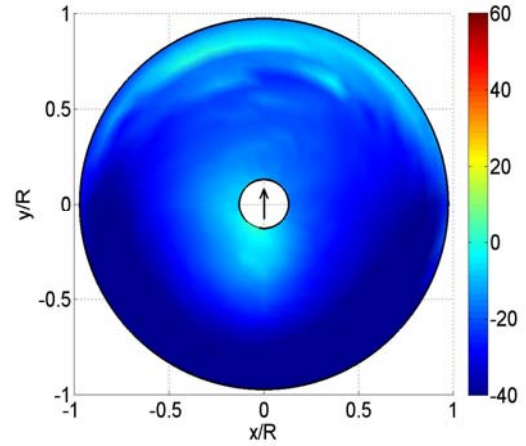
g.) Baseline: Inflow (AR=0.1)   **h.) CAMRAD II: Inflow (AR=0.1)**

Figure 3.2 a-h: Induced Inflow Comparisons: Comparisons of induced inflow distributions (ft/s) between the baseline results and CAMRAD II distributions.

3.2 Lattice Spacing

It is also important to demonstrate how dependent the solutions are on the discritization of the problem. In all cases where data is presented, the blade and wake are broken into 15 radial segments with 16 trailing filaments and the wake is divided into 10° azimuthal segments. In order to demonstrate the dependence of solution on the lattice spacing, figure 3.3 shows the baseline solution described in chapter 4.1 against two alternatively denser grids.
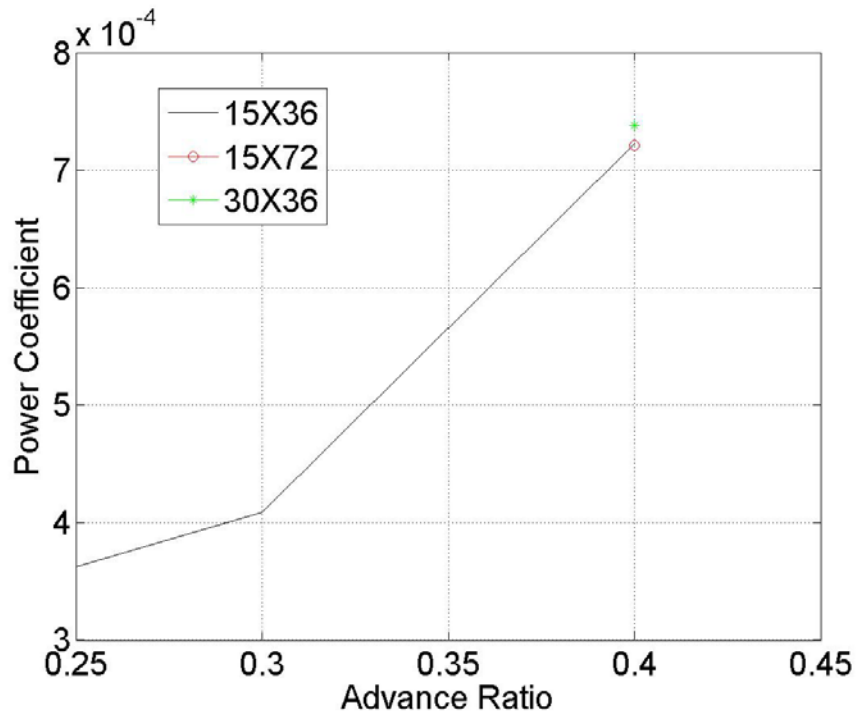
Figure 3.3: Grid Dependence of the Baseline Rotor: The circle doubles the azimuthal grid density while the asterisk doubles the radial grid density.

Bhagwat[70] cites the need for azimuthal variation of five degrees or less to ensure the accuracy of the solutions but in order to solve for the optimization gradients, the problem must be solved for each perturbation equivalent to the product of the number of spanwise and azimuthal elements. This limits the allowable grid size. Figure 3.3 demonstrates that doubling the grid density azimuthally has very little difference in the solution. Doubling the radial grid density does change the power coefficient by almost 3%. The greater increase in this case is attributable to better resolution of the spanwise formation and location of the tip vortex due to the higher trailing filament density.

Figure 3.4 shows the same results for optimized results at an advance ratio of 0.4. Again, the solution for doubling the azimuthal discretization makes little difference to the optimized solution. For the increased radial density, there is a larger change in power coefficient again due to the increased resolution of the tip vortex. These results justify the choice of the grid size used for this optimization study.
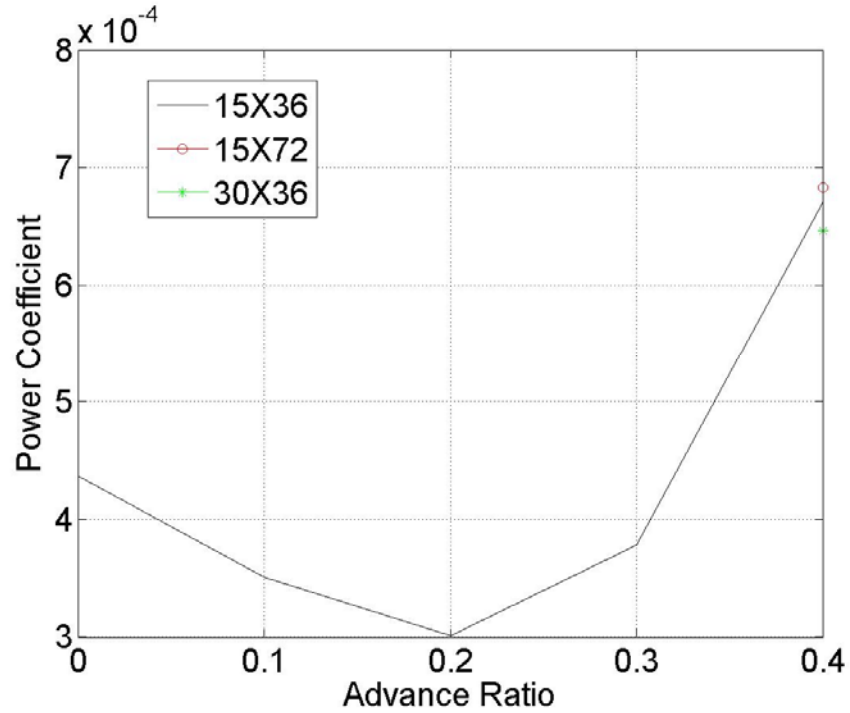
Figure 3.4: Grid Dependence of the Optimized Rotor: The circle doubles the azimuthal grid density while the asterisk is double the radial grid density.

Chapter 4:   Results and Discussion

4.1 Physical Model:

The baseline configuration used for all of the results is presented below. Table 4.1.1 presents the characteristics of the baseline rotor. For the optimized rotor, the circulation is allowed to vary continuously both radially and azimuthally as an unconstrained morphing rotor.

Blades (N):	4
Tip Radius (R):	20 ft
Root Cutout (c):	10%
Airfoil:	NACA 0012
Blade Solidity (σ):	0.1
Linear Twist (θ_{tw}):	-6°
Tip Speed (V_{tip}):	600 ft/s
Angular Velocity (Ω):	30 rad/sec
Air Density (ρ):	0.0023769 slug/ft^3
Vehicle Weight (W):	7527.0 lbs
Flat Plate Drag Coefficient (S·C_D):	15 ft^2

Table 4.1.1: Model Helicopter Properties

The rotor blades for all cases outside of validation were divided into 15 radial elements producing 16 trailing wake filaments. One revolution of the wake was divided into 10° elements yielding 36 segments per revolution.

Radial Discritization:	15 elements
Azimuthal Discretization:	36 segments

Table 4.1.2: Helicopter Disk Discretiztion

Discritized radial elements were divided using the formulas shown in table 4.1.3 which describes the position of the end points of each element. The forward flight discretization yields a uniform spacing while the hover elements are weighted toward the root and tip where there is more change in circulation expected.

Forward Flight:	$r = R[c \cdot +(1-c) \cdot x]$	$x = \frac{0}{15}, \frac{1}{15}, \ldots, \frac{14}{15}, \frac{15}{15}$
Hover:	$r = R[c \cdot +(1-c) \cdot \sin(x)]$	$x = \frac{0}{15}, \frac{1}{15}, \ldots, \frac{14}{15}, \frac{15}{15}$

Table 4.1.3: Spanwise Discretiztion of Blade Elements: The r is the radial position, *R* is the rotor radius, and *c* is the fraction of the cutout distance to rotor radius

Table 4.1.4 shows the length of wake used for each case. Regions beyond the free wake move with an average downwash.

Advance Ratio (*µ*)	Length	Free Tip Length	Free Inboard Filament Length
Hover	20	3	3
Forward Flight	3	3	0.25

Table 4.1.4: Number of Spanwise Elements Used to Model the Wake: (Number of Revolutions)

The tip vortex is modeled to grow according to the equation 2.3.5. The inboard and shed filaments have a diameter equivalent to the average of the width of the blade radial element on either side of the trailing vortex.

4.2 Results:

The results presented below compare the baseline rotor with its optimized solution. The total power coefficients and its respective components are shown in figure 4.2.1a. The total power coefficient is broken into two components. The first component is profile power caused by viscous effects on the blades. The second is the inviscid power which is the result of rotating the lift and drag vectors. Two sources of inviscid power are distinguished by the source of the inflow causing the relative force vector to tilt. The first is the induced component which is the portion of power attributed to the velocity (or inflow) induced by producing lift, i.e. produced by the shed and trailing vorticity in the wake. The second component caused by inflow present because the rotor disk is tilted by the amount of the shaft tilt angle into the direction of the on coming free stream velocity. The component of the free stream now perpendicular to the lift at the rotor disk, equivalent to *V·sin(α)* as seen in figure 4.2.2, creates a pressure drag. This component known as the ram power is approximated to be the product of the lift

produced across the disk and this perpendicular component of velocity. This component is in part the cost to overcome the vehicle parasite drag in forward flight. The in-plane longitudinal force produced by the rotor disk directed in the drag direction and its respective component of free stream velocity, equivalent to $V \cdot cos(\alpha)$ as seen in figure 4.2.2, produce what CDI[1] have referred to as the rotor parasite power. This provides the second portion balancing the power lost by the vehicle parasite power. As defined in this effort, the vehicle parasite drag is always in line with the free stream velocity, thus requiring an equivalent force to be created by the thrust and longitudinal force toward the direction of flight. The rotor parasite power described here comes from a momentum theory approximation using the gross parameters of rotor longitudinal force, shaft tilt angle, and flight speed. The actual source of this power consumption results from both the profile and induced drag on the blade. Changes in this parameter between the baseline and optimum reflect changes in both the profile and induced drag distributions. The reason for analyzing the power decomposition through the ram and rotor parasite powers rather than just attributing these two components to the vehicle parasite power is that they draw directly from the physics of the rotor disk. These two components of power illustrate how the rotor compensates for the presence of the vehicle fuselage, whose force is transmitted through the rotor shaft and therefore affects the trim, but has no other direct effect on the rotor aerodynamics in this model.
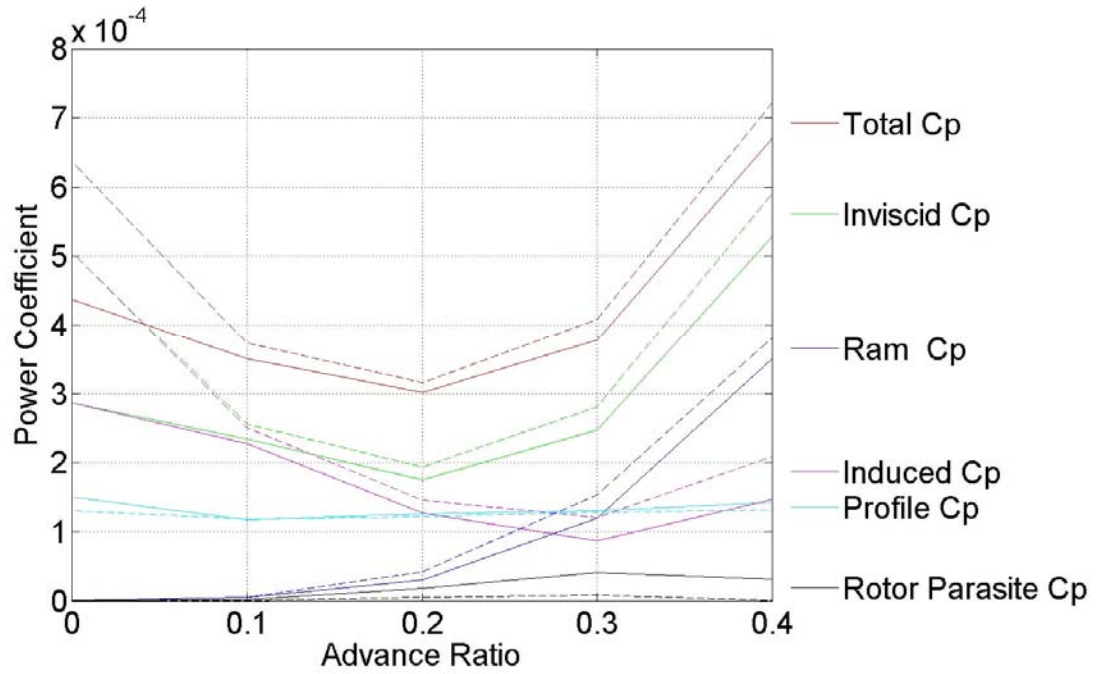
a.) Power Coefficient
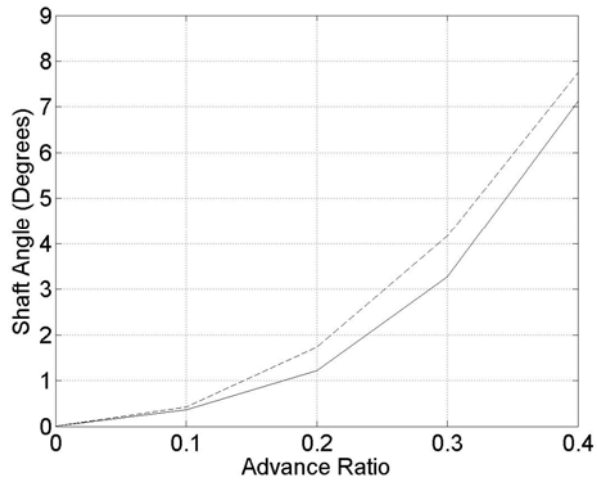
b.) Shaft Angle
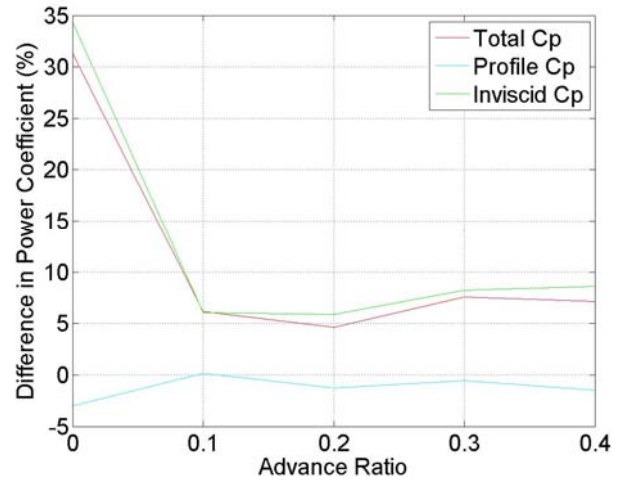
c. Percent Change in Component Powers

Figure 4.2.1 a-c: Power Comparisons: Comparison of the power coefficients and shaft angles between the optimum and baseline. Dashed lines correspond with the baseline values and solid with the optimized solution. c.) Percentages are of the baseline total *Cp*.
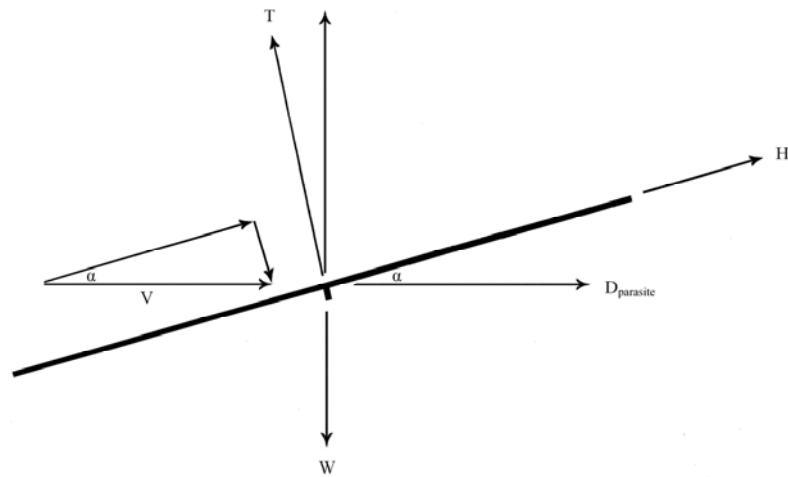
Figure 4.2.2: Trim of the Main Rotor

As can be seen in figure 4.2.1a, the optimized total power is lower than the baseline at all advance ratios. Looking at the components which form the total power, one can see that the profile power, when compared with the other sources, is relatively constant over the range of the advance ratios and shows minimal change between the optimized and baseline solutions. The limited change between the baseline and optimized cases results from the major factors which influence the profile power remaining fixed in the optimization. The rotor speed and flight speed were fixed leaving only the usually minor velocity component of induced flow to modify the relative velocity experienced by the rotor at any given point. The rotor chord distribution, which certainly is not optimal, was also held constant. Therefore, the only way to lower the profile power is to change the angle of attack which is highly constrained by the need to simultaneously produce lift. The resulting profile power is actually higher for the optimized solution in some cases, which suggests the need for a specific lift distribution outweighs the push for lower profile drag given these constraints.

Turning to the inviscid power and its components the induced and ram powers, one can see that the inviscid power decreases until about an advance ratio of 0.2 and then begins to build again. In general, the induced drag decreases with increased advance ratio until the final advance ratio breaks this trend. The nature of this trend will be analyzed in the context of the lift and drag distributions including an exploration of the

last point. The ram power increases with forward speed. Informing an understanding of the ram power is the difference in the shaft tilt angle which can be seen to decrease for the optimized solution in figure 4.2.1 b. By redistributing the lift and drag production, the rotor apparently does not need as large a shaft tilt angle to trim the optimized solution and therefore requires less ram power. The rotor parasite power seems to grow with advance ratio, though in this case, the optimized rotor has higher power consumption.

To explore the issue of the shaft tilt angle and the associated change in the ram power term, it is illustrative to look at the trim equations.

$$T \cdot \cos(\alpha_{shaft}) + H \cdot \sin(\alpha_{shaft}) - W = 0 , \tag{4.2.1a}$$

$$T \cdot \sin(\alpha_{shaft}) - H \cdot \sin(\alpha_{shaft}) - D_{parasite} = 0 , \tag{4.2.1b}$$

$$M_x = 0 , \tag{4.2.1c}$$

$$M_y = 0 . \tag{4.2.1d}$$

One can see that equations 4.2.1 c and d simply require the vertical force, when integrated over the rotor disk, to yield zero roll or pitch moments. This condition is applies to both the baseline and optimized solutions and does not provide any obvious source of power reduction. For a given advance ratio, both the parasite drag ($D_{parasite}$) and weight (W) are assumed constant, while α_{shaft}, H, and T are variable. Equation 4.2.1b represents the force balance in the axis of the free stream velocity. By taking the product of this entire expression by the free stream velocity, each term forms a component of power (ram, rotor parasite, and vehicle parasite respectively).

$$T \cdot V_\infty \cdot \sin(\alpha_{shaft}) - H \cdot V_\infty \cdot \sin(\alpha_{shaft}) - D_{parasite} \cdot V_\infty = 0 \tag{4.2.2}$$

As pointed out above, reducing the shaft tilt angle reduces the ram drag and power, but since the vehicle parasite drag, and therefore power, will be constant, the rotor parasite drag and power must increase to compensate. Therefore, those components of power collectively can not be improved. The vehicle drag would be required to decrease in order to reduce these terms. The trade off between the ram and rotor parasite power does provide a source for transferring induced drag to profile power. Although this does not

directly reduce the power consumption required for forward flight, it does reduce the amount of thrust that the rotor is required to produce to balance the weight by reducing the shaft tilt angle. At least from a gross perspective, lowering the required thrust may lower the induced drag and power. Therefore, retrimming the rotor is one source for power savings. This potential source of power savings is lost in a purely inviscid optimization.

Figure 4.2.1c shows the change in power as a percentage of the baseline total power. It is apparent from this figure that most power savings is inviscid and that changes in the profile power are actually slightly detrimental. Since the inviscid power improvements are a few times larger than the profile power increases, there is obviously a second more important mechanism for reducing power which is to change the lift distributions. This will be explored further below.

Figure 4.2.3 displays a component of the forces produced by the rotors. The forces in any direction do not change significantly but figure 4.2.3 c alleviates one possible source of concern of this analysis. Although there is no power consumption associated with the side force as there is no component of free stream velocity in the side component and any induced velocity is included in the inviscid power component, it does raise the concern of how the results would be different if a full vehicle trim were used. A wind tunnel trim does not consider the lateral force or yawing moment and the code could exploit this fact and may therefore predict impossible power improvements. Given only modest shifts in the lateral force, it is unlikely this is the case here.
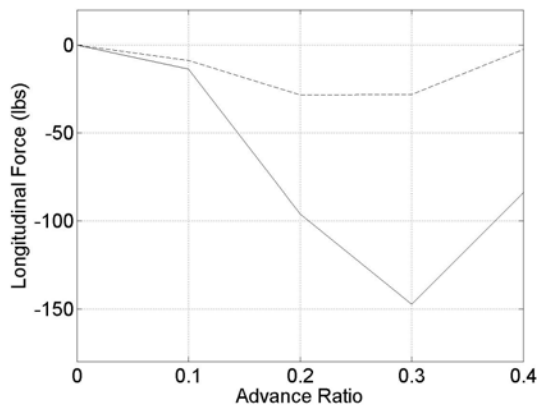
a.) Longitudinal Rotor Disk Force
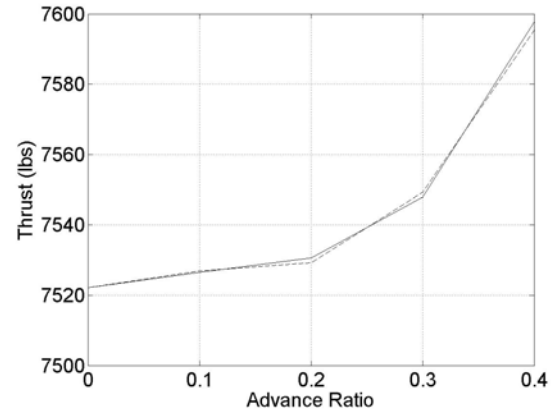
b.) Vertical Rotor Disk Force
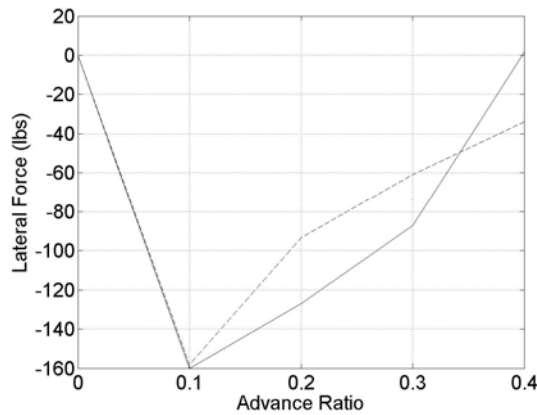
c.) Lateral Rotor Disk Force

Figure 4.2.3 a-c: Force Comparisons: Comparison of the longitudinal, vertical, and lateral forces (lbs) between the optimum and baseline rotor. Dashed lines correspond to the baseline values and solid to the optimized solution.

Presented below in figures 4.2.4 and 4.2.5, one can see the baseline and optimized lift distributions and the differences between them at different advance ratios. One can generally say that there is a decrease in lift toward the blade tip with a corresponding increase in lift inboard for the optimized contours, especially on the advancing side of the disk. This is especially clear in the difference contours. The changes tend to be largely symmetric fore and aft on the disk at higher advance ratios while being more uniformly redistributed azimuthally as the advance ratio decreases. These trends seem to change at an advance ratio of 0.4. The shifting of lift inboard is pronounced on the advancing side where the higher advance ratios yield a high relative velocity. An increase in the size of the reverse flow region on the retreating side reduces the potential for obtaining extra lift.

Therefore the rotors in both baseline and optimized cases must resort to producing more lift toward at the tips which lead to higher induced velocities and explains the reversal of the induced drag trend at 0.4. The optimization also responded differently. Now lift is increased fore and aft while decreasing in the center. In hover, there is a shift of lift inboard over the baseline which concentrates much of its lift near the tips.

Comparing these results with previous results, both Moffitt and Bissell[27] and Hall and Yang[35] cite a more symmetric force distribution fore and aft. This observation is different from Rand[7,8] and the current results which do not see exact symmetry but do tend toward this direction. The discrepancy here has to do with the difference in assumptions in the analysis. A fixed wake analysis is used by Moffitt[27] and Hall[35] while Rand[7,8] and the current results are relaxed wake methods. A relaxed wake destroys the near symmetry of a fixed wake. A second commonly cited effect of optimization which is not seen here is the reduction of a negative tip load. Because the blade twist for the baseline configuration is so shallow the tip on the advancing side is rarely actually at a negative angle of attack.
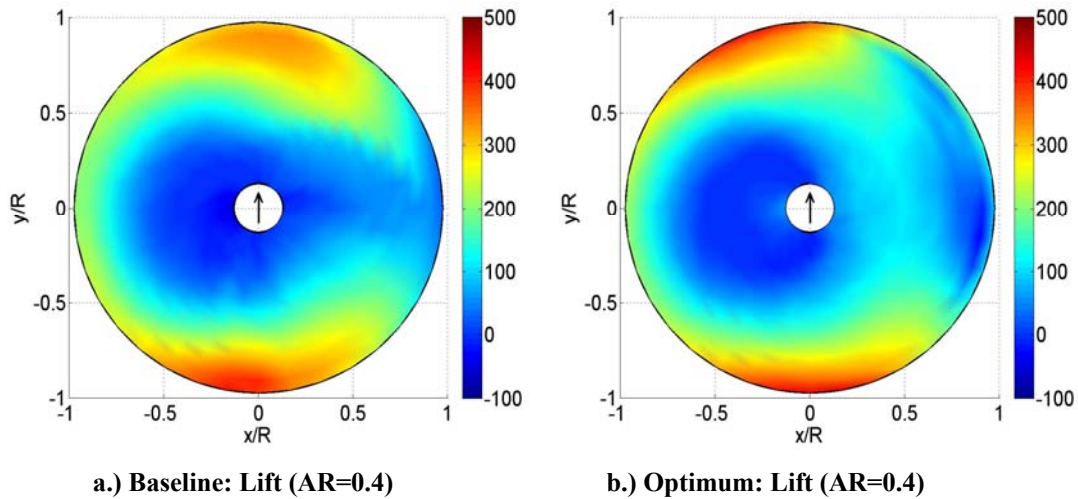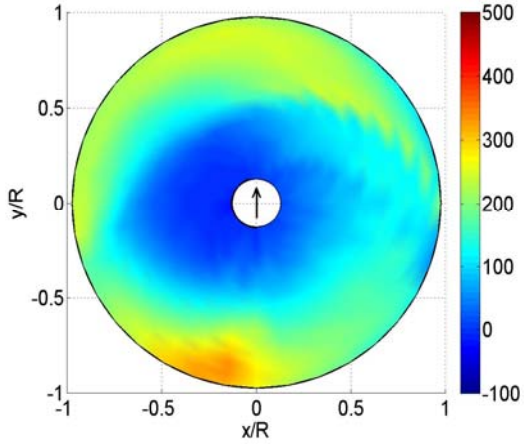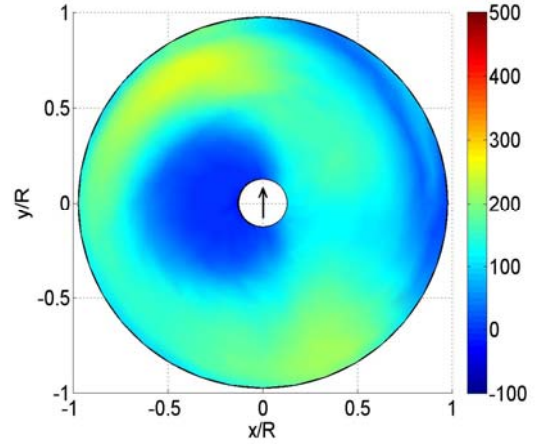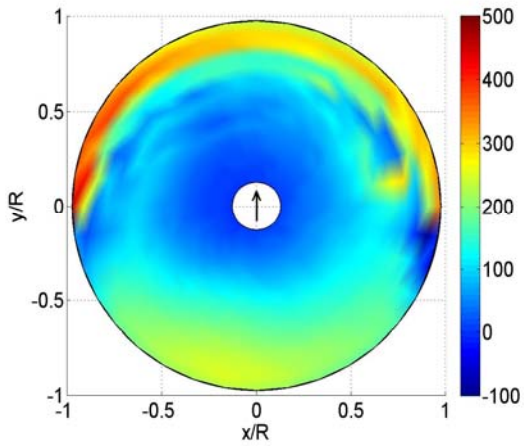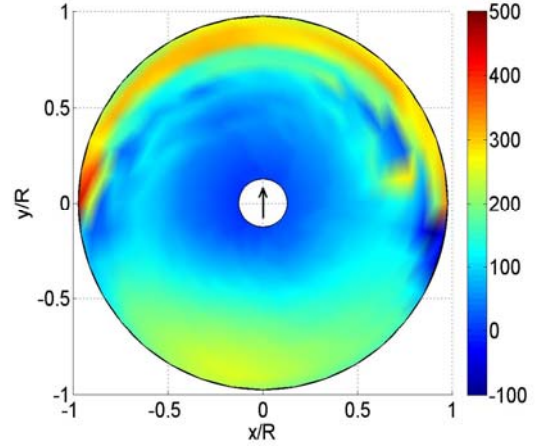
a.) Baseline: Lift (AR=0.4)   b.) Optimum: Lift (AR=0.4)

c.) Baseline: Lift (AR=0.3)

d.) Optimum: Lift (AR=0.3)

e.) Baseline: Lift (AR=0.2)
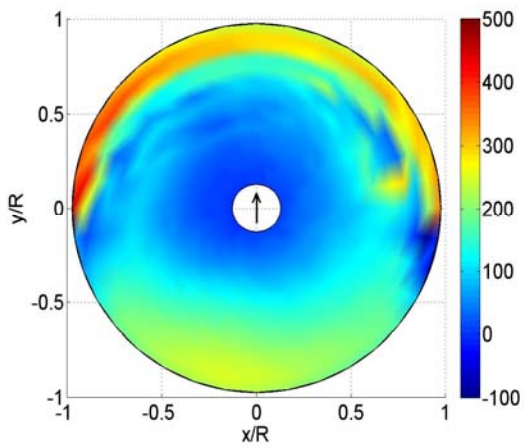
f.) Optimum: Lift (AR=0.2)

g.) Baseline: Lift (AR=0.1)
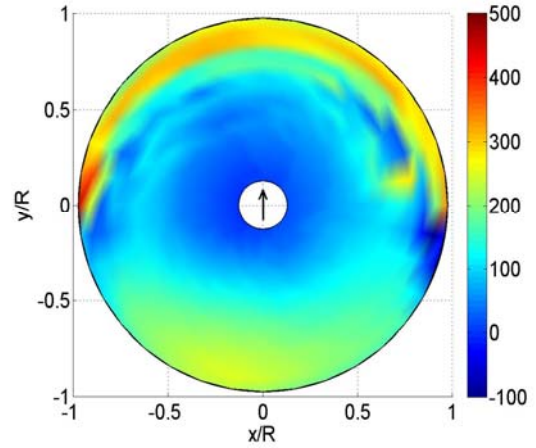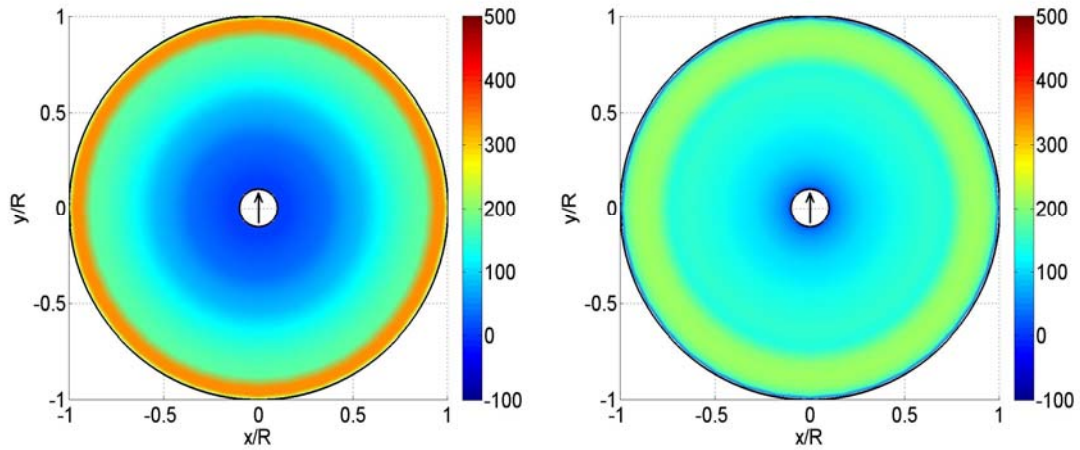
h.) Optimum: Lift (AR=0.1)

i.) Baseline: Lift (AR=0.0) **j.) Optimum: Lift (AR=0.0)**

Figure 4.2.4 a-j: Lift Distribution Comparisons: Comparison of the lift distribution (lbs/ft) between the optimum and baseline. The 2-D plots show eight radial slices separated by 45° and are oriented at shown below in figure 4.2.5.

a.) Lift Difference (AR=0.4)

b.) Lift Difference (AR=0.3)

c.) Lift Difference (AR=0.2)

d.) Lift Difference (AR=0.1)

e.) Lift Difference (AR=0.0)
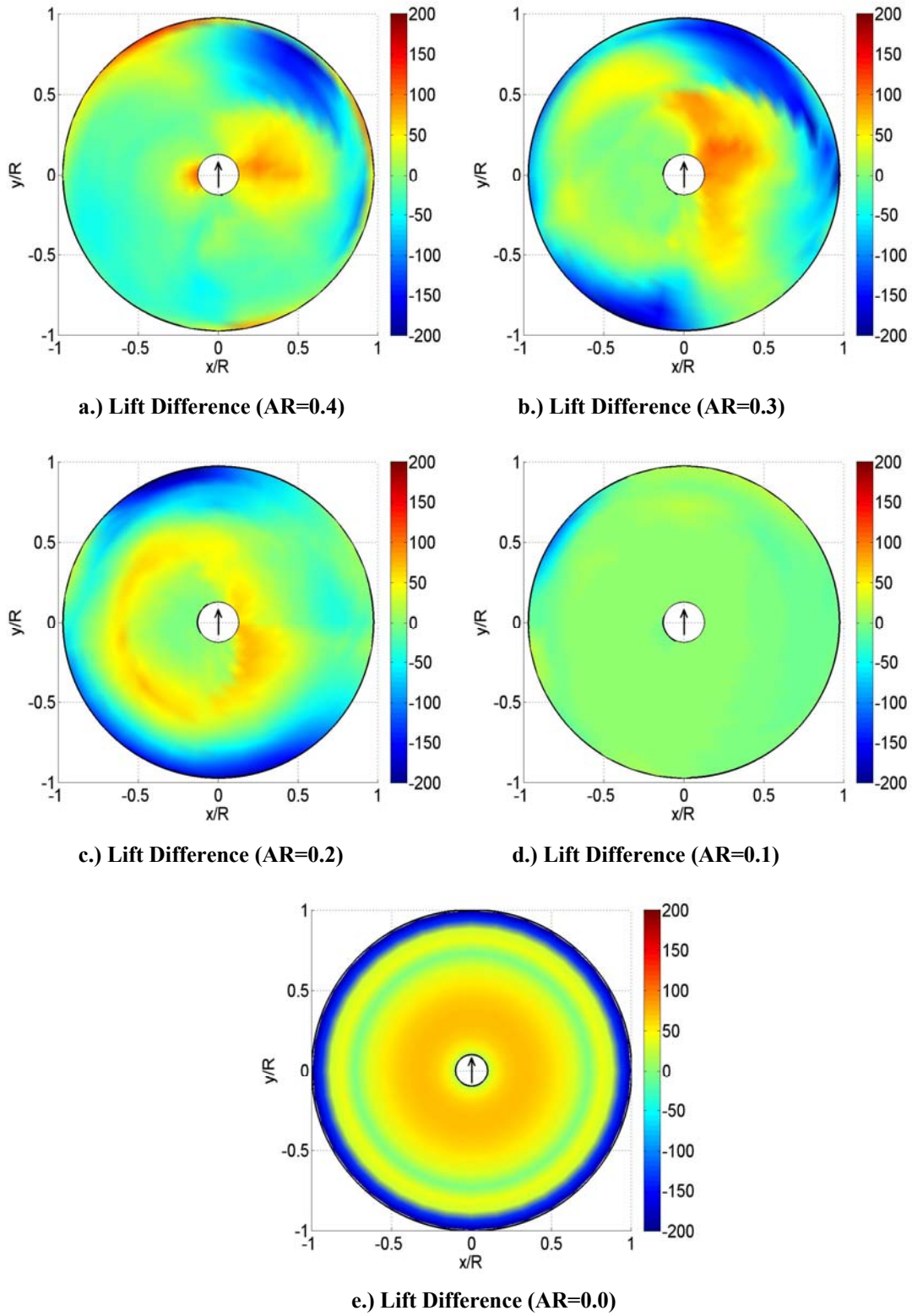
Figure 4.2.5 a-e: Lift Distribution Differences: Difference between the optimum and baseline lift distributions (lbs/ft).

The circulation which is linearly proportional to the lift shows similar trends in figure 4.2.6 and 4.2.7. The optimized circulation tends to increase toward the root and decrease at the tip relative to the baseline as does the lift. Quackenbush,[1] Moffitt[27] and Rand,[7,8] have demonstrated nearly flat circulation contours in hover. Quackenbush[1] and Moffitt[27] demonstrate a peak in circulation due to near blade vortex interaction which induces an up wash on the blade. Rand does not seem to display this phenomenon. In the current results, the optimum hover solution is relatively flat up to the tip with a peak in circulation at the tip.
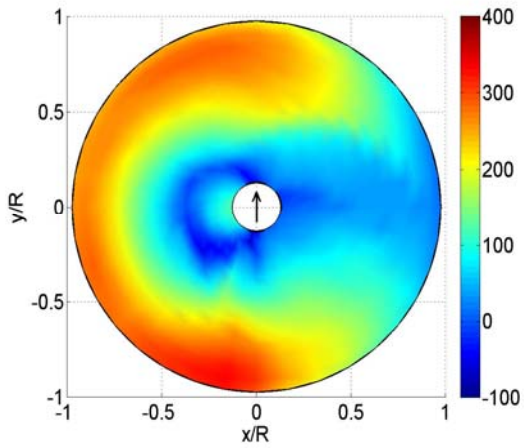
a.) Baseline: Circulation (AR=0.4)   b.) Optimum: Circulation (AR=0.4)
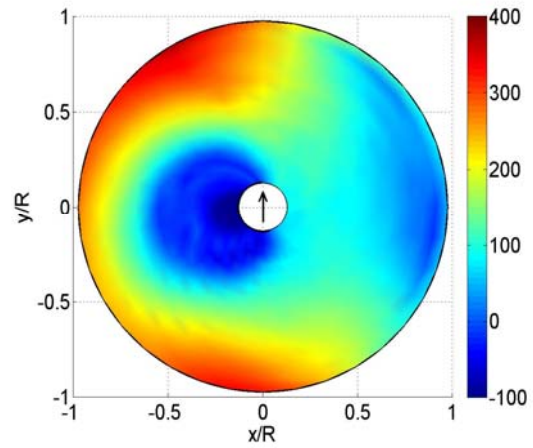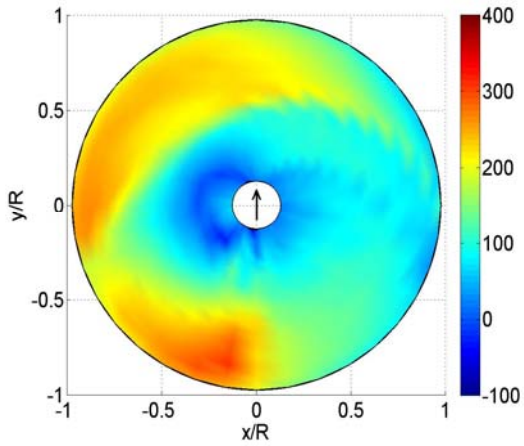
c.) Baseline: Circulation (AR=0.3)   d.) Optimum: Circulation (AR=0.3)
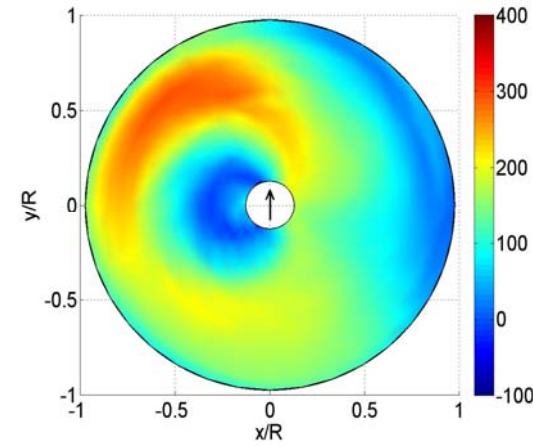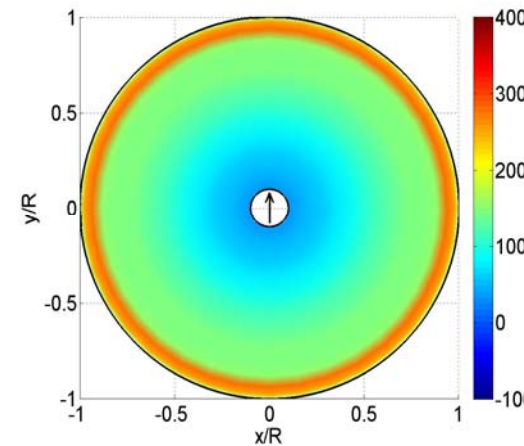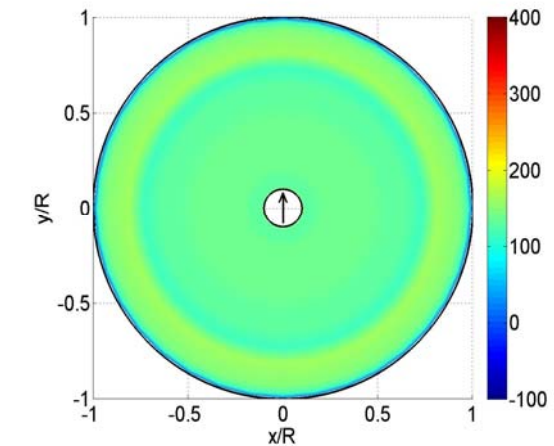
e.) Baseline: Circulation (AR=0.0)   f.) Optimum: Circulation (AR=0.0)

Figure 4.2.6 a-f: Circulation Distribution Comparisons: Comparison of the circulation distribution (ft/s^2) between the optimum and baseline.

a.) Circulation Difference (AR=0.4)   **b.) Circulation Difference (AR=0.3)**

c.) Circulation Difference (AR=0.0)
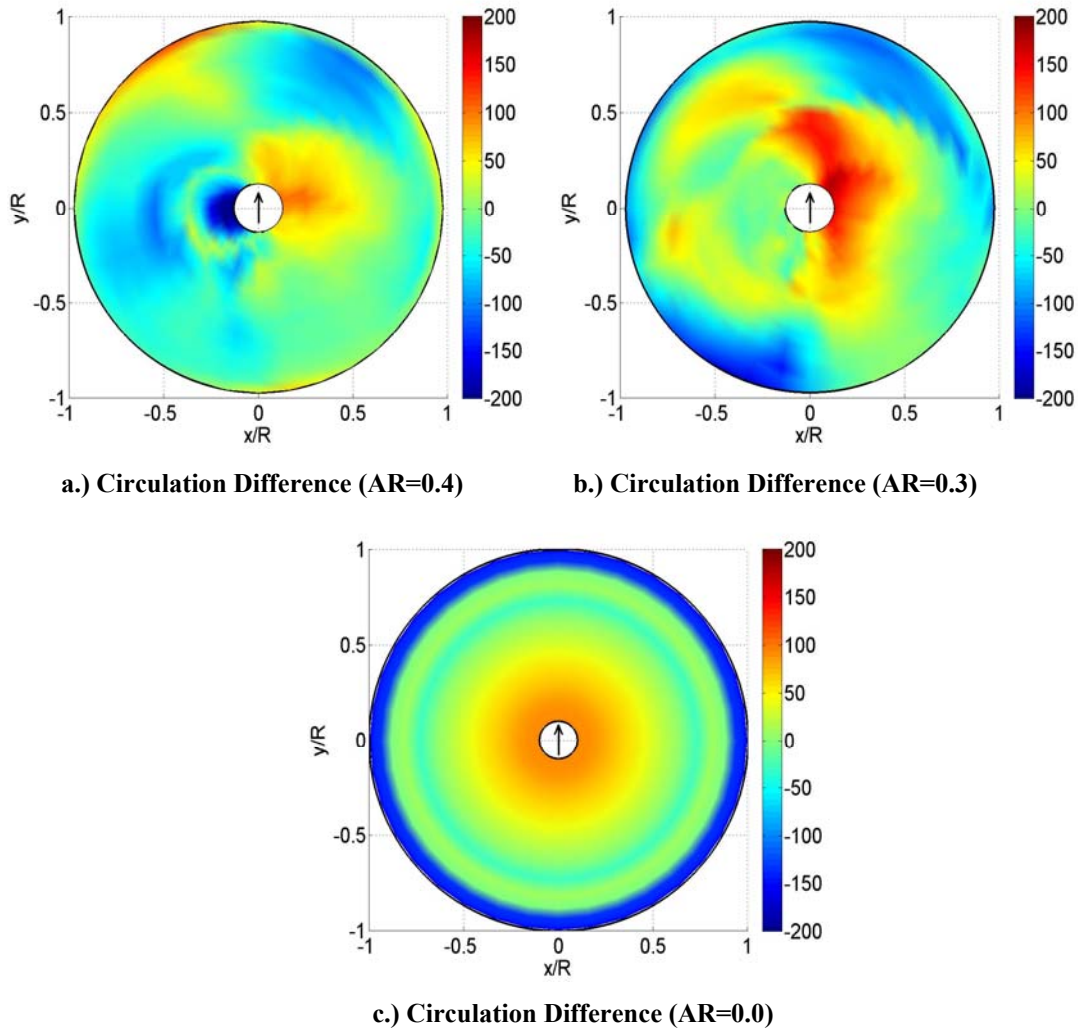
Figure 4.2.7 a-c: Circulation Distribution Differences: Difference between the optimum and baseline circulation distributions (ft^2/s).

The total drag contours are shown below in figure 4.2.8. One thing immediately obvious is the prominence of discrete features due to the vorticity in the wake. The drag contours show a general trend matching the increases in lift with increased drag. Drag tends to be reduced toward the blade tips at the expense of the higher drag inboard as can be seen in figure 4.2.9. This trend lowers required power by concentrating more of the drag inboard where the rotor speed is lower, and since rotor power is the product of the drag and rotor speed, this clearly leads to less power consumption. This trend is contradicted at an advance ratio of 0.4 again where the necessary lift can not be generated on the inboard portion of the retreating side. For this case, the reduced power consumption comes from shifting drag inboard on the advancing side which more than

offsets increases in the drag at other points at the tip on the retreating side. In hover, there is actually a substantial decrease in drag at the blade tips compared both to the baseline or even its own inboard portion. Again, moving the drag inboard lowers the rotor power.
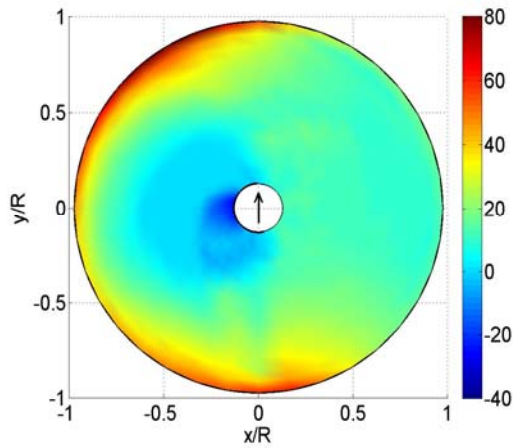
a.) Baseline: Drag (AR=0.4)
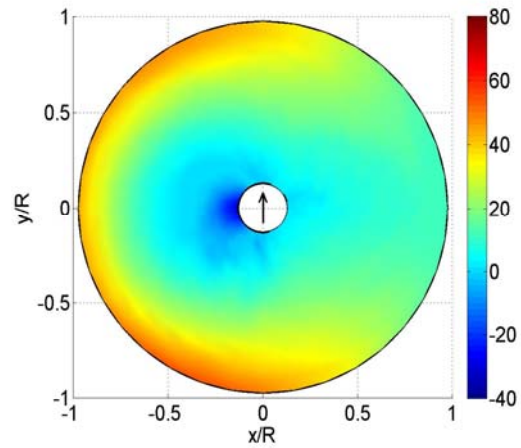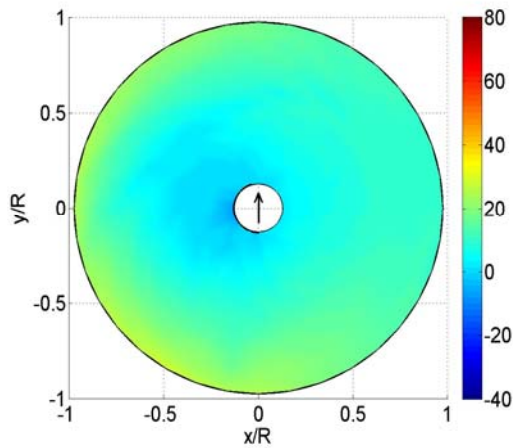
b.) Optimum: Drag (AR=0.4)

c.) Baseline: Drag (AR=0.3)
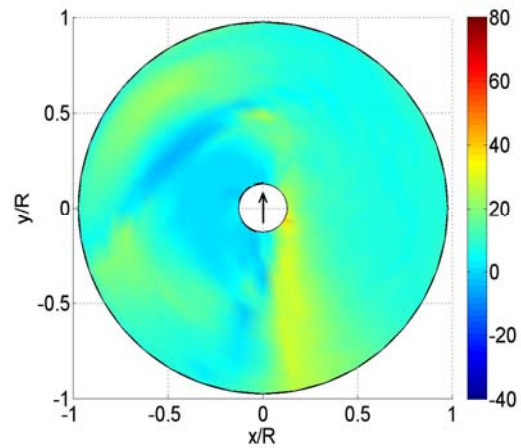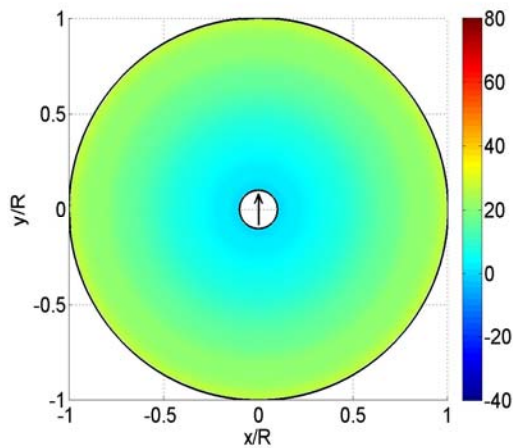
d.) Optimum: Drag (AR=0.3)

e.) Baseline: Drag (AR=0.0)
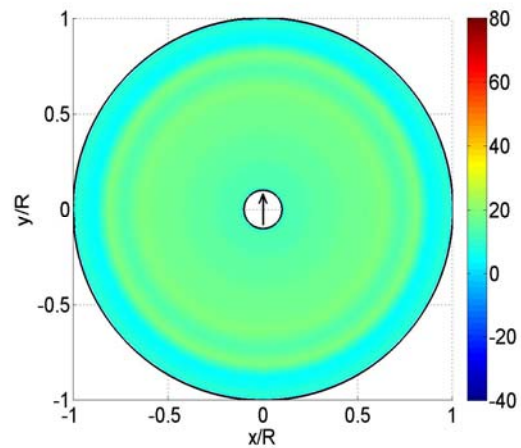
f.) Optimum: Drag (AR=0.0)

Figure 4.2.8 a-f: Drag Distribution Comparisons: Comparison of the drag distribution between the optimum and baseline (lbs/ft).

a.) Drag Difference (AR=0.4)

b.) Drag Difference (AR=0.3)

c.) Drag Difference (AR=0.0)
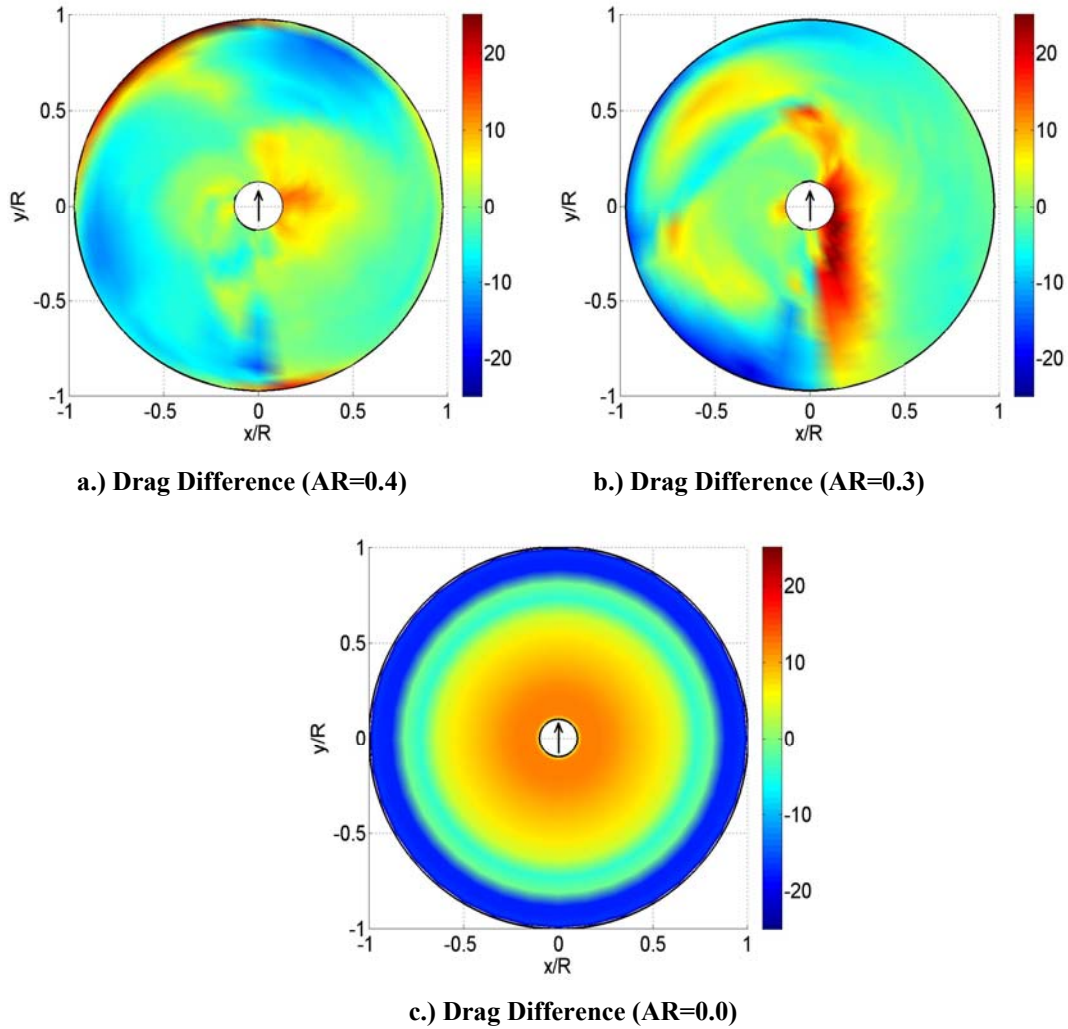
Figure 4.2.9 a-c: Drag Distribution Differences: Difference between the optimum and baseline drag distributions (lbs/ft).

One can see from the similarity and relative scale between figure 4.2.9, 4.2.11, and 4.2.13 that most of the drag consumption, drag savings, and distinct features in the total drag contours are attributable to the inviscid drag, which is consistent with the power plots that appear in figure 4.2.1. For the inviscid drag, the trends are the same as those described above for the total drag. Since inviscid forces are the product of tilting the section force vector, the lift and drag, around the spanwise axis of the blades, regions of increased induced drag correspond to increased lift and/or inflow in those regions and vise versa for decreases in drag. Some of the more discrete features in the optimized inviscid drag contours, especially at the advance ratio of 0.3, are caused by close interactions between the wake and the blades. Since the shaft angle is decreased in the

optimum solution for all forward flight cases, the wake will not be washed down, away from the blades, as quickly. As will be seen below, the inflow in the optimized cases demonstrates the features seen in the induced drag contours. Interestingly for hover, the induced drag at the blade tip is near zero or slightly negative. This implies that the blade tips are almost neutral or actually extracting power from the air. This point will be further addressed below.
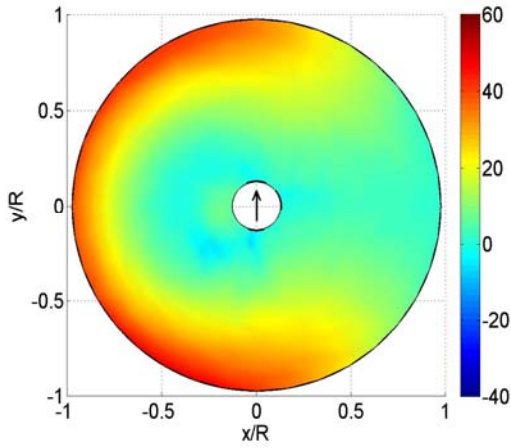
a.) Baseline: Inviscid Drag (AR=0.4)   b.) Optimum: Inviscid Drag (AR=0.4)
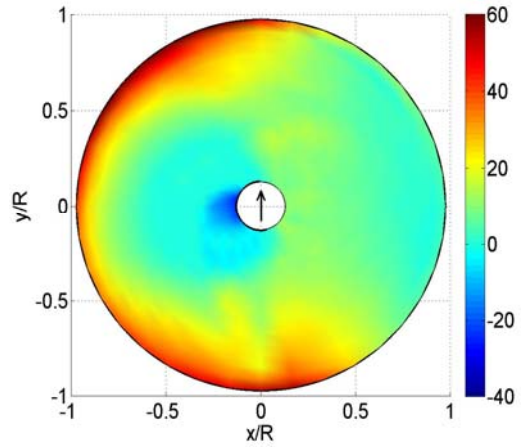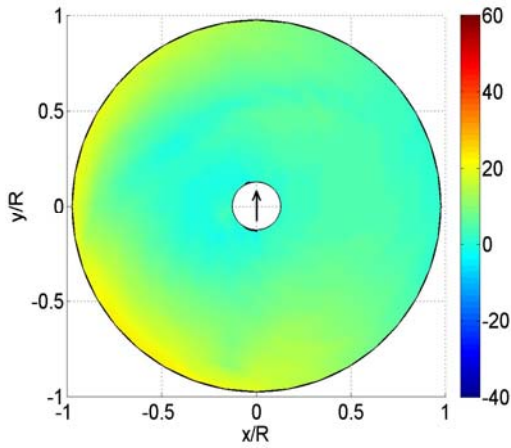
c.) Baseline: Inviscid Drag (AR=0.3)   d.) Optimum: Inviscid Drag (AR=0.3)
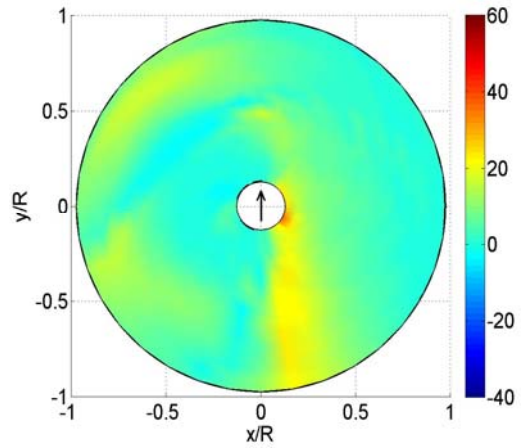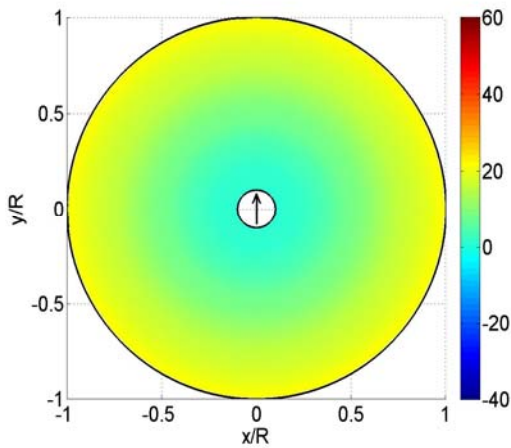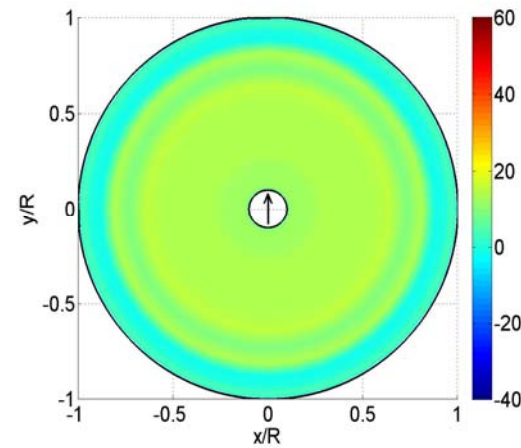
e.) Baseline: Inviscid Drag (AR=0.0)   f.) Optimum: Inviscid Drag (AR=0.0)

Figure 4.2.10 a-f: Inviscid Distribution Comparison: Comparison of the inviscid drag distribution (lbs/ft) between the optimum and baseline.

a.) Inviscid Drag Difference (AR=0.4)

b.) Inviscid Drag Difference (AR=0.3)

c.) Inviscid Drag Difference (AR=0.0)
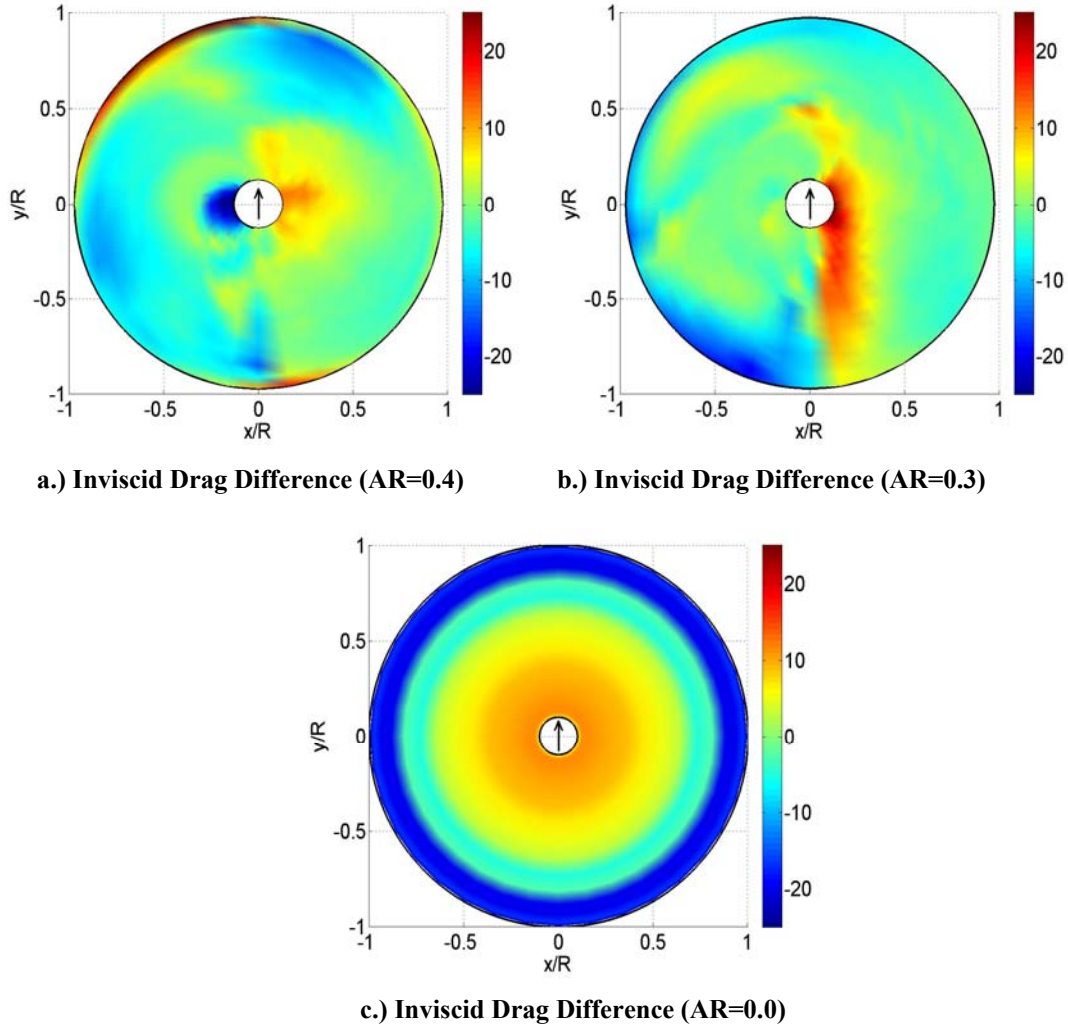
Figure 4.2.11 a-c: Inviscid Drag Distribution Differences: Difference between the optimum and baseline Inviscid drag distributions (lbs/ft).

The profile drag contours are much smoother over the surface of the disk than the inviscid component and correspond closely with changes in lift. There is one exception which is in the reverse flow region where the optimization restricted the possible range of drag coefficients. The code only allowed the airfoil on the optimized rotor to operate in the small angle of attack range between its $c_{\ell\ min}$ and $c_{\ell\ max}$ to eliminate the problem of the c_l and c_d being a multi-valued and with the idea that the high stall angle would produce excessive drag. The implication of this decision is that the pitch of the blade can vary a full 360 degrees. The effect of this can be seen especially well by comparing the reverse flow region of the disk for both cases at an advance ratio of 0.4, figures 4.2.12a and b.   Compared to the baseline case, stall has been almost completely eliminated in

the optimized case. In order to accomplish this drag reduction, as noted above, the blade undergoes extreme, non-physical, twisting as it moves around the disk. The only way to really approach this mode of flight would be to have a segmented rotor, and even so, the current model neglects some unsteady aerodynamics effects: dynamic stall, apparent mass and rotational effects, which would certainly degrade the performance of the optimal solution.
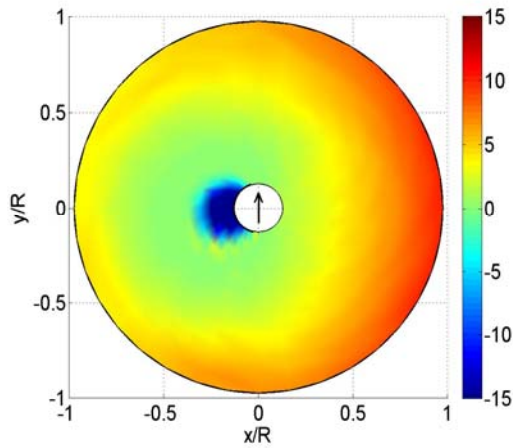
a.) Baseline: Profile Drag (AR=0.4)   b.) Optimum: Profile Drag (AR=0.4)
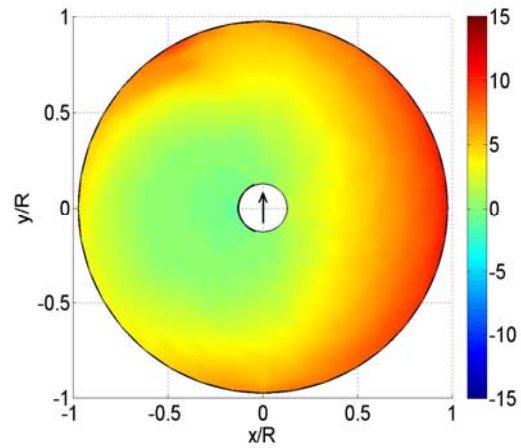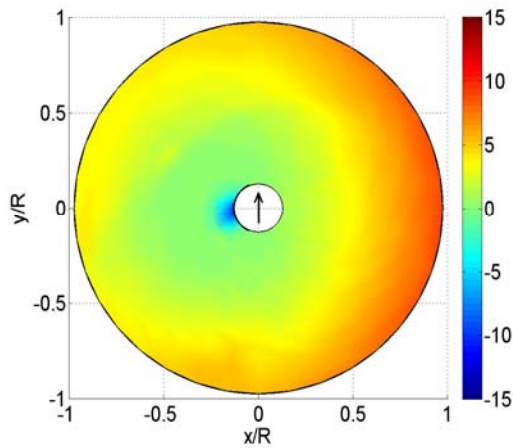
c.) Baseline: Profile Drag (AR=0.3)   d.) Optimum: Profile Drag (AR=0.3)
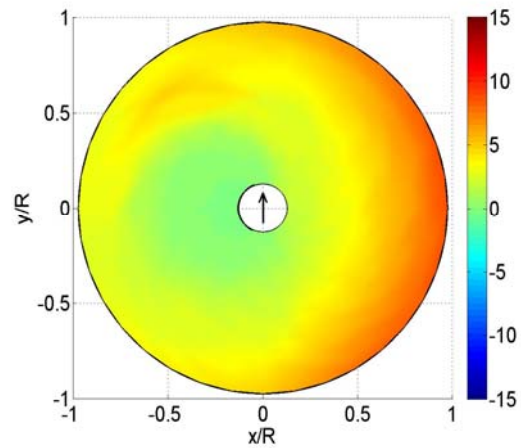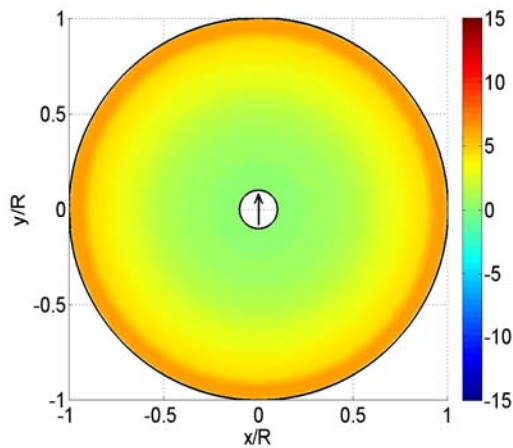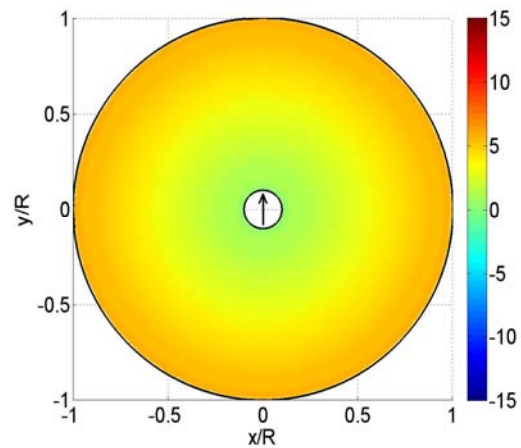
e.) Baseline: Profile Drag (AR=0.0)   f.) Optimum: Profile Drag (AR=0.0)

Figure 4.2.12 a-f: Profile Drag Distribution Comparisons: Comparisons of the profile drag distributions (lbs/ft) between the optimum and baseline. Note this is on a different scale than previous drag contour plots.

a.) Profile Drag Difference (AR=0.4)

b.) Profile Drag Difference (AR=0.3)

c.) Profile Drag Difference (AR=0.0)
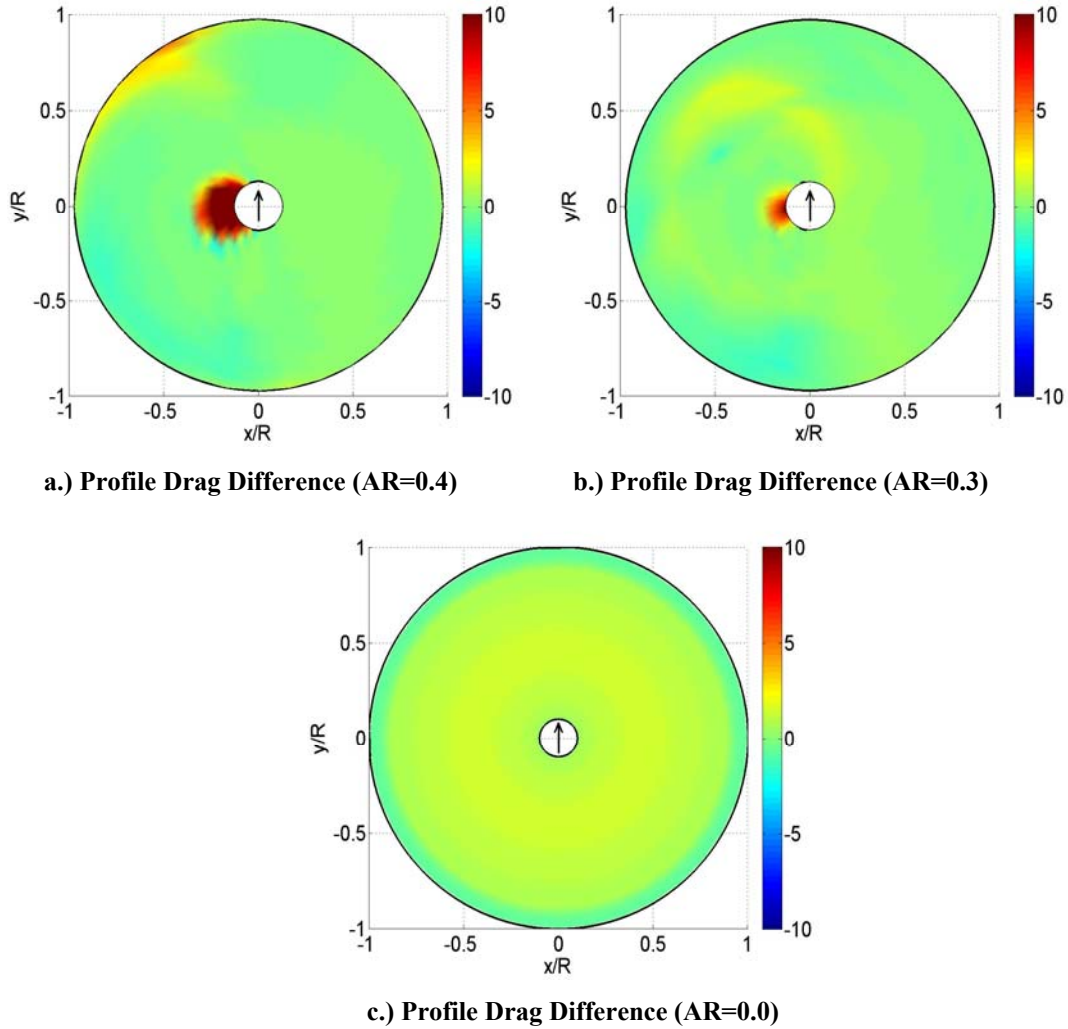
Figure 4.2.13 a-c: Profile Drag Distribution Differences: Difference between the optimum and baseline profile drag distributions (lbs/ft).

Given the way the reverse flow region was treated for the optimized solution, it is important to investigate the amount of power concentrated in the reverse flow region. In figure 4.2.14 the percentage of the power in the reverse flow region relative to the total power appears. Given the relative magnitude of these components, it is probably appropriate to assume that the treatment of the reverse flow region used here does not have a major influence on the calculated possible power savings and that most of the power savings could still be achieved without the same treatment of the reverse flow region.
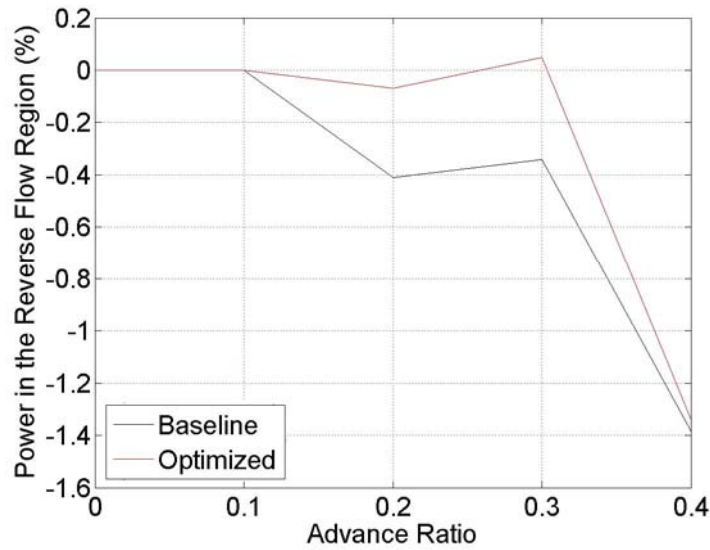
Figure 4.2.14: Percentage of Power in the Reverse Flow Region: Percent difference of the power in the inflow region verses the total power.

To further illustrate why the relative magnitude of the power in the reverse flow region is this small, the total power contours are displayed below in figure 4.2.15. The reverse flow region is designated by the dashed circle. To emphasize the difference between power consumption and propulsive power, which the reverse flow region will typically display, the color scale is skewed to emphasize this transition from consumption to propulsion. One can see that the amount of power is rather insignificant compared to the total power. Regions of propulsive power outside the reverse flow region are due to upwash through the disk from close passage of vortices. These can be seen reflected in the induced drag as well.

a.) Baseline: Total Power (AR=0.4)   **b.) Optimized: Total Power (AR=0.4)**

c.) Baseline: Total Power (AR=0.3)   d.) Optimized: Total Power (AR=0.3)

e.) Baseline: Total Power (AR=0.2)   f.) Optimized: Total Power (AR=0.2)

g.) Baseline: Total Power (AR=0.1)   h.) Optimized: Total Power (AR=0.1)
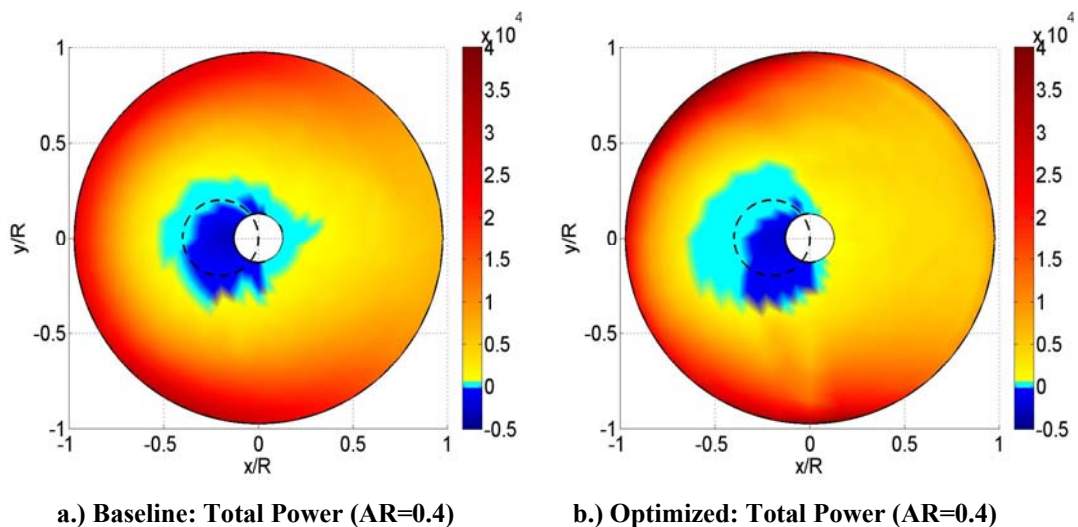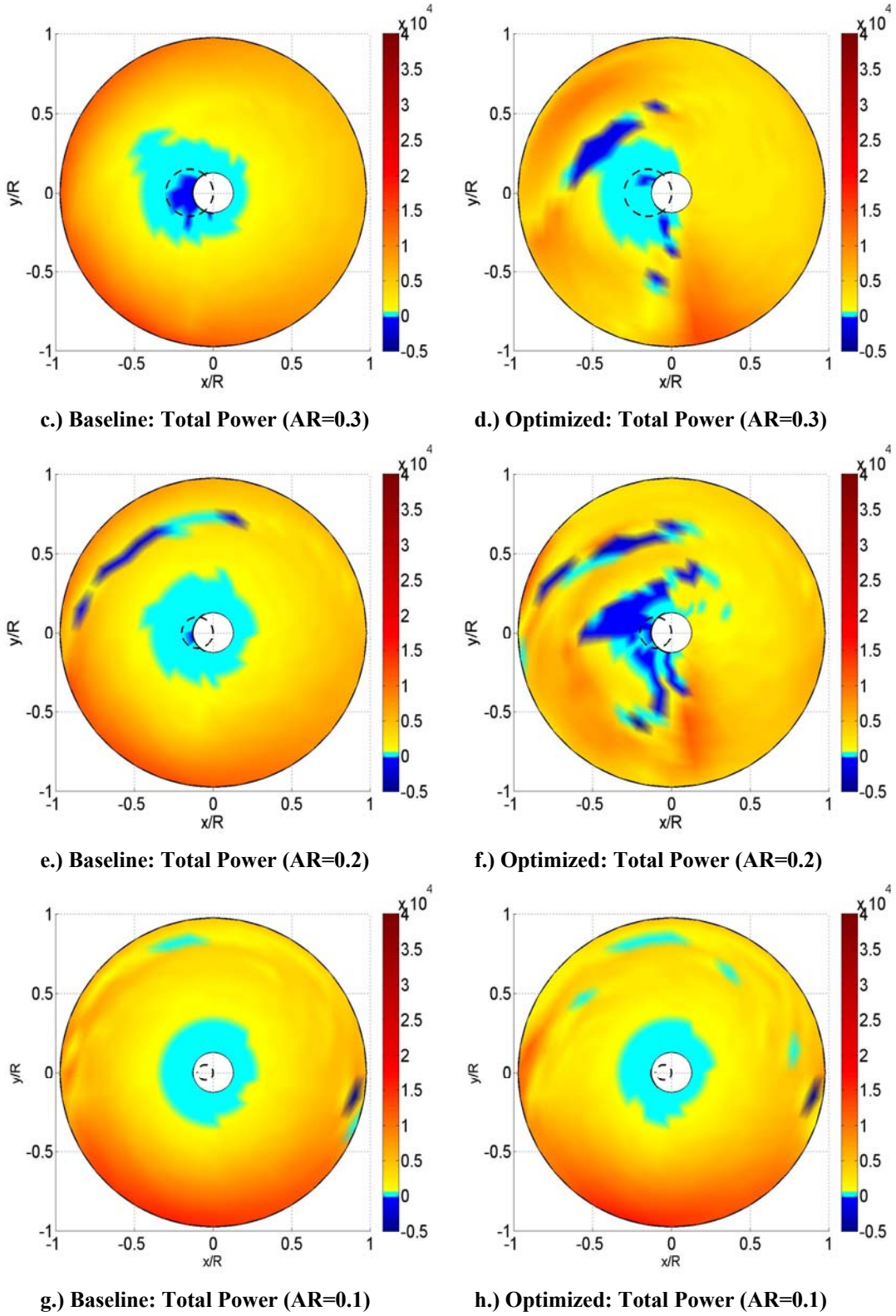
Figure 4.2.15 a-h: Total Power Distribution Comparisons: Difference between the optimum and baseline profile drag distributions (lbs/s). The reverse flow region is designated by the dashed circle.

The pitch distribution shows extreme changes in the reverse flow region where the blade in moving through up to 360° changes to limit the relative angle of attack. In figure 4.2.16 it can be seen that the pitch is responding to changes in the inflow around the disk. The pitch for the optimized solution has the restricted range of c_ℓ, therefore, the pitch only varies from the inflow angle enough to obtain the desired c_ℓ within the limits of the stall angles. Even in hover, this solution diverges from the simple ideal of equation 1.1.1.   The hover case demonstrates a dip in the pitch at the tips for the optimum case. Across the entire blade there is about 30° of twist in hover. In forward flight, pitch variation is on the same level as for hover, excluding the reverse flow region where it is much higher, but is distributed in a very different pattern characterized by large azimuthal variation.
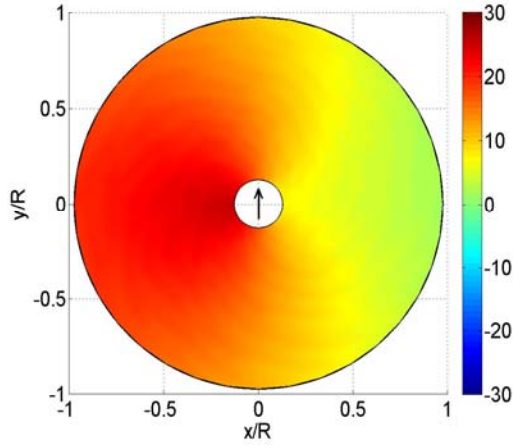
a.) Baseline: Pitch (AR=0.4)
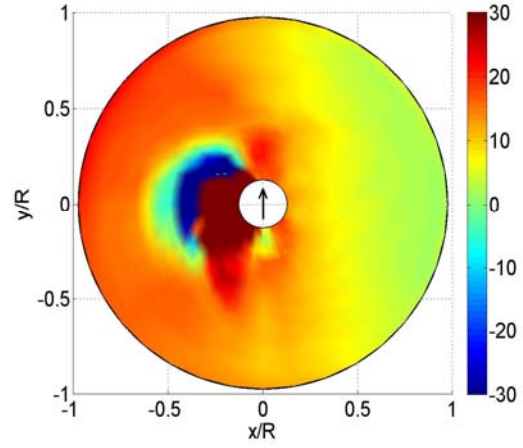
b.) Optimum: Pitch (AR=0.4)
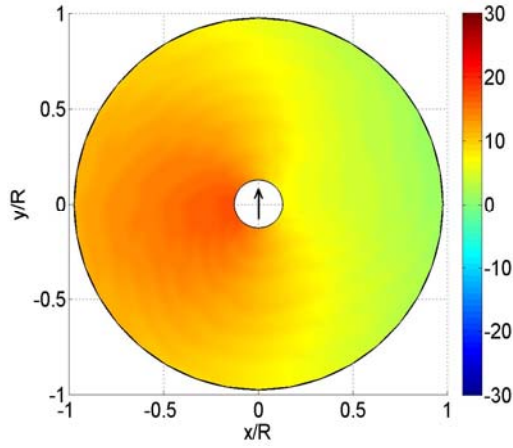
c.) Baseline: Pitch (AR=0.3)
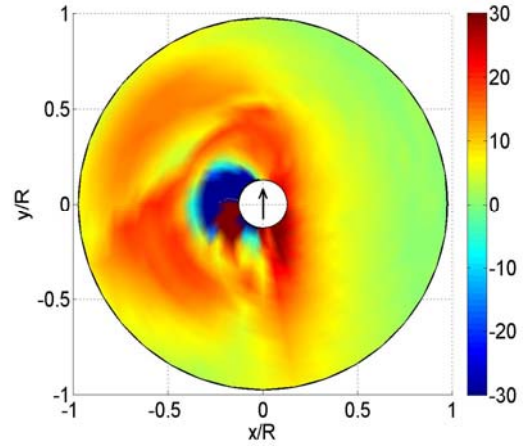
d.) Optimum: Pitch (AR=0.3)
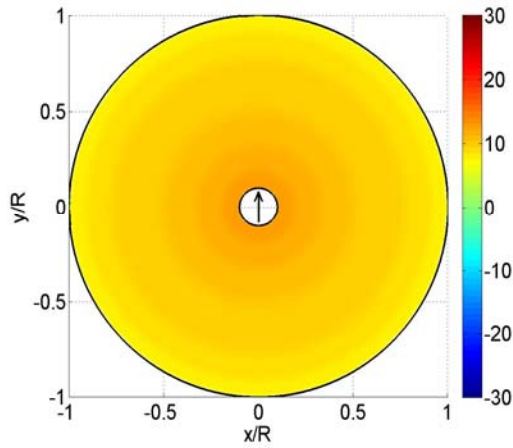
e.) Baseline: Pitch (AR=0.0)
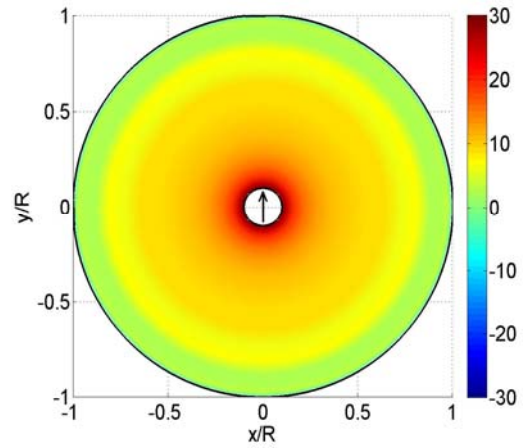
f.) Optimum: Pitch (AR=0.0)

Figure 4.2.16 a-t: Pitch Distribution Comparisons: Close-up comparison of the pitch distribution (degrees) between the optimum and baseline. The reverse flow region is obscured by the scale.

a.) Pitch Difference (AR=0.4)   b.) Pitch Difference (AR=0.3)

c.) Pitch Difference (AR=0.0)
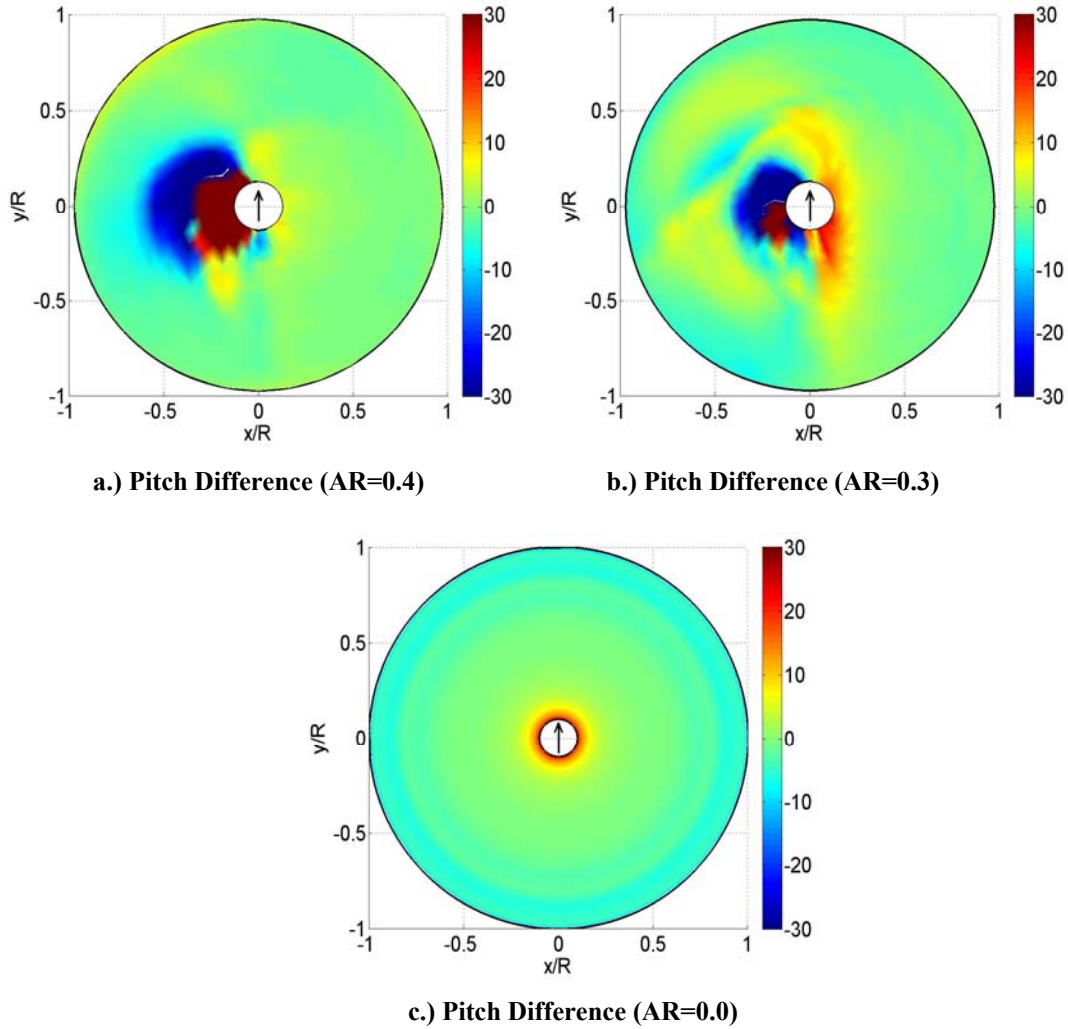
Figure 4.2.17 a-c: Pitch Distribution Differences: Difference between the optimum and baseline pitch distributions (degrees). The reverse flow region is obscured by the scale.

As noted above, discrete features in the inflow, figure 4.2.18, make it evident that the rotor is responding to the close proximity of vortices. In hover, the constant downwash predicted by Betz[24] is largely seen inboard but there is a sudden drop and then an up wash at the tip which produces a large dip in the pitch distribution. This is the disk taking advantage of a propulsive power produced by driving an up wash through a lifting surface. This up wash is the result of the contracting wake below the rotor disk and this same phenomenon was seen by Moffitt and Bissell[27] and others for hover. One can see slightly higher inflow in the baseline due input to the higher shaft tilt angle.
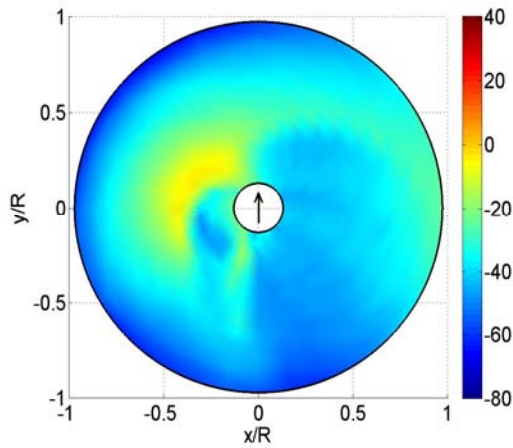
a.) Baseline: Inflow (AR=0.4)
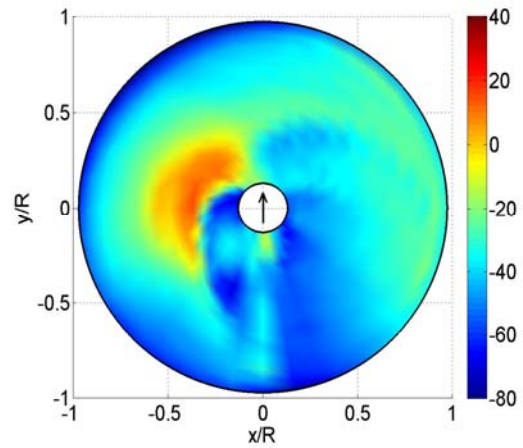
b.) Optimum: Inflow (AR=0.4)
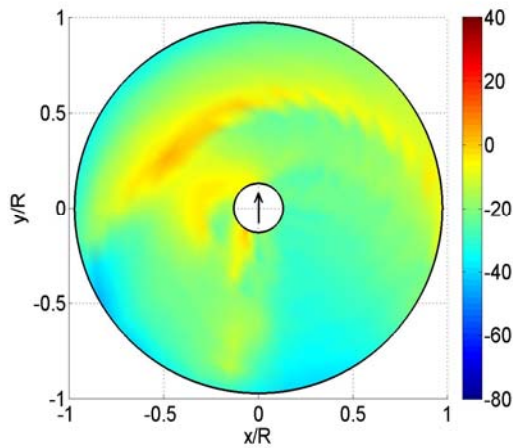
c.) Baseline: Inflow (AR=0.3)
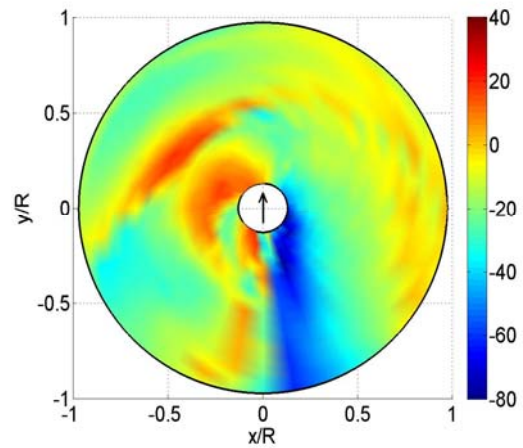
d.) Optimum: Inflow (AR=0.3)
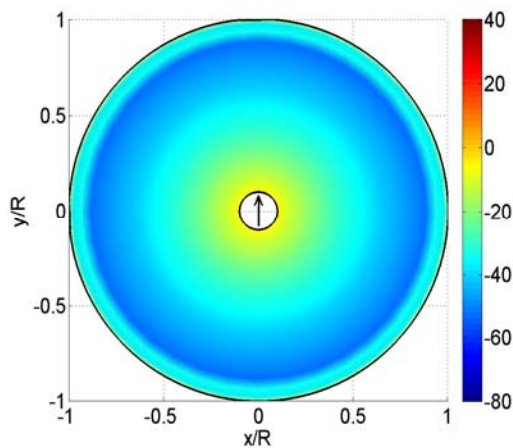
e.) Baseline: Inflow (AR=0.0)
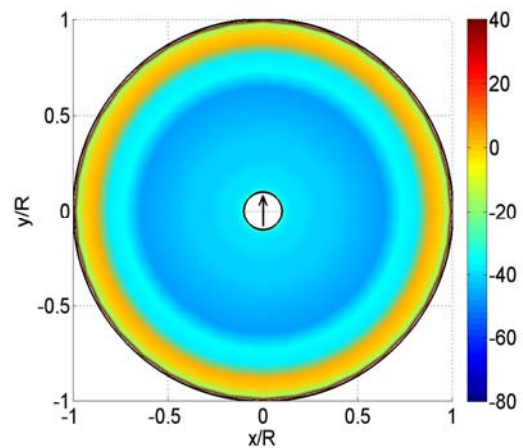
f.) Optimum: Inflow (AR=0.0)

Figure 4.2.18 a-f: Inflow Distribution Comparisons: Close-up comparison of the Inflow distribution (ft/s) between the optimum and baseline. The reverse flow region is obscured by the scale.

a.) Inflow Difference (AR=0.4)

**b.) Inflow Difference (AR=0.3)**

c.) Inflow Difference (AR=0.0)
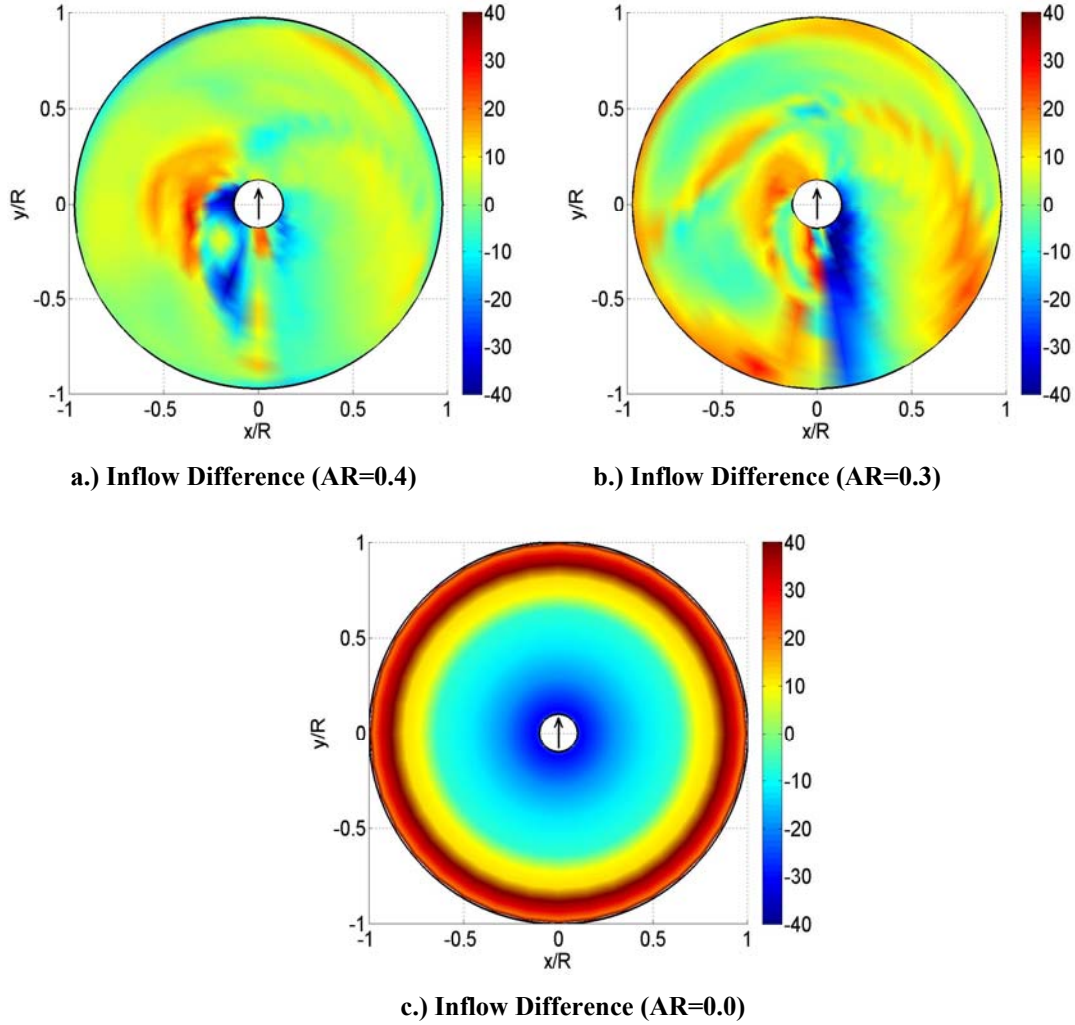
Figure 4.2.19 a-j: Inflow Distribution Differences: Difference between the optimum and baseline Inflow distributions (ft/s).

In an effort to understand what terms are necessary to approach the optimized solution and what physical mechanisms might be used to attain them, the pitch and circulation contours in forward flight are decomposed into Fourier coefficients at various radial stations. The coefficients describe the equation,

$$f(\theta) = \sum_{n=0}^{N} A_n \cdot \cos(n\theta - \phi_n),$$ (4.2.3)

where A_n and ϕ_n represent the amplitude and phase respectively. The pitch distributions, which naturally only have harmonics up to one per revolution for the baseline, are shown below along with the optimized pitch distribution in figure 4.2.20. The inboard sections of the blade in the reverse flow region (which appear on the blue side) show extreme

variability. In the outboard regions (toward the red), the amplitude of the pitch decays with higher frequencies. Ignoring the inboard sections of the blade where power consumption is lowest and where the reverse flow region is located, the pitch phases, figure 4.2.21, tend to be relatively coherent only for the 1st harmonic with a difference of 10° across spanwise locations. Some linearly skewed relationships do exist for some speeds but beyond three per revolution, ideal response is so incoherent to likely be unbeneficial. Another interesting trend can be seen in the amplitude decomposition for the 0th harmonic. For all advance ratios except 0.4, the initial pitch on the blade would have a higher washout than the shallow baseline configuration, but at 0.4 a nearly flat if not slightly positive slope on the twist seems required. This may imply that the traditionally twisted rotor blade is particularly detrimental to high advance ratio flight. In hover there is a steeper/non-linear slope.
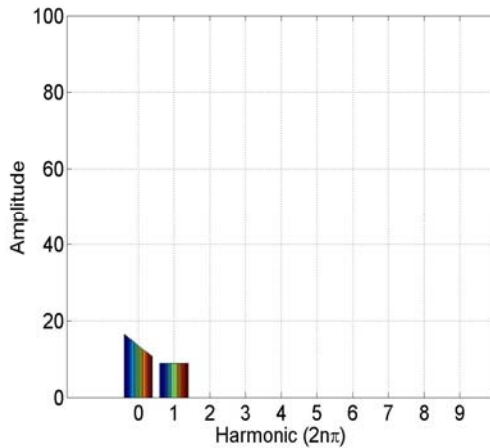
a.) Baseline: Pitch Amplitude (AR=0.4)   b.) Optimum: Pitch Amplitude (AR=0.4)
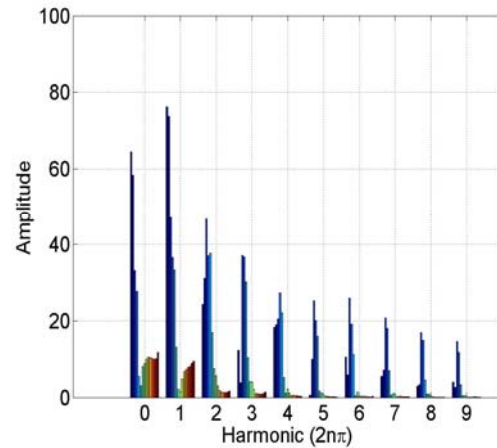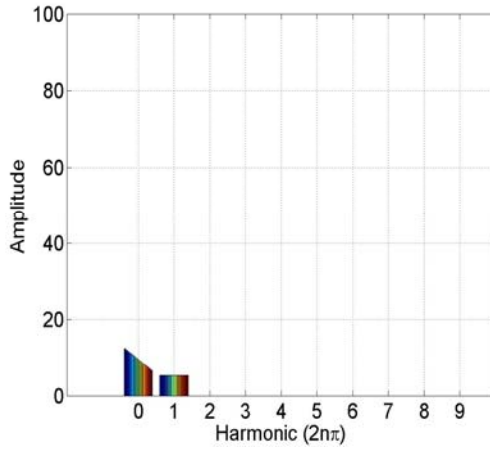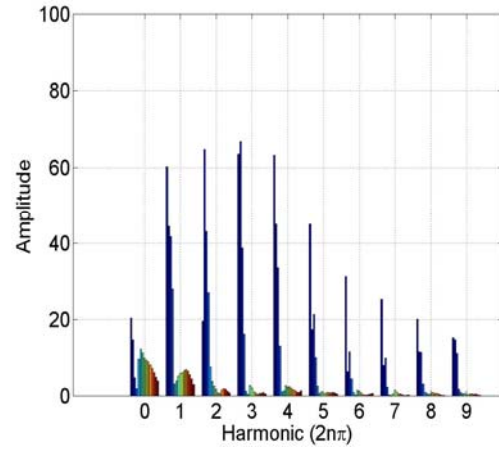
c.) Baseline: Pitch Amplitude (AR=0.3)   **d.) Optimum: Pitch Amplitude (AR=0.3)**
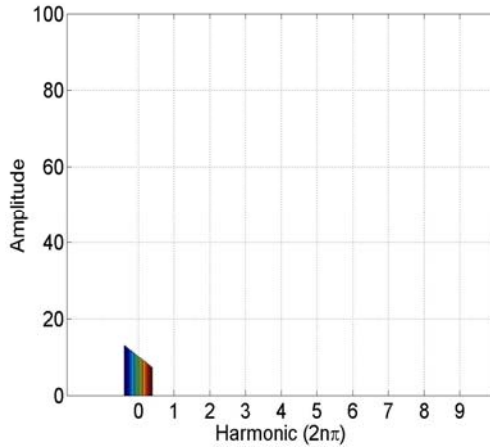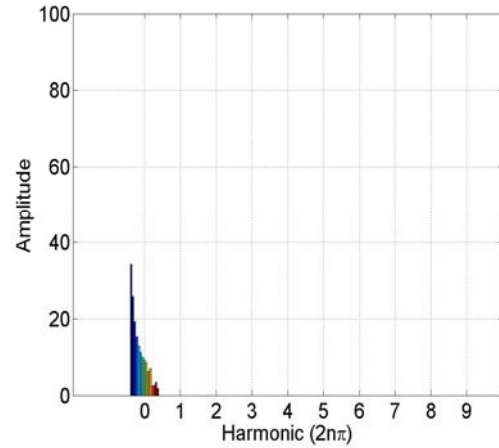
e.) Baseline: Pitch Amplitude (AR=0.0)   **f.) Optimum: Pitch Amplitude (AR=0.0)**

Figure 4.2.20 a-f: Fourier Decomposition of Pitch Magnitude: Comparison of the pitch distribution for the baseline and optimum. Blue represents the most inboard radial location and progresses toward the tip represented by red.
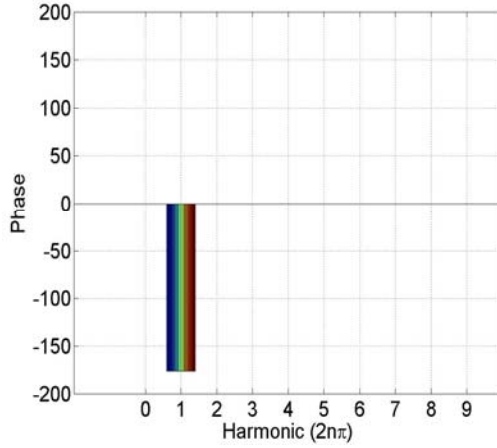
a.) Baseline: Pitch Phase (AR=0.4)   **b.) Optimum: Pitch Phase (AR=0.4)**
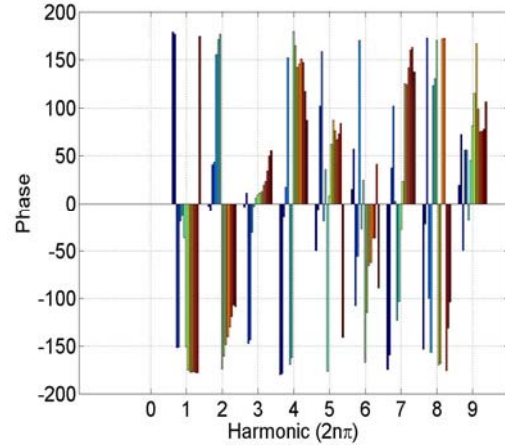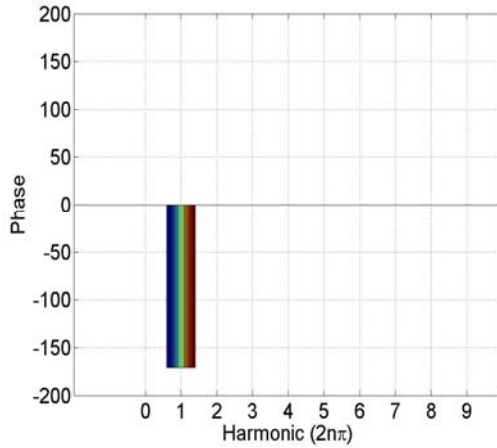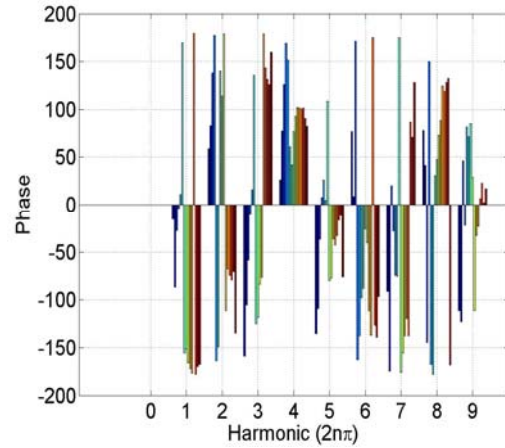
c.) Baseline: Pitch Phase (AR=0.3)   **d.) Optimum: Pitch Phase (AR=0.3)**

Figure 4.2.21 a-d: Fourier Decomposition of Pitch Phase: Comparison of the pitch distribution for the baseline and optimum. Blue represents the most inboard radial location and progresses toward the tip represented by red.

Figures 4.2.22 and 4.2.23 show a similar decomposition of the circulation. The relative decay of the circulation compared with the pitch is higher with most of its amplitude limited to the 0th-2nd harmonics. As with the pitch, there is little coherence of phase between the radial positions, especially at higher harmonics. In hover, the optimal circulation is flattened compared to the baseline which is consistent with other work suggesting a largely flat circulation profile as being ideal for hover.
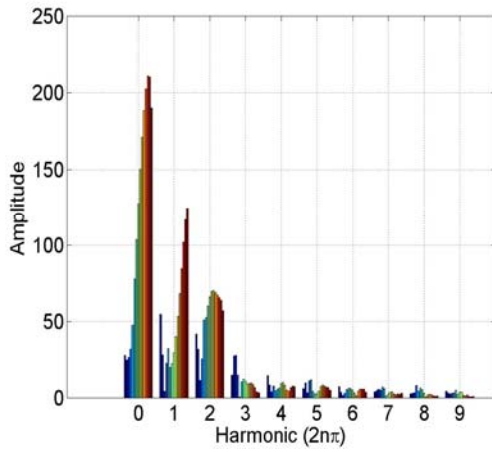
a.) Baseline: Circulation Amplitude (AR=0.4)
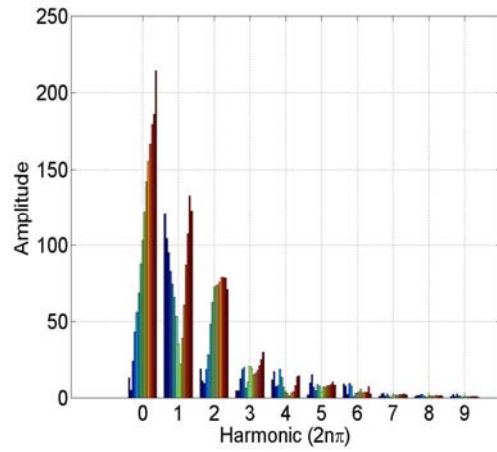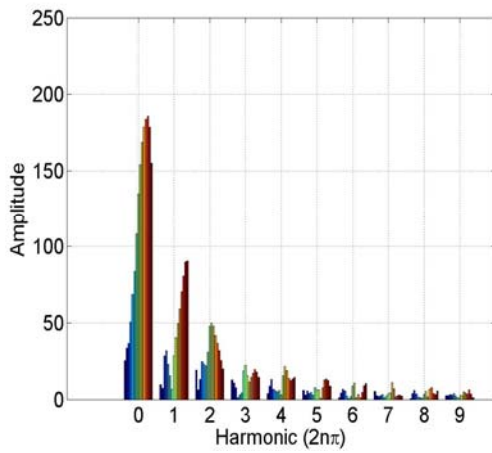
b.) Optimum: Circulation Amplitude (AR=0.4)

c.) Baseline: Circulation Amplitude (AR=0.3)
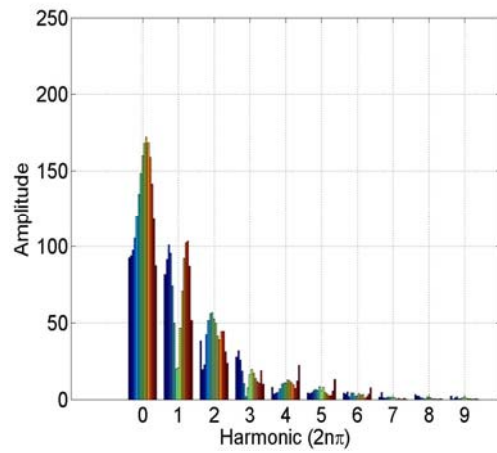
d.) Optimum: Circulation Amplitude (AR=0.3)
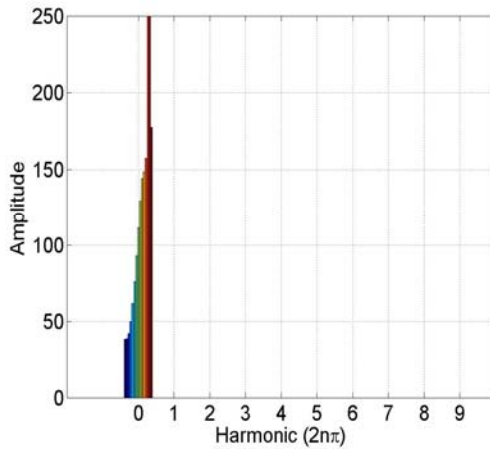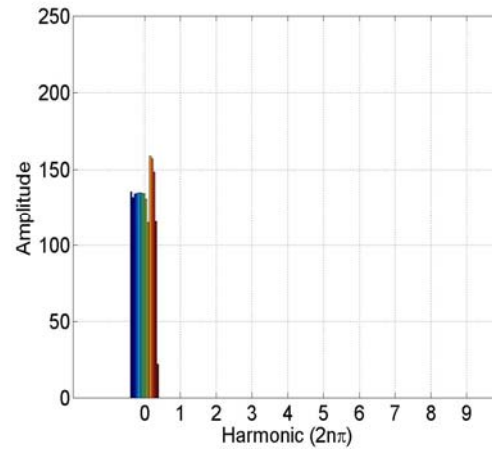
e.) Baseline: Circulation Amplitude (AR=0.0)   **f.) Optimum: Circulation Amplitude (AR=0.0)**

Figure 4.2.22 a-f: Fourier Decomposition of Circulation Magnitude: Comparison of the circulation distribution for the baseline and optimum. Blue represents the most inboard radial location and progresses toward the tip represented by red.
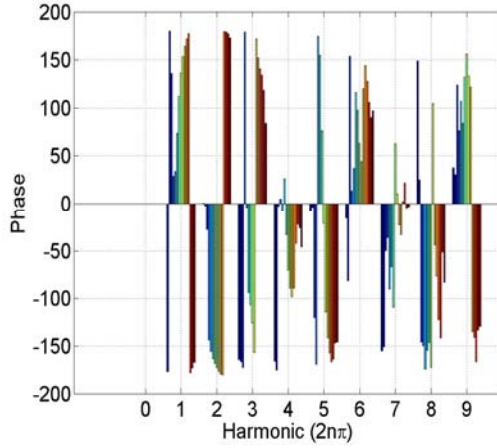
a.) Baseline: Circulation Phase (AR=0.4)   **b.) Optimum: Circulation Phase (AR=0.4)**
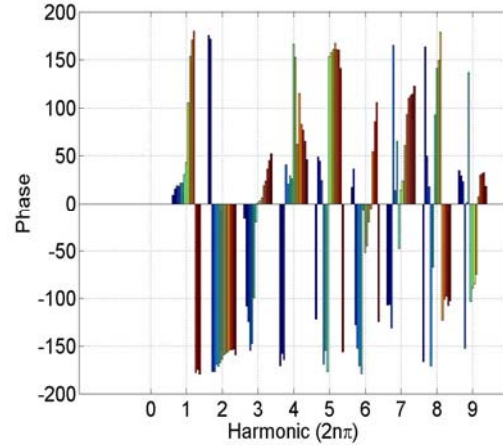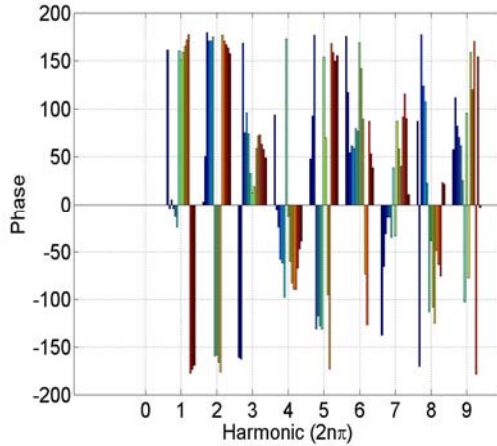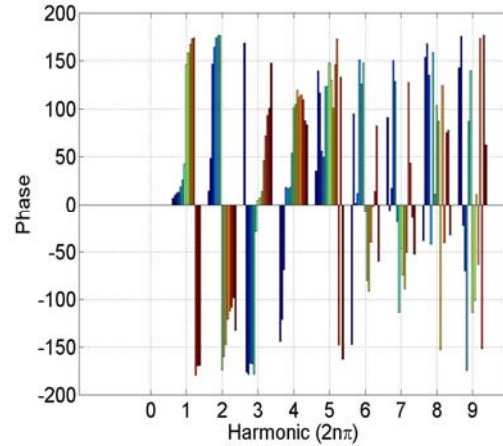
c.) Baseline: Circulation Phase (AR=0.3)   **d.) Optimum: Circulation Phase (AR=0.3)**

Figure 4.2.23 a-d: Fourier Decomposition of Circulation Phase: Comparison of the circulation distribution for the baseline and optimum. Blue represents the most inboard radial location and progresses toward the tip represented by red.

Performance calculations with higher frequencies removed demonstrates the relative importance of these higher frequencies. Two types of inputs were compared with the baseline, the circulation and the twist, both of which were systematically pared down from the decomposition above in figures 4.2.20 and 4.2.22 by removing the higher frequencies in the optimized curves at each radial position. In doing so, radial variation was preserved but the frequency of azimuthal variation was reduced. This was only done at an advance ratio of 0.3. Interestingly, as can be seen in figure 4.2.24 for the case of the circulation as input, results were nearly constant until the second harmonics was removed

and even this was not very detrimental. This implies that the desired circulation contour is very smooth azimuthally. This also suggests that the problem as solved here was extremely inefficient as the circulation was perturbed at 36 azimuthal locations at each of the 15 radial stations to create a perturbation contour for each optimization iteration. Instead it appears only a few harmonics of azimuthal variation were required.
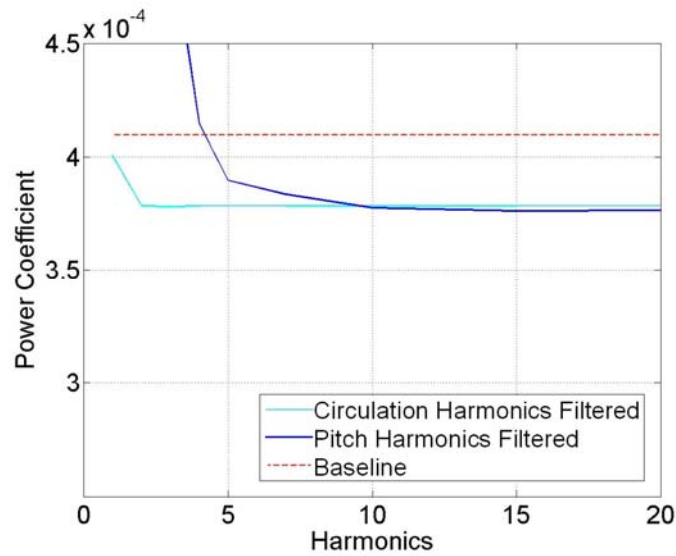
Figure 4.2.24: Power Coefficient: Power coefficient for various pitch and circulation contours with harmonics equal to and higher than the ordinate value removed.

For the filtered solutions where higher frequencies in the twist were systematically removed, the effects were seen more quickly. Here the performance started to drift as the solutions approached the eighth harmonic. The higher order terms are more important in the pitch for obtaining the same performance. The difference in the behavior between the two inputs is a product of a complex relationship between them. A smooth circulation contour does not result in a smooth pitch distribution which has to change with a continually variable relative velocity distribution. This difference between the circulation and twist decompositions implies that some of the more discrete features in the flow were required to be reflected in the pitch to obtain this ideal value. For example, a smooth circulation distribution in the vicinity of a near vortex/blade interaction would lead to a velocity and pitch spike. Thus, it appears that a smooth circulation contour is optimal but would be difficult to achieve.

The gradients for optimization were based on perturbing discrete points in the circulation distribution, 36 azimuthally and 15 radially. Not only was this inefficient given that the solutions tended to be strongly periodic with only the first few harmonics, but this also has the potential of finding poor perturbation contours. Since inviscid flow behavior is highly elliptical, signal point perturbations may not yield much information about how a contour built from these perturbations will behave. Figure 4.2.22 shows that the ideal circulation had large components with higher harmonics 0th-5th, but performance with filtered inputs suggest that only the 0th and 1st are needed. This again adds weight to the suggestion to use harmonic perturbations rather than signal point perturbations.

Chapter 5:   Conclusion

5.1 Conclusions:

Efforts have been made to describe the generalized solution of an optimized lift distribution for reduced power consumption. It was found that all of the power reduction was in the inviscid power often at the expense of higher profile power. Changing the trim condition leads to a reduced shaft tilt angle in trim and a corresponding decrease in inflow and ram power which necessitates an increase in rotor parasite power negating the ram power reductions. Although the net effect of this is neutral to the power consumption, it allows for a decrease in required thrust and therefore a decrease in the induced power. Besides this effect, a greater reduction in the inviscid power is due to a redistribution of the lift and induced velocity at the rotor disk. In general, a tread toward moving more lift or circulation inboard over the distribution of a conventionally twisted blade can be seen. The optimized lift is relatively smooth but not the pitch. The pitch chases contours in the induced flow to create this smooth lift contour. The profile power plays a minor roll in reducing the power because of the constraints in this optimization.

Higher harmonic control beyond three per revolution is unlikely to be a particularly effective method of reducing power because the phases of the higher harmonics are radially inconsistent. Second order control has more potential as these frequencies remain more coherent. Methods allowing radial variation in twist or c_ℓ would be necessary to obtain higher harmonics. Even so, it is unlikely even a combination of mechanisms will produce the necessary deflections to match these contours.

Some of the results and trends found here may differ from those found elsewhere because of the limited about stall or negative lift on the baseline rotor as a result of the low blade twist in the baseline model. These are often the effects noted as having been alleviated in other studies or by mechanisms such as HHC. The importance of trim is also apparent from this study. Several of the studies cited repeatedly in this work have employed inviscid techniques to explore optimizing rotor power often assuming a shaft angle of zero. Although it seems from this study that the profile power is less significant in reducing the total power, it plays an important role in determining the trim orientation

and thus the relative velocity field around the disk. As such, it is questionable how practical it is to perform an inviscid optimization. Inviscid studies usually performed with zero shaft tilt will probably display the same general trends in redistributing the circulation distribution as shown here but will exaggerate the impulsive loading of vortices which will shed closer to the blades in this orientation.

The gradients for optimization were based on perturbing discrete points in the circulation distribution, 36 azimuthally and 15 radially. Not only was this inefficient given that the solutions tended to only require the first few harmonics, but this also has the poor potential of finding perturbation contours. Since inviscid flow behavior is highly elliptical, single point perturbations may not yield much information about how a contour built from these perturbations will behave. Figure 4.2.22 shows that the ideal circulation has strong/large components with higher harmonics 0th-3rd, but performance with filtered inputs suggest that only the 0th and 1st are needed. The fact that the method introduced these harmonics into the solution is reflective of there minimal impact on the solution as seen in the harmonic decompositions. This again adds weight to the suggestion to use harmonic perturbations rather than single point perturbations.

From this study, it also does not seem advisable to approach the problem of rotor design outside of the available flow control mechanisms. As seen here, although power savings have been predicted, translating them to a meaningful system would prove difficult. For example, placement of constrains on the pitch or use of a model specific to a flap device would yield more applicable solutions.

5.2 Recommendations for Future Work:

The original impulse behind this effort was to find optimized circulation distributions for a helicopter in flight in a similar fashion to that performed by Munk for fixed wing and Rand for inviscid rotors with zero shaft-angle. Unfortunately, unlike a fixed wing aircraft or a helicopter in hover, the profile drag can not be realistically separated from the determination of the optimal lift distribution. Therefore this distribution based perspective lead to a less than ideal formulation of the problem. Given a certain circulation strength, and therefore c_ℓ, there are often several possible angles of attack which can be selected. The choice made here lead to the lowest angle of attack but

also unrealistic physical solutions. In future efforts, it would be more appropriate to focus on a pitch based effort where solutions would maintain a physically realizable solution or a mechanism-based effort employing, for example, partial span trailing-edge flaps or distributed Gurney flaps.

The code could certainly be improved by including more features that better capture real rotor behavior. The inclusion of flapping, lagging, bending, and twisting motions would improve the accuracy of the method. Aerodynamic features like dynamic stall, apparent mass, and rotational effects would also improve the realism of the code and reduce some of the high variability in pitch response. Another important alteration would be to perform a full vehicle trim rather than wind tunnel trim. One should also consider the many time saving methods that are included in many of the existing comprehensive codes. Of most significance is to perform this study with a relaxation rather than time marching code to increase the speed of each iteration.

The optimization routine may not be yielding an absolute minimum power. The optimizer used here is purely gradient based and therefore only has the capability to "slide" to the bottom of the valley it starts on. In other words, the minimum value found here may be a function of the initial conditions, the baseline rotor configuration is this case. One can imagine the several arrangements and deformations of the shed and trailing wake filaments could yield a very "bumpy" non-linear design space with many peaks and valleys. Using some sort of evolutionary algorithm or another technique to account for this dependence on initial conditions would be valuable.

It would be interesting to consider improving current predictions by using a non-linear shed vortex sheet rather than discrete filaments. These have been used in the fixed wing community as well as being an option in codes like CAMRAD II to model the inboard sheets of vorticity. There are several advantages to this method including possibly requiring fewer panels than the corresponding filaments, but mainly, these panels yield much smoother velocity distributions than do discrete filaments which would "clean-up" the induced velocity and perhaps yield smoother pitch contours.

From the above contour plots, it is clear that in many cases, the number of elements is insufficient to smoothly resolve the solution. Although at higher advance ratios, this may be sufficient as is indicated by the grid dependence study performed at a

high advance ratio, the hover case is not well resolved. Were this work to be pursued further, the grid density would need to be increased at least in hover.

Bibliography

[1] Wachspress, D., Quackenbush, T., and Solomon, C., "On Minimum Induced Power of the Helicopter Rotor," Proceedings of the 61st Annual Forum of the American Helicopter Society, 2005.

[2] Chattopadhyay, A., McCarthy, T.,R., Pagaldipti, N., "Multilevel Decomposition Procedure for Efficient Design Optimization of Helicopter Rotor Blades," AIAA Journal, Volume 33(2), February 1995, pp. 223-230.

[3] Keys, C., Tarzanin, F., and McHugh, F., "Effect of Twist on Helicopter Performance and Vibratory Loads," the Thirteenth European Rotorcraft Forum, Arles, France, 1987.

[4] Leishman, J.G., "Principles of Helicopter Aerodynamics," Cambridge Press, UK, 2000.

[5] Ormiston, R.,A., "Induced Power of the Helicopter Rotor," Proceedings of the 60th Annual Forum of the American Helicopter Society, Baltimore, Maryland, May 2004, pp. 33-35.

[6] Ormiston, R.A., "Further Investigations of Helicopter Rotor Induced Power," Proceedings of the 61st Annual Forum of the American Helicopter Society, Grapevine, Texas, June 2005, pp. 1779-1801.

[7] Rand, O., Khromov, V., and Peyran, R., "Minimum-Induced Power Loss of a Helicopter Rotor via Circulation Optimization," Proceedings of the 57th Annual Forum of the American Helicopter Society, Washington D.C., May 2001.

[8] Rand, O., Khromov, V., and Peyran, R., "Minimum-Induced Power Loss of a Helicopter Rotor via Circulation Optimization," Journal of Aircraft, Volume 41 (1), 2004, pp. 104-109.

[9] Blackwell, R.,H. and Merkley, D.,J., "The Aeroelastically Conformable Rotor Concept," Proceedings of the 34th Annual Forum of the American Helicopter Society, Washington D.C., May 1978, pp.37-44

[10] Stewart, W., "Second Harmonic Control on the Helicopter Rotor," Ministry of Supply, Aeronautical Research Council Reports and Memoranda, R&M # 2997, London, UK, August 1952.

[11] Cheng, R.,P., and Celi, R., "Optimum Two-Per-Revolution Inputs for Improved Rotor Performance," Journal of Aircraft, Volume 42(6), November – December, 2005, pp. 1409-1417.

[12] Cesnik, C.,E.,S., Shin, S., Wilkie, W.,K., Wilbur, M.,L., and Mirick, P.,H., "Modeling, Design, and Testing of the NASA/ARMY/MIT Active Twist Rotor Prototype Blade," Proceedings of the 55th Annual Forum of the American Helicopter Society, Montréal, Canada, May 1999, pp. 533-544.

[13] Bernhard, A.,P.,F., and Wong, J., "Wind-Tunnel Evaluation of a Sikorsky Active Rotor Controller Implemented on the NASA/ARMY/MIT Active Twist Rotor," Journal of the American Helicopter Society, Volume 50(1), pp. 65-81.

[14] Sekula, M.,K., Wilbur, M.,L., and Yeager, W.,T. "A Parametric Study of the Structural Design for an Advance Active Twist Rotor," Proceedings of the 61st Annual Forum of the American Helicopter Society, Grapevine, Texas, June 2005 pp. 82-95.

[15] Wilbur, M.,L., and Sekula, M.,K., "The Effect of Tip Geometry on Active-Twist Rotor Response," Proceedings of the 61st Annual Forum of the American Helicopter Society, Grapevine, Texas, June 2005 pp. 137-148.

[16] Straub, F.,K., "A Feasibility Study of Using Smart Materials for Rotor Control," Journal of Smart Materials and Structures, Volume 5(1), February 1996, pp. 1-10.

[17] Koratkar, N.,A., and Chopra, I., "Design, Fabrication and Testing of a Mach Scaled Rotor Model with Trailing-Edge Flap," Proceedings of the 55th Annual Forum of the American Helicopter Society, Montréal, Canada, May 1999, pp. 558-578.

[18] Fulton, M.,V., and Ormiston, R.,A., "Hover Testing of a Small-Scale Rotor with On-Blade Elevons," Proceedings of the 53rd Annual Forum of the American Helicopter Society, Virginia Beach, Virginia, April - May 1997, pp. 249-273.

[19] Kinzel, M.,P., Maughmer, M.D., and Lesieutre, G.L., "Numerical Investigation of Miniature Trailing-Edge Effectors on Static and Oscillating Airfoils," the 43rd AIAA Aerospace Sciences Meeting and Exhibit, Reno, Nevada, January 2005, AIAA 2005-1039.

[20] Maughmer, M., Lesieutre, G., and Kinzel, M., "Miniature Trailing-Edge Effectors for Rotorcraft Performance Enhancement," Proceedings of the 61st Annual Forum of the American Helicopter Society, Grapevine, Texas, June 2005 pp. 1886-1898.

[21] Anusonti-Inthra, P., Sarjeant, R., Frecker, M., and Gandhi, F., "Design of a Conformable Rotor Airfoil Using Distributed Piezoelectric Actuators," AIAA Journal, Volume 43(8), August 2005.

[22] Munk, M., "The Minimum Induced Drag of Aerofoils", NACA Report Number 121, pp 95-110.

[23] Karamcheti, K., "Principles of Ideal-Fluid Aerodynamics," Krieger Publishing Company, Malabar, Florida, 1980.

[24] Durand, W., "Aerodynamic Theory, A General Review of Progress", Julius Springer, Berlin, 1935, Vol. IV, pp.251-269.

[25] Goldstein, S., "On the Vortex Theory of Screw Propellers," Proceedings of the Royal Society of London. Series A, Volume 123(792), 1929, pp. 440-465.

[26] Landgrebe, A. and Cheney, M., "Rotor Wakes – Key to Performance Prediction," NATO Aerodynamics of Rotary Wings, 1972.

[27] Moffitt, R. and Bissell, J., "Theory and Application of Optimum Airloads to Rotors in Hover and Forward Flight," 38th Annual Forum of the American Helicopter Society, Anaheim, California, May 1982, pp.1-12.

[28] Gessow, A., "Effects of Rotor-Blade Twist and Plan-Form Taper on Helicopter Hover Performance," NACA TR 1542, February 1948.

[29] Harris, F. and McVeigh, M., "Uniform Downwash with Rotors Having a Finite Number of Blades", Journal of the American Helicopter Society, Volume 21(1), 1976, pp. 9-20.

[30] Prouty, R., "A Second Approximation to the Induced Drag of a Rotor in Forward Flight," Journal of the American Helicopter Society, Volume 21(3), 1976, pp.13-15.

[31] Theodorsen, T., "Theory of Static Propellers and Helicopter Rotors," Proceedings of the 25th Annual Forum of the American Helicopter Society, Washington D.C., May 1969, pp. 326.

[32] Blackwell, R.H. and Merkley, D.J., "The Aeroelastically Conformable Rotor Concept," 34th Annual Forum of the American Helicopter Society, Washington D.C., May 1978, pp.37-44.

[33] Bennett, R. L., "Application of Optimization Method to Rotor Design Problems," Vertica 7(3), 1983, pp. 225-239.

[34] Walsh, J.L., Bingham, G., J., and Riley, M., F., "Optimization Methods Applied to the Aerodynamic Design of Helicopter Rotor Blades," Journal of American Helicopter Society, 32(4), October 1987, pp. 39-44.

[35] Hall, S., Yang, K., and Hall, K., "Helicopter Rotor Lift Distributions for Minimum-Induced Power Loss," Journal of Aircraft, Volume 31(4), 1994, pp. 837-845.

[36] Quackenbush, T., et. al., "Rotor Design Optimization using a Free Wake Analysis," NASA CR 177612, April 1993.

[37] Quackenbush, T., Wachspress, and Kaufman, A.E., "Optimization of Rotor Performance in Hover Using a Free Wake Analysis," Journal of Aircraft, Volume 28(3), 1991, pp. 200-207.

[38] Davis, S.J., Moffit, R., Quackenbush, T.R., and Washpress, D.A. "Aerodynamic Design Optimization of a Variable Diameter Tilt Rotor," Proceedings of the 51st Annual Forum of the American Helicopter Society, Fort Worth, Texas, 1995, pp. 101-111.

[39] Mantay, W., R., and Adelman, H., M., - "Status of Research on Multi.. Proceedings of the 46th Annual Forum of the American Helicopter Society, May 1990, pp. 471-481.

[40] Chattopadhyay, A., McCarthy, T.,R., "Optimum design of helicopter rotor blades with multidisciplinary couplings," 30th meeting of the AIAA, Aerospace Sciences Meeting and Exhibit, Reno, NV, January 1994.

[41] Zibi, J., Leconte, P., Geoffroy, P., "An Optimization Method Applied to the Aerodynamics of Helicopter Rotor Blades" The 21st European Rotorcraft Forum, Saint Petersburg, Russia, August - September, 1995.

[42] Sun H., Kim, Y., Lee, S., and Lee, D., "Aerodynamic Design of Helicopter Rotor Blade in Forward Flight Using Response Surface Methodology," Proceedings of the 55th Annual Forum of the American Helicopter Society, Montréal, Canada, May 1999, pp. 2270-2280.

[43] Mangler, K., and Squire, H., "The Induced Velocity Field of a Rotor," Ministry of Supply, Aeronautical Research Council Report and Memoranda, R&M No. 2642, 1953.

[44] Morillo, J.,A., "A Fully Three-Dimensional Unsteady Rotor Inflow Model From a Galerkin Approach," Doctor of Science, Saint Louis, Missouri, Washington University, December 2001.

[45] Anusonti-Inthra, P. "Development of Rotorcraft Wake Capturing Methodology Using Fully Coupled CFD and Particle Vortex Transport Method," the 11th International Workshop on Rotorcraft Dynamics and Aeroelasticity, Boca Raton, Florida, October 2005.

[46] Bhagwat, M.J., Moulton, M.,A., and Caradonna, F.,X., "Development of a CFD-based Hover Performance Prediction Tool for Engineering Analysis," Proceedings of the 61st Annual Forum of the American Helicopter Society, Grapevine, Texas, June 2005 pp. 333-348.

[47] Egolf, T., "Helicopter Free Wake Prediction of Complex Wake Structures Under Blade-Vortex Interaction Operating Conditions," Proceedings of the 44th Annual Forum of the American Helicopter Society, 1988.

[48] Egolf, T.,A., and Massar, J.,P., "Helicopter Free Wake Implementation On Advanced Computer Architectures," 2nd International Conference on Basic Rotorcraft Research, University of Maryland, College Park, Maryland, February 1988.

[49] Scully, M., "Computational of Helicopter Rotor Wake Geometry and Its Influence on Rotor Harmonic Airloads," Massachusetts Institute of Technology, ASRL TR 178-1, March 1975.

[50] Scully, M., "A Method of Computing Helicopter Vortex Wake Distortion," Massachusetts Institute of Technology, ASRL TR 138-1, June 1967.

[51] Scully, M.,P., "On the Computation of Helicopter Rotor Wake Geometry, (Interim Report #2 Final)," Massachusetts Institute of Technology ASRL, Cambridge, Massachusetts, AD 702 774, December 1968.

[52] Clark, D. and Leiper, A., "The Free Wake Analysis: A Method for the Prediction of Helicopter Rotor Hovering and Performance," Journal of the American Helicopter Society, Volume 15(1), 1970, pp. 3-11.

[53] Landgrebe, A., "An Analytic Method for Predicting Rotor Wake Geometry," Journal of the American Helicopter Society, Volume 14 (4), 1969, pp. 20-32.

[54] Johnson, A., "Comprehensive Analytical Model of Rotorcraft Aerodynamics and Dynamics," NASA TM 81182, June 1980.

[55] Sadler, S. G., "A Method for Predicting Helicopter Wake Geometry, Wake-Induced Flow and Wake Effects on Blade Airloads," Proceedings of the 27th Annual Forum of the American Helicopter Society, May 1971.

[56] Sadler, S.G., "Development and Application of a Method for Predicting Rotor Free Wake Positions and Resulting Rotor Blade Air Loads. Volume 1: Model and results," NASA CR 1911, Dec. 1971.

[57] Berry, J.,D., "Prediction of Time Dependent Fuselage Pressures in the Wake of a Helicopter Rotor," 2nd International Conference on Basic Rotorcraft Research, University of Maryland, College Park, Maryland, February 1988.

[58] Bliss, D., Teske, M., and Quackenbush, T., "A New Methodology for Free Wake Analysis Using Curved Vortex Elements," NASA CR 3958, 1987.

[59] Quackenbush, Bliss, Wachpress, "New Free Wake Analysis of Rotorcraft Hover Performance Using Influence Coefficients," Journal of Aircraft, Volume 26(12), December 1989.

[60] Miller, W. and Bliss, D., "Direct Periodic Solutions of Rotor Free Wake Calculations," Journal of the American Helicopter Society, Volume 38(2), 1993, pp. 53-60.

[61] Bliss, D. and Miller, W., "Efficient Free Wake Calculations Using Analytical/Numerical Matching," Journal of the American Helicopter Society, Volume 38(2), 1993, pp. 43-52.

[62] Johnson, W., "A General Free Wake Geometry Calculation for Wings and Rotors," Proceedings of the 51st Annual Forum of the American Helicopter Society, Fort Worth, Texas, May 1995.

[63] Johnson, W., "Rotorcraft Aerodynamics Models for a Comprehensive Analysis," Proceedings of the 54th Annual Forum of the American Helicopter Society, Washington, D.C., 20-22 May 1998.

[64] Crourse, G.L. and Leishman, J.G., "A New Method for Improved Rotor-Wake Convergence," 31st AIAA Aerospace Sciences Meeting and Exhibit, Reno Nevada, January 1993.

[65] Bagai A. and Leishman J.,G., "Rotor free-wake modeling using a pseudo-implicit technique - Including comparisons with experimental data ," Journal of the American Helicopter Society, Volume 40(3), 1995.

[66] Bagai A., "Contributions to the Mathematical Modeling of Rotor Flow-Fields Using a Pseudo-Implicit Free-Wake Analysis," Doctoral Dissertation, University of Maryland, College Park, Maryland, 1995.

[67] Bagai A., Leishman, J.G., and Park, J., "Aerodynamic Analysis of a Helicopter in Steady Maneuvering Flight Using a Free-Vortex Rotor Wake Model", Journal of the American Helicopter Society, Volume 44(2), April 1999, pp. 109-120.

[68] Wachspress, D.A. Quackenbush, T.R., and Boschitsch, A.H., "First-Principles, Free-Vortex Wake Model for Helicopters and Tiltrotors," Proceedings of the 59th Annual Forum of the American Helicopter Society, Phoenix, AZ, May 2003, pp. 1763-1786.

[69] Vatistas, G.,H., Kozel, V., and Mih, W.,C., "A Simpler Model for Concentrated Vortices," Experiments in Fluids, 1991, pp. 73-76.

[70] Bhagwat, M.,J. and Leishman, J.,G., "Stability, Consistency and Convergence of Time-Marching Free-Vortex Rotor Wake Algorithms," Journal of the American Helicopter Society, January 2001, Volume 46(1), pp. 59-71.

[71] Bhagwat, M.,J. and Leishman, J.,G., "Rotor Aerodynamics During Maneuvering Flight Using a Time-Accurate Free-Vortex Wake," Journal of the American Helicopter Society, Volume 48(3), July 2003.

[72] Von Karman, T., "Aerodynamics, History and Analysis of Flight," (originally Cornell University Press 1954), McGraw-Hill Book Company, New York, New York, 1963

[73] Boas, M.,L., "Mathematical Methods in the Physical Sciences, Second Edition" John Wiley & Sons, New York, New York, 1983.

[74] Castles, W., and De Leeuw, J., H., "The Normal Component of the Induced Velocity in the Vicinity of a Lifting Rotor and Some Examples of Its Application," NACA Technical Report 1184, 1954.

[75] Sandeep, G., and Leishman, J.,G., "Accuracy of the Induced Velocity from Helicoidal Vortices Using Straight-Line Segmentation," AIAA Journal, Volume 43(1), January 2005.

# Appendix A: Comparisons of Baseline and Optimum Distributions

A.1 Lift Distributions
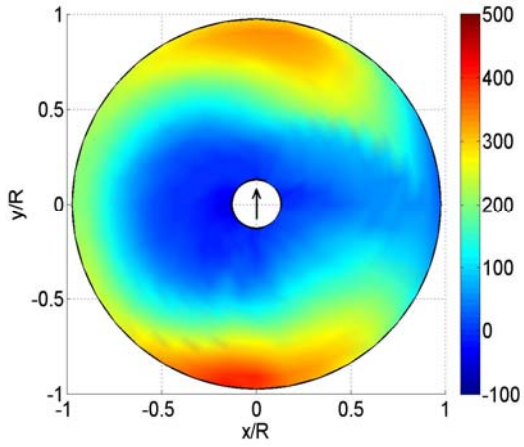


a.) Baseline: Lift (AR=0.4)
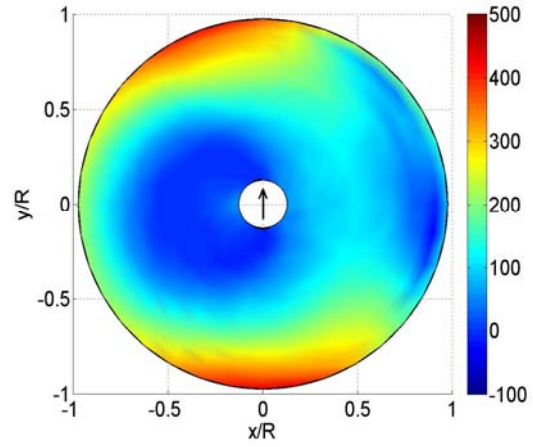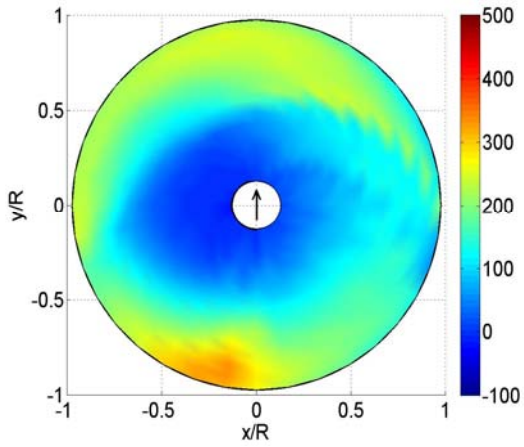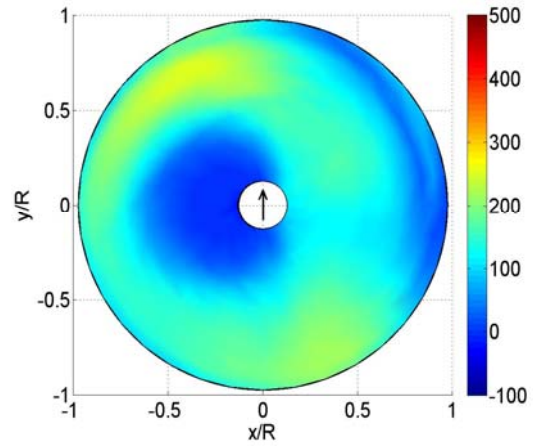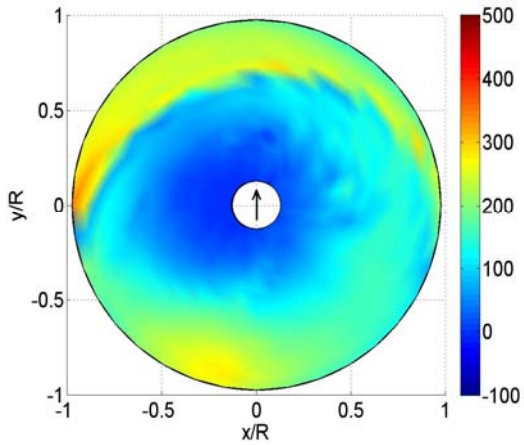
b.) Optimum: Lift (AR=0.4)

c.) Baseline: Lift (AR=0.3)

d.) Optimum: Lift (AR=0.3)

e.) Baseline: Lift (AR=0.2)
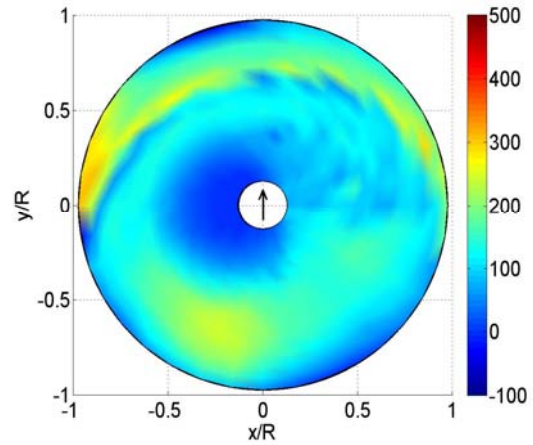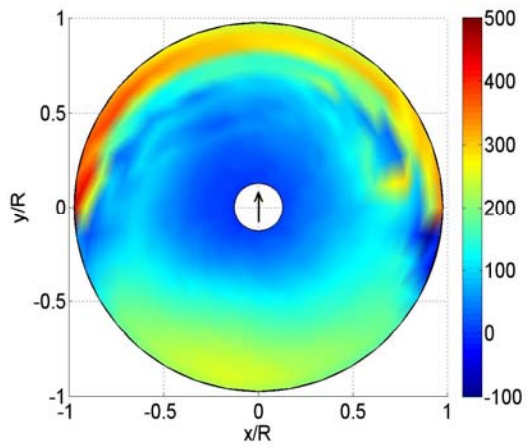
f.) Optimum: Lift (AR=0.2)

g.) Baseline: Lift (AR=0.1)
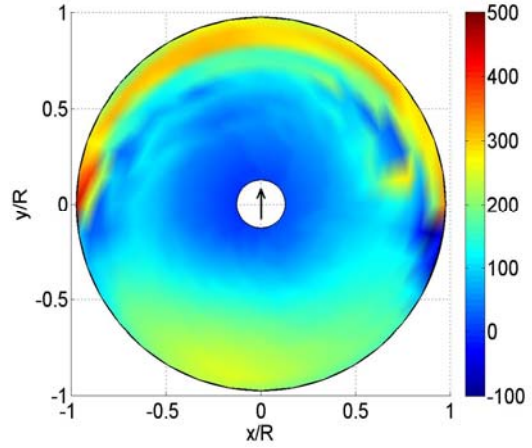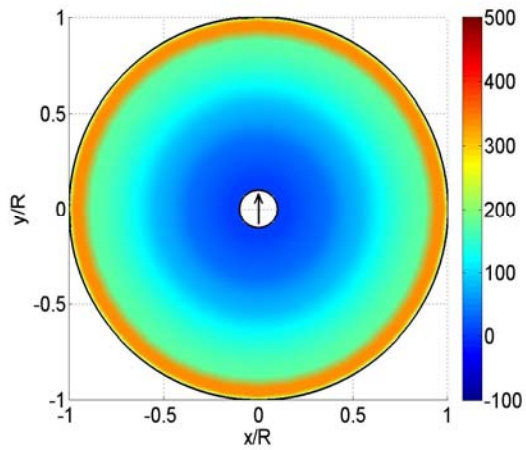
h.) Optimum: Lift (AR=0.1)

i.) Baseline: Lift (AR=0.0)
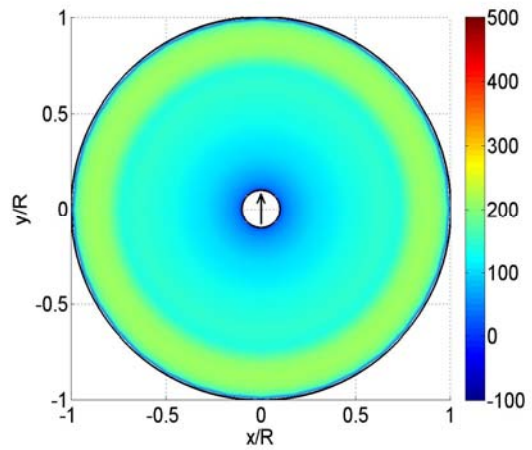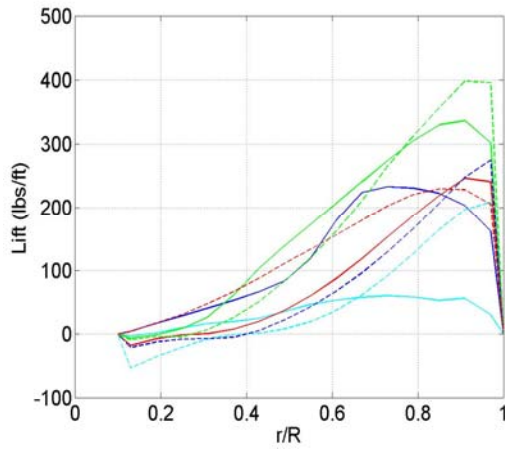
j.) Optimum: Lift (AR=0.0)

k.) Baseline: Lift (AR=0.4)
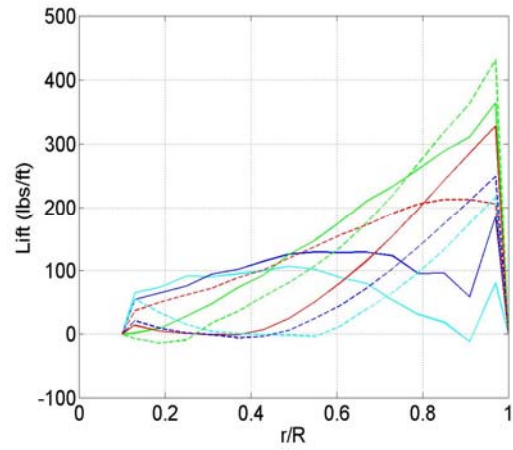
l.) Optimum: Lift (AR=0.4)
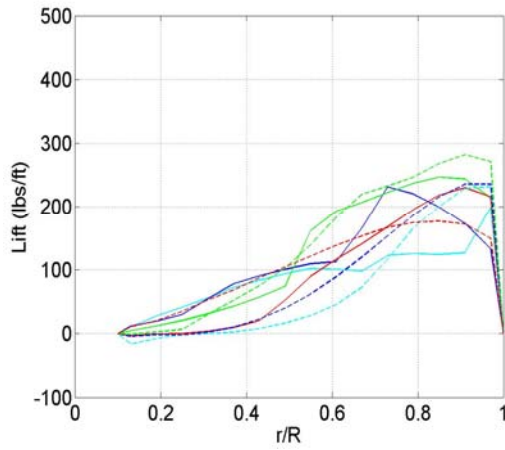
m.) Baseline: Lift (AR=0.3)
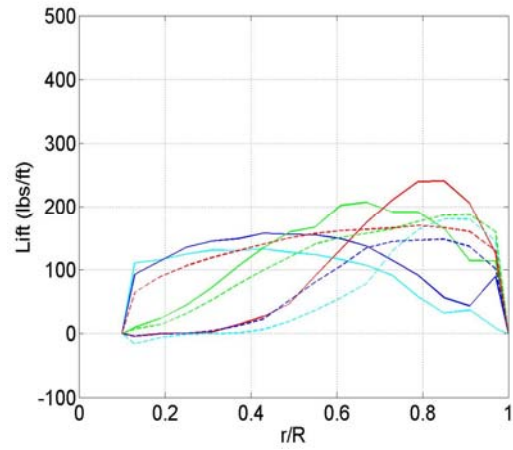
n.) Optimum: Lift (AR=0.3)
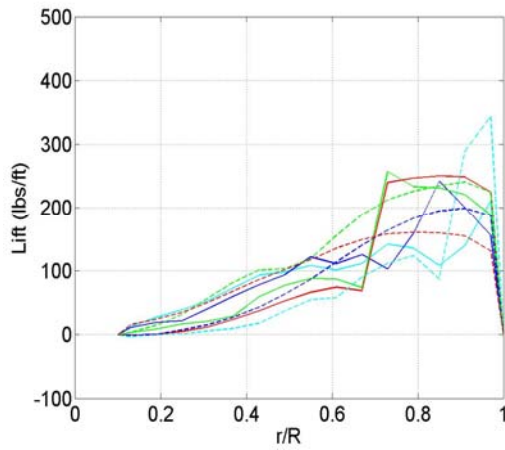
o.) Baseline: Lift (AR=0.2)
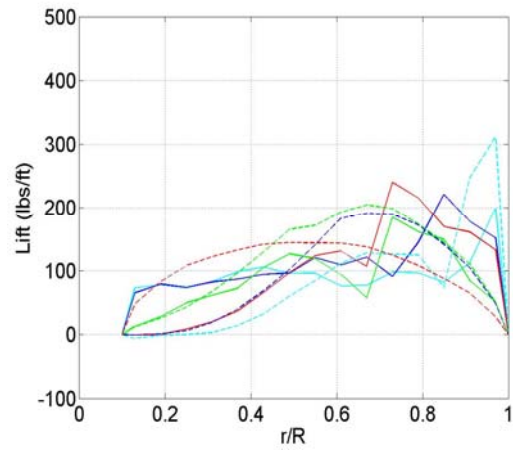
p) Optimum: Lift (AR=0.2)

104
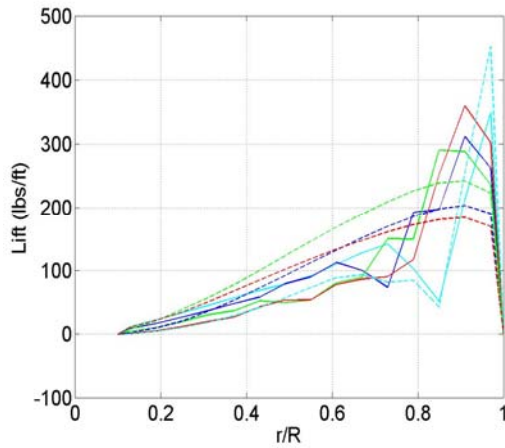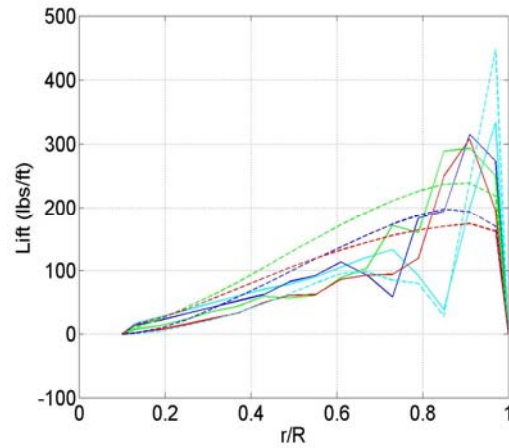
q.) Baseline: Lift (AR=0.1)   **r.) Optimum: Lift (AR=0.1)**
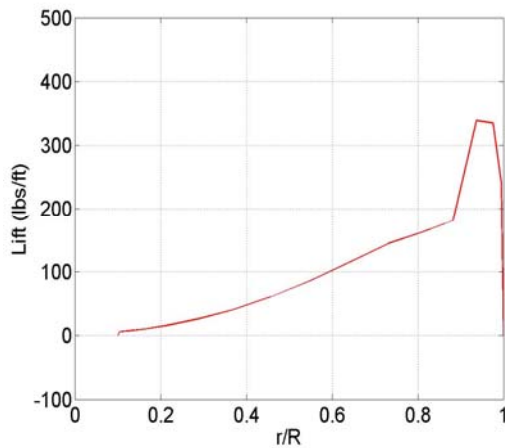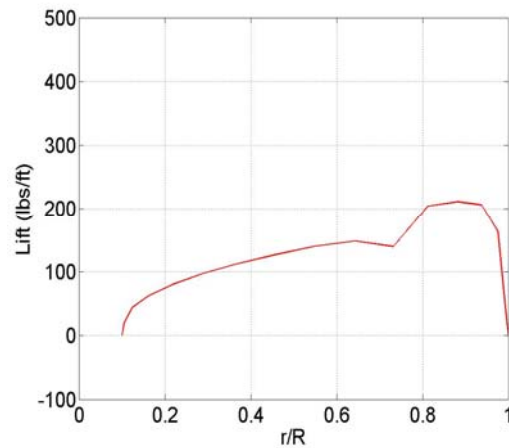
s.) Baseline: Lift (AR=0.0)   **t.) Optimum: Lift (AR=0.0)**

Figure A.1 a-t: Lift Distribution Comparisons: Comparison of the lift distribution (lbs/ft) between the optimum and baseline. The 2-D plots show eight radial slices separated by 45° and are oriented at shown below in figure 4.2.5.

A.2 Azimuthal Positions of Two Dimensional Plots
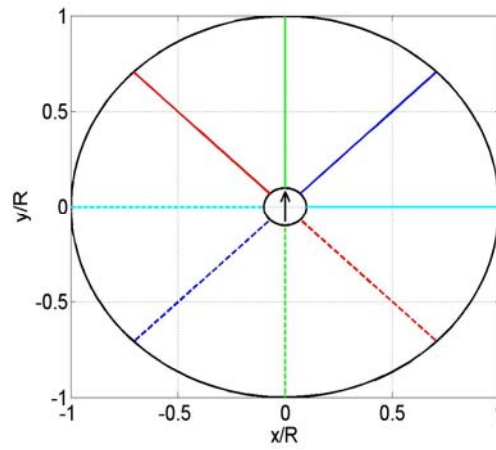
Figure A.2: Azimuthal Position for 2-D Plots: The solid cyan, blue, green, and red lines respectively represent at 90°, 135°, 180°, and 225°. The dashed cyan, blue, green, and red lines respectively represent at 270°, 315°, 0°, and 45°.

A.3 Lift Difference Distributions
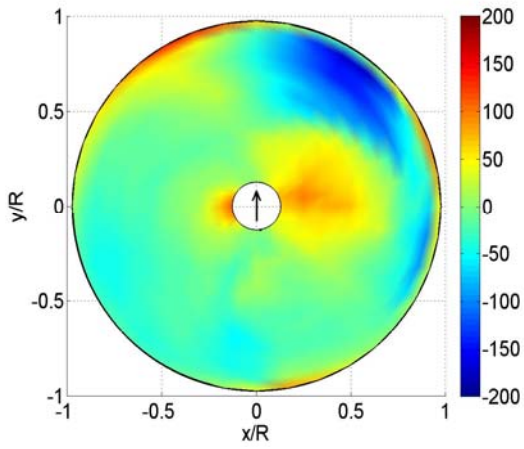
a.) Lift Difference (AR=0.4)
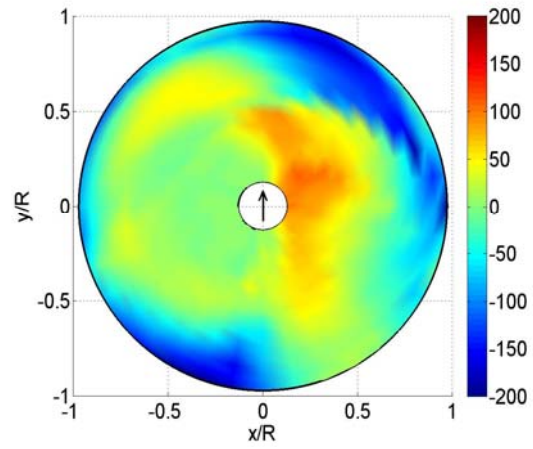
b.) Lift Difference (AR=0.3)
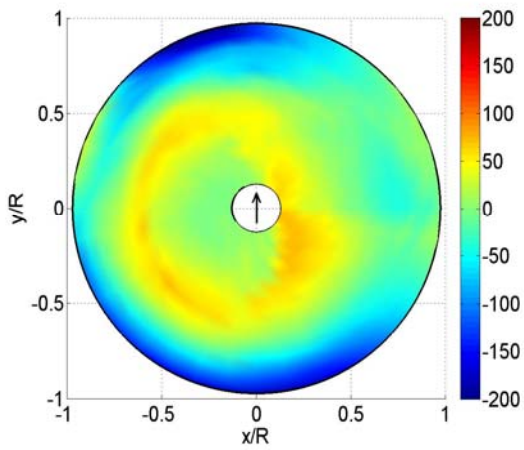
c.) Lift Difference (AR=0.2)
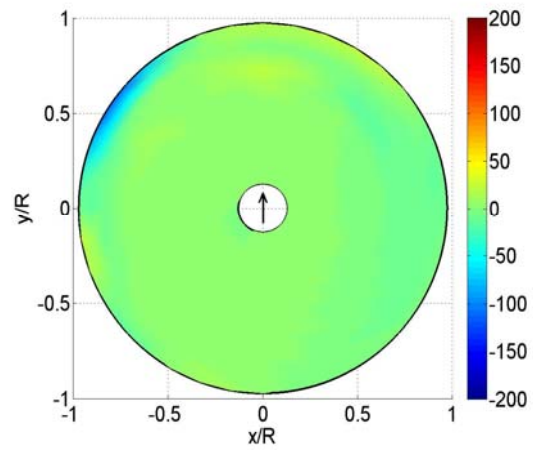
d.) Lift Difference (AR=0.1)
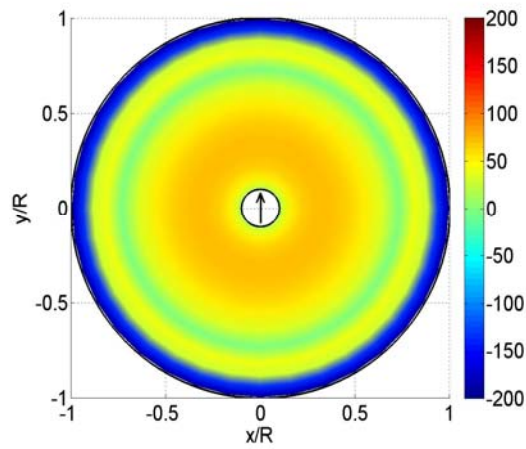
e.) Lift Difference (AR=0.0)
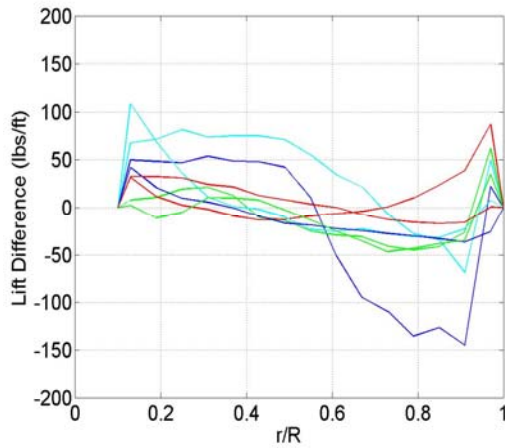
f.) Lift Difference (AR=0.4)
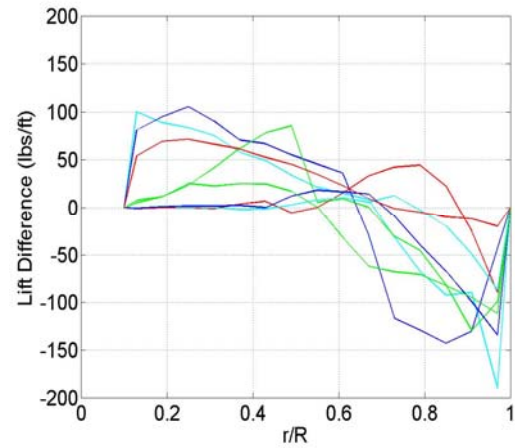
g.) Lift Difference (AR=0.3)
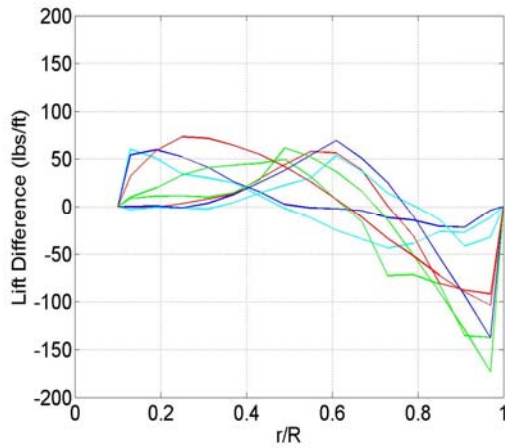
h.) Lift Difference (AR=0.2)
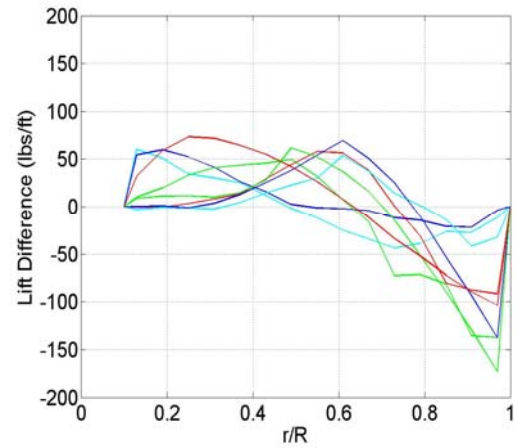
i.) Lift Difference (AR=0.1)
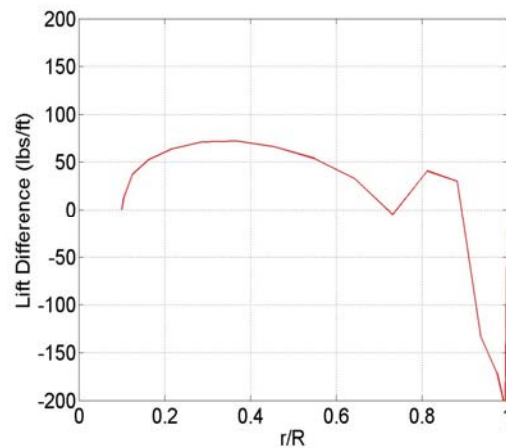
j.) Lift Difference (AR=0.0)

Figure A.3 a-j: Lift Distribution Differences: Difference between the optimum and baseline lift distributions (lbs/ft).

A.4 Circulation Distributions
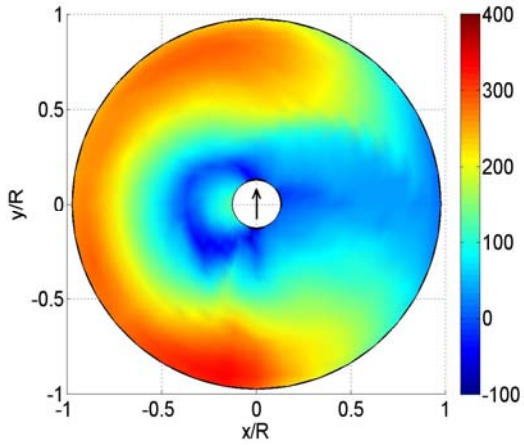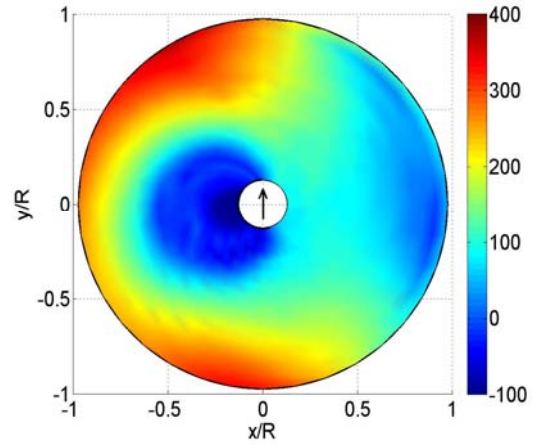
a.) Baseline: Circulation (AR=0.4)

b.) Optimum: Circulation (AR=0.4)
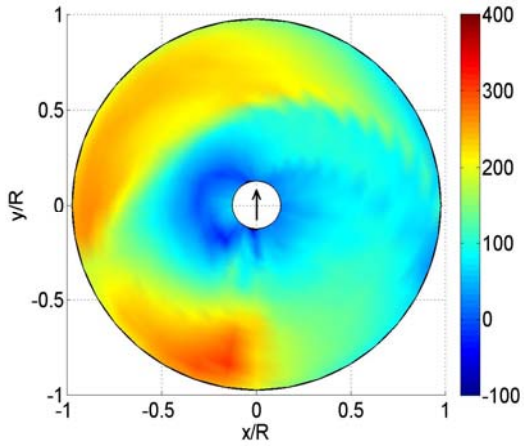
c.) Baseline: Circulation (AR=0.3)
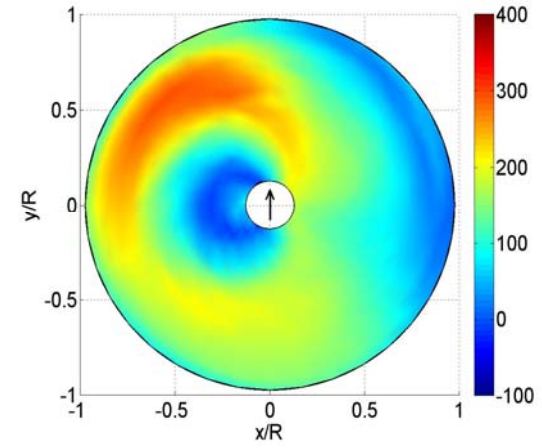
d.) Optimum: Circulation (AR=0.3)
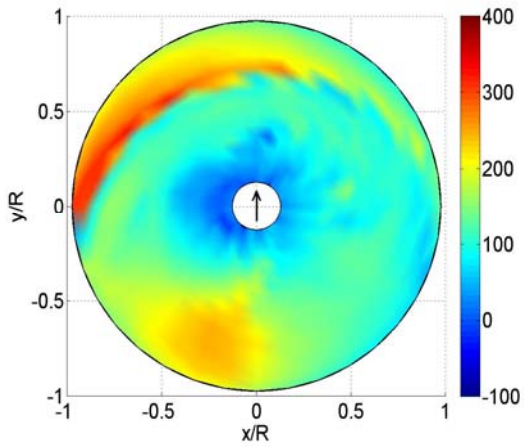
e.) Baseline: Circulation (AR=0.2)
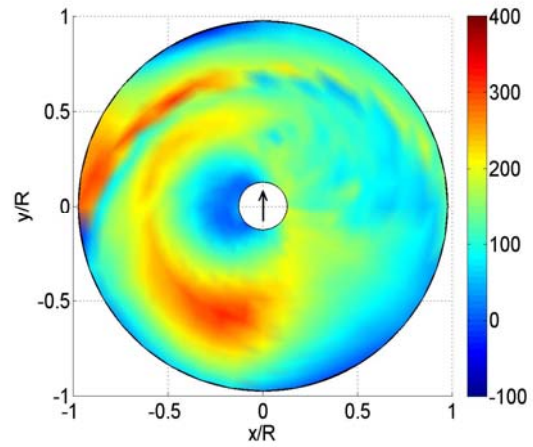
f.) Optimum: Circulation (AR=0.2)
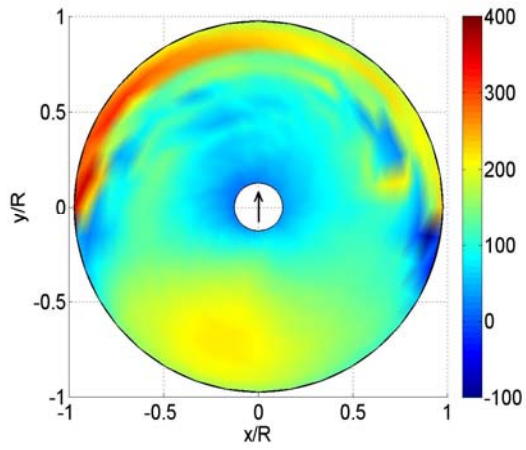
g.) Baseline: Circulation (AR=0.1)
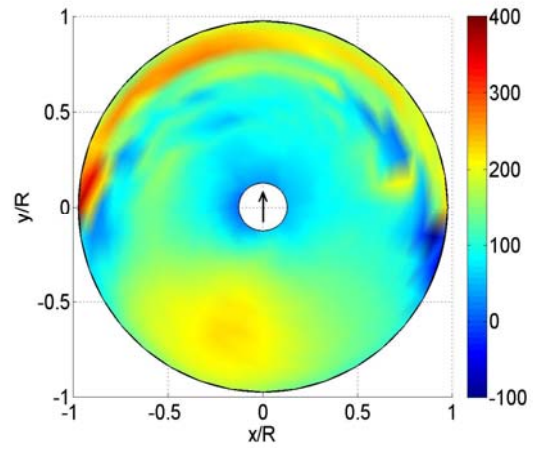
h.) Optimum: Circulation (AR=0.1)
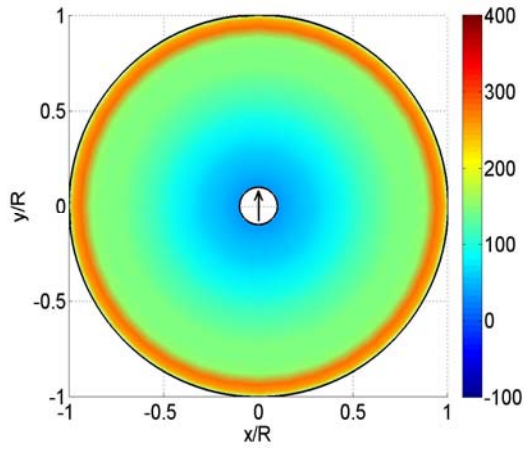
i.) Baseline: Circulation (AR=0.0)
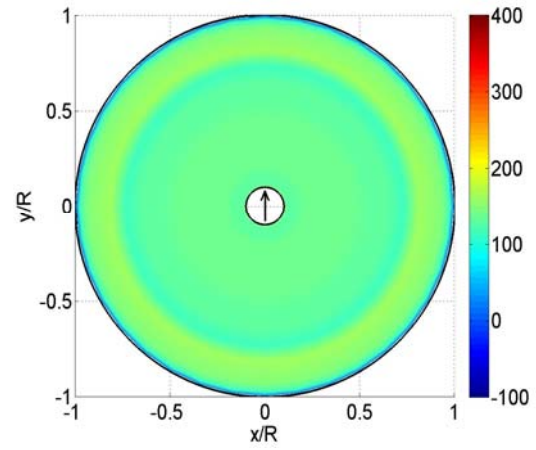
j.) Optimum: Circulation (AR=0.0)
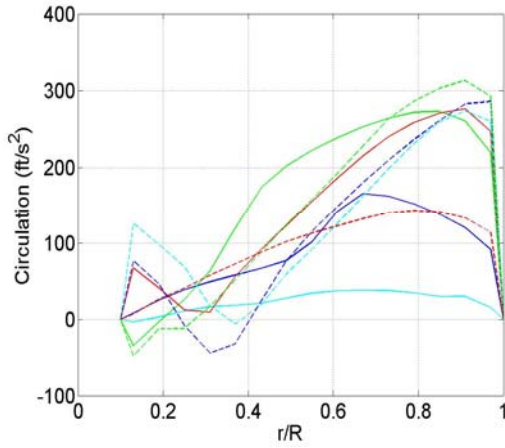
k.) Baseline: Circulation (AR=0.4)
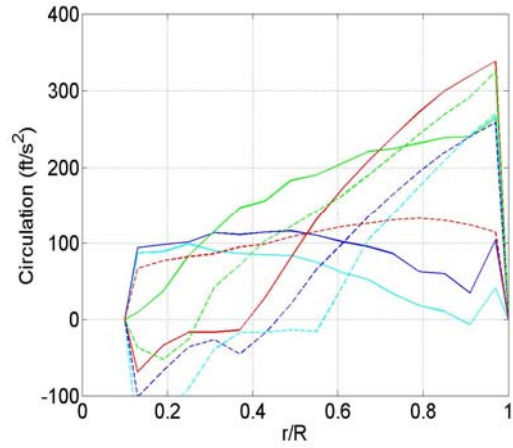
l.) Optimum: Circulation (AR=0.4)
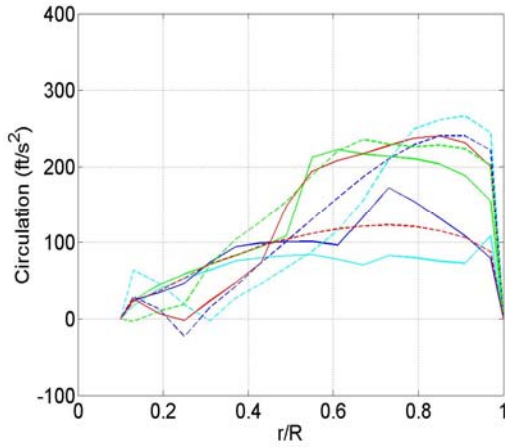
m.) Baseline: Circulation (AR=0.3)
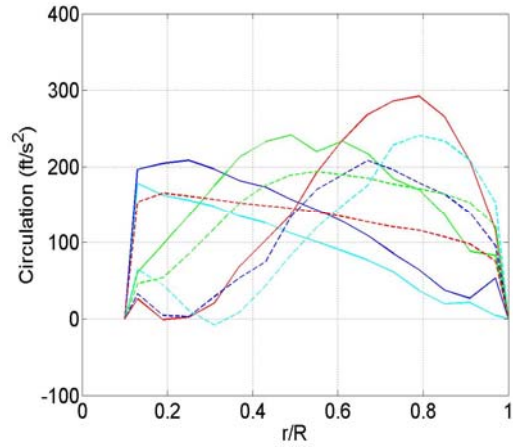
n.) Optimum: Circulation (AR=0.3)
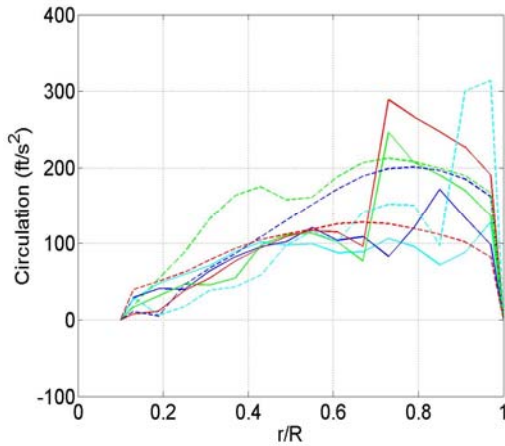
o.) Baseline: Circulation (AR=0.2)
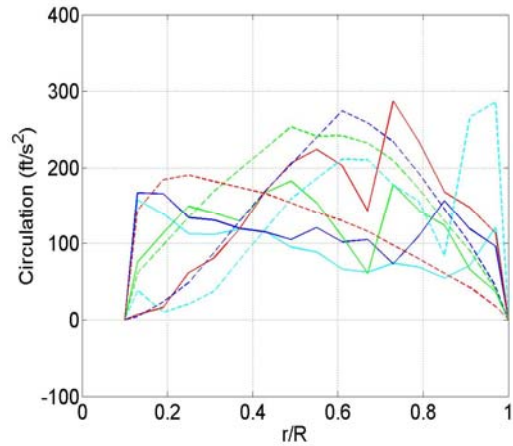
p) Optimum: Circulation (AR=0.2)
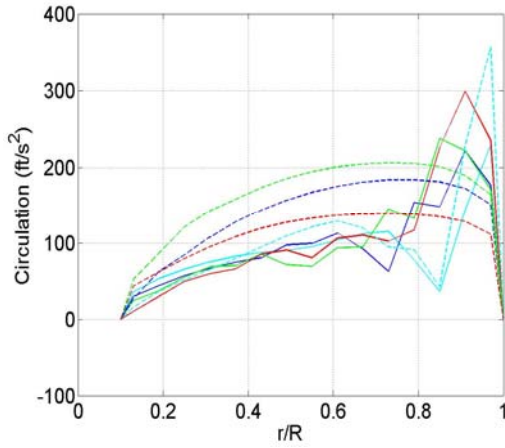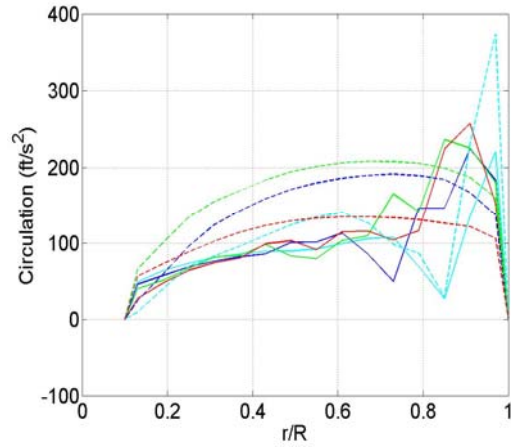
q.) Baseline: Circulation (AR=0.1) **r.) Optimum: Circulation (AR=0.1)**
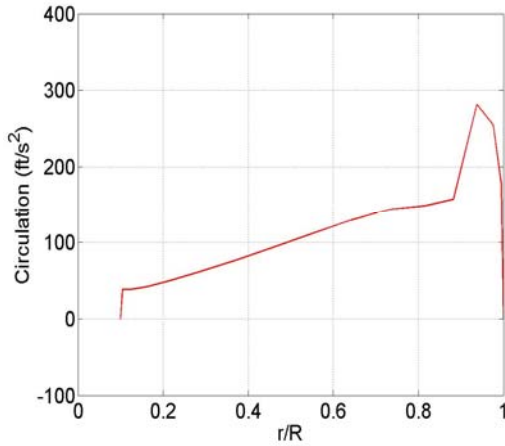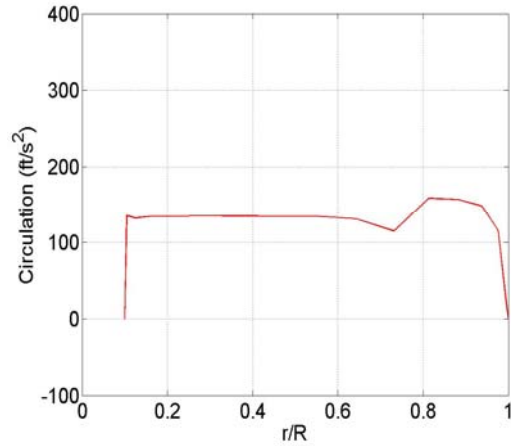
s.) Baseline: Circulation (AR=0.0) **t.) Optimum: Circulation (AR=0.0)**

Figure A.4 a-t: Circulation Distribution Comparisons: Comparison of the circulation distribution (ft/s^2) between the optimum and baseline.

A.5 Circulation Difference Distributions
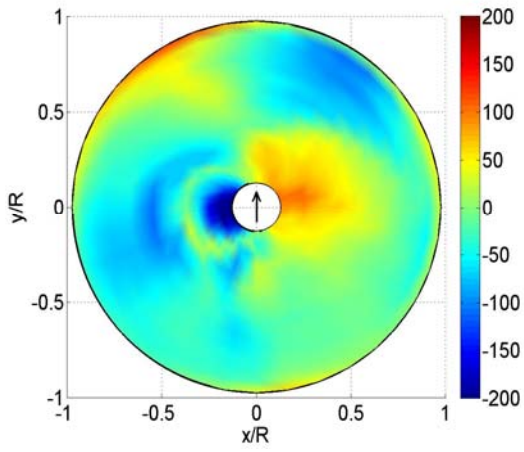
a.) Circulation Difference (AR=0.4)
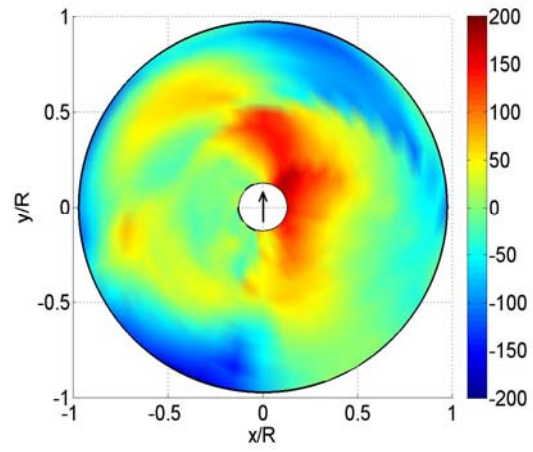
b.) Circulation Difference (AR=0.3)
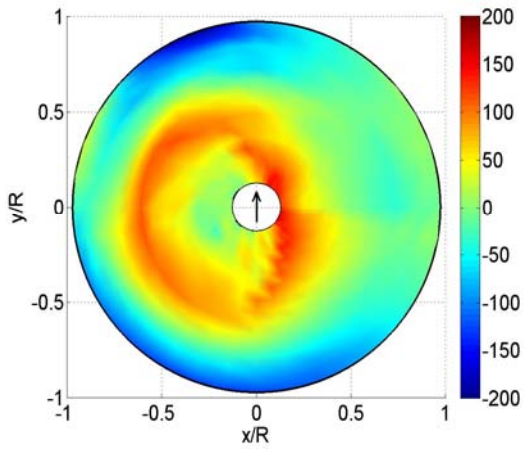
c.) Circulation Difference (AR=0.2)
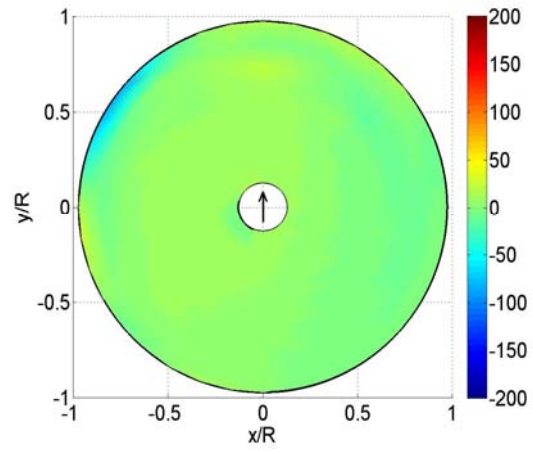
d.) Circulation Difference (AR=0.1)
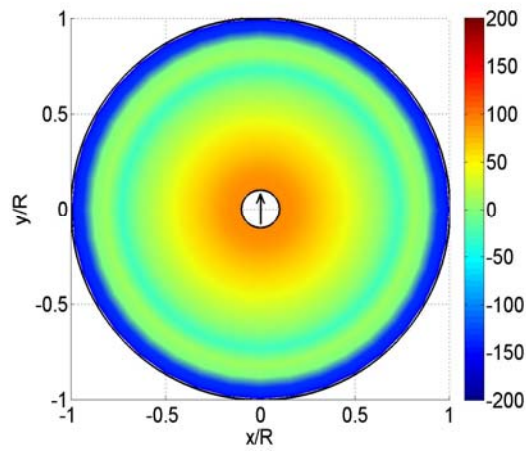
e.) Circulation Difference (AR=0.0)
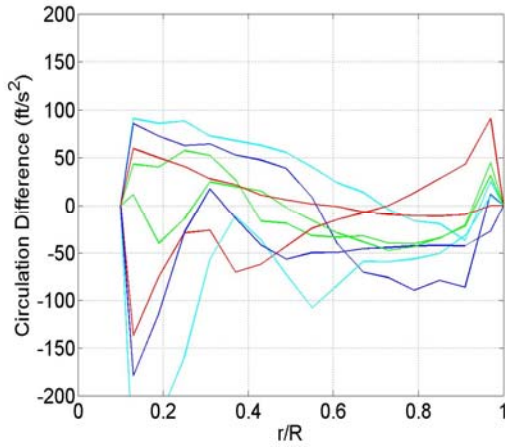
f.) Circulation Difference (AR=0.4)
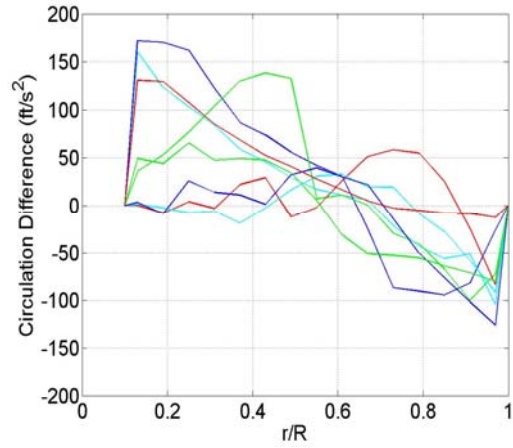
g.) Circulation Difference (AR=0.3)
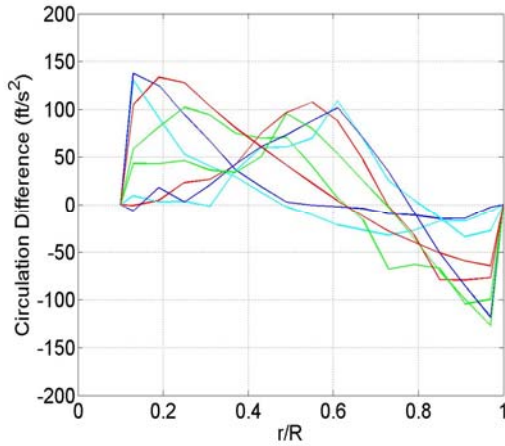
h.) Circulation Difference (AR=0.2)
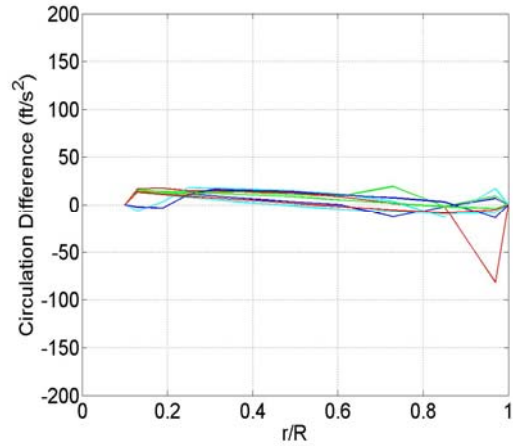
i.) Circulation Difference (AR=0.1)
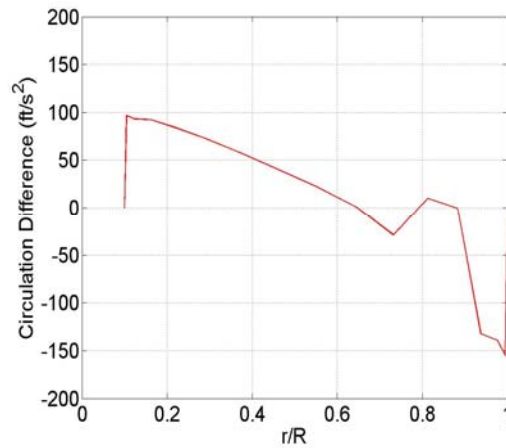
j.) Circulation Difference (AR=0.0)

Figure A.5 a-j: Circulation Distribution Differences: Difference between the optimum and baseline circulation distributions (ft²/s).

A.6 Drag Distributions
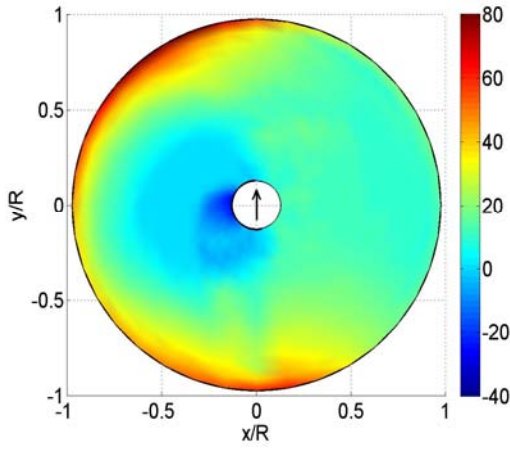
a.) Baseline: Drag (AR=0.4)
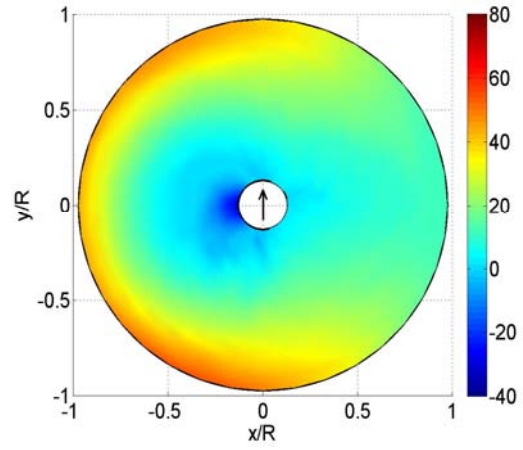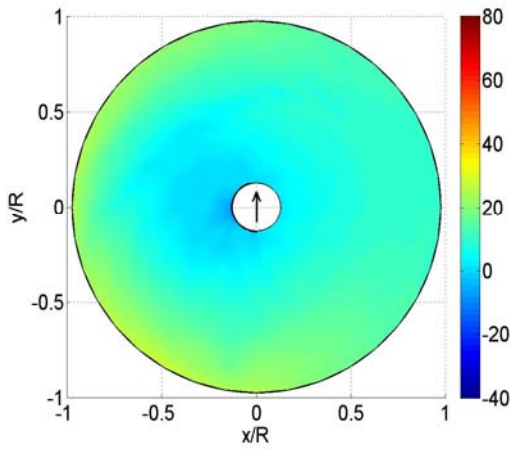
b.) Optimum: Drag (AR=0.4)

c.) Baseline: Drag (AR=0.3)
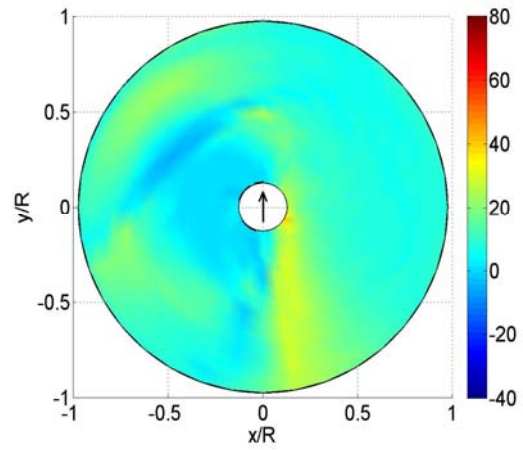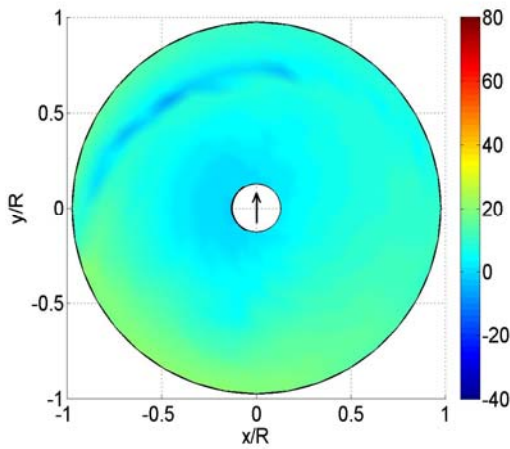
d.) Optimum: Drag (AR=0.3)

e.) Baseline: Drag (AR=0.2)
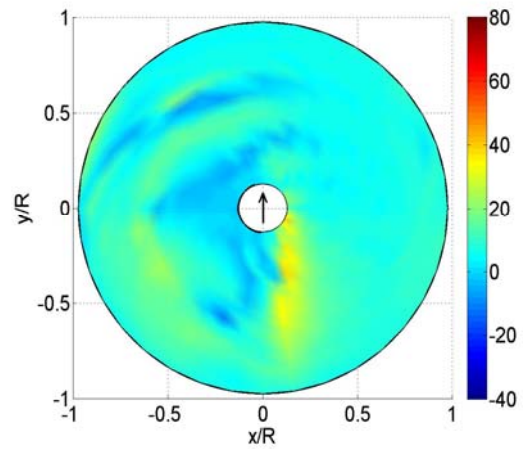
f.) Optimum: Drag (AR=0.2)
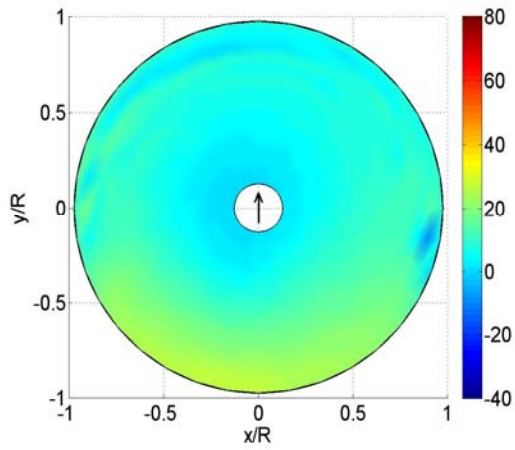
g.) Baseline: Drag (AR=0.1)
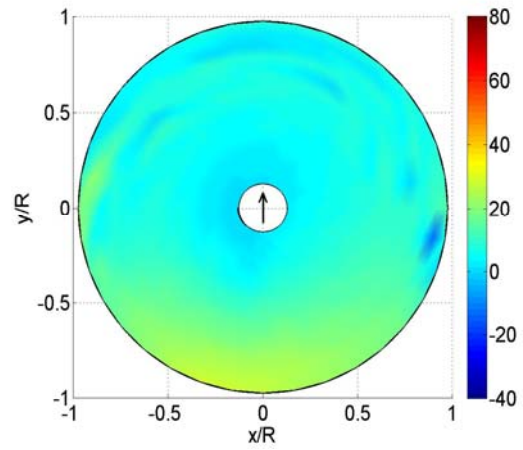
h.) Optimum: Drag (AR=0.1)
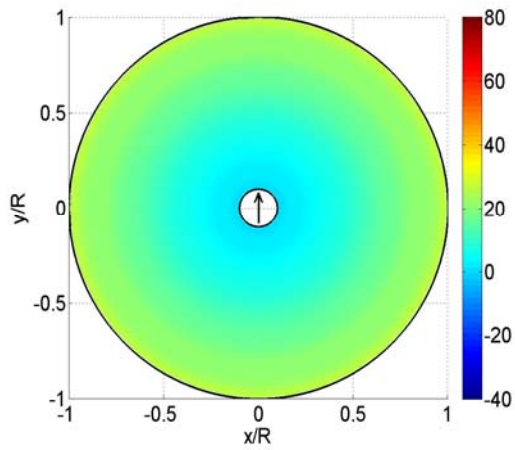
i.) Baseline: Drag (AR=0.0)
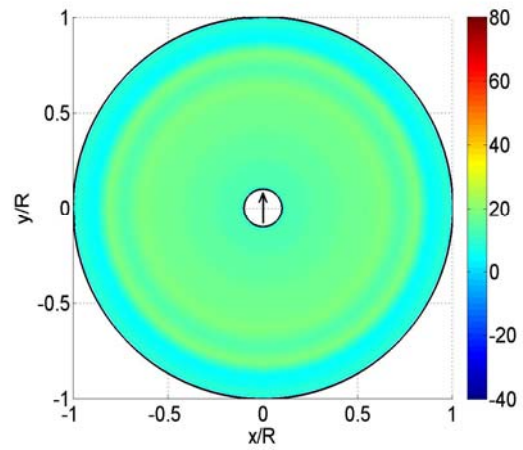
j.) Optimum: Drag (AR=0.0)
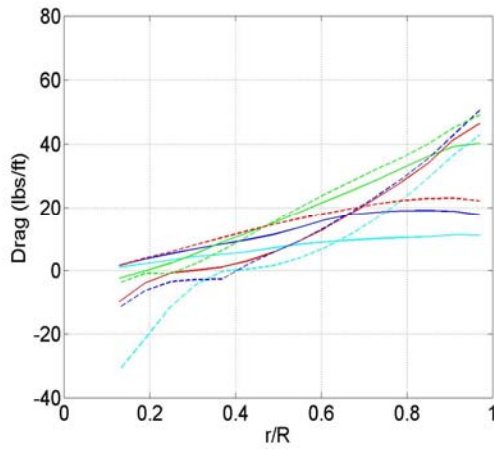
k.) Baseline: Drag (AR=0.4)
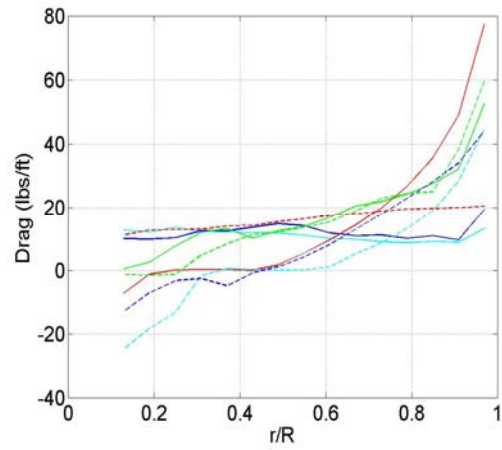
l.) Optimum: Drag (AR=0.4)
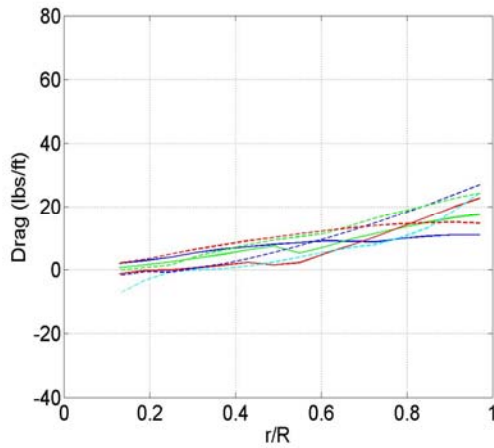
m.) Baseline: Drag (AR=0.3)
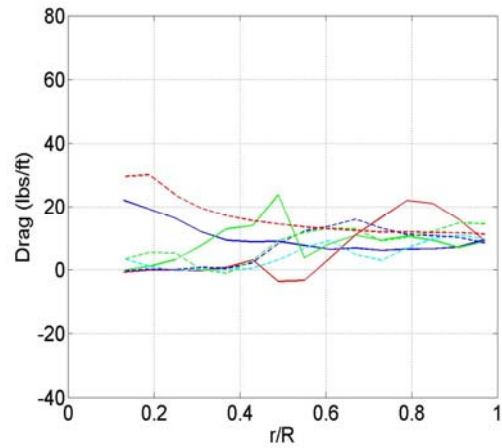
n.) Optimum: Drag (AR=0.3)
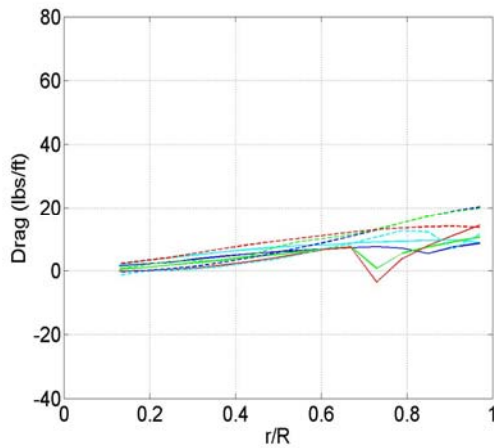
o.) Baseline: Drag (AR=0.2)
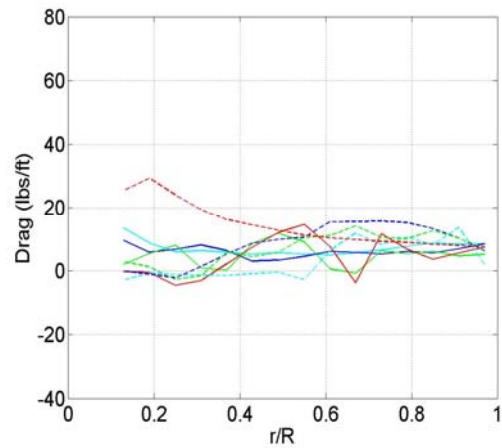
p) Optimum: Drag (AR=0.2)

117
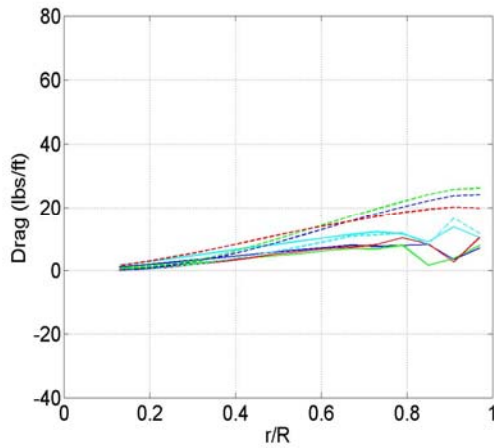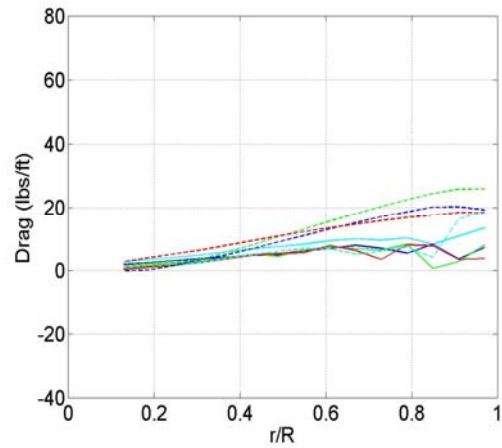
q.) Baseline: Drag (AR=0.1)   **r.) Optimum: Drag (AR=0.1)**
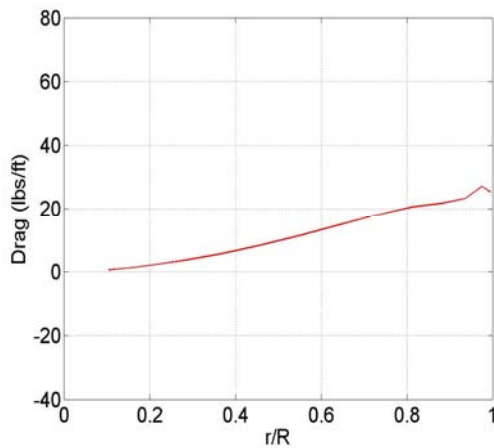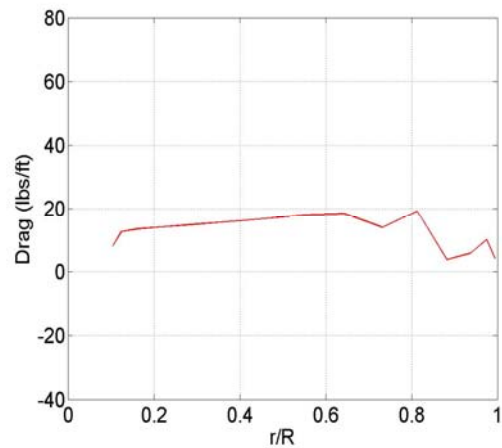
s.) Baseline: Drag (AR=0.0)   **t.) Optimum: Drag (AR=0.0)**

Figure A.6 a-t: Drag Distribution Comparisons: Comparison of the drag distribution between the optimum and baseline (lbs/ft).

A.7 Drag Difference Distributions
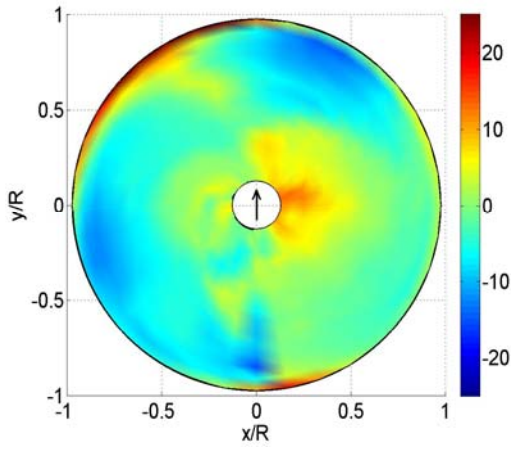
a.) Drag Difference (AR=0.4)
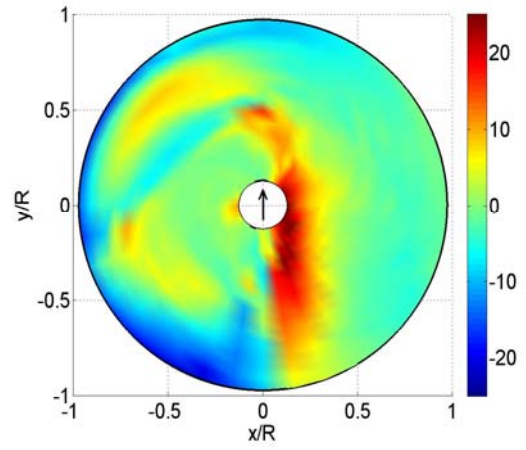
b.) Drag Difference (AR=0.3)
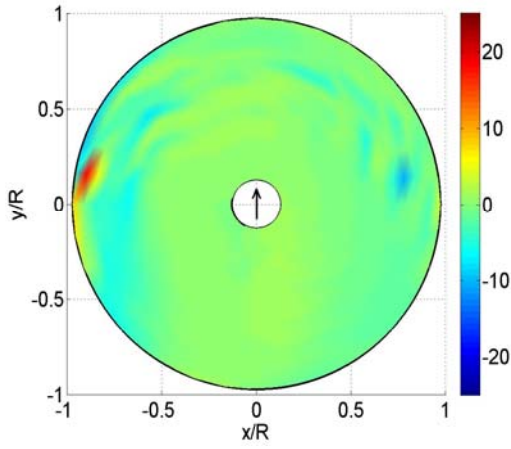
c.) Drag Difference (AR=0.2)
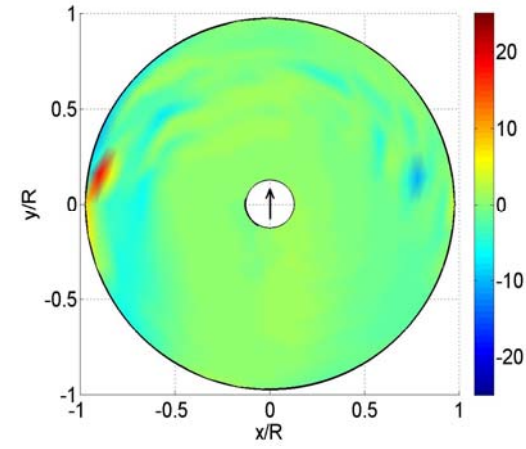
d.) Drag Difference (AR=0.1)
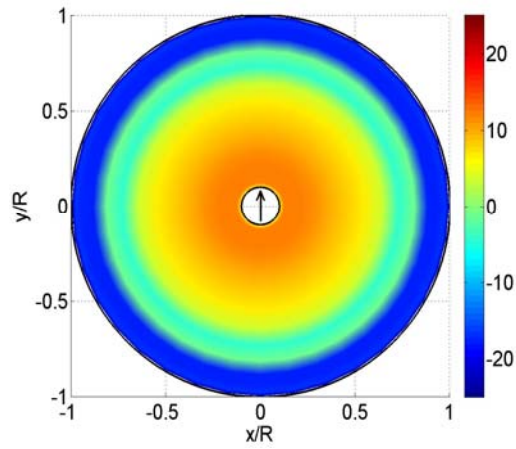
e.) Drag Difference (AR=0.0)
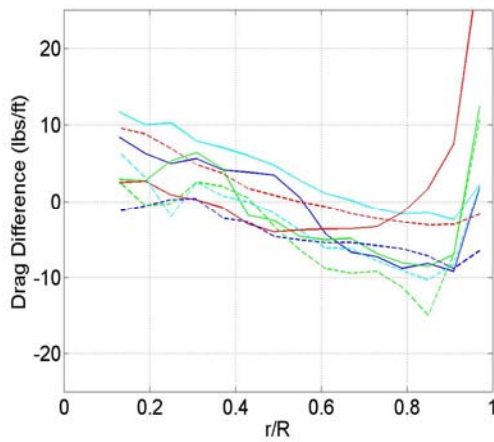
f.) Drag Difference (AR=0.4)
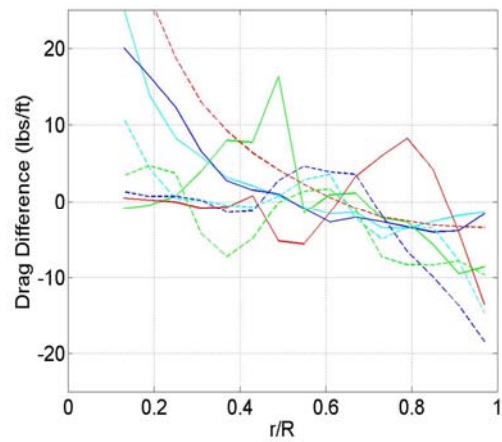
g.) Drag Difference (AR=0.3)
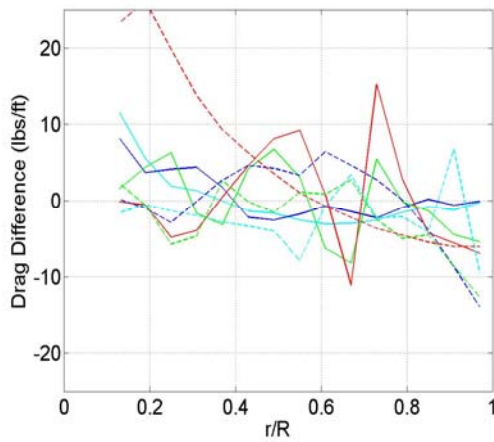

h.) Drag Difference (AR=0.2)
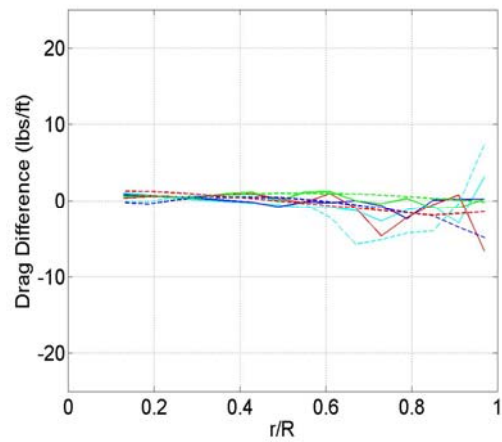
i.) Drag Difference (AR=0.1)
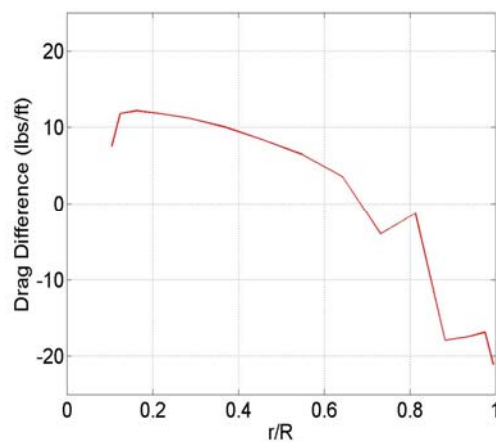
**j.) Drag Difference (AR=0.0)**

Figure A.7 a-j: Drag Distribution Differences: Difference between the optimum and baseline drag distributions (lbs/ft).

A.8 Inviscid Drag Distributions
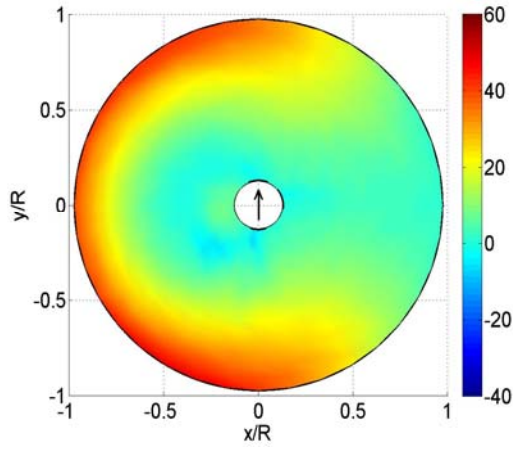
a.) Baseline: Inviscid Drag (AR=0.4)
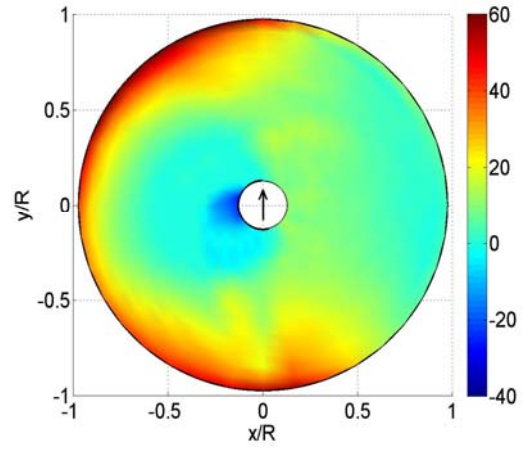
b.) Optimum: Inviscid Drag (AR=0.4)
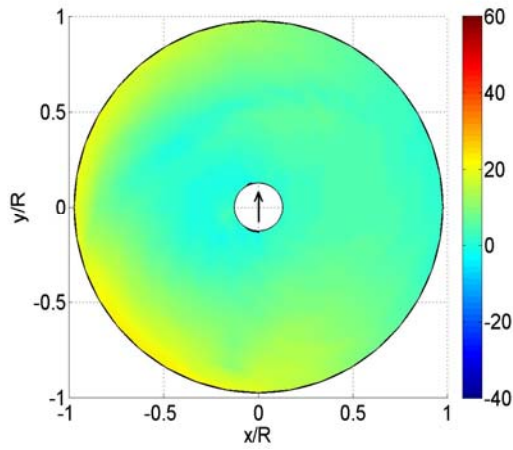
c.) Baseline: Inviscid Drag (AR=0.3)
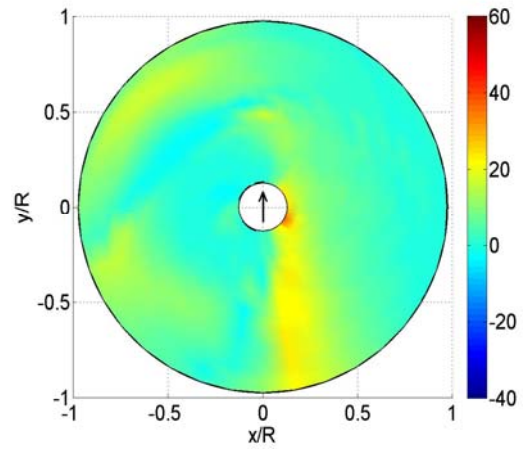
d.) Optimum: Inviscid Drag (AR=0.3)
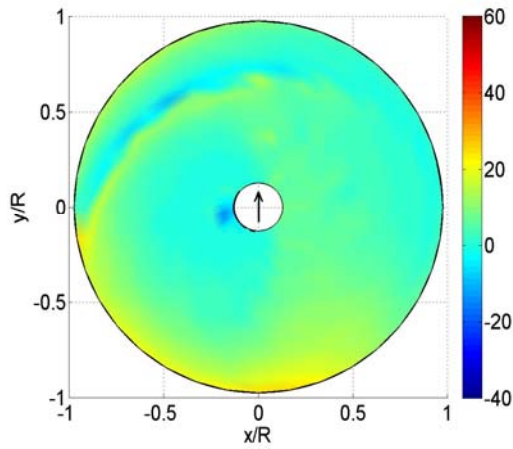
e.) Baseline: Inviscid Drag (AR=0.2)
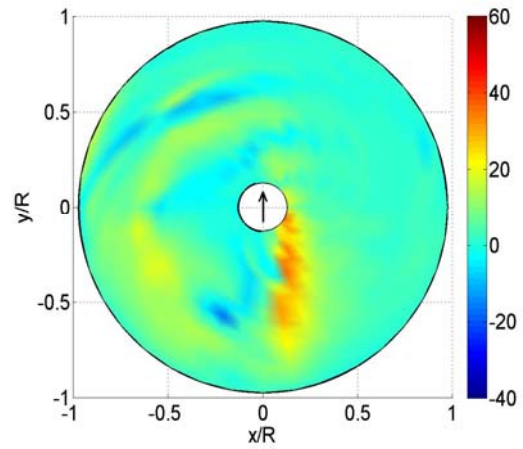
f.) Optimum: Inviscid Drag (AR=0.2)
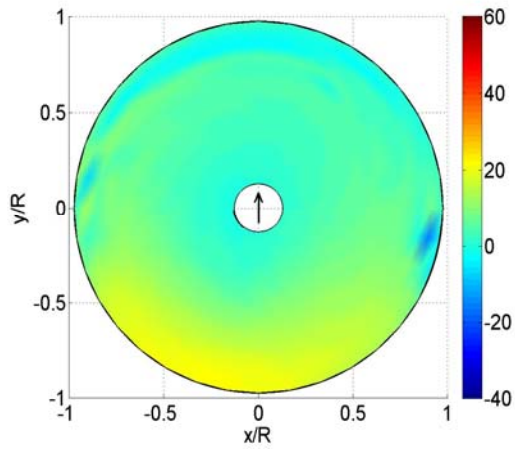
g.) Baseline: Inviscid Drag (AR=0.1)
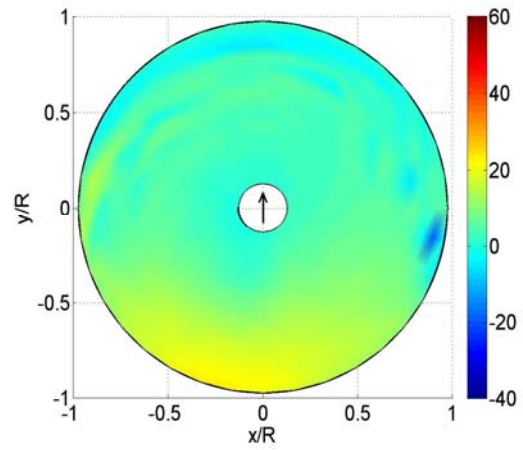
h.) Optimum: Inviscid Drag (AR=0.1)
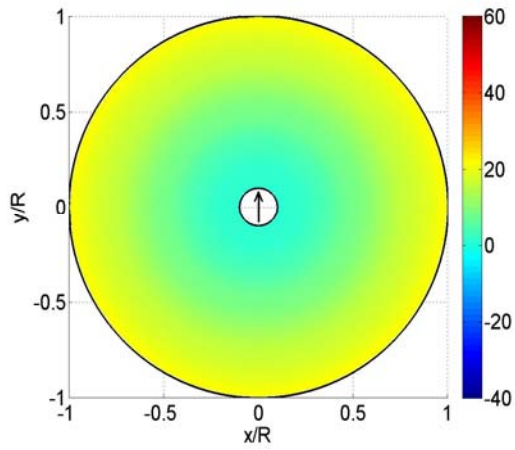
i.) Baseline: Inviscid Drag (AR=0.0)
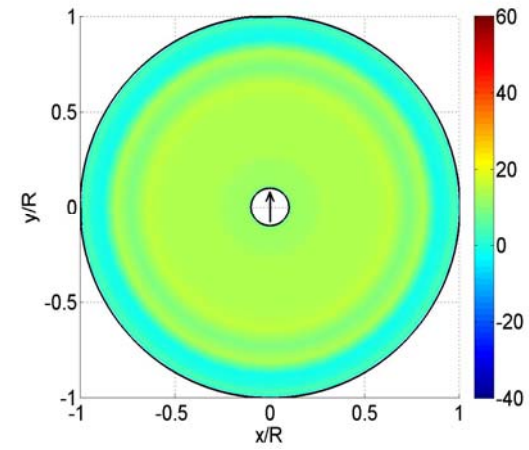
j.) Optimum: Inviscid Drag (AR=0.0)
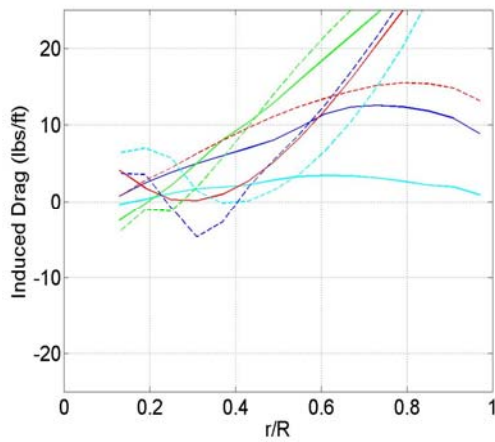
k.) Baseline: Inviscid Drag (AR=0.4)
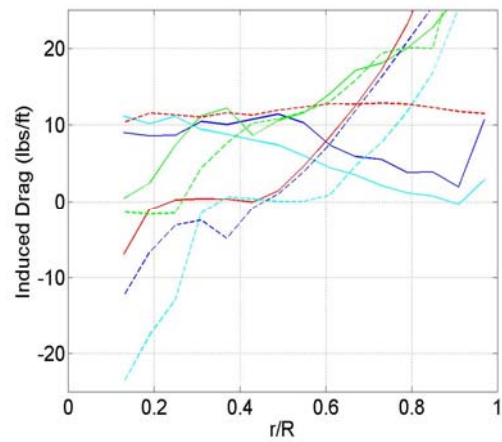
l.) Optimum: Inviscid Drag (AR=0.4)
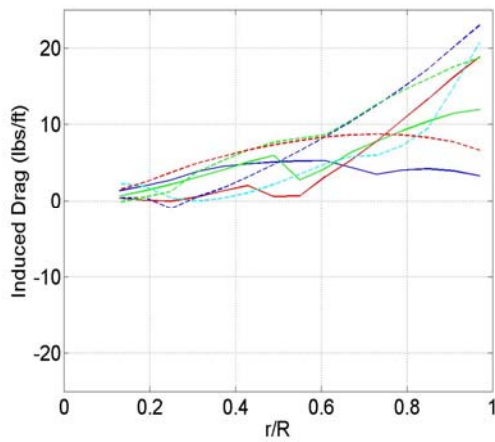
m.) Baseline: Inviscid Drag (AR=0.3)
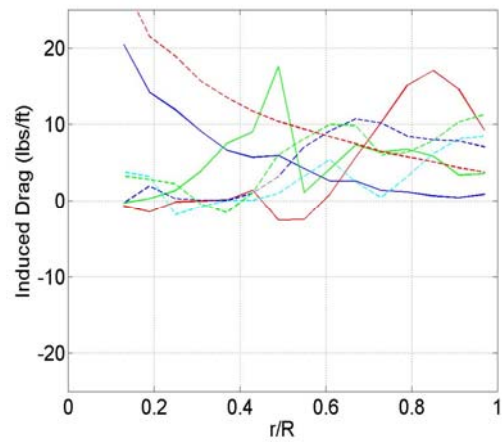
n.) Optimum: Inviscid Drag (AR=0.3)
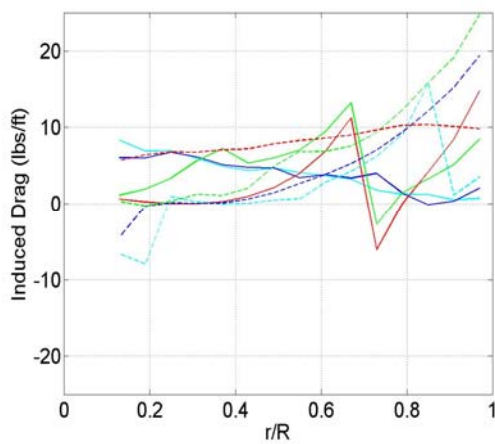
o.) Baseline: Inviscid Drag (AR=0.2)
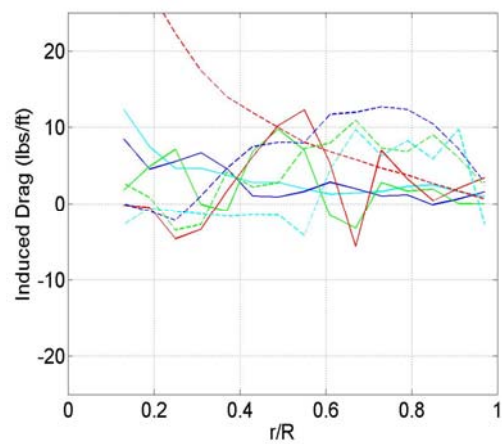
p) Optimum: Inviscid Drag (AR=0.2)
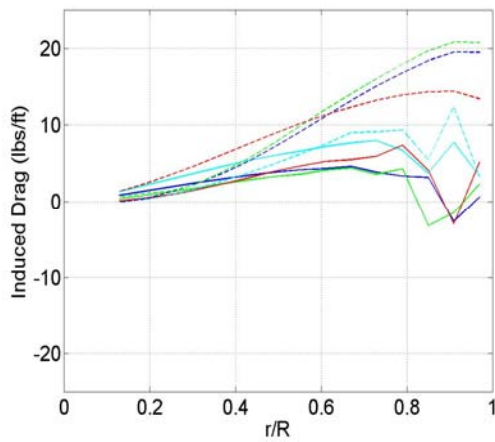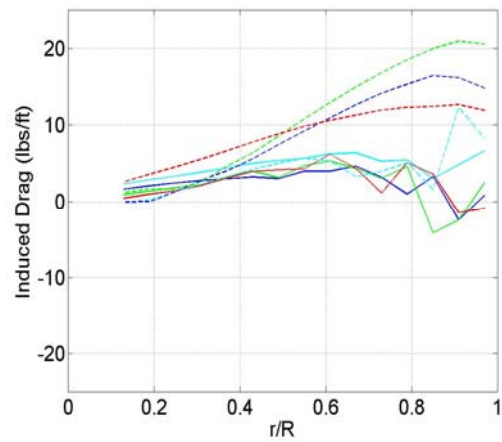
q.) Baseline: Inviscid Drag (AR=0.1) **r.) Optimum: Inviscid Drag (AR=0.1)**
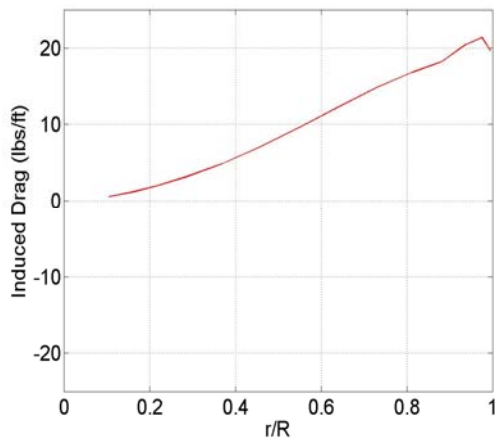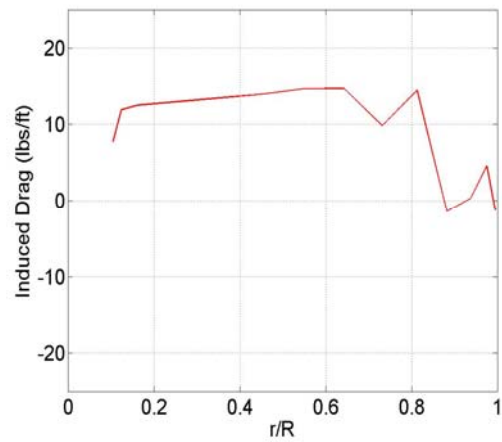
s.) Baseline: Inviscid Drag (AR=0.0) **t.) Optimum: Inviscid Drag (AR=0.0)**

Figure A.8 a-t: Inviscid Distribution Comparison: Comparison of the inviscid drag distribution (lbs/ft) between the optimum and baseline.

A.9 Inviscid Drag Difference Distributions
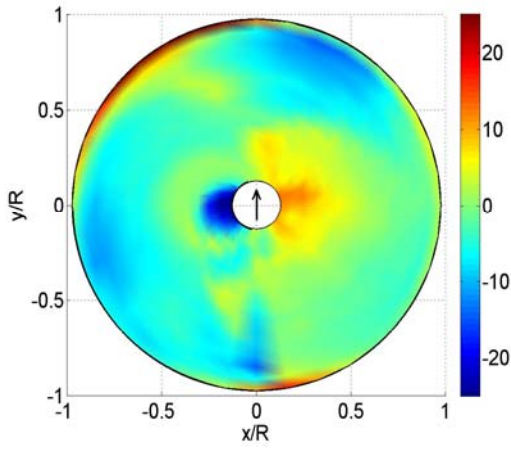
a.) Inviscid Drag Difference (AR=0.4)
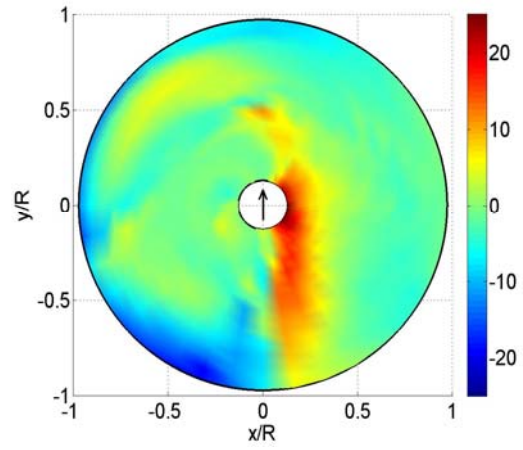
b.) Inviscid Drag Difference (AR=0.3)
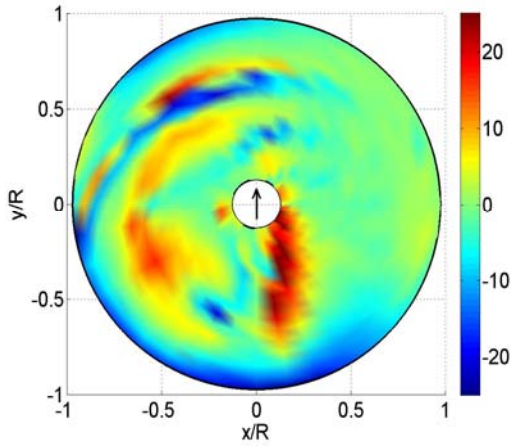
c.) Inviscid Drag Difference (AR=0.2)
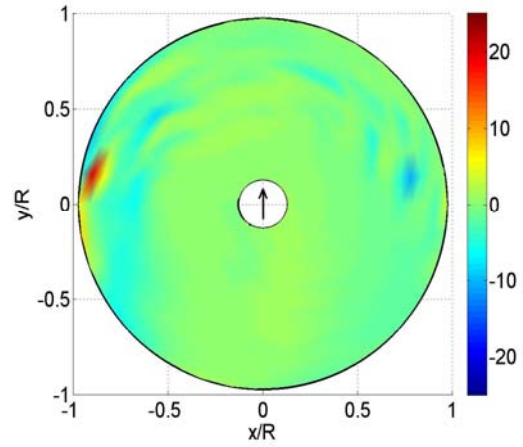
d.) Inviscid Drag Difference (AR=0.1)
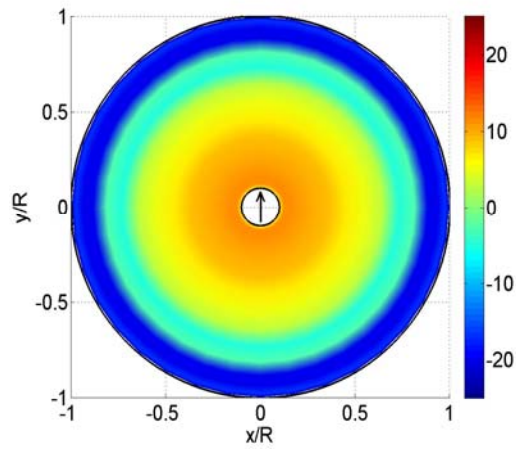
e.) Inviscid Drag Difference (AR=0.0)
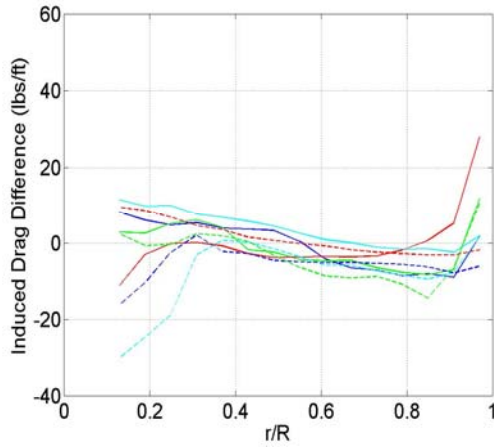
f.) Inviscid Drag Difference (AR=0.4)
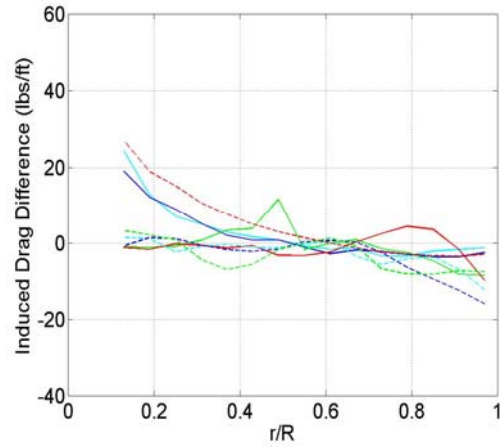
g.) Inviscid Drag Difference (AR=0.3)
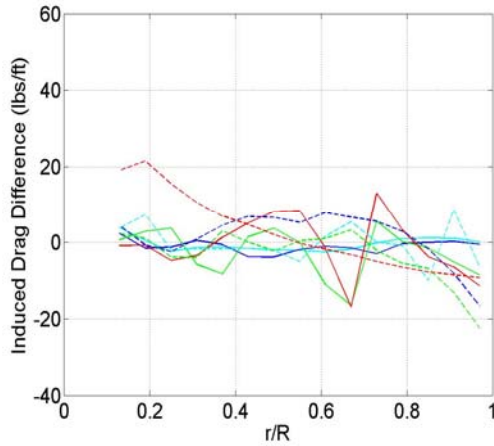
h.) Inviscid Drag Difference (AR=0.2)
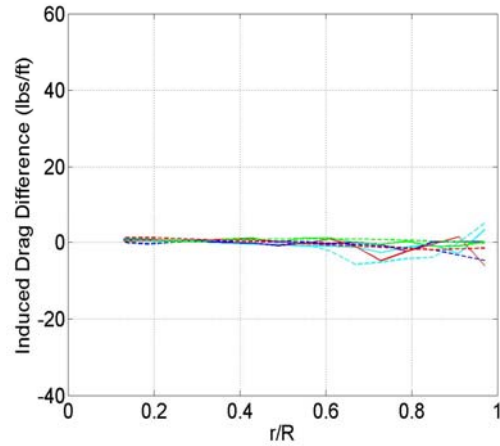
i.) Inviscid Drag Difference (AR=0.1)
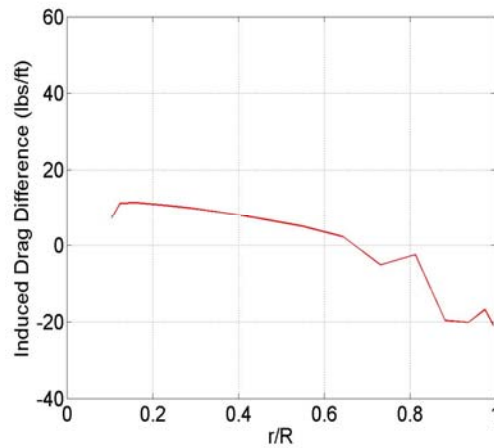
j.) Inviscid Drag Difference (AR=0.0)

Figure A.9 a-j: Inviscid Drag Distribution Differences: Difference between the optimum and baseline Inviscid drag distributions (lbs/ft).

A.10 Profile Drag Distributions
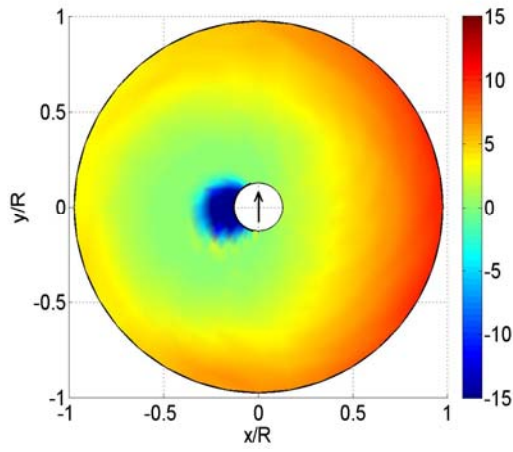
a.) Baseline: Profile Drag (AR=0.4)
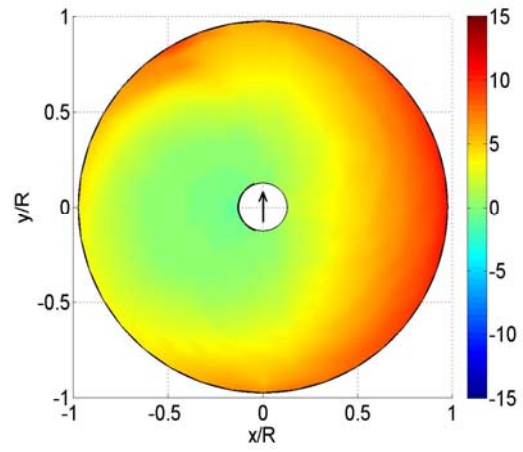
b.) Optimum: Profile Drag (AR=0.4)
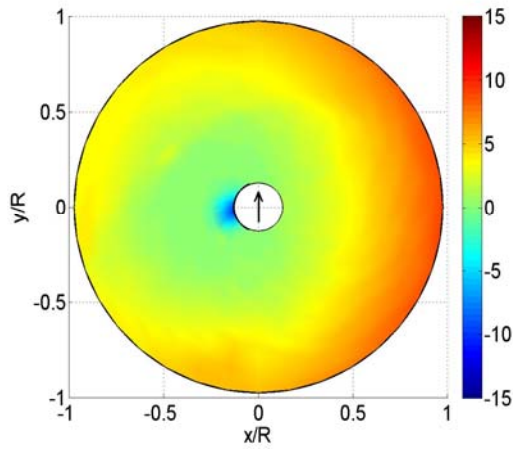
c.) Baseline: Profile Drag (AR=0.3)
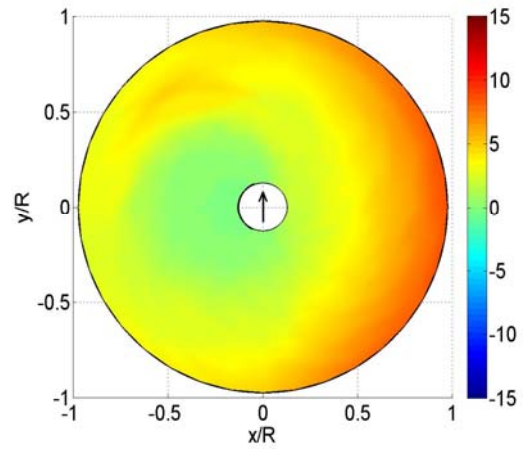
d.) Optimum: Profile Drag (AR=0.3)
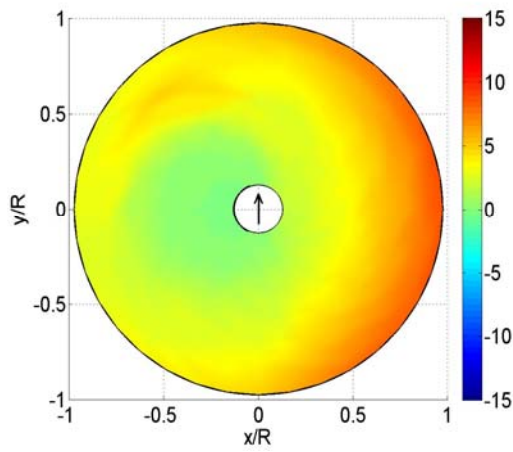
e.) Baseline: Profile Drag (AR=0.2)
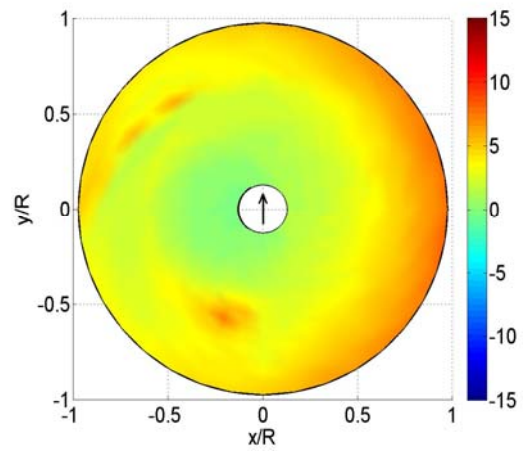
f.) Optimum: Profile Drag (AR=0.2)
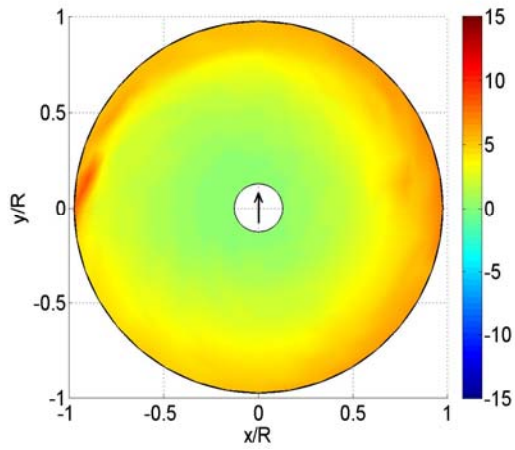
g.) Baseline: Profile Drag (AR=0.1)
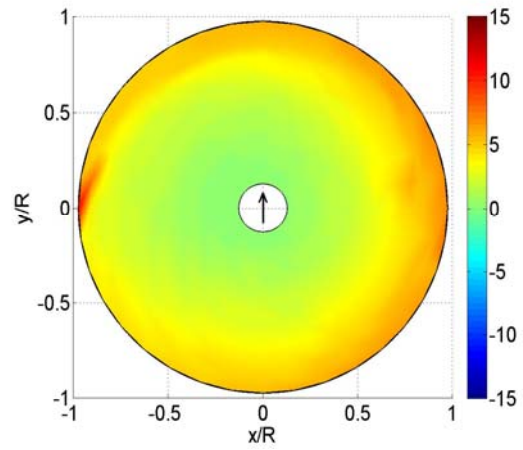
h.) Optimum: Profile Drag (AR=0.1)
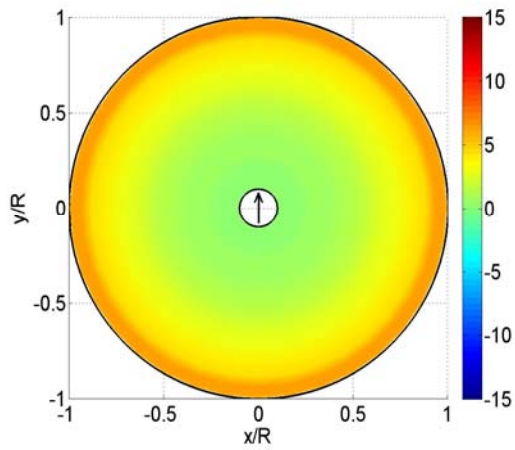
i.) Baseline: Profile Drag (AR=0.0)
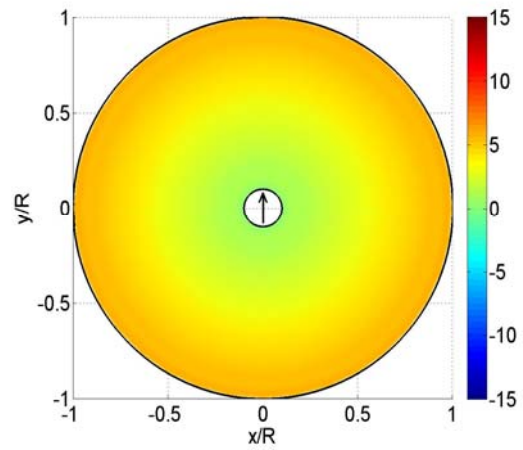
j.) Optimum: Profile Drag (AR=0.0)
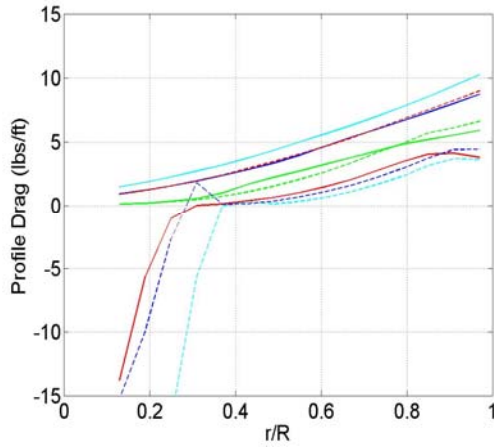
k.) Baseline: Profile Drag (AR=0.4)
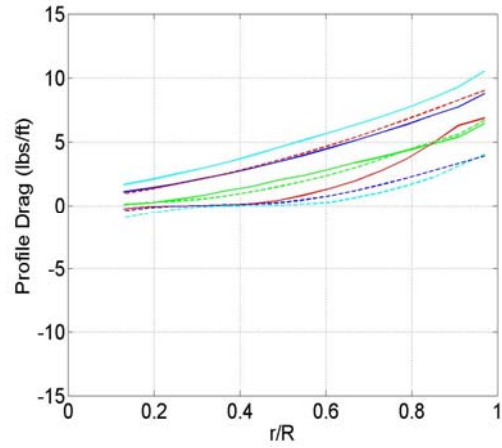
l.) Optimum: Profile Drag (AR=0.4)
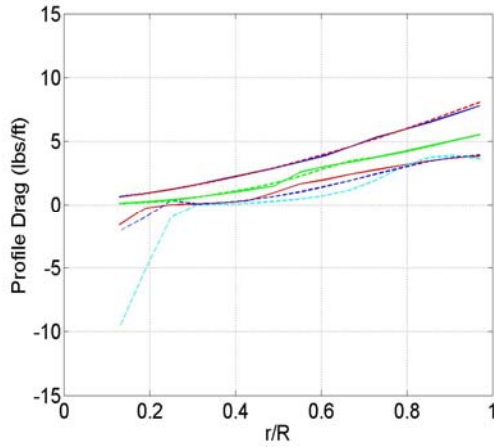
m.) Baseline: Profile Drag (AR=0.3)
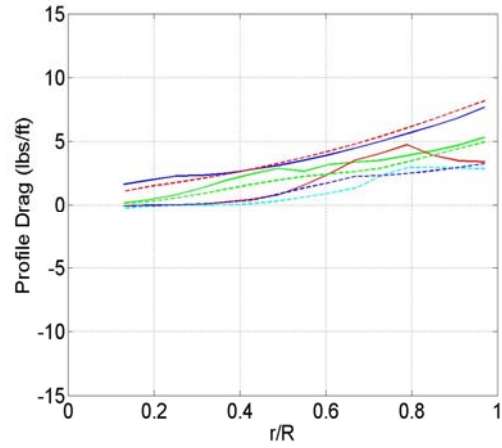
n.) Optimum: Profile Drag (AR=0.3)
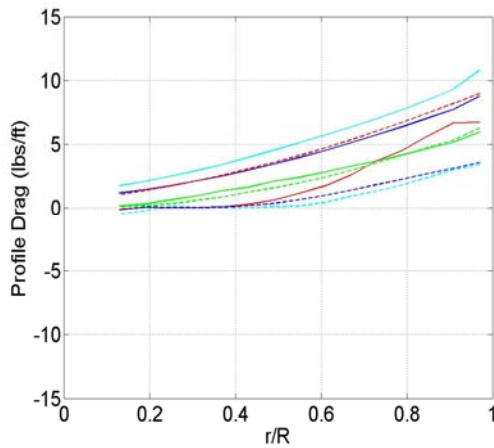
o.) Baseline: Profile Drag (AR=0.2)
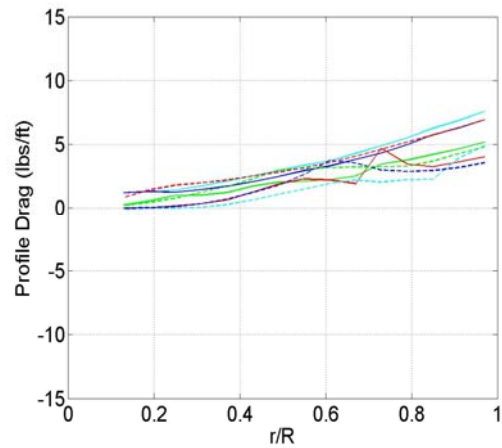
p) Optimum: Profile Drag (AR=0.2)

129
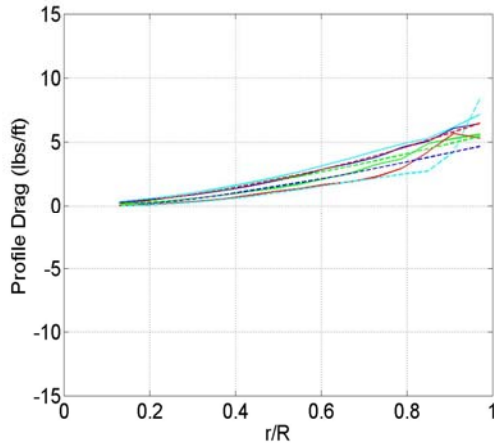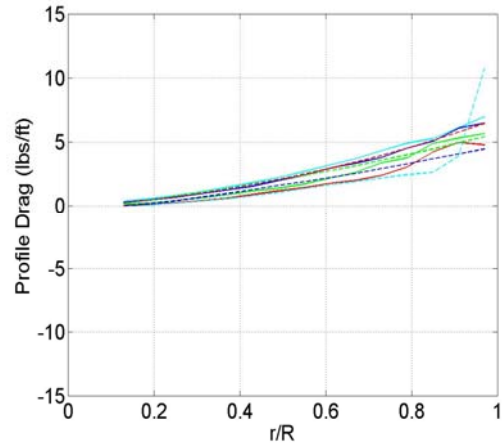
q.) Baseline: Profile Drag (AR=0.1)   **r.) Optimum: Profile Drag (AR=0.1)**
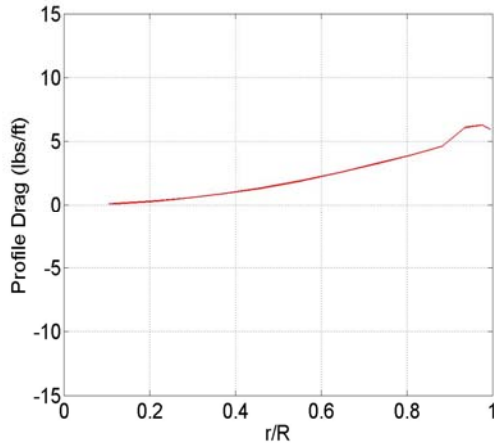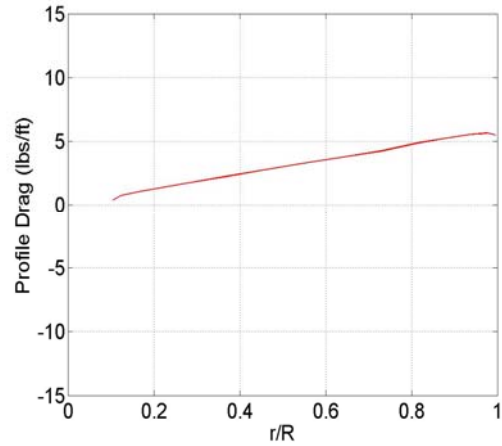
s.) Baseline: Profile Drag (AR=0.0)   **t.) Optimum: Profile Drag (AR=0.0)**

Figure A.10 a-t: Profile Drag Distribution Comparisons: Comparisons of the profile drag distributions (lbs/ft) between the optimum and baseline. Note this is on a different scale than previous drag contour plots.

A.11 Profile Drag Difference Distributions
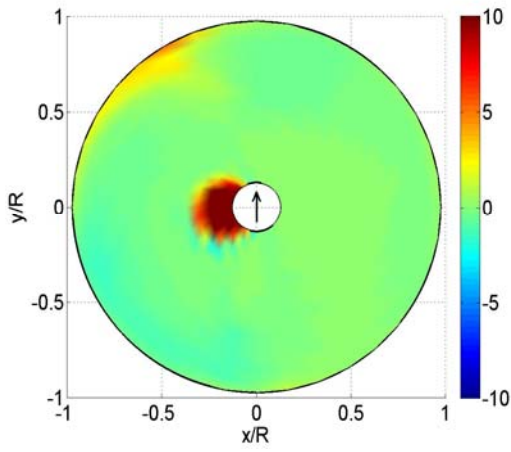
a.) Profile Drag Difference (AR=0.4)
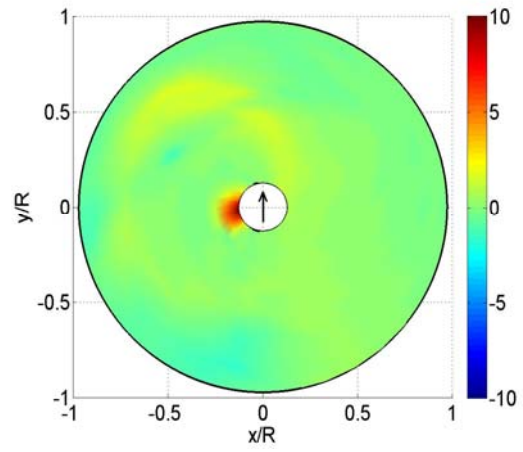
b.) Profile Drag Difference (AR=0.3)
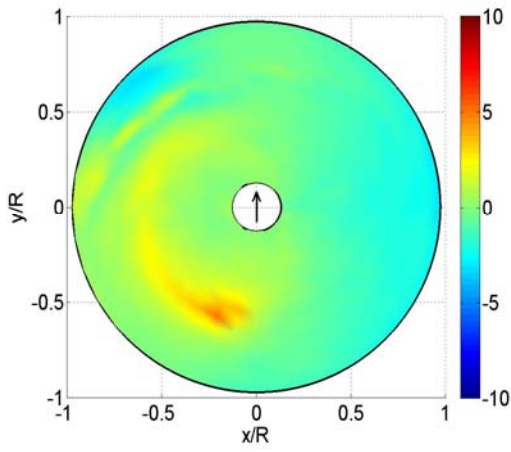
c.) Profile Drag Difference (AR=0.2)
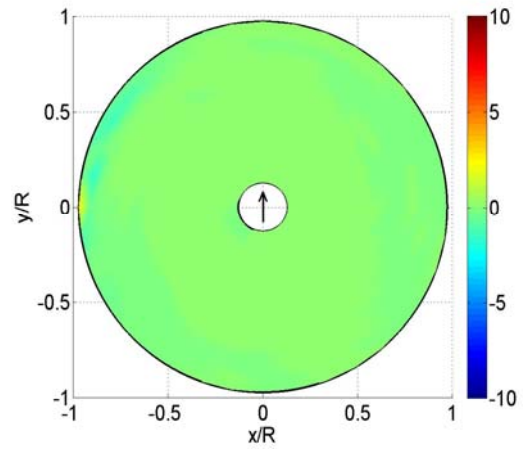
d.) Profile Drag Difference (AR=0.1)
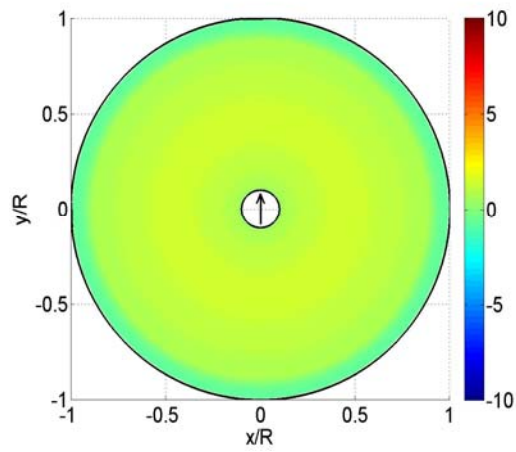
e.) Profile Drag Difference (AR=0.0)
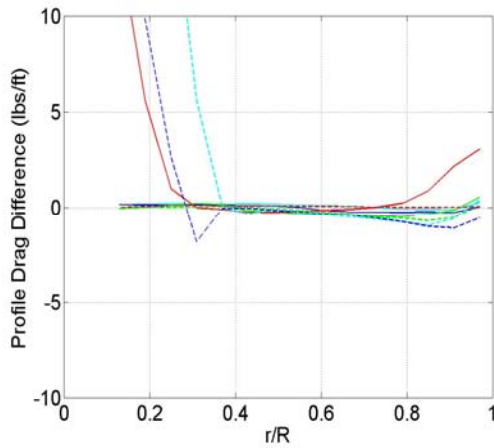
f.) Profile Drag Difference (AR=0.4)
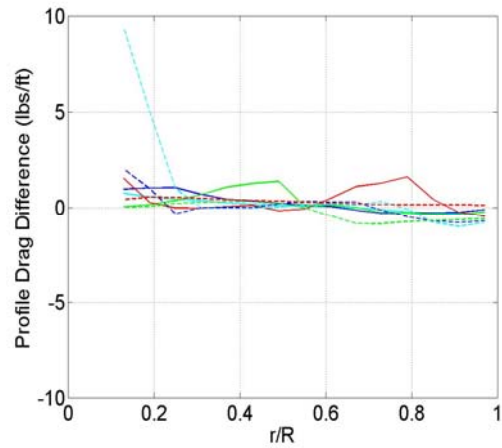
g.) Profile Drag Difference (AR=0.3)
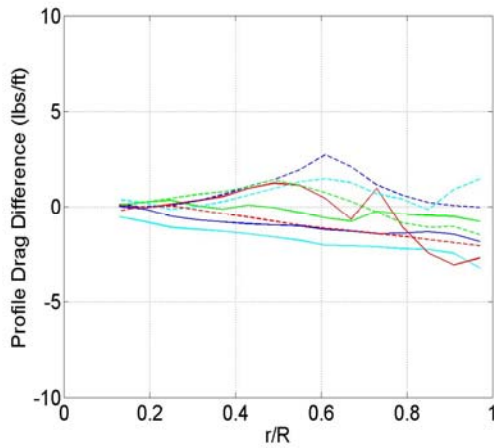
h.) Profile Drag Difference (AR=0.2)
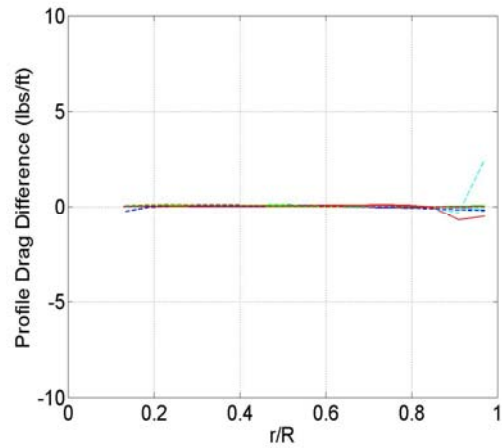
i.) Profile Drag Difference (AR=0.1)
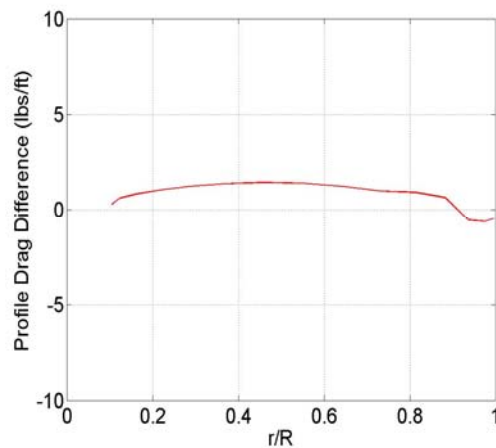
j.) Profile Drag Difference (AR=0.0)

FigureA.11 a-j: Profile Drag Distribution Differences: Difference between the optimum and baseline profile drag distributions (lbs/ft).

A.12 Angle of Attack Distributions
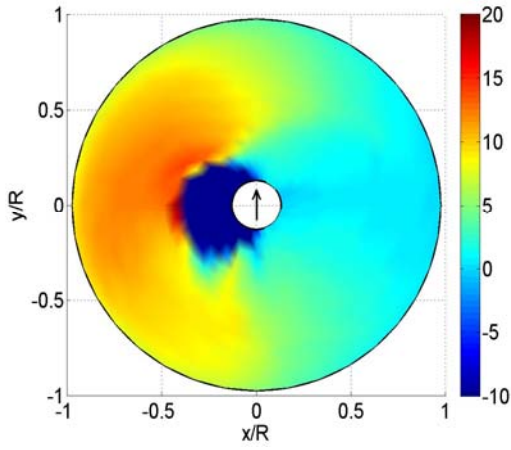
a.) Baseline: Angle of Attack (AR=0.4)
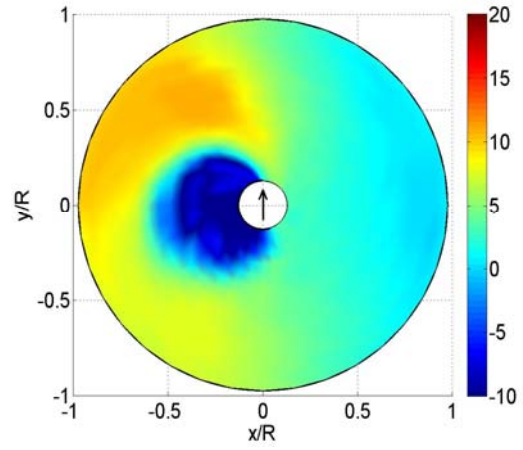
b.) Optimum: Angle of Attack (AR=0.4)
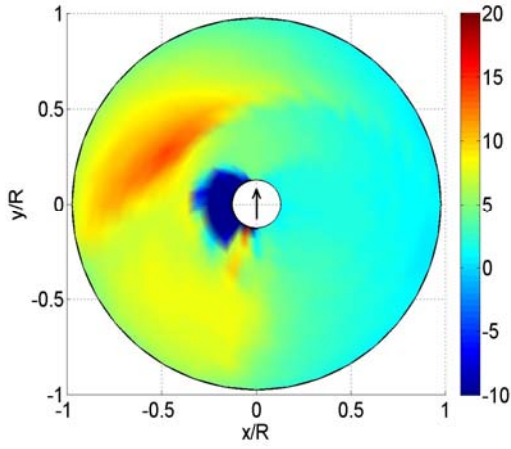
c.) Baseline: Angle of Attack (AR=0.3)
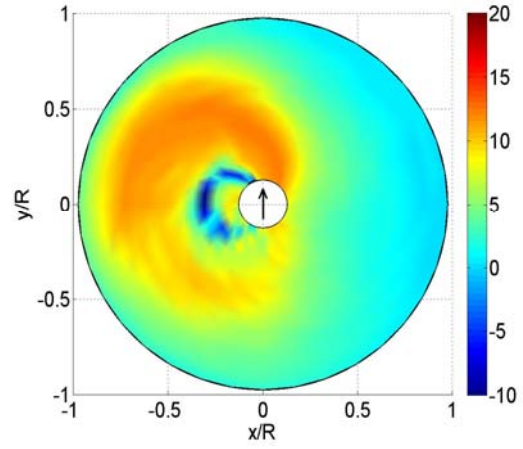
d.) Optimum: Angle of Attack (AR=0.3)
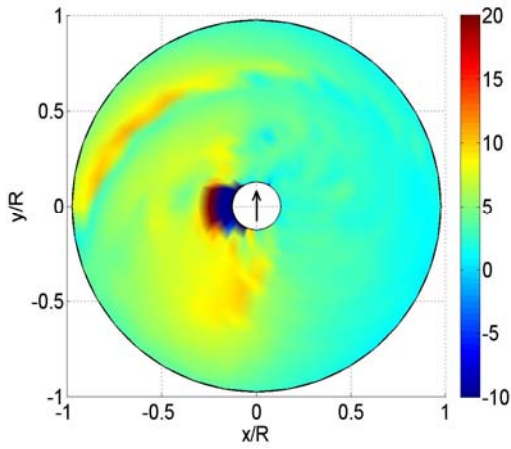
e.) Baseline: Angle of Attack (AR=0.2)
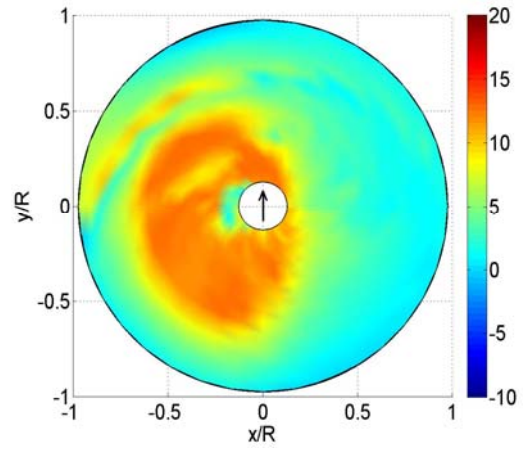
f.) Optimum: Angle of Attack (AR=0.2)
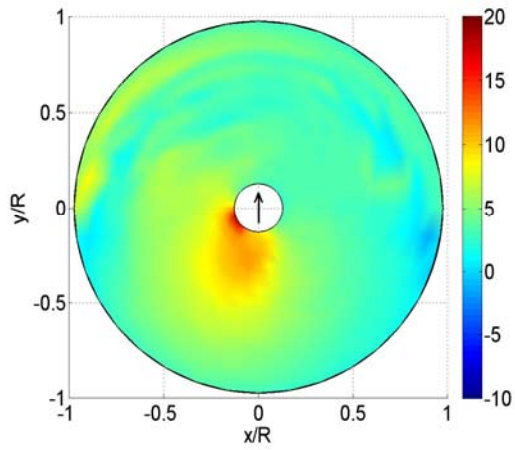
g.) Baseline: Angle of Attack (AR=0.1)
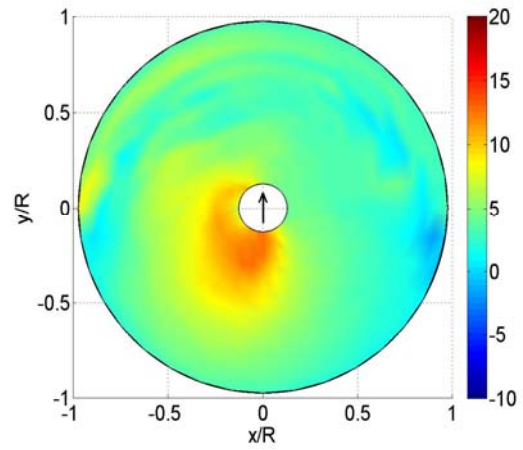
h.) Optimum: Angle of Attack (AR=0.1)
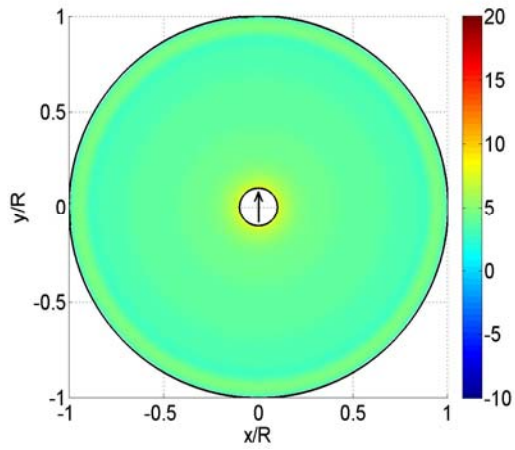
i.) Baseline: Angle of Attack (AR=0.0)
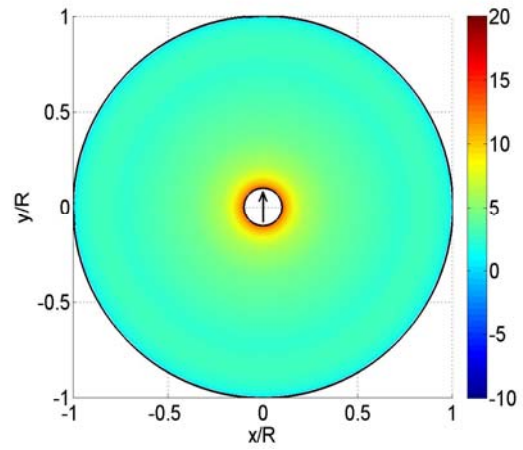
j.) Optimum: Angle of Attack (AR=0.0)
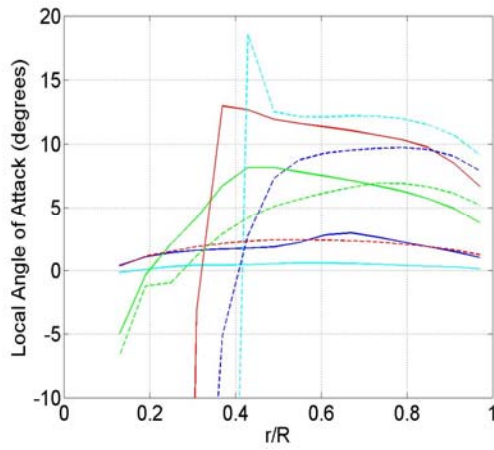
k.) Baseline: Angle of Attack (AR=0.4)
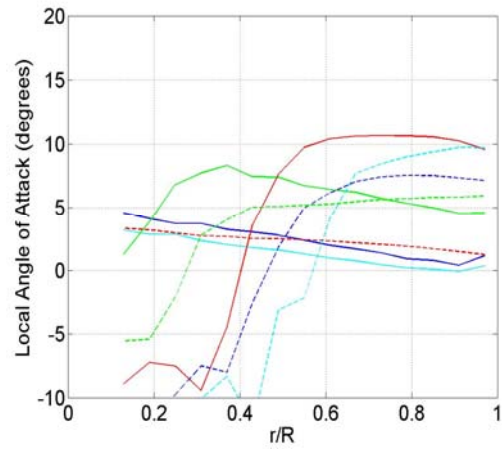
l.) Optimum: Angle of Attack (AR=0.4)
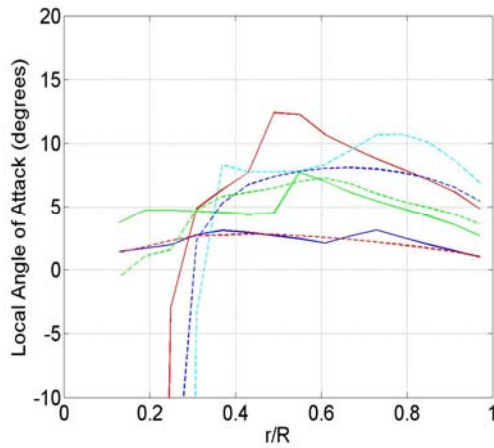
m.) Baseline: Angle of Attack (AR=0.3)
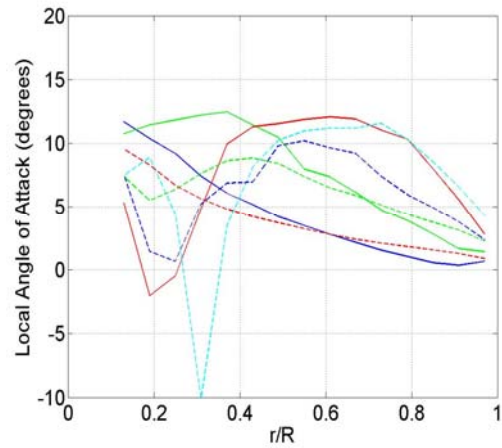
n.) Optimum: Angle of Attack (AR=0.3)
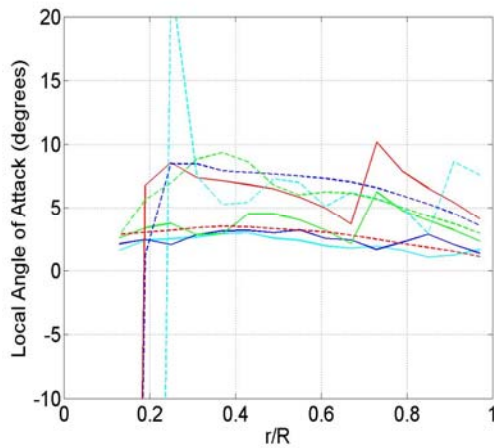
o.) Baseline: Angle of Attack (AR=0.2)
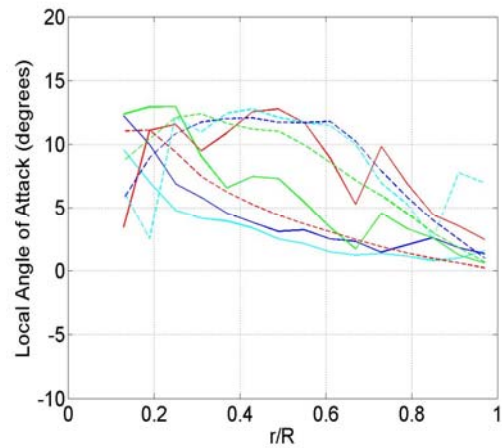
p.) Optimum: Angle of Attack (AR=0.2)
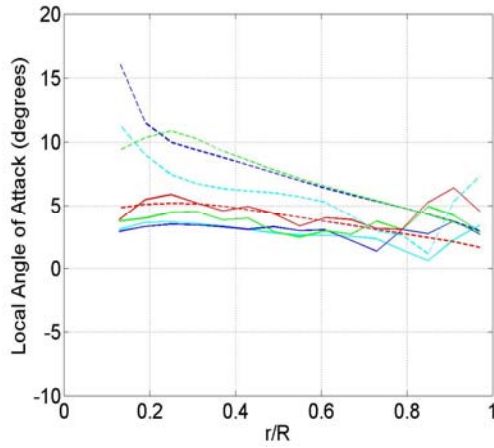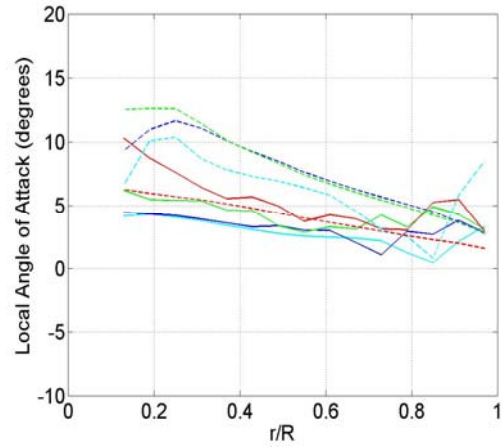
q.) Baseline: Angle of Attack (AR=0.1)   **r.) Optimum: Angle of Attack (AR=0.1)**
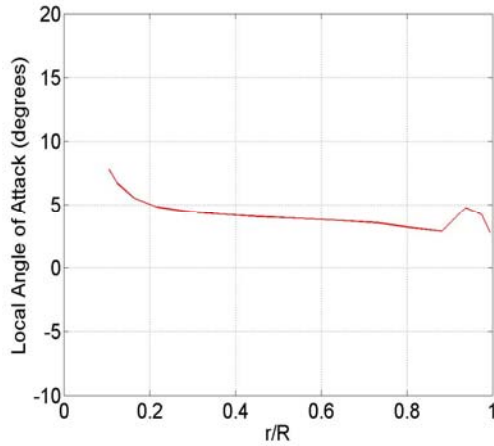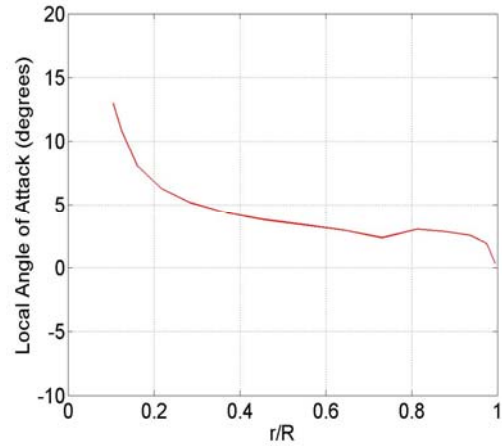
s.) Baseline: Angle of Attack (AR=0.0)   **t.) Optimum: Angle of Attack (AR=0.0)**

Figure A.12 a-t: Local Angle of Attack Distribution Comparisons: Comparison of the local angle of attack distribution (degrees) between the optimum and baseline.

A.13 Angle of Attack Difference Distributions
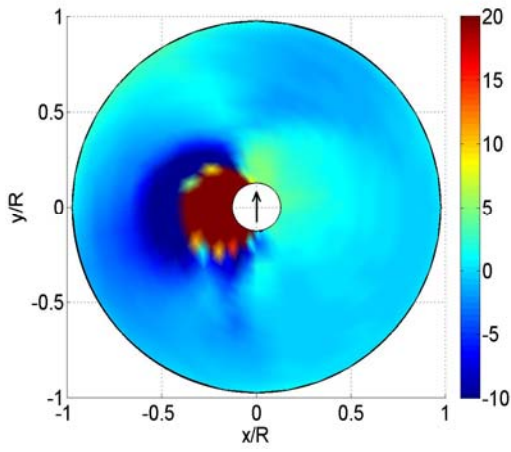
a.) Angle of Attack Difference (AR=0.4)
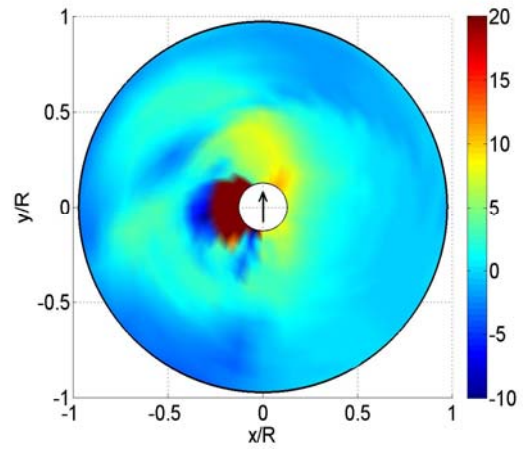
b.) Angle of Attack Difference (AR=0.3)
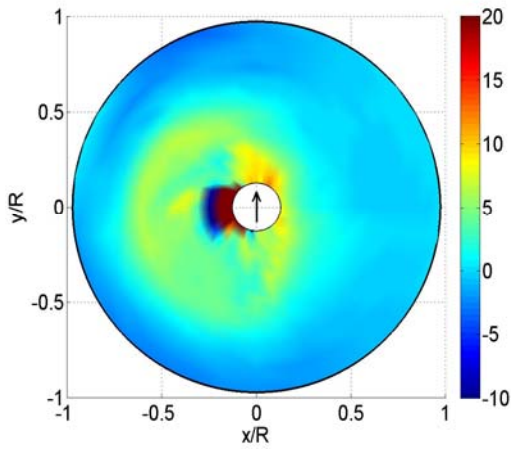
c.) Angle of Attack Difference (AR=0.2)
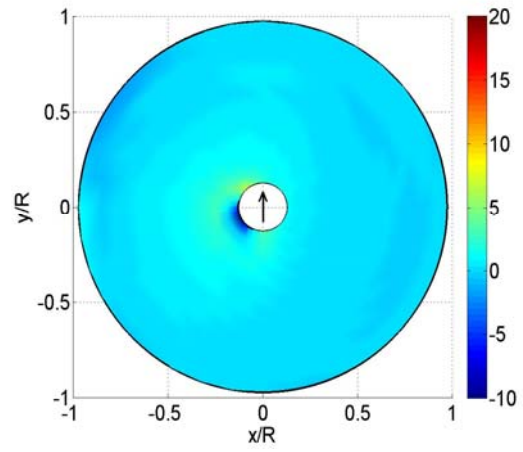
d.) Angle of Attack Difference (AR=0.1)
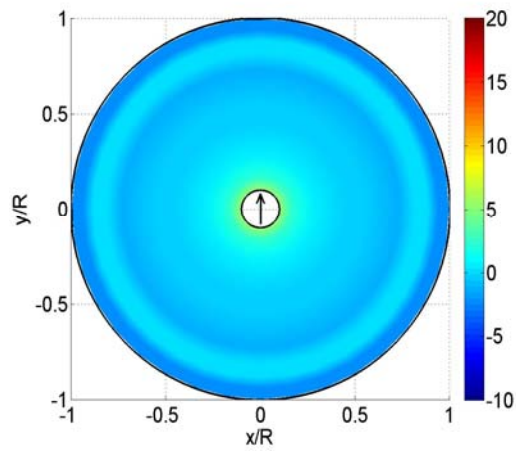
e.) Angle of Attack Difference (AR=0.0)
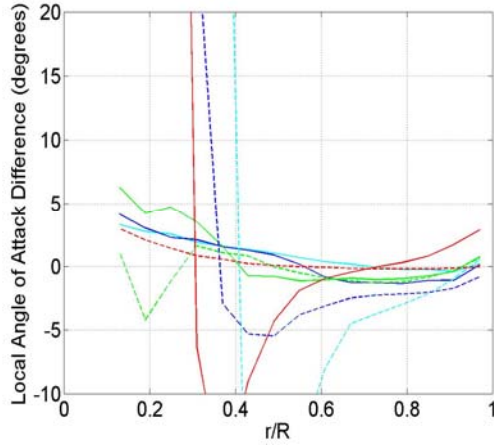
f.) Angle of Attack Difference (AR=0.4)
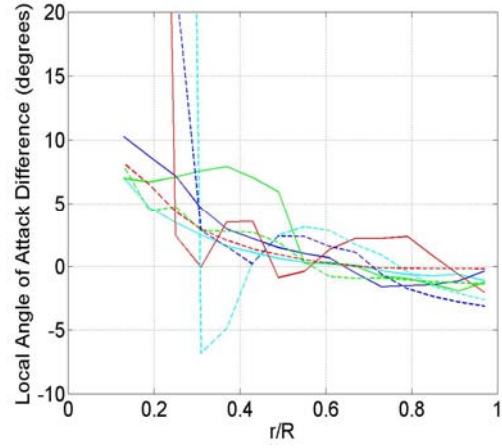
g.) Angle of Attack Difference (AR=0.3)
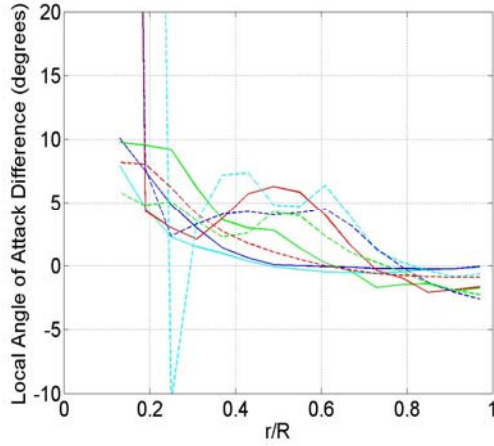
h.) Angle of Attack Difference (AR=0.2)
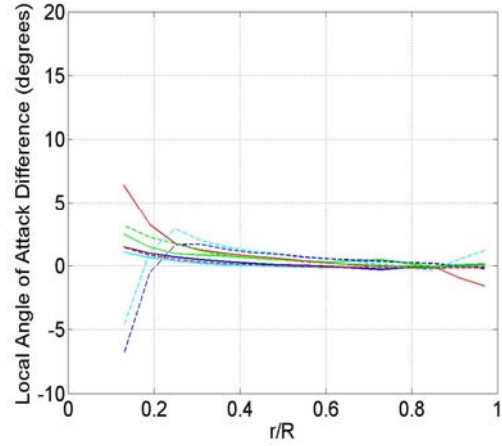
i.) Angle of Attack Difference (AR=0.1)
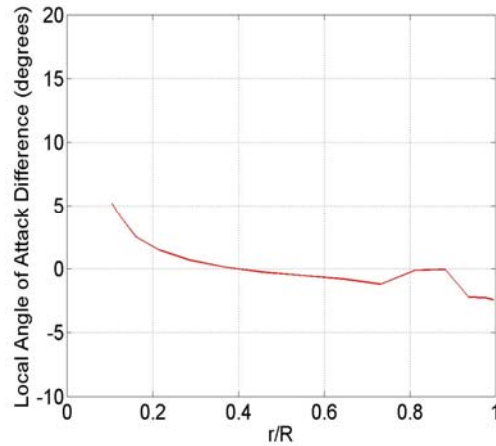
j.) Angle of Attack Difference (AR=0.0)

Figure A.13 a-j: Local Angle of Attack Distribution Differences: Difference between the local angle of attack distribution (degrees) between the optimum and baseline.
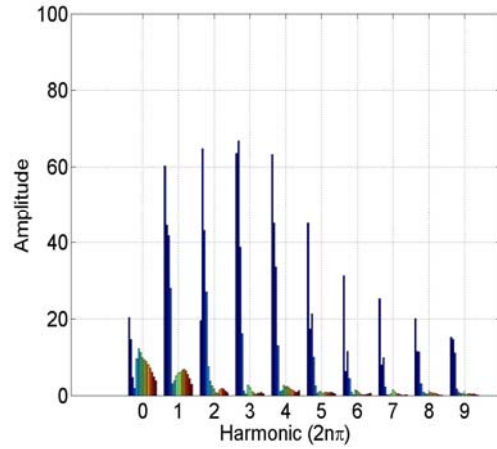
A.14 Pitch Distributions
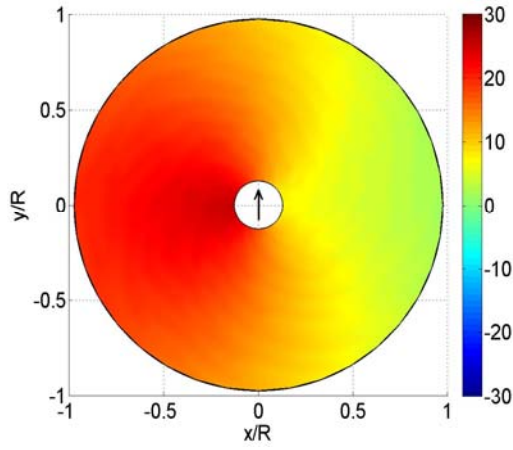
a.) Baseline: Pitch (AR=0.4)
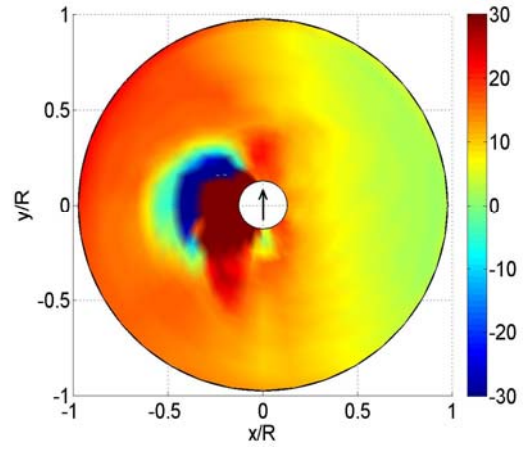
b.) Optimum: Pitch (AR=0.4)
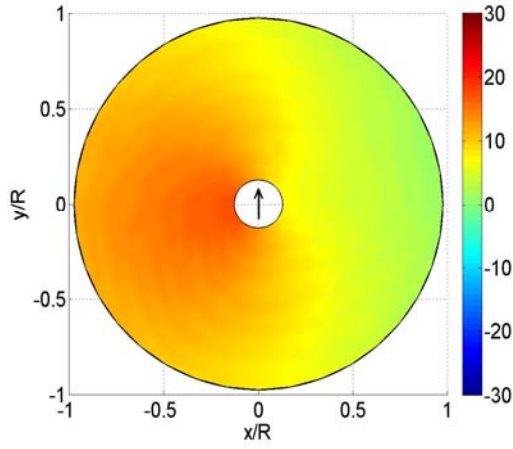
c.) Baseline: Pitch (AR=0.3)
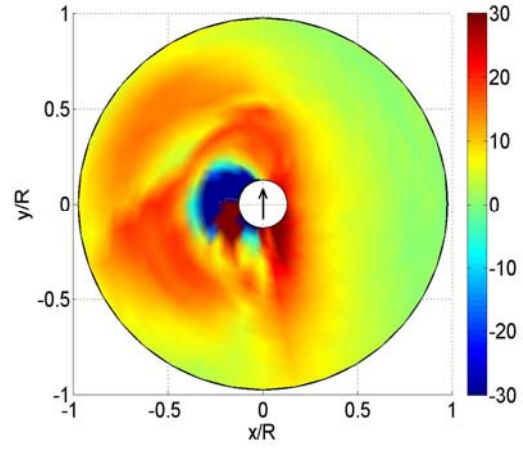
d.) Optimum: Pitch (AR=0.3)
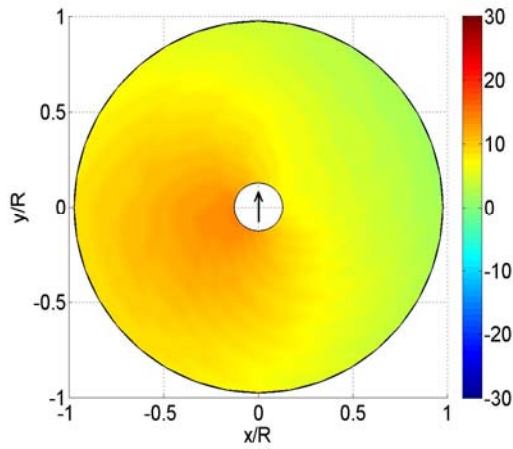
e.) Baseline: Pitch (AR=0.2)
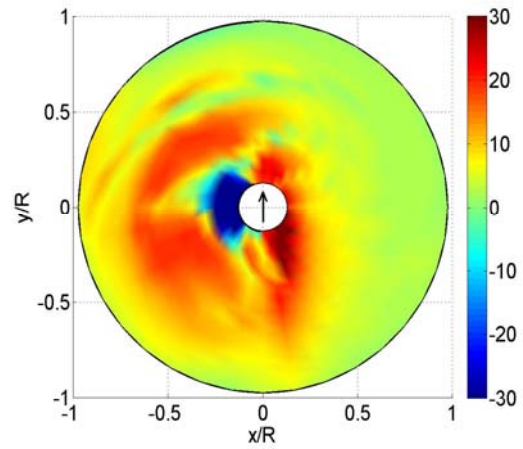
f.) Optimum: Pitch (AR=0.2)
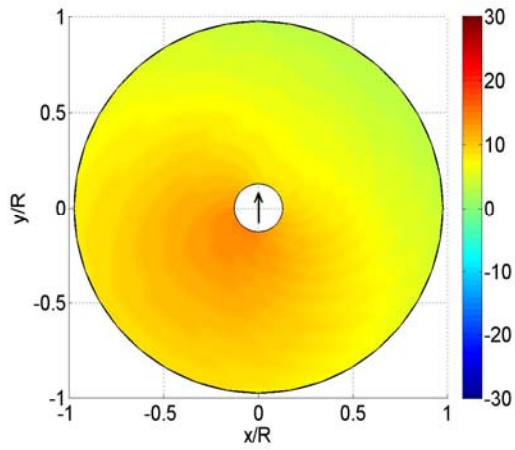
g.) Baseline: Pitch (AR=0.1)
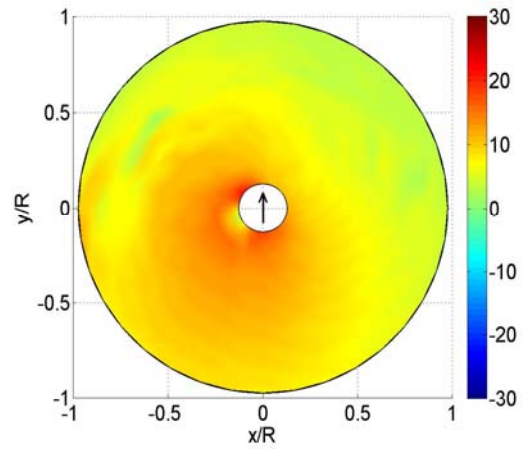
h.) Optimum: Pitch (AR=0.1)
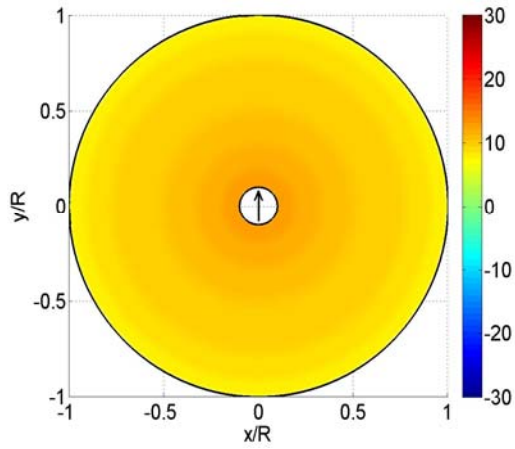
i.) Baseline: Pitch (AR=0.0)
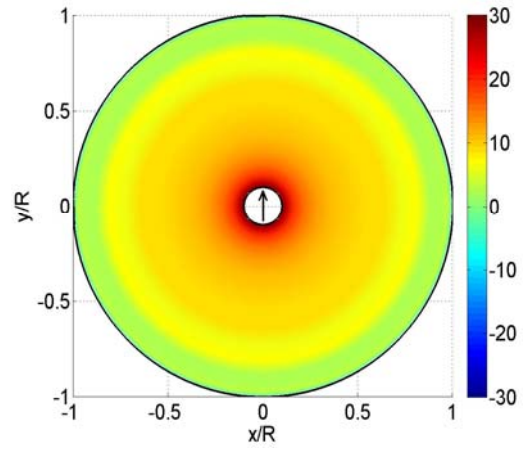
j.) Optimum: Pitch (AR=0.0)
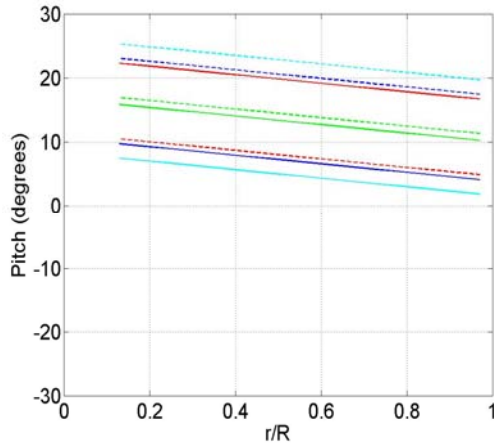
k.) Baseline: Pitch (AR=0.4)
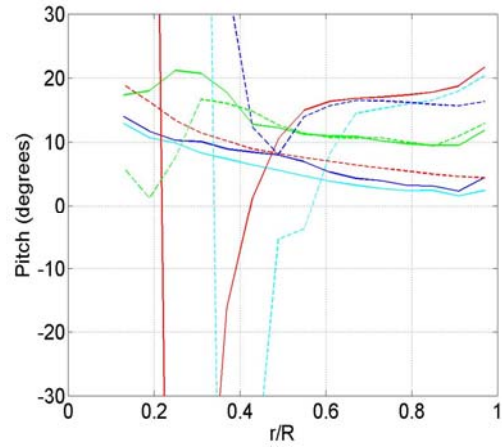
l.) Optimum: Pitch (AR=0.4)
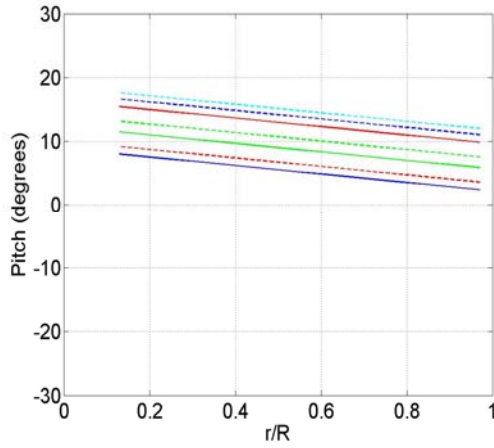
m.) Baseline: Pitch (AR=0.3)
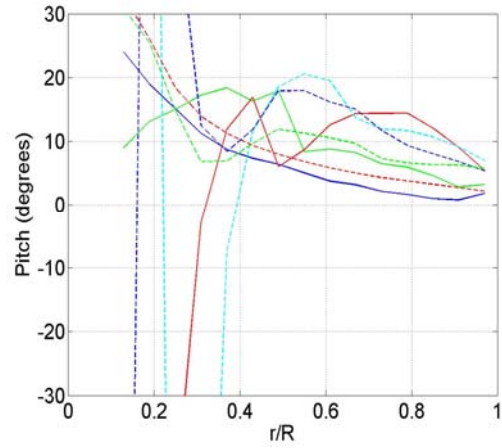
n.) Optimum: Pitch (AR=0.3)
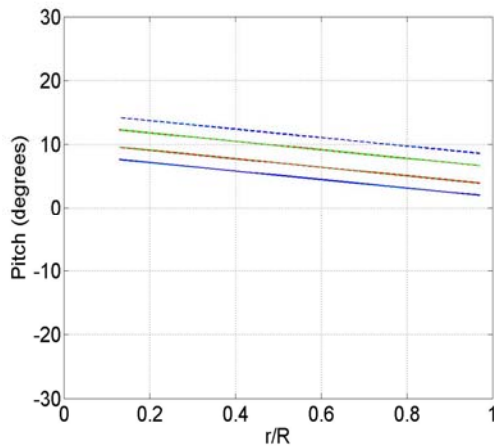
o.) Baseline: Pitch (AR=0.2)
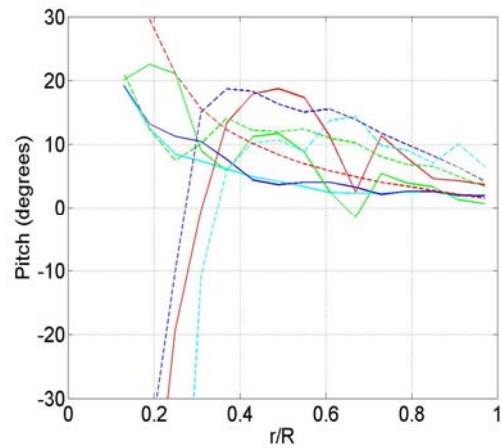
p) Optimum: Pitch (AR=0.2)

141
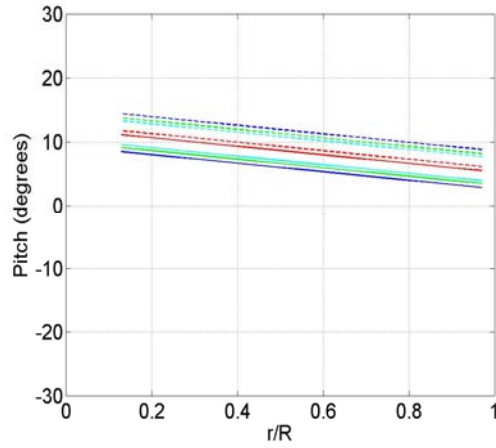
q.) Baseline: Pitch (AR=0.1)
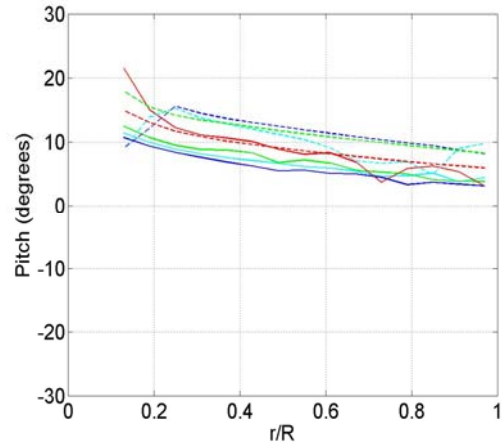
r.) Optimum: Pitch (AR=0.1)
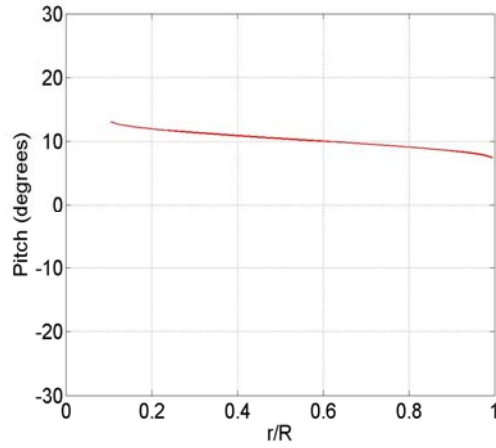
s.) Baseline: Pitch (AR=0.0)
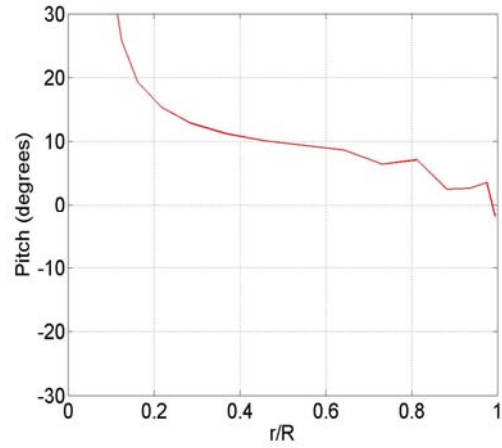
t.) Optimum: Pitch (AR=0.0)

Figure A.14 a-t: Pitch Distribution Comparisons: Close-up comparison of the pitch distribution (degrees) between the optimum and baseline. The reverse flow region is obscured by the scale.

A.15 Pitch Difference Distributions
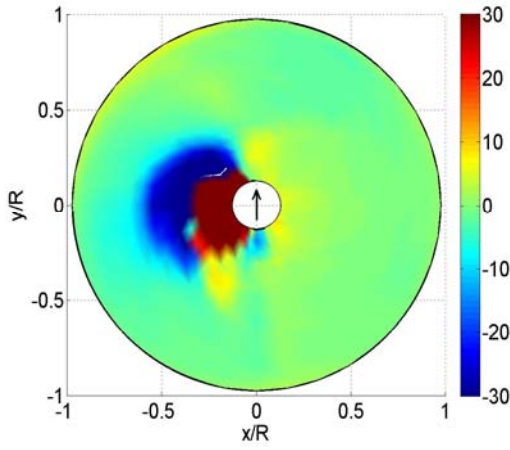
a.) Pitch Difference (AR=0.4)
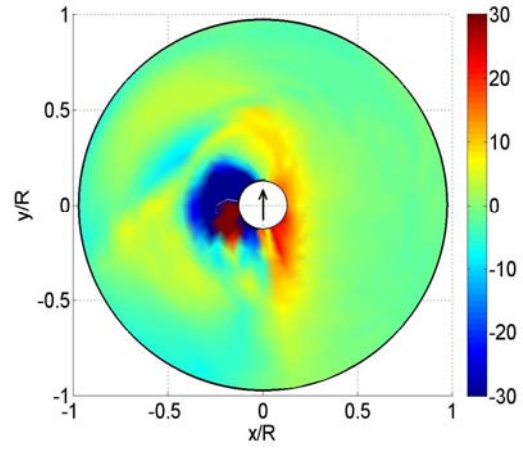
b.) Pitch Difference (AR=0.3)
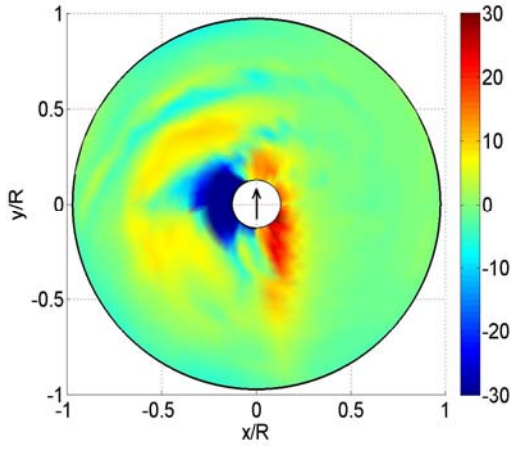
c.) Pitch Difference (AR=0.2)
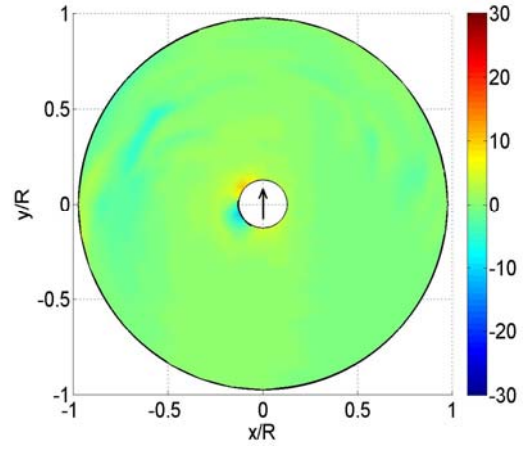
d.) Pitch Difference (AR=0.1)
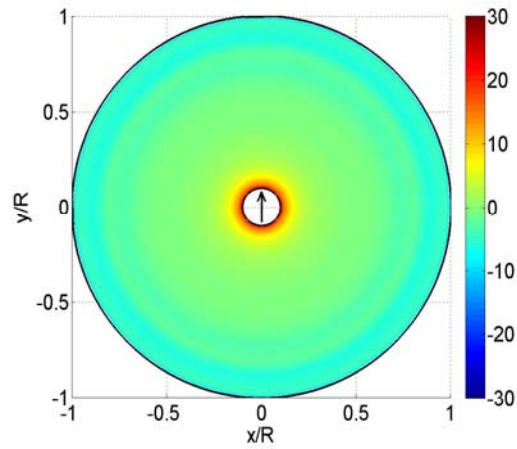
e.) Pitch Difference (AR=0.0)
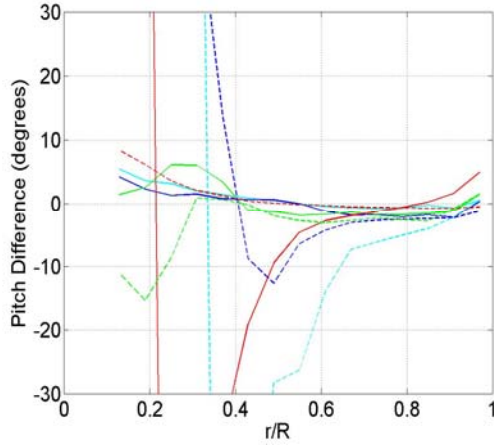
f.) Pitch Difference (AR=0.4)
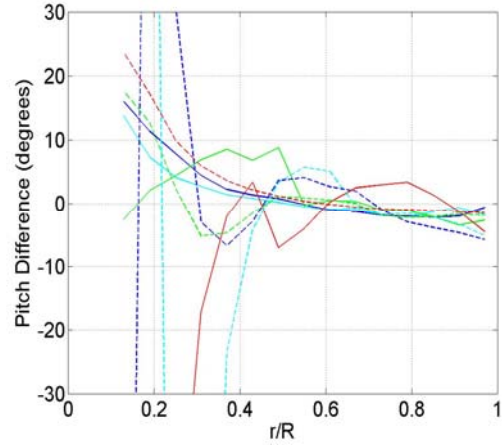
g.) Pitch Difference (AR=0.3)
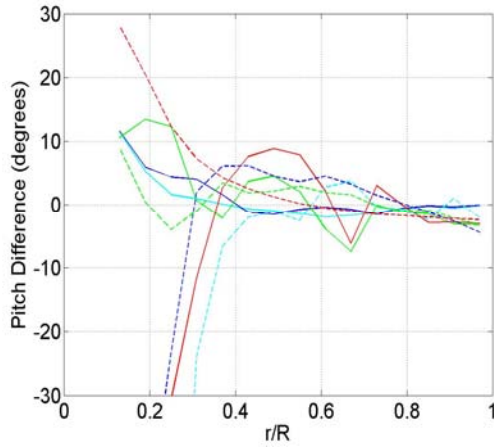
h.) Pitch Difference (AR=0.2)
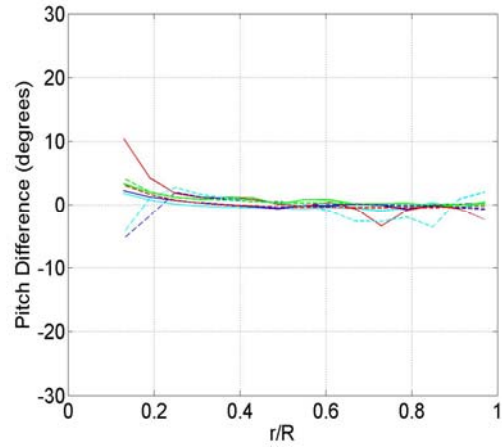
i.) Pitch Difference (AR=0.1)
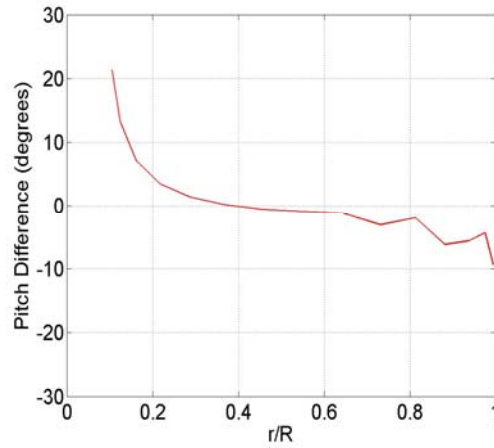
j.) Pitch Difference (AR=0.0)

Figure A.15 a-j: Pitch Distribution Differences: Difference between the optimum and baseline pitch distributions (degrees). The reverse flow region is obscured by the scale.

A.16 Inflow Distributions
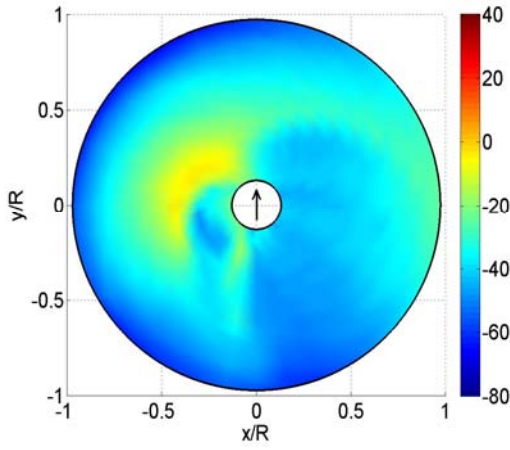
a.) Baseline: Inflow (AR=0.4)
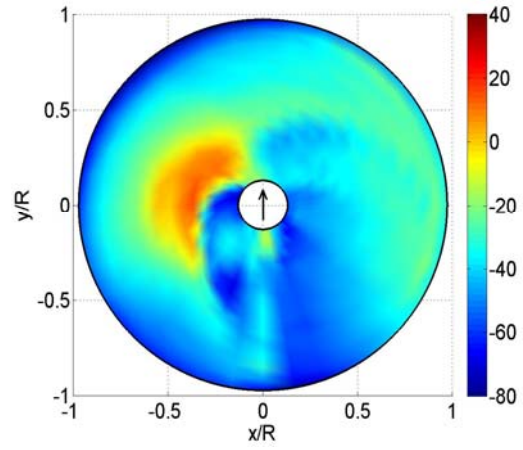
b.) Optimum: Inflow (AR=0.4)
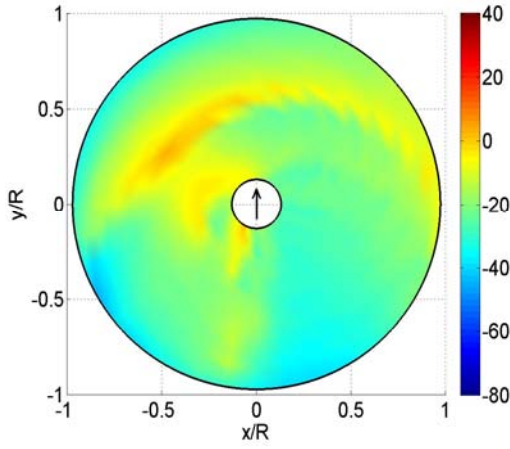
c.) Baseline: Inflow (AR=0.3)
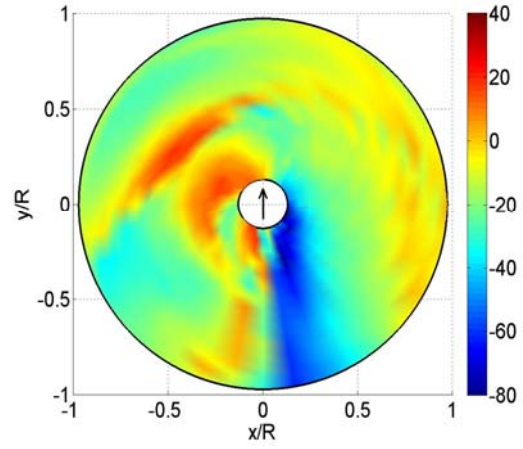
d.) Optimum: Inflow (AR=0.3)
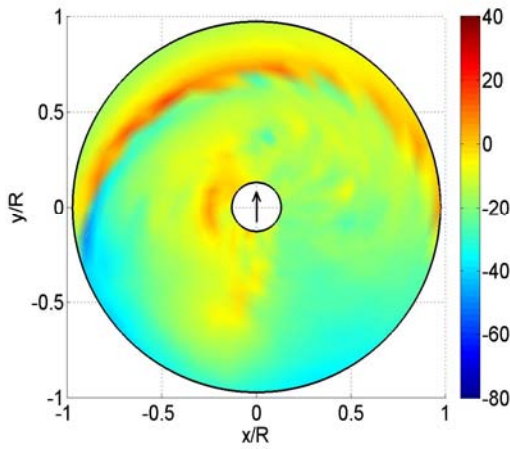
e.) Baseline: Inflow (AR=0.2)

f.) Optimum: Inflow (AR=0.2)

145
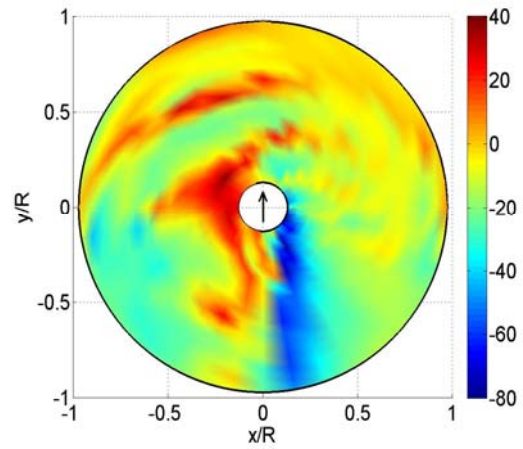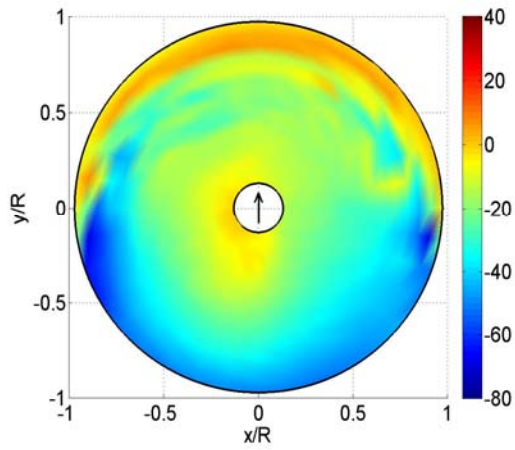
g.) Baseline: Inflow (AR=0.1)
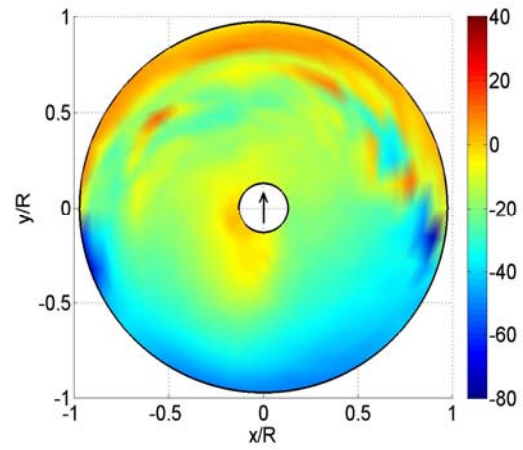
h.) Optimum: Inflow (AR=0.1)
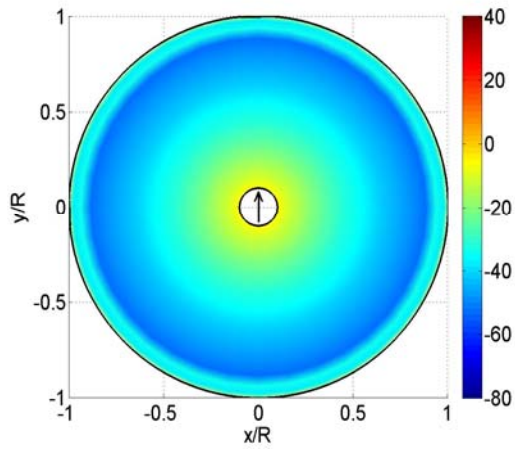
i.) Baseline: Inflow (AR=0.0)
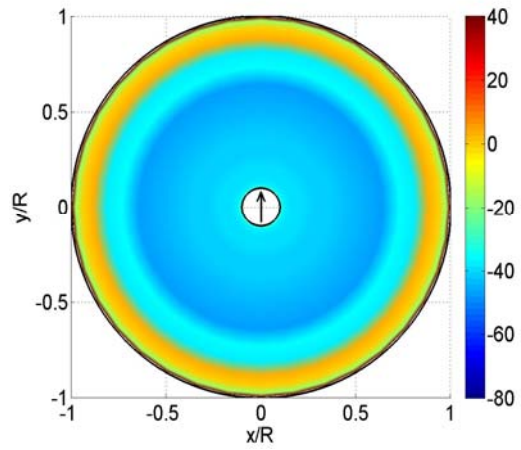
j.) Optimum: Inflow (AR=0.0)
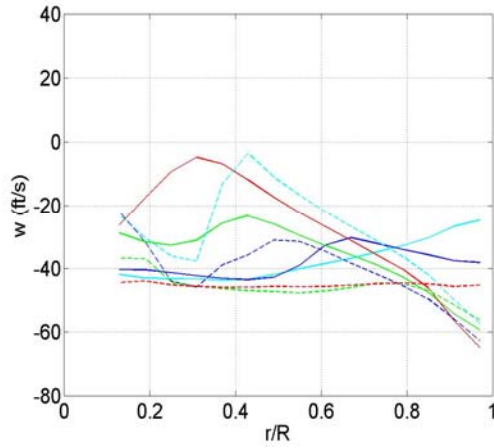
k.) Baseline: Inflow (AR=0.4)
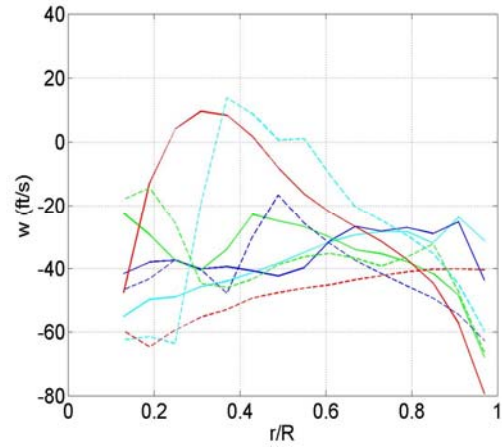
l.) Optimum: Inflow (AR=0.4)
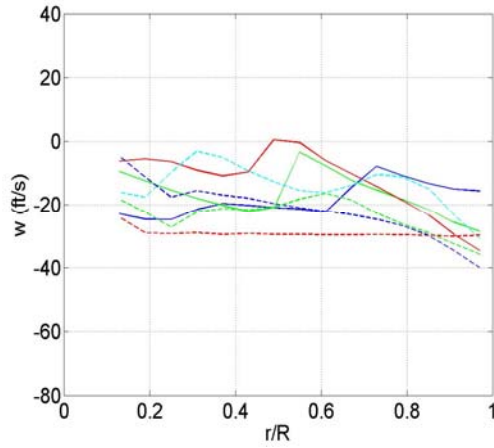
m.) Baseline: Inflow (AR=0.3)
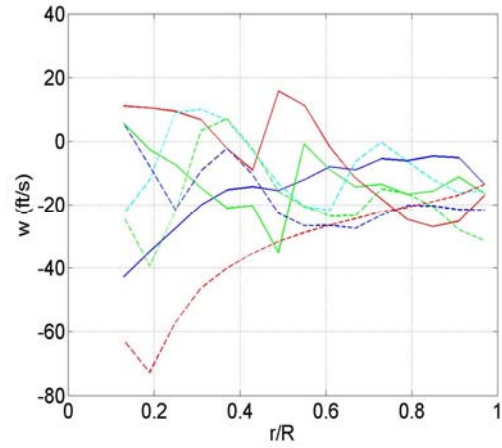
n.) Optimum: Inflow (AR=0.3)
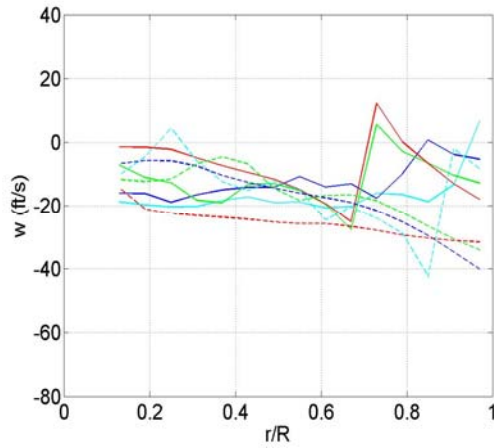
o.) Baseline: Inflow (AR=0.2)
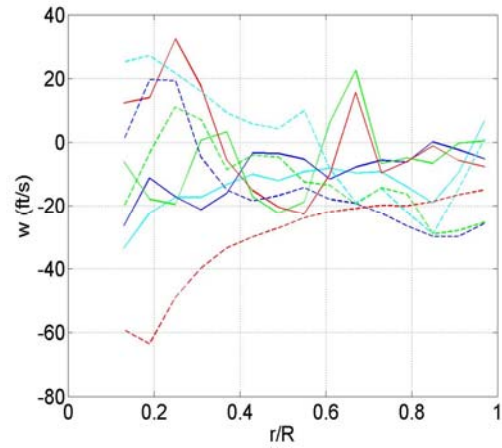
p) Optimum: Inflow (AR=0.2)

147
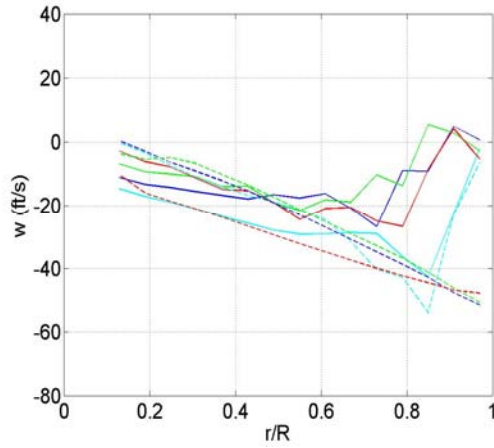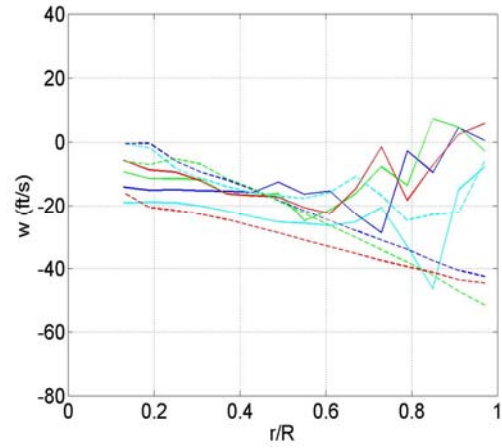
q.) Baseline: Inflow (AR=0.1)   **r.) Optimum: Inflow (AR=0.1)**
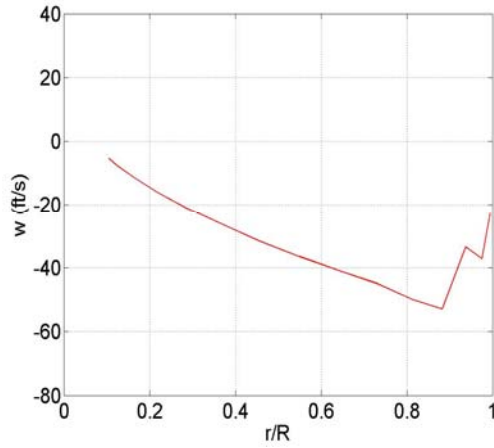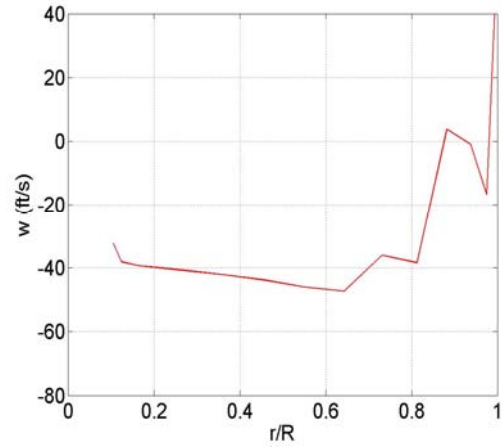
s.) Baseline: Inflow (AR=0.0)   **t.) Optimum: Inflow (AR=0.0)**

Figure A.16 a-t: Inflow Distribution Comparisons: Close-up comparison of the Inflow distribution (ft/s) between the optimum and baseline. The reverse flow region is obscured by the scale.

A.17 Inflow Difference Distributions
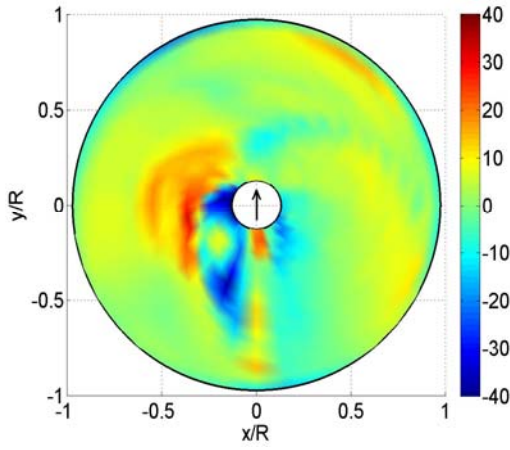
a.) Inflow Difference (AR=0.4)
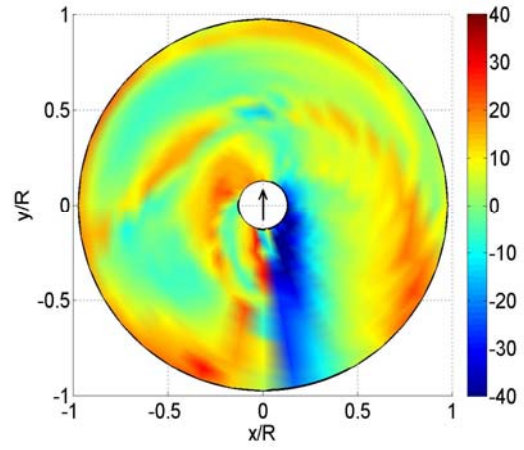
b.) Inflow Difference (AR=0.3)
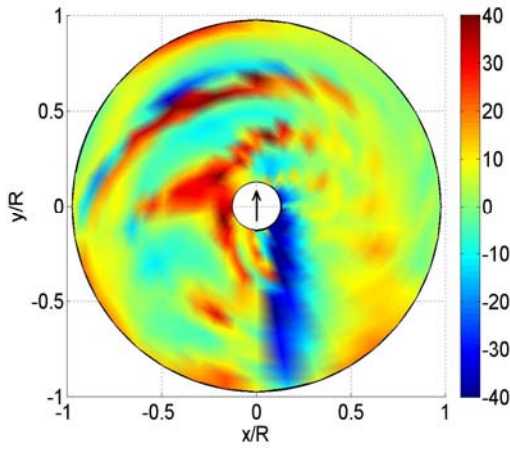
c.) Inflow Difference (AR=0.2)
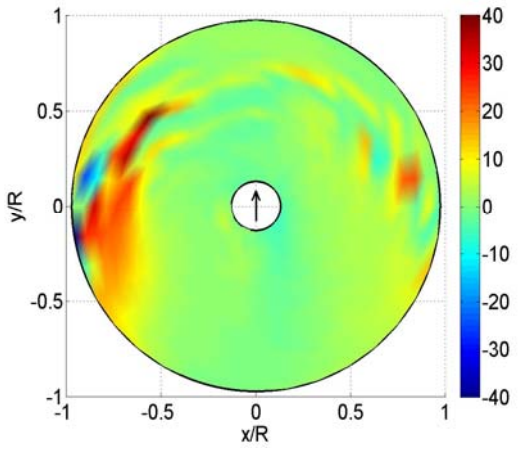
d.) Inflow Difference (AR=0.1)
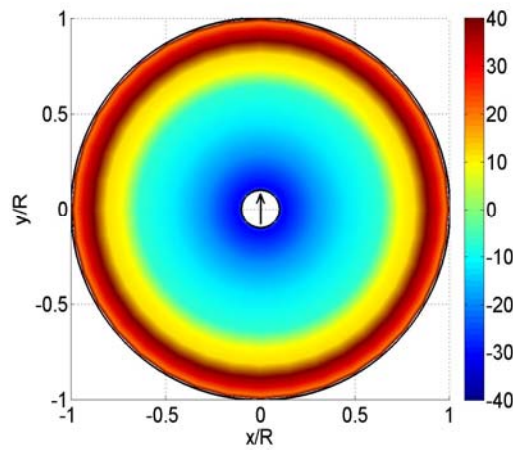
e.) Inflow Difference (AR=0.0)
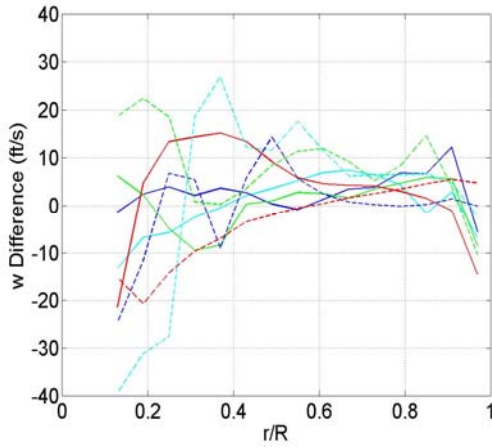
f.) Inflow Difference (AR=0.4)
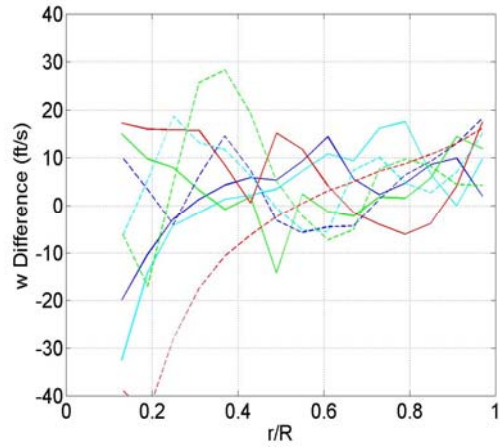
g.) Inflow Difference (AR=0.3)
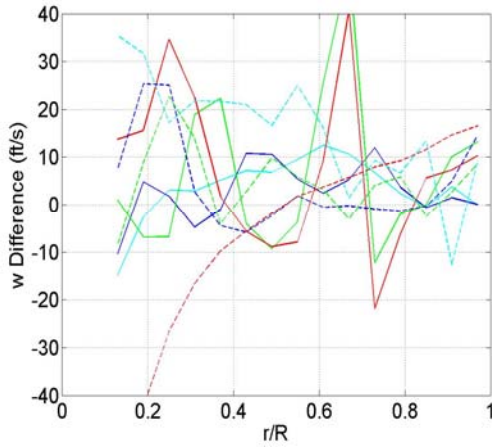
h.) Inflow Difference (AR=0.2)
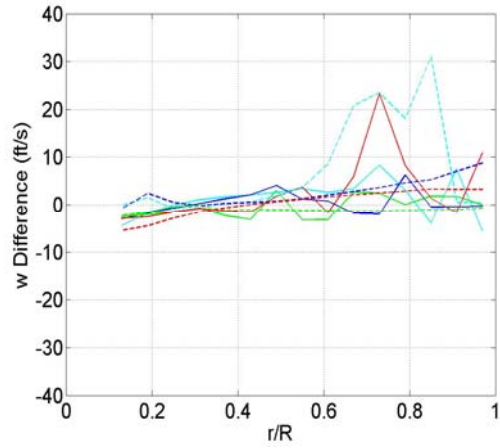
i.) Inflow Difference (AR=0.1)
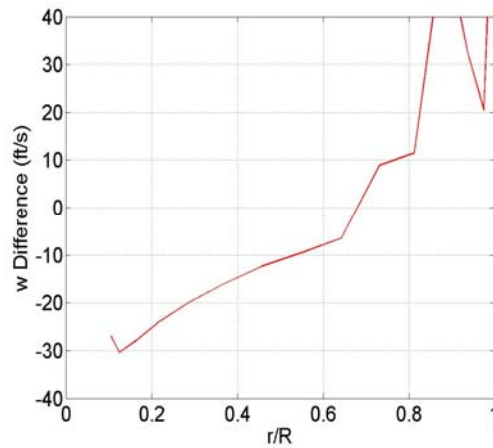
j.) Inflow Difference (AR=0.0)

Figure A.17 a-j: Inflow Distribution Differences: Difference between the optimum and baseline Inflow distributions (ft/s).

Appendix B: Fourier Decomposition

## B.1: Amplitude Fourier Decomposition of the Pitch Distributions
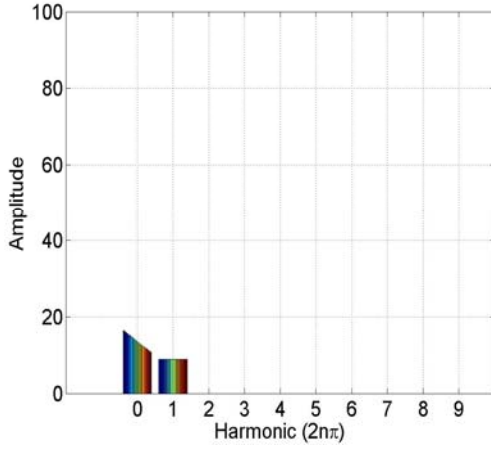
a.) Baseline: Pitch Amplitude (AR=0.4)
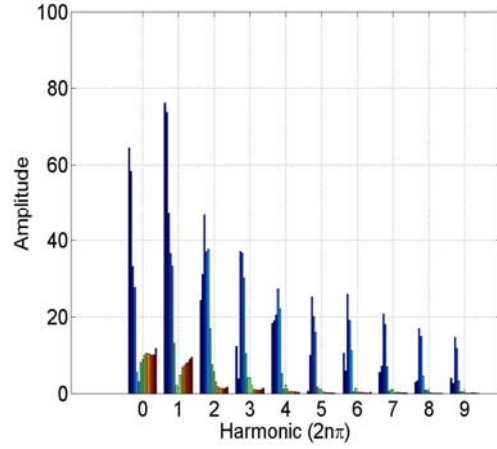
b.) Optimum: Pitch Amplitude (AR=0.4)
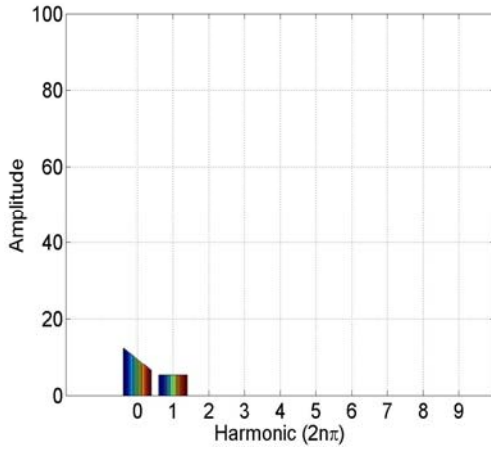
c.) Baseline: Pitch Amplitude (AR=0.3)

d.) Optimum: Pitch Amplitude (AR=0.3)
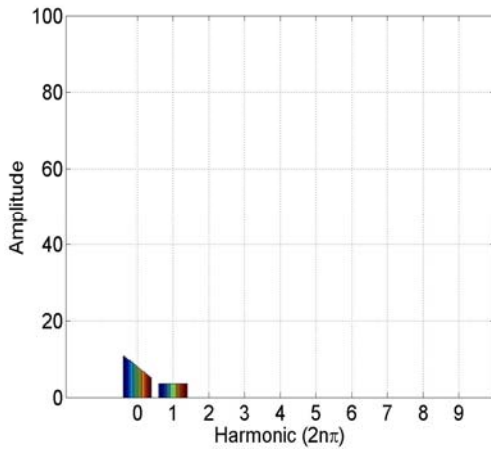
e.) Baseline: Twist Amplitude (AR=0.2)
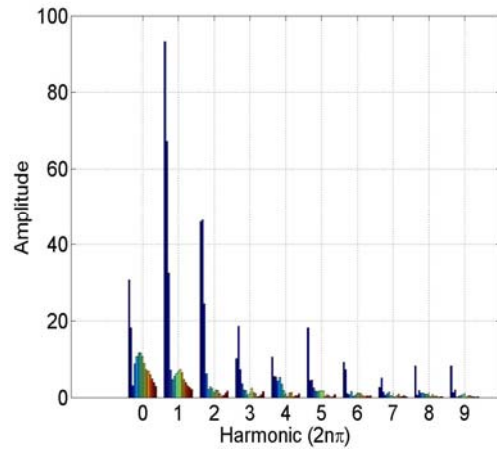
f.) Optimum: Pitch Amplitude (AR=0.2)

151
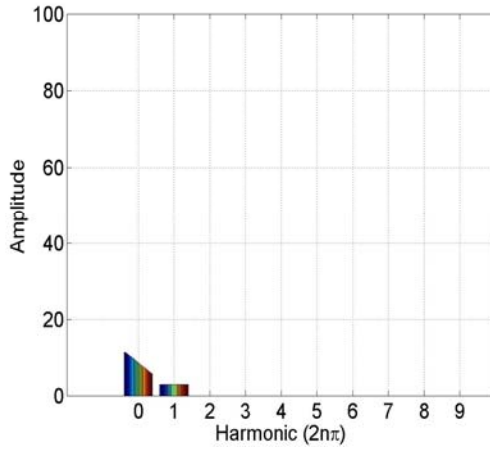
g.) Baseline: Pitch Amplitude (AR=0.1)
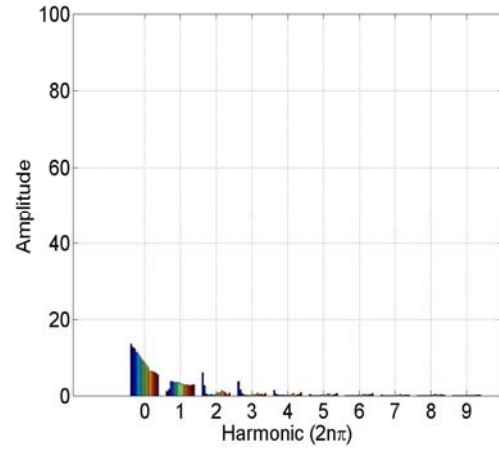
h.) Optimum: Pitch Amplitude (AR=0.1)
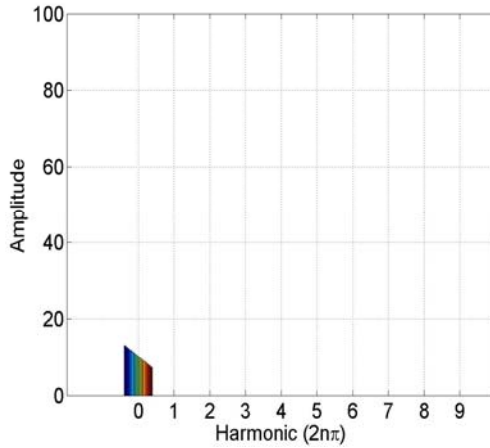
i.) Baseline: Pitch Amplitude (AR=0.0)
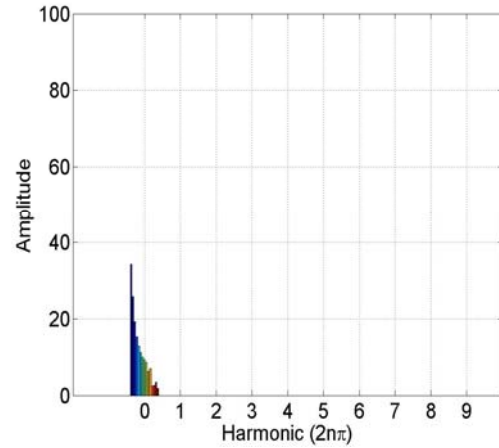
j.) Optimum: Pitch Amplitude (AR=0.0)

Figure B.1 a-j: Amplitude Fourier Decomposition of Pitch: Comparison of the pitch distribution for the baseline and optimum. Blue represents the most inboard radial location and progresses toward the tip represented by red.

B.2: **Phase Fourier Decomposition of the Pitch Distributions**
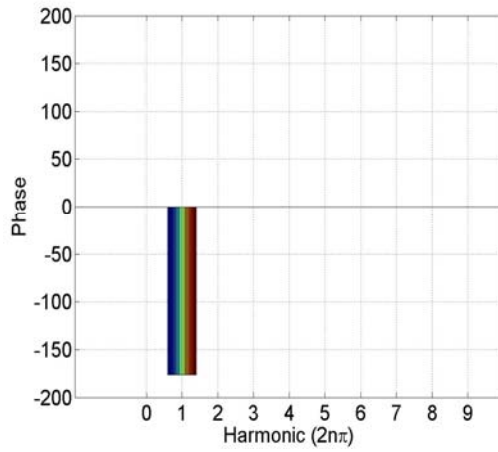
a.) Baseline: Pitch Phase (AR=0.4)
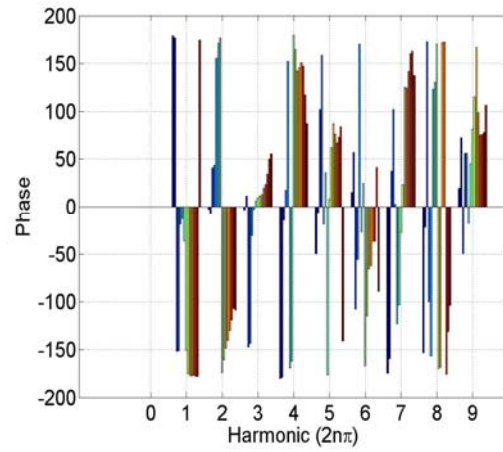
b.) Optimum: Pitch Phase (AR=0.4)
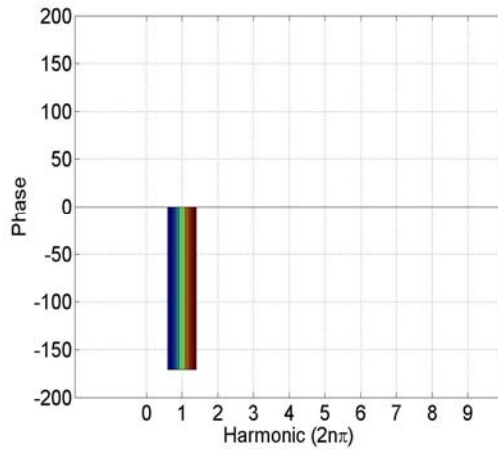
c.) Baseline: Pitch Phase (AR=0.3)
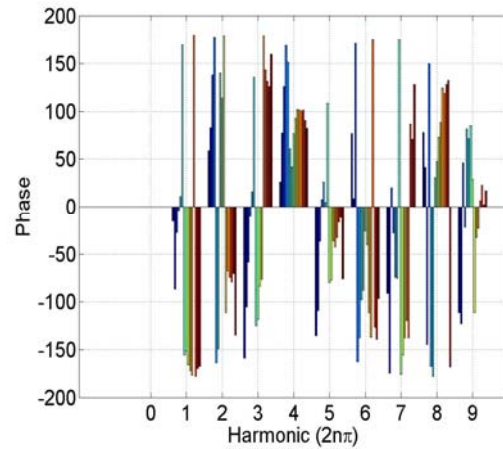
d.) Optimum: Pitch Phase (AR=0.3)
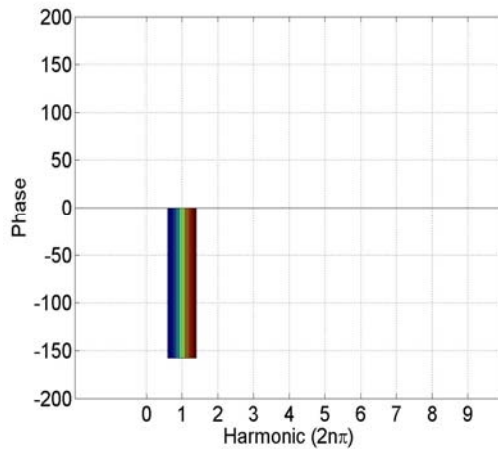
e.) Baseline: Pitch Phase (AR=0.2)
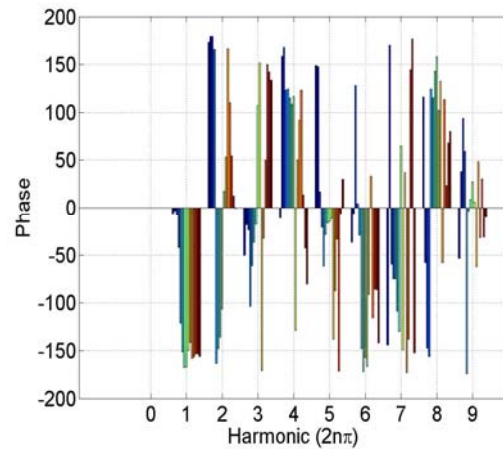
f.) Optimum: Pitch Phase (AR=0.2)
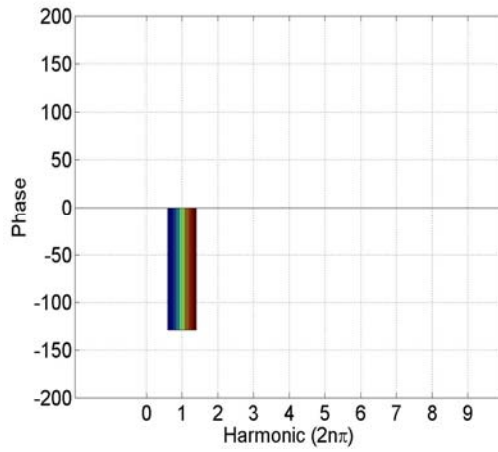
g.) Baseline: Pitch Phase (AR=0.1)   **h.) Optimum: Pitch Phase (AR=0.1)**
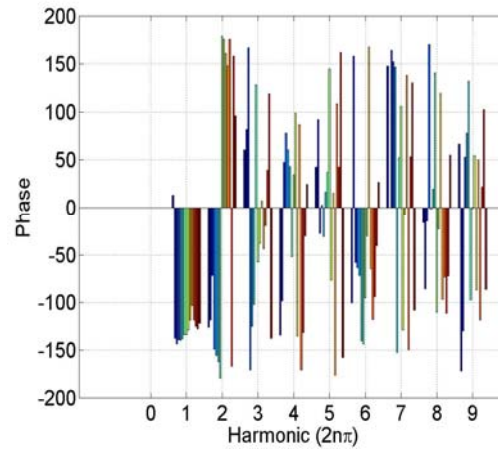
Figure B.2 a-h: Phase Fourier Decomposition of Pitch: Comparison of the pitch distribution for the baseline and optimum. Blue represents the most inboard radial location and progresses toward the tip represented by red.

B.3:   Amplitude Fourier Decomposition of the Circulation Distributions
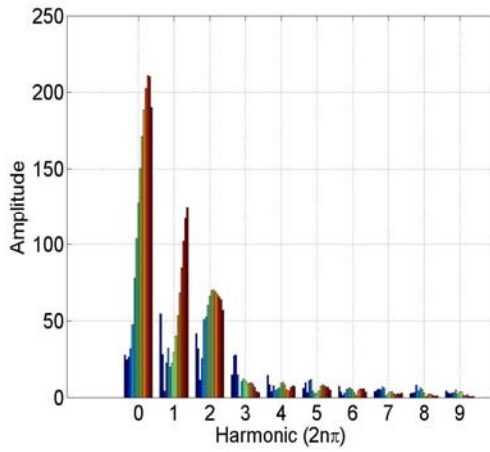
a.) Baseline: Circulation Amplitude (AR=0.4)
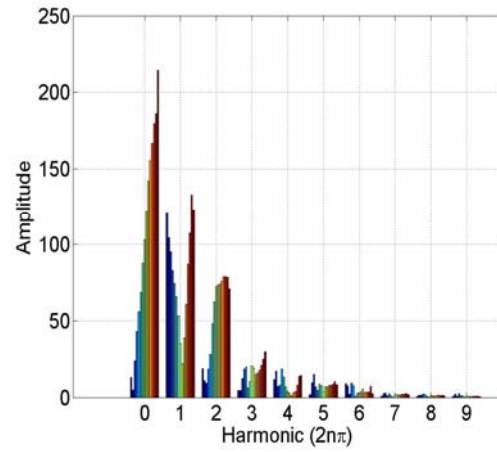
b.) Optimum: Circulation Amplitude (AR=0.4)
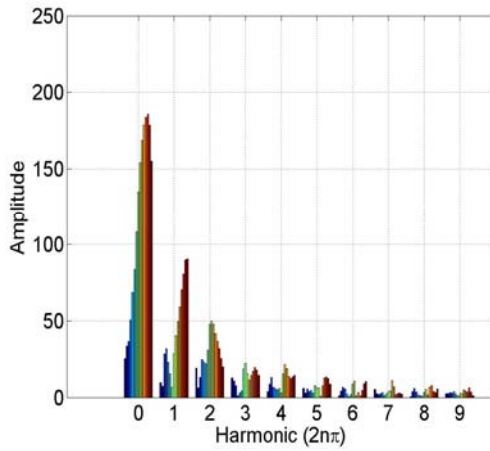
c.) Baseline: Circulation Amplitude (AR=0.3)
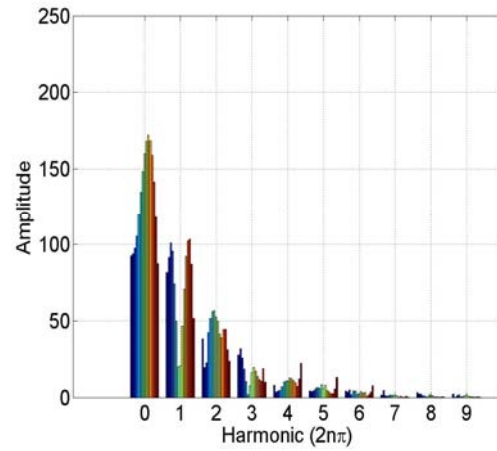
d.) Optimum: Circulation Amplitude (AR=0.3)
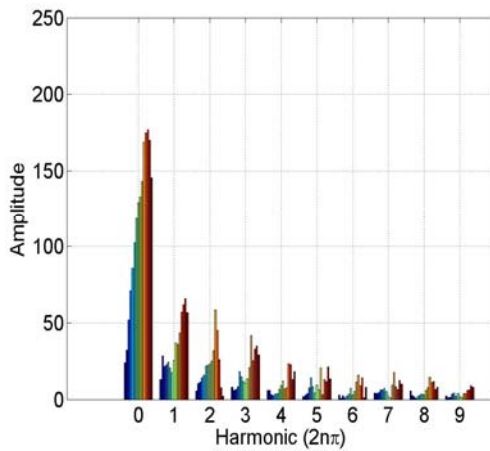
e.) Baseline: Circulation Amplitude (AR=0.2)
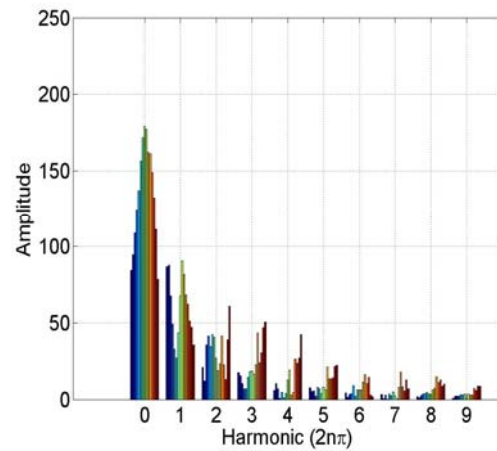
f.) Optimum: Circulation Amplitude (AR=0.2)
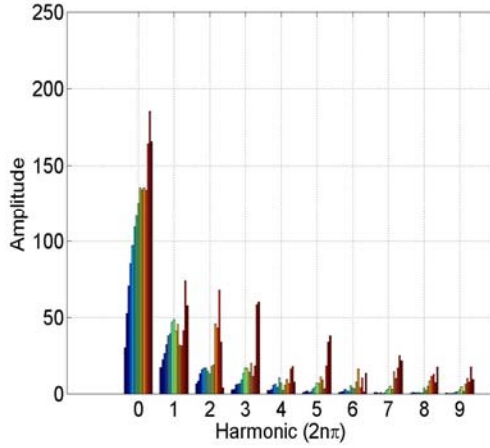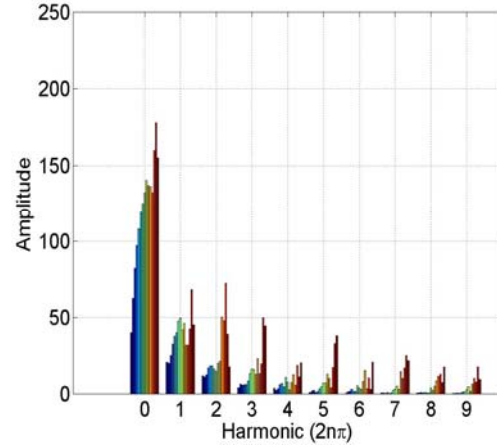
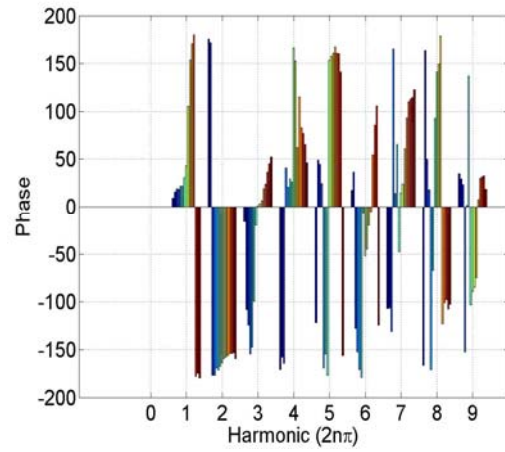**g.) Baseline: Circulation Amplitude (AR=0.1)**   **h.) Optimum: Circulation Amplitude (AR=0.1)**
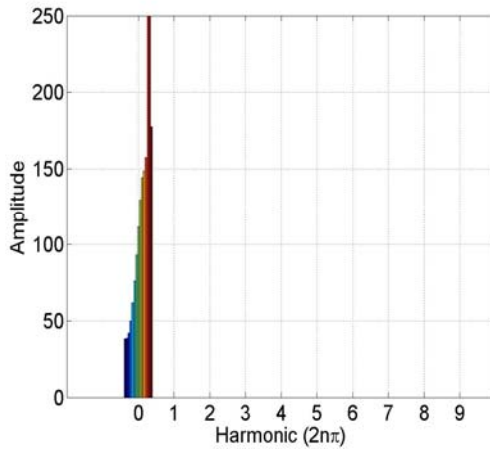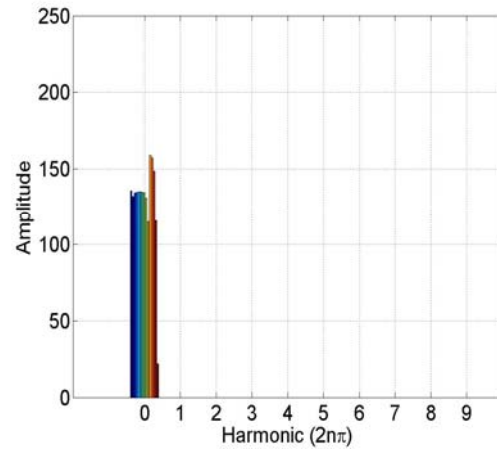
i.) Baseline: Circulation Amplitude (AR=0.0)   **j.) Optimum: Circulation Amplitude (AR=0.0)**

Figure B.3 a-j: Amplitude Fourier Decomposition of Circulation: Comparison of the circulation distribution for the baseline and optimum. Blue represents the most inboard radial location and progresses toward the tip represented by red.
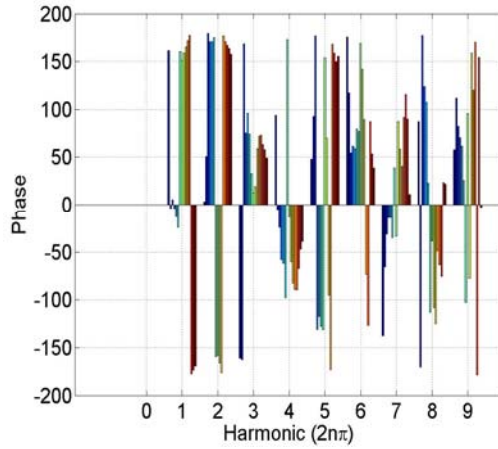
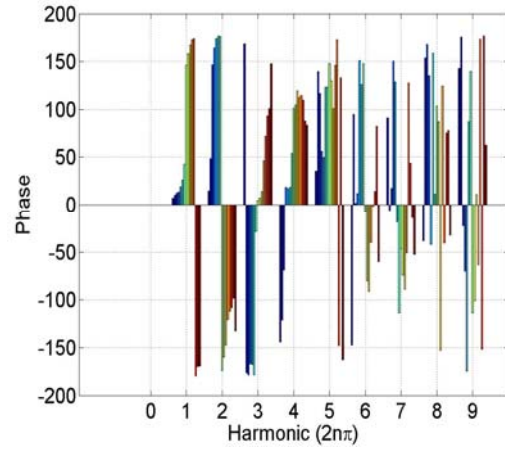**B.4:   Phase Fourier Decomposition of the Circulation Distributions**
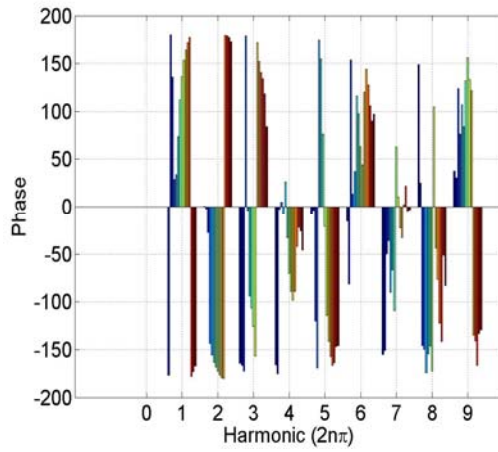
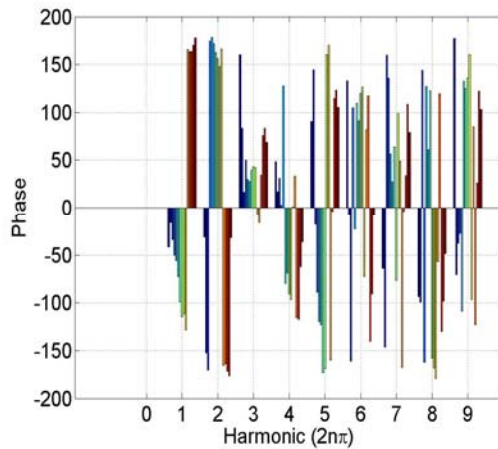a.) Baseline: Circulation Phase (AR=0.4)
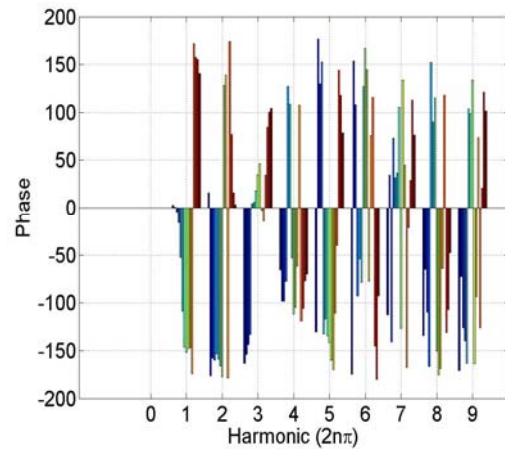
b.) Optimum: Circulation Phase (AR=0.4)

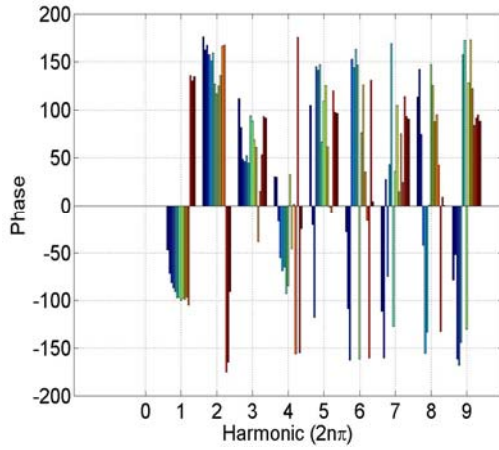c.) Baseline: Circulation Phase (AR=0.3)

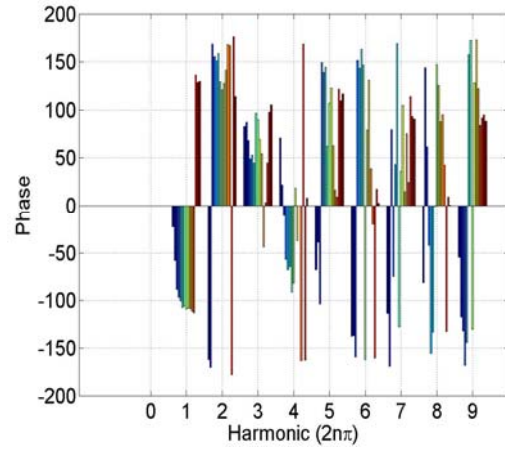d.) Optimum: Circulation Phase (AR=0.3)

e.) Baseline: Circulation Phase (AR=0.2)

f.) Optimum: Circulation Phase (AR=0.2)

g.) Baseline: Circulation Phase (AR=0.1)   **h.) Optimum: Circulation Phase (AR=0.1)**

Figure B.4 a-h: Phase Fourier Decomposition of Circulation: Comparison of the circulation distribution for the baseline and optimum. Blue represents the most inboard radial location and progresses toward the tip represented by red.